

# Lead-Free Piezoelectric Ceramics

Vom Fachbereich Material- und Geowissenschaften der  
Technischen Universität Darmstadt

zur Erlangung des akademischen Grades  
**Doktor-Ingenieur**  
(Dr.-Ing.)

Genehmigte Dissertation von  
**Klaus Seifert, MPhys**  
aus Mönchengladbach

Referent:	Prof. Dr. Jürgen Rödel
Korreferent:	Prof. Dr. Karsten Albe

Tag der Einreichung:	29.07.2010
Tag der mündlichen Prüfung:	07.12.2010

Darmstadt 2010  
D17

Bitte zitieren Sie dieses Dokument als:

URN: urn:nbn:de:tuda-tuprints-23657

URL: <http://tuprints.ulb.tu-darmstadt.de/2365>

Dieses Dokument wird bereitgestellt von tuprints,  
E-Publishing-Service der TU Darmstadt.

<http://tuprints.ulb.tu-darmstadt.de>

[tuprints@ulb.tu-darmstadt.de](mailto:tuprints@ulb.tu-darmstadt.de)

Diese Arbeit wurde im Fachbereich Material- und Geowissenschaften, Fachgebiet Nichtmetallisch-Anorganische Werkstoffe in der Zeit von Oktober 2005 bis Juni 2009 unter der Betreuung von Prof. Dr. Jürgen Rödel angefertigt.

# *Danksagung, Acknowledgements*

Diese Arbeit wäre ohne die tatkräftige Unterstützung einer Vielzahl von Personen nicht möglich gewesen, welchen ich hiermit danken möchte.

Ich danke Professor Jürgen Rödel für die Gelegenheit, unter seiner ausgezeichneten Aufsicht und Betreuung in diesem Thema zu promovieren.

Professor Dr. Karsten Albe danke ich für die Übernahme des Zweitgutachtens.

Dr. Wook Jo möchte ich ebenfalls für die hervorragende Betreuung und fachliche sowie persönliche Unterstützung bedanken.

Der gesamten Arbeitsgruppe NAW möchte ich für die tolle Zusammenarbeit und das gute Arbeitsklima danken. Besonders Thorsten Leist und Jami Winzer möchte ich für die langjährige Hilfe und Freundschaft danken.

Ohne Emil Aulbach, als der Entwickler und Hersteller unzähliger Messaufbauten, wäre ein Großteil der Messungen in dieser Arbeit unmöglich gewesen, wofür ich mich bedanken möchte.

Herbert Hebermehl und Michael Heyse danke ich für ihre Hilfe bei der Probenfertigung.

Besonderer Dank gilt natürlich auch meinen ehemaligen Hiwis Christine Jamin, Julia Maibach, Silvia Vestweber, Ofer Hirsch und Stefanie Stuckenholtz für ihre tatkräftige Unterstützung.

Ljuba Schmitt danke ich für die TEM Untersuchungen meiner Proben und die fachliche Hilfe bei der Interpretation selbiger.

Jean-Christophe Jaud danke ich für die intensive Unterstützung bei den Röntgenstrukturmessungen vieler hunderter Proben.

Außer Konkurrenz möchte ich natürlich meine Eltern danken, ohne die diese Arbeit niemals möglich gewesen wäre.

# Content

1.	Introduction .....	1
1.1.	References .....	3
2.	Theory and Literature .....	4
2.1.	Basics of Ferroelectrics .....	4
2.1.1	Dielectrics .....	4
2.1.2	Electrostriction and Piezoelectricity .....	5
2.1.3	Field-Induced Phase Change Materials .....	7
2.1.4	Ferroelectricity and Antiferroelectricity .....	7
2.1.5	Relaxor Ferroelectrics .....	10
2.1.6	Perovskites and Other Ferroelectric Structures .....	10
2.1.7	References .....	14
2.2.	Bismuth Alkali Titanates .....	15
2.2.1	Structure and Phase Transitions of BNT and BKT .....	15
2.2.2	Preparation of Pure BNT and BKT .....	17
2.2.3	Properties of BNT and BKT .....	18
2.2.4	BNT-BT and Related Materials .....	19
2.2.5	BNT-BKT and Related Materials .....	21
2.2.6	BNT-BKT-BT .....	23
2.2.7	Dopants, Modification and Their Effects .....	24
2.2.8	Sol-Gel, Orientated Grain Growth and Single Crystals Bi-Based Materials .....	29
2.2.9	Other Bismuth-based Ferroelectrics .....	32
2.2.10	Summary of BNT-Based Materials .....	32
2.2.11	References .....	33
2.2.12	Tables of Properties of BNT-Based Materials .....	41
2.3.	Potassium Sodium Niobates .....	59
2.3.1	Introduction .....	59
2.3.2	The Structure of KNN .....	59
2.3.3	First Reported Results .....	60
2.3.4	Processing .....	61
2.3.5	Influence of Dopants .....	67
2.3.6	Summary .....	71
2.3.7	References .....	72
2.3.8	Tables of Properties of KNN-Based Materials .....	79
3.	Concepts and Required Properties .....	89
3.1.	Element Selection .....	89
3.1.1	Toxicity, Price and Availability .....	89
3.1.2	Required Properties .....	91
3.2.	Search Concepts .....	93
3.2.1	High Temperature BiMeO <sub>3</sub> -PbTiO <sub>3</sub> Analogue .....	95
3.2.2	Barium Copper Tungstenate .....	97
3.2.3	Ion Replacement in Known Systems .....	99
3.2.4	Doping to Raise Phase Transition Temperatures .....	100
3.2.5	Broadening of the Phase Regions and Transition in BNT .....	101
3.2.6	Morphotropic Phase Boundaries .....	101
3.2.7	Combining Bismuth Alkali Titanates and Alkali Niobates .....	102
3.3.	Summary .....	103
3.4.	References .....	104
4.	Experimental Techniques .....	107
4.1.	Powder and Ceramic Processing .....	107
4.2.	Structure and Microstructure .....	110
4.2.1	Density .....	110
4.2.2	High-Resolution Electron Microscopy .....	110
4.2.3	X-Ray Diffraction .....	111

4.2.4	Transmission Electron Microscopy .....	112
4.3.	Large-Signal Electrical Measurements .....	113
4.4.	Small-Signal Electrical Measurements .....	118
4.4.1	Small-Signal Piezoelectric Constant.....	118
4.4.2	Temperature-Dependent Impedance Spectroscopy .....	118
4.4.3	Low Frequency Impedance Spectroscopy .....	119
4.5.	Ferroelastic Measurements .....	120
4.5.1	Sample Preparation.....	120
4.5.2	Measurement Procedure .....	120
4.6.	References.....	122
5.	Experimental Results .....	123
5.1.	Nomenclature.....	123
5.2.	Broad Composition Search .....	124
5.3.	Structure and Microstructure .....	126
5.3.1	Density.....	126
5.3.2	Powder Diffraction .....	127
5.3.3	Scanning Electron Microscopy.....	132
5.3.4	Transmission Electron Microscopy .....	135
5.3.5	Summary of Structure and Microstructure Parameters.....	138
5.4.	Room Temperature Electrical Results .....	139
5.4.1	Bipolar Strain.....	139
5.4.2	Unipolar Strain .....	144
5.4.3	Energy Content.....	147
5.4.4	Small-Signal $d_{33}$ .....	149
5.4.5	Radial Strain .....	150
5.5.	Temperature-Dependent Properties .....	154
5.5.1	Strain and Polarisation at Elevated Temperatures.....	154
5.5.2	Temperature-Dependent Remanent Strain .....	164
5.5.3	Temperature-Dependent Ferroelastic Properties .....	166
5.5.4	Temperature-Dependent Permittivity and Loss.....	170
5.6.	Frequency-Dependent Large-Signal Behaviour.....	174
5.6.1	Bipolar Strain.....	174
5.6.2	Polarisation .....	175
5.6.3	Bipolar Strain Versus Square of Polarisation .....	176
5.6.4	Summaries of Frequency-Dependent Strain and Polarisation .....	177
5.7.	References.....	182
6.	Discussion.....	183
6.1.	Concepts for the Development of New Lead-Free Ferroelectrics.....	183
6.2.	The MPB-to-MPB Search.....	184
6.2.1	Processing and Storage.....	185
6.2.2	Structure and Microstructure .....	186
6.3.	Room Temperature Electrical Properties.....	189
6.3.1	Large Field Strain and Polarisation Behaviour.....	189
6.3.2	Small-Signal $d_{33}$ .....	193
6.3.3	Radial Strain .....	193
6.3.4	Composition 20;0.5 .....	194
6.4.	Temperature-Dependent Properties .....	195
6.4.1	Large Field Strain and Polarisation .....	195
6.4.2	Temperature-Dependent Ferroelastic Properties .....	197
6.4.3	Temperature-Dependent Permittivity .....	197
6.5.	Frequency-Dependent Properties.....	199
6.6.	References.....	200
7.	Conclusion.....	202
7.1.	References.....	204
8.	Curriculum vitae.....	205

---

8.1.	Education: .....	205
8.2.	Work history: .....	205
9.	Publications .....	206
10.	Erklärung.....	207

## ***Table of Figures***

Fig 1: The number of publications per year on lead-free piezoceramics plotted from 1950 to 2008 (November). .....	2
Fig 2: a) The force exerted onto a sample induces a strain, which in turn induces a polarisation and electric field related by Eq 5 and Eq 6. b) In the reversed situation, the applied electric field induces a strain.....	6
Fig 3: Typical saw-tooth-shaped voltage signal used in bipolar large field characterisation.....	8
Fig 4: Polarisation vs. large electric field.....	9
Fig 5: Strain in field direction in a large electric field as shown in Fig 3. ....	9
Fig 6: Unit cell of an undistorted perovskite structure.....	10
Fig 7: The unit cell of an ilmenite structure.....	12
Fig 8: The unit cell of bismuth-layer structure with two repeating perovskite layers and the bismuth oxide layer.....	13
Fig 9: The BNT rich part of the BNT-BKT-BT phase diagram with all compositions reported in literature sorted by their respective authors.....	24
Fig 10: All known literature of modified BNT-BT, which contained $d_{33}$ with reported $T_d$ was compiled .....	25
Fig 11: All known literature of modified BNT-BT, which contained $k_p$ with reported $T_d$ was compiled.....	26
Fig 12: Phase diagram of $K_xNa_{(1-x)}NbO_3$ . Regions labelled with Q, K, and L are monoclinic (or orthorhombic in most literature) ferroelectric, M, G is orthorhombic ferroelectric; F, H and J are tetragonal ferroelectric. Region P is orthorhombic antiferroelectric .....	60
Fig 13: Density and $k_p$ of KNN ceramics as a function of heating rate and sintering temperature .....	63
Fig 14: Dielectric constant versus temperature for a single crystal of $KNbO_3$ .....	65
Fig 15: The piezoelectric constant $d_{33}$ is plotted against the temperature of the O-T phase transition for some Li-doped KNN systems.....	71
Fig 16: All potentially relevant elements in the search for new piezoelectric materials sorted into A-site and B-site positions.....	91
Fig 17: The ionic radii of the selected elements as well as reports of known perovskite structures .....	93
Fig 18: The $Bi(Cu,Y)O_3$ structures are analogues to $Ba(Cu,Y)O_3$ .....	96
Fig 19: 3D crystal structure of $Ba(Cu_{1/2}W_{1/2})O_3$ generated with Diamond 3.2a and POV-Ray from powder diffraction data. ....	97
Fig 20: Possible combinations of materials that force ferroelectrically active ions into distorted octahedra of tetragonal crystal systems due to mismatch of the B-site ion ratios.....	98



Fig 21: Materials based on ion replacement of currently known ferroelectric systems. ....	99
Fig 22: Proposed replacement of $\text{Nb}^{5+}$ in KNN with a combination of $\text{Ti}^{4+}$ , $\text{Zr}^{4+}$ and $\text{W}^{6+}$ , $\text{Mo}^{6+}$ . ....	100
Fig 23: The two quasi-ternary phase diagrams of BNT-BKT-KNN are shown on the left and BNT-BT-KNN on the right. ....	103
Fig 24: The self-made sintering setup, comprising of the alumina plate, alumina pipes and alumina lids, is shown in its disassembled state. ....	109
Fig 25: Diagram showing the extended Sawyer-Tower setup used for large-signal electrical characterisation. ....	113
Fig 26: Picture of the radial strain setup build in-group by Emil Aulbach. ....	115
Fig 27: Typical zigzag or saw tooth shaped voltage signal used in bipolar (a) and unipolar (b) large field characterisation. ....	116
Fig 28: Schematic drawing of the ferroelastic testing setup <sup>[5]</sup> . ....	121
Fig 29: The BNT-BKT-KNN phase diagram (a) with the investigated line of compositions highlighted in blue. On the right (b), the matrix of investigated compositions near the BNT-BKT MPB is displayed with position and nomenclature. ....	123
Fig 30: The results of the broad composition search. ....	124
Fig 31: The refinement of the region 20;0 to 20;10. ....	125
Fig 32: Relative density of the investigated compositions. ....	126
Fig 33: The diffraction patterns of all 10 matrix compositions after calcination and milling. ....	127
Fig 34: The diffraction patterns of all 10 matrix compositions crushed after sintering. ....	128
Fig 35: a) The unit cell length $a$ of the calcined and milled powder vs. composition X;Y. b) The unit cell length $a$ of the sintered and crushed samples vs. composition X;Y. c) The $t$ -factor of each composition calculated from the average ionic radius of A- and B-site. ....	130
Fig 36: Diffraction patterns of a) 19;Y, b) 20;Y and c) 21;Y after unipolar load of 6 kV/mm for 15 seconds. ....	131
Fig 37: Typical microstructure of a polished and chemically etched BNT-BKT-KNN-BKT sample of composition 19;2 recorded in BSE mode with a voltage of 20.0 kV. ....	132
Fig 38: Fracture surfaces of compositions a) 20;0, b) 20;0.5, c) 20;1, d) 20;2 recorded in SE mode at 20.0 kV. ....	133
Fig 39: The fracture surface of a sample of composition 20;0.5 showing the void left by an abnormal elongated grain of at least 6 $\mu\text{m}$ length. ....	134
Fig 40: TEM image of the microstructure of composition 20;1. The high contrast of some grains is a result of them being oriented to meet to Bragg conditions. ....	135
Fig 41: TEM images of single grains of 20;0 (top) and 20;0.5 (bottom). The high contrast grains are oriented as shown in the inlays. On the left, the orientation ( $[001]_c$ or $[111]_c$ ) is such that it displays the	

$\frac{1}{2}\{00e\}$ superstructure reflexes (marked in inlay). On the right, the $[011]_c$ orientation is used to show the $\frac{1}{2}\{000\}$ reflexes (marked in inlay).....	136
Fig 42: TEM images of single grains of 20;1 (top) and 20;2 (bottom). ....	137
Fig 43: SAED pattern of sample 20;1 along $[001]_c$ zone. The splitting along $[100]$ is marked with a red rectangle and zoomed in.....	138
Fig 44: Bipolar Strain hystereses of a) 20;0, b) 20;0.5, c) 20;1 and d) 20;2 for fields of 4 kV/mm (black), 6 kV/mm (red) and 8 kV/mm (blue). ....	139
Fig 45: Bipolar polarisation hystereses of a) 20;0, b) 20;0.5, c) 20;1 and d) 20;2 for fields of 4 kV/mm (black), 6 kV/mm (red) and 8 kV/mm (blue). ....	140
Fig 46: a), b) and c) show the maximum unipolar and bipolar normalised strain values of all 10 compositions at 4, 6 and 8 kV/mm, respectively. d) shows a comparison of the bipolar strain values of all compositions at these three field strengths. ....	141
Fig 47: The maximum and remanent polarisation values at a) 4 kV/mm, b) 6 kV/mm and c) 8 kV/mm. The coercive field, collected from the 4, 6 and 8 kV/mm polarisation hystereses is summarised in d). ....	142
Fig 48: The strain and polarisation of composition 21;2 at fields of 4, 6 and 8 kV/mm.....	143
Fig 49: The unipolar strain of compositions a) 19;Y, b) 20;Y and c) 21;Y at 4 kV/mm is shown on the left. Their corresponding polarisation hystereses are shown in d), e) and f) on the right. ....	144
Fig 50: Normalised unipolar strain values at 4, 6 and 8 kV/mm.....	145
Fig 51: Strain versus the square of the polarisation for a) 19;Y, b) 20;Y and c) 21;Y. Since 20;1 and 20;2 show a higher polarisation, d) shows 20;Y with a larger scale. ....	146
Fig 52: The energy content of the unipolar 4 kV/mm polarisation hysteresis are shown in red. ....	148
Fig 53: Small-signal $d_{33}$ as a function of composition directly after poling and after 24 h.....	149
Fig 54: The axial and radial strain of the composition series 19;Y recorded with an 8 kV/mm bipolar electric field. The axial strain is shown in black, the radial strain in red. ....	150
Fig 55: The axial and radial strain of the composition series 20;Y recorded with an 8 kV/mm bipolar electric field. The axial strain is shown in black, the radial strain in red. ....	151
Fig 56: The axial and radial strain of the composition series 21;Y recorded with an 8 kV/mm bipolar electric field. The axial strain is shown in black, the radial strain in red. ....	152
Fig 57: The maximum volume expansion in per cent as a function of composition and electric field. The larger errors of the 4 kV/mm values are due to asymmetry of the axial strain curve. ....	153
Fig 58: The bipolar strain evolution at 4 kV/mm recorded at 50, 75, 100 and 150 °C for compositions a) 20;0, b) 20;0.5, c) 20;1 and d) 20;2. ....	154
Fig 59: The bipolar polarisation evolution at 4 kV/mm recorded at 50, 75, 100 and 150 °C for compositions a) 20;0, b) 20;0.5, c) 20;1 and d) 20;2.....	155
Fig 60: Temperature-dependent unipolar and bipolar maximum strain of compositions a) 19;0, b) 19;1 and c) 19;2.....	157

Fig 61: Temperature-dependent unipolar and bipolar maximum strain of compositions a) 20;0, b) 20;0.5, c) 20;1 and d) 20;2. ....	158
Fig 62: Temperature-dependent unipolar and bipolar maximum strain of compositions a) 21;0, b) 21;1 and c) 21;2. ....	159
Fig 63: Temperature-dependent maximum and remanent polarisation of compositions a) 19;0, b) 19;1 and c) 19;2. ....	160
Fig 64: Temperature-dependent maximum and remanent polarisation of compositions a) 20;0, b) 20;0.5, c) 20;1 and d) 20;2. ....	161
Fig 65: Temperature-dependent maximum and remanent polarisation of compositions a) 21;0, b) 21;1 and c) 21;2. ....	162
Fig 66: Temperature-dependent coercive field of a) 19;Y, b) 20;Y and c) 21;Y. The temperature, where the largest change in the coercive field occurs, is listed in Tab 17 on the right. ....	163
Fig 67: The remanent strain of a) 19;Y, b) 20;Y and c) 21;Y as a function of temperature. ....	164
Fig 68: The first two strain versus electric field cycles recorded at room temperature for composition 21;0. The blue dots show the remanent strain values after 1/2 of a cycle (lowest), one full cycle (middle) and after two full cycles (top). ....	165
Fig 69: Compressive strain versus applied stress at temperatures of 25 °C to 150 °C in steps of 25 K for composition 20;0. ....	166
Fig 70: Compressive strain versus applied stress at temperatures of 25 °C to 150 °C in steps of 25 K for composition 20;0.5. ....	167
Fig 71: Compressive strain versus applied stress at temperatures of 25 °C to 150 °C in steps of 25 K for composition 20;1. ....	168
Fig 72: Compressive strain versus applied stress at temperatures of 25 °C to 150 °C in steps of 25 K for composition 20;2. ....	168
Fig 73: Summary of the maximum and remanent strain and the energy dissipated during the cycle for compositions 20;0 to 20;2. ....	169
Fig 74: The dielectric permittivity and loss for compositions 19;0 to 19;2 from room temperature to 400 °C recorded every order of magnitude between 1 kHz and 1 MHz. ....	170
Fig 75: The dielectric permittivity and loss for compositions 20;0 to 20;2 from room temperature to 400 °C recorded every order of magnitude between 1 kHz and 1 MHz. ....	171
Fig 76: The dielectric permittivity and loss for compositions 21;0 to 21;2 from room temperature to 400 °C recorded every order of magnitude between 1 kHz and 1 MHz. ....	172
Fig 77: Variation of $T_M$ with composition. ....	173
Fig 78: Bipolar large-signal strain evolution with frequency at 4 kV/mm for compositions 20;0 and 20;2 between 1 Hz and 500 Hz. ....	174
Fig 79: Bipolar large-signal polarisation evolution with frequency at 4 kV/mm for compositions 20;0 and 20;2 between 1 Hz and 500 Hz. ....	175

Fig 80: Strain vs. square of polarisation evolution with frequency at 4 kV/mm for compositions 20;0 and 20;2 between 1 Hz and 500 Hz.....	176
Fig 81: The frequency dependence of permittivity, positive and total bipolar strain of compositions 19;0, 19;1 and 19;2 are shown on the left. On the right, the frequency dependence of the maximum polarisation, remanent polarisation and the coercive field is shown.....	178
Fig 82: The frequency dependence of permittivity, positive and total bipolar strain of compositions 20;0, to 20;2 are shown on the left. On the right, the frequency dependence of the maximum polarisation, remanent polarisation and the coercive field is shown.....	179
Fig 83: The frequency dependence of permittivity, positive and total bipolar strain of compositions 21;0, 21;1 and 21;2 are shown on the left. On the right, the frequency dependence of the maximum polarisation, remanent polarisation and the coercive field are shown.....	180
Fig 84: The polarisation hystereses of compositions 21;2, 20;1 and 20;2 were used to identify the exact polarisation hysteresis shape required for the induction of a giant strain response.....	191
Fig 85: The ratio of the maximum volume increase relative to the maximum strain plotted as a function of composition at 8 kV/mm with the combined error of both values.....	194
Fig 86: Phase diagram deduced from the matrix of the 10 investigated compositions. The polar phase (white) and the non-polar phase region (green) are shown at room temperature.....	195
Fig 87: Remanent and total strain vs. temperature (4 kV/mm) for composition 20;0.....	196

## ***Table of Tables***

Tab 1: Properties of $\text{Bi}_{1/2}\text{Na}_{1/2}\text{TiO}_3$ (Unmodified).....	41
Tab 2: Properties of $\text{Bi}_{1/2}\text{K}_{1/2}\text{TiO}_3$ (Unmodified) .....	45
Tab 3: Properties of $\text{Bi}_{1/2}\text{Na}_{1/2}\text{TiO}_3$ (Modified).....	48
Tab 4: Properties of $94(\text{Bi}_{1/2}\text{Na}_{1/2}\text{TiO}_3)\text{-}6(\text{BaTiO}_3)$ .....	49
Tab 5: Properties of Doped BNT-BT .....	51
Tab 6: Properties of Pure BNT-BKT .....	52
Tab 7: Properties of BNT-BKT-BT .....	55
Tab 8: Some Properties of Potassium Niobate (KN) and of Sodium Niobate (NN) .....	60
Tab 9: Properties of $\text{K}_{0.5}\text{Na}_{0.5}\text{NbO}_3$ (unmodified).....	79
Tab 10: Properties of $\text{K}_{0.5}\text{Na}_{0.5}\text{NbO}_3$ (Modified).....	82
Tab 11: Potential A-site ions, Standard Charge and Ionic Radii.....	94
Tab 12: All Potential B-site ions, Standard Charge and Ionic Radii.....	94
Tab 13: Chemicals Used in Ceramic Processing.....	107
Tab 14: Summary of Structure and Microstructure Data .....	138
Tab 15: Results of Exponential Fit of the $S(P^2)$ Graphs Shown in Fig 47. ....	147
Tab 16: Energy Content of Polarisation Hystereses.....	148
Tab 17: Large-Signal Depolarisation Temperature.....	163
Tab 18: Summary of Temperature-Dependent Permittivity and Loss Data.....	173
Tab 19: Change in Strain and Polarisation with Frequency .....	181

## ***Table of Constants and Abbreviations***

All constants and abbreviations are defined and explained at their first occurrence. Some, which are used infrequently are listed here for easier reference. Due to the large number, only the ones particular to this topic are listed. The units listed are the typically used ones in this field and not the SI-units.

<b>Constant/ Abbreviation</b>	<b>Name</b>	<b>SI Units or Formula</b>
BKT	bismuth potassium niobate	$\text{Bi}_{1/2}\text{K}_{1/2}\text{TiO}_3$
BNT	bismuth sodium niobate	$\text{Bi}_{1/2}\text{Na}_{1/2}\text{O}_3$
KNN	potassium sodium niobate	$\text{K}_{1/2}\text{Na}_{1/2}\text{NbO}_3$
KN	potassium niobate	$\text{KNbO}_3$
NN	sodium niobate	$\text{NaNbO}_3$
BT	barium titanate	$\text{BaTiO}_3$
PZT	lead zirconate titanate	$\text{Pb}(\text{Ti}_{1/2}\text{Zr}_{1/2})\text{O}_3$
PT	lead titanate	$\text{PbTiO}_3$
BF-PT	bismuth ferrite lead titanate	$\text{BiFeO}_3\text{-PbTiO}_3$
$E_{(c/\text{max}/\text{min})}$	electric field (coercive/maximal/minimal)	kV/mm
$P_{(\text{max}/r)}$	(maximum/remanent) polarisation	$\mu\text{C}/\text{cm}^2$
$S_{(\text{max}/\text{min}/r)}$	(maximum/minimum/remanent) strain	%
$\epsilon_{0/r}$	dielectric permittivity/ relative dielectric constant	F/m / no units
$\chi_e$	dielectric susceptibility	no units
$k_p, k_t, k_{xx}$	(planar, transverse, xy) coupling factor	no units
$d_{xy}$	piezoelectric constant	pC/N or pm/V
RoHS	EU directive: „Restriction of the use of certain Hazardous Substances in electrical and electronic equipment“	
WEEE	EU directive: „Waste Electrical and Electronic Equipment“	
HR(S)EM	High Resolution Scanning Electron Microscope	
SEM	Scanning Electron Microscope	
TEM	Transmission Electron Microscope	
XRD	X-ray diffraction	

# 1. Introduction

Piezoelectrics have experienced a great deal of attention for more than half a century. Initially, with the discovery of ferroelectricity in polycrystalline ceramics, they were used as capacitor materials making use of their high dielectric constants. With the introduction of new materials, in particular lead-zirconate-titanate (PZT), applications spread to sonar, transducers, micro positioning systems and actuators amongst many others<sup>[1]</sup>.

International efforts in removing toxic substances from everyday applications are increasing. The EU passed the „Waste Electrical and Electronic Equipment“ (WEEE) and „Restriction of the use of certain Hazardous Substances in electrical and electronic equipment“ (RoHS) in 2003<sup>[2]</sup>. While the WEEE regulates the disposal, reuse and recycling of the mentioned equipment, the RoHS is a necessary requirement to ensure this can be accomplished safely without endangering the environment or people's health. Mercury, cadmium, hexavalent chromium, the flame-retardants PBB and PBDE and, the focus of this work, lead, have been identified as a primary risk during recycling, disposal or just improper use. Therefore, as of June 2006, any products introduced to the open market may not include more than 0.1 wt.% of any one of these substances with the exception of cadmium where the limit is even lower than 0.01 wt.%.

Currently, an exemption is made for piezoelectrics. However, known lead-free piezoceramics are not yet good enough to replace lead containing materials. While this exemption currently holds for almost all piezoelectric components on the market, this is subject to regular review. New applications using these materials can only be introduced if “elimination or substitution ... is technically or scientifically impracticable, or where the negative environmental, health and/or consumer safety impacts caused by substitution are likely to outweigh the environmental, health and/or consumer safety benefits”<sup>[2]</sup>. This would for example likely not hold for the use of lead in newly invented consumer electronics. It is, therefore, desirable to find alternatives to the currently market-dominating lead containing piezoelectrics in all current or future applications.

A significant research effort into lead-free alternatives to PZT began a little over ten years ago (Fig 1) even though the base materials have been known for more than half a century<sup>[3,4]</sup>. The research activities before 1990 mostly aimed at searching for the systems, whose properties are better than those of PZT. Increased Curie temperature or polarisation is often desirable for example. However, this was not meant for environmental protection but merely a search for the systems with improved properties over PZT. Since about 1990, the search has mostly directed to

improving the already known lead-free materials to the point where they might reach PZT-like properties due to before-mentioned legislation.

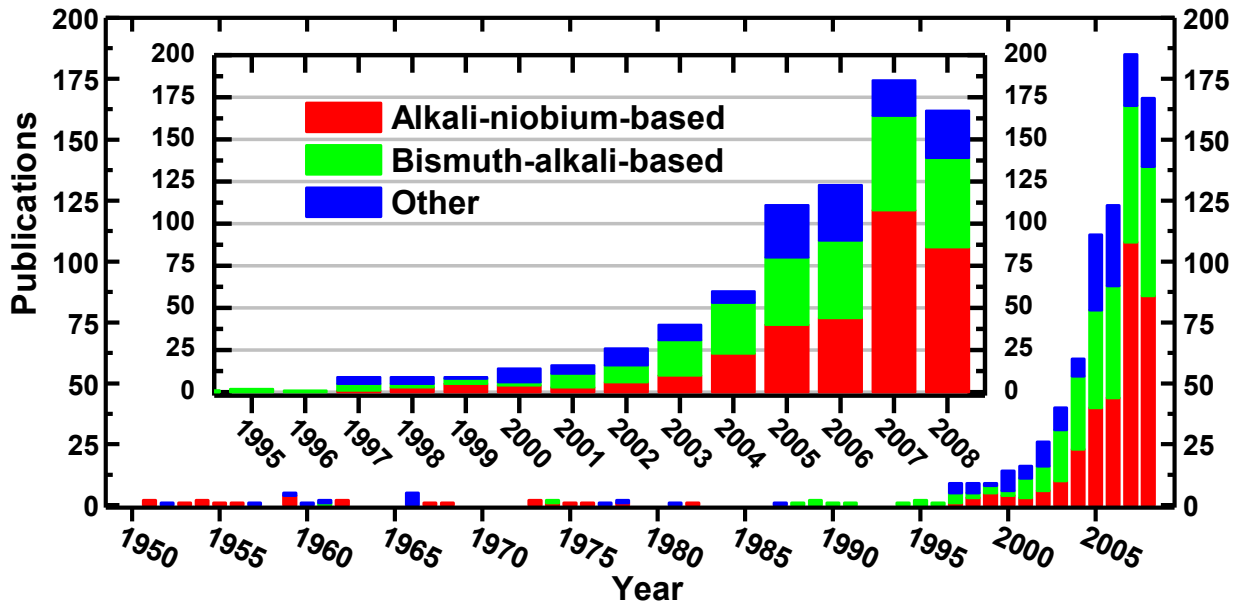


Fig 1: The number of publications per year on lead-free piezoceramics plotted from 1950 to 2008 (November).

The publications include materials based on polycrystalline ceramics, thin film and single crystals and cover all directly related research specifically but not exclusively processing, development, mechanical, electrical and structural characterization, theoretical predictions, mechanistic studies and applications of lead-free piezoceramics. The statistic is the result of a three-step search process. Firstly, citations of the papers by Saito et al.<sup>[5]</sup>, Takenaka et al.<sup>[6,7]</sup>, Elkechai et al.<sup>[8]</sup>, Sasaki et al.<sup>[9]</sup> and Shrout et al.<sup>[10]</sup>. Secondly, the internet search engines of “ISI Web of Science” and “Sciencedirect” with keywords such as “lead-free”, “piezoelectric”, “ferroelectric”, “KNN,”, “BNT” and similar were used. At last, the collected papers were searched again manually for relevant references until a randomly selected sample of 60-70 papers revealed no relevant new citations. The number for 2008 may not be final since new work may not be cited yet.

In this work, the known lead-free ferroelectric materials, bismuth potassium titanate (BKT)<sup>[11]</sup>, bismuth sodium niobate (BNT)<sup>[4]</sup> and potassium sodium niobate (KNN)<sup>[3]</sup> are combined in such a way as to attempt to harness advantages from all of them whilst also eliminating disadvantages of the individual components. KNN by itself has a Curie temperature of nearly 400 °C but sintering under normal conditions, i.e. without pressure, is difficult. BNT is more easily sintered but the depolarisation temperature of 200 °C and a coercive field of about 7 kV/mm disqualify it for most applications. BKT again does not sinter well but when combined with BNT, the sinterability is greatly enhanced. In addition, the solid solutions lower the coercive field of BNT to more usable 3.5 kV/mm<sup>[12]</sup>. The three materials were combined in accordance with concepts



introduced in chapter 3.2.7. Ionic size, crystal structures and properties given in literature lead to the final choice of two mixed systems BNT-BKT and KNN-BKT, which were already known in literature. These were mixed in different ratios to regions of interest. Once interesting properties had been identified, efforts were directed to characterising the electrical and mechanical properties of the found materials to evaluate their suitability for different applications.

## 1.1. References

- [1] G. H. Haertling, "Ferroelectric ceramics: history and technology," *Journal of the American Ceramic Society*, **82**[4] 797-818 (1999).
- [2] "EU-Directive 2002/95/EC: Restriction of the use of certain hazardous substances in electrical and electronic equipment (RoHS)," *Official Journal of the European Union*, **46**[L37] 19-23 (2003).
- [3] L. Egerton and D. M. Dillon, "Piezoelectric and dielectric properties of ceramics in the system potassium sodium niobate," *Journal of the American Ceramic Society*, **42**[9] 438-42 (1959).
- [4] G. A. Smolenskii and A. I. Agranovskaya, "Dielectric Polarization of a Number of Complex Compounds," *Soviet Physics-Solid State*, **1**[10] 1429-37 (1960).
- [5] Y. Saito, H. Takao, T. Tani, T. Nonoyama, K. Takatori, T. Homma, T. Nagaya, and M. Nakamura, "Lead-free piezoceramics," *Nature*, **432**[7013] 84-7 (2004).
- [6] T. Takenaka, K. Maruyama, and K. Sakata, "(Bi<sub>1/2</sub>Na<sub>1/2</sub>)TiO<sub>3</sub>-BaTiO<sub>3</sub> system for lead-free piezoelectric ceramics," *Japanese Journal of Applied Physics Part 1-Regular Papers Short Notes & Review Papers*, **30**[9B] 2236-9 (1991).
- [7] T. Takenaka and H. Nagata, "Current status and prospects of lead-free piezoelectric ceramics," *Journal of the European Ceramic Society*, **25**[12] 2693-700 (2005).
- [8] O. Elkechai, M. Manier, and J. P. Mercurio, "Na<sub>0.5</sub>Bi<sub>0.5</sub>TiO<sub>3</sub>-K<sub>0.5</sub>Bi<sub>0.5</sub>TiO<sub>3</sub> (NBT-KBT) system: A structural and electrical study," *Physica Status Solidi A: Applied Research*, **157**[2] 499-506 (1996).
- [9] A. Sasaki, T. Chiba, Y. Mamiya, and E. Otsuki, "Dielectric and piezoelectric properties of (Bi<sub>1/2</sub>Na<sub>1/2</sub>)TiO<sub>3</sub>-(Bi<sub>0.5</sub>K<sub>0.5</sub>)TiO<sub>3</sub> systems," *Japanese Journal of Applied Physics Part 1-Regular Papers Short Notes & Review Papers*, **38**[9B] 5564-7 (1999).
- [10] T. R. Shrout and S. J. Zhang, "Lead-free piezoelectric ceramics: Alternatives for PZT?," *Journal of Electroceramics*, **19**[1] 113-26 (2007).
- [11] Y. Hiruma, R. Aoyagi, H. Nagata, and T. Takenaka, "Ferroelectric and piezoelectric properties of (Bi<sub>1/2</sub>K<sub>1/2</sub>)TiO<sub>3</sub> ceramics," *Japanese Journal of Applied Physics Part 1-Regular Papers Brief Communications & Review Papers*, **44**[7A] 5040-4 (2005).
- [12] K. Yoshii, Y. Hiruma, H. Nagata, and T. Takenaka, "Electrical properties and depolarization temperature of (Bi<sub>1/2</sub>Na<sub>1/2</sub>)TiO<sub>3</sub>-(Bi<sub>1/2</sub>K<sub>1/2</sub>)TiO<sub>3</sub> lead-free piezoelectric ceramics," *Japanese Journal of Applied Physics Part 1-Regular Papers Brief Communications & Review Papers*, **45**[5B] 4493-6 (2006).

## 2. Theory and Literature

### 2.1. Basics of Ferroelectrics

The purpose of this chapter is to give background information of basics of ferroelectrics and related materials. Unless stated otherwise, the information given here is a brief summary of books by A. S. Sonin and B. A. Strukov<sup>[1]</sup>, B. Jaffe, W. Cook and H. Jaffe<sup>[2]</sup>, B. A. Strukov and A. P. Levanyuk<sup>[3]</sup> and A. J. Moulson and J. M. Herbert<sup>[4]</sup>. These can be consulted for in-depth study of the properties and phenomena described.

#### 2.1.1 Dielectrics

Dielectrics are a class of materials comprising of gases, liquids and solids that have virtually no free charge carriers. When such materials are exposed to an external electric field, they are polarised. This polarisation can occur by several mechanisms of limited charge rearrangement. There are four types of polarisations. One is atomic polarisation, where electrons and nucleus of an atom or ion are displaced with respect to each other. Another is ionic polarisation, where anion and cations of a crystal shift in opposite direction to each other in the presence of an electric field. There are also dipole and space charge polarisations where dipoles in the material reorient and charges accumulate at interfaces in the material. The relationship between polarisation (P) and electric field (E) is given by:

$$P = \chi_e \epsilon_0 E$$

Eq 1

Where  $\chi_e$  is the electric susceptibility and  $\epsilon_0$  is the dielectric constant or permittivity of free space. The electric susceptibility is a function of the material parameters incorporating the above mentioned polarisation mechanisms. It is always frequency-dependent and only constant at a given frequency for linear dielectrics. It can also be written as:

$$\chi_e = \epsilon_r - 1$$

Eq 2

Where  $\epsilon_r$  is the relative dielectric constant, the more commonly use material parameter in the field of functional ceramics. Normally, dielectrics are used simply for their insulating capabilities.

Real (non-perfect) dielectric materials always have some losses arising from conductivity or charge redistribution via any of the before-mentioned polarisation mechanisms.

In the search for new materials, even basic properties like the dielectric breakdown strength play an important role. Dielectric strength is the electric field that has to be applied to a material to cause electric breakdown. Generally, three types of dielectric breakdown are distinguished. Intrinsic breakdown happens when the current conducted through the material suddenly and sharply increases as a certain maximum field is reached. Thermal breakdown results when the conductivity of the material is high enough to cause joule heating, which in turn increases the conductivity consequentially leading to „thermal runaway“ as the two effects aggravate each other. Discharge breakdown happening in pores or cracks in the materials is caused by the increased electric field in the pores due to the low dielectric constant of air as well as its lower intrinsic breakdown strength.

### 2.1.2 Electrostriction and Piezoelectricity

All dielectric materials experience a dimensional change when exposed to an electric field as depicted in Fig 2b. This change can be written as a power series in terms of the electric field or the polarisation<sup>[5]</sup>:

$$S_{ij} = d_{kij}E_k + M_{ijkl}E_kE_l + \dots$$

Eq 3

$$S_{ij} = g_{kij}P_k + Q_{ijkl}P_kP_l + \dots$$

Eq 4

Or more simply if the tensor nature of the coefficients is ignored.

$$S = dE + ME^2 + \dots$$

Eq 5

$$S = gP + QP^2 + \dots$$

Eq 6

If an applied electric field  $E$  or the equivalent polarisation  $P$  cause a strain linearly related by  $d$  and  $g$  only, this is called the converse piezoelectric effect (Fig 2a). The direct piezoelectric effect gives an electric field and a polarisation when strain is induced into the material (Fig 2a). This

linear relationship usually only holds true for small fields and the coefficients  $d$  and  $g$  are most precisely called small-signal piezoelectric strain and voltage coefficients, respectively.

If the strain  $S$  in the material and the applied electric field  $E$  or polarisation  $P$  are related by the even order terms only, e. g.  $M$  and  $Q$ , the material is called electrostrictive. It follows that electrostrictive behaviour is independent of the field polarity.

Electrostriction can be of particular relevance when coefficients  $d$  and  $g$  are small and the relative permittivity is high. Both are commonly true for ferroelectrics around the Curie point or the depolarisation temperature.

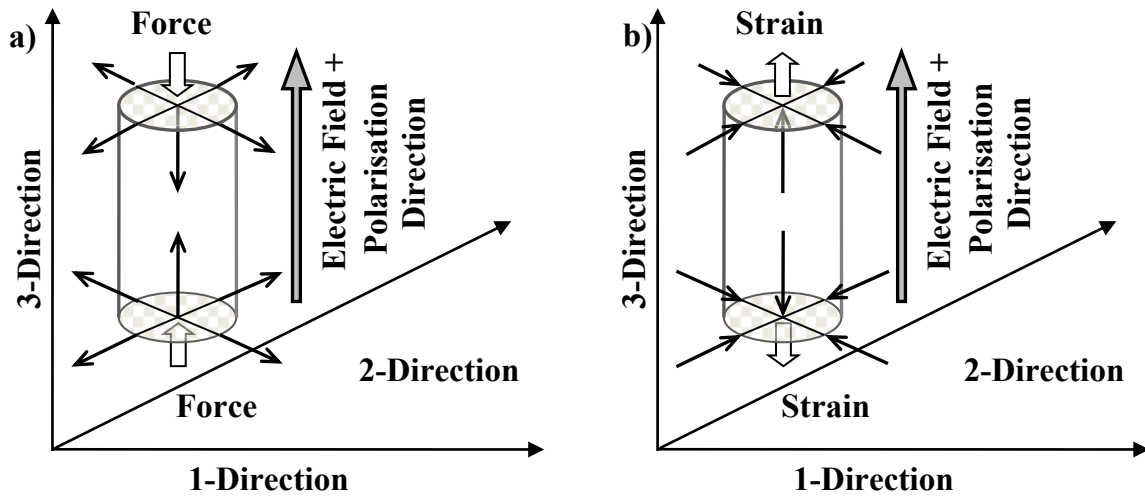


**Fig 2: a) The force exerted onto a sample induces a strain, which in turn induces a polarisation and electric field related by Eq 5 and Eq 6. b) In the reversed situation, the applied electric field induces a strain. In a cylindrical sample for typical experimental use all in-plane directions are symmetrically equivalent in this sample symmetry leading to identical  $d_{xy}$  when  $x$  or  $y$  equals 1 or  $x$  or  $y$  equals 2. i.e.  $d_{x1}$  is equal to  $d_{x2}$  and  $d_{1y}$  is equal to  $d_{2y}$ .**

Strictly speaking the coefficient  $\chi_\epsilon$  is a second rank tensor,  $d$  and  $g$  are third rank tensor and  $Q$  and  $M$  are fourth rank<sup>[5]</sup> but their tensor nature has been ignored for the purpose of this introduction since it has little impact on the understanding of upcoming work. However, the piezoelectric coefficients and electrostrictive coefficients have a simplified labelling system, where the tensor is reduced to second order 6x6 matrix<sup>[6]</sup> by using the symmetry in the tensor if the material is regarded as torque-free and poled. The piezoelectric coefficient is written as  $d_{xy}$  where  $x$  and  $y$  takes values between 1 and 6. By convention, the 3-direction is the poling direction and 1 and 2 are the two orthogonal directions. Numbers 4 to 6 denote the shear planes perpendicular to 1 to 3. For example  $d_{31}$  relates the field in 3-direction to the strain in 1-direction. For symmetry reasons,  $d_{25}$  is equal to  $d_{15}$  and  $d_{66}$  is always zero.

### 2.1.3 Field-Induced Phase Change Materials

While the term field-induced phase change material describes all dielectric material to some degree, in this instance it is used to describe materials, where the main effect cannot be attributed to either typical electrostrictive or piezoelectric behaviour. In this context, the phrase 'phase change' means a reversible or irreversible change from for example cubic to rhombohedral symmetry under an applied field. This phase change can be accompanied by a change in volume like in the case of doped PZT<sup>[7-9]</sup>. However, this does not necessarily have to be the reason for a large strain response as is the case in modified  $\text{Bi}_{1/2}\text{Na}_{1/2}\text{TiO}_3$  (BNT) where irreversible phase changes accompanied by a volume change and reversible phase changes with very little volume change occurs<sup>[10,11]</sup>.

### 2.1.4 Ferroelectricity and Antiferroelectricity

Piezoelectric materials, where the direction of polarisation can be changed through the application of an external field, are called ferroelectrics. In ferroelectric materials, the unit cell exhibits a net permanent dipole moment. This dipole moment does not immediately translate into a macroscopic polarisation of the material due to the distribution of the randomly oriented dipole moments in the case of polycrystalline ceramics. In polycrystalline materials but also in single crystals, the orientation distribution of the dipole moments is not completely random on the unit cell level but organised in groups called domains. Domains are areas where the dipole direction of individual adjacent unit cells is the same. These domains have a net non-zero polarisation. A large number of domains arrange in such a way within the material that the macroscopic polarisation of the material is zero. For reasons beyond the scope of this work, this is usually more energetically favourable than either dipole cancellation on the unit cell level or a single domain state of the material<sup>[1]</sup>. While single crystals with more than one domain state are not single crystals in the strictest crystallographic definition, they are commonly regarded as such in the field of materials science.

Kittel<sup>[12]</sup> defined the antiferroelectric state "as one, in which lines of ions in the crystal spontaneously polarised but with neighbouring lines polarised in antiparallel direction" even before experimental evidence existed<sup>[13]</sup>. The "lines" as defined by Kittel are nowadays referred to as sub cells of antipolar order but the general principles are unchanged. Antiferroelectric domains are then regions where a certain type of antipolar order exists. Antipolar domains do not have a net polarisation. Antiferroelectric are also defined as antipolar crystals with free energies comparable to polar crystals<sup>[2]</sup>.

While polar and antipolar materials are known to exist, there is conceivably a third group, in which the polarisation of the unit cell is randomly oriented with respect to neighbouring cells and no discernable antipolar order can be found. This is implied by the careful use of „non-symmetrical phase“ in some literature<sup>[3,14,15]</sup>.

Switchable polarisation in ferroelectrics is of particular importance for any actuator, sensor and ferroelectric memory applications amongst others. The ability to influence the direction of polarisation determines the strain direction of the actuator under an electric field. This strain direction needs to be controllable in order for multilayer actuators to be useful. In ferroelectric memory the polarisation state (up or down) defines the bit zero or one. The electric field at which a macroscopic polarisation changes sign is called the coercive field ( $E_c$ ).

The polarisation (macroscopic and/or microscopic) of a ferroelectric or antiferroelectric only exists up to the Curie temperature. The Curie temperature is defined as the temperature where a ferroelectric or antiferroelectric phase changes to a paraelectric phase.

When a ferroelectric material is subjected to a large electric field, it shows hysteretic behaviour of the strain and polarisation. A large field in this case is usually regarded as one that gives rise to a saturated strain and polarisation values. Sometimes, it is also regarded as the field required for domain switching to occur. Depending on the material, usually a value of at least twice the coercive field is chosen in experimental settings.

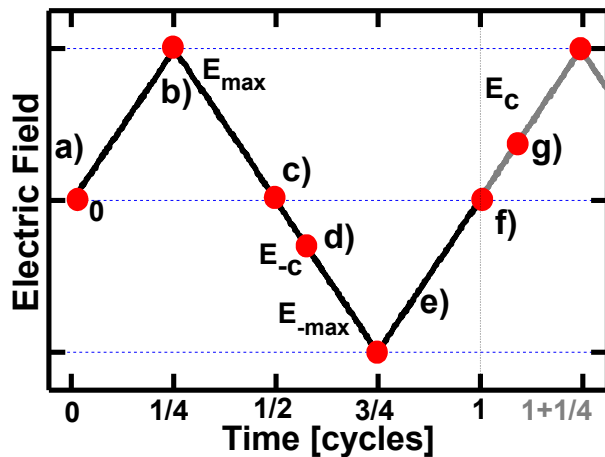


**Fig 3: Typical saw-tooth-shaped voltage signal used in bipolar large field characterisation.**

The applied electric field goes linearly with time from zero(a) to  $E_{\max}$ (b) and back to zero(c) through to  $E_{-\max}$ (e), back to zero again(f), back to  $E_{\max}$ (b) where the cycle can begin again. Points d) and g) are relevant in conjunction with the strain (Fig 5) and polarisation (Fig 4) hysteresis where they are defined.

In a typical ferroelectric beginning with an unpoled material ( $E=0$ ,  $P_0=0$ ,  $S_0=0$  by definition) at zero field, strain and polarisation increased up to the maximum applied field ( $E_{\max}$ ) to their respective maximum values ( $S_{\max}$  and  $E_{\max}$ ). On a microscopic scale, the ferroelectric domains are originally randomly distributed. As the field increases, domain walls move so that domains oriented in field direction grow at the expense of the others. When the field is now removed, strain and polarisation are reduced but do not return to their initial values entirely in a ferroelectric because only a small portion of the domains returns to their original state. These

new values are a remanent strain ( $S_r$ ) and remanent polarisation ( $P_r$ ). If an electric field in opposite direction is now applied the polarisation will return to zero at the negative coercive field ( $-E_c$ ). The corresponding strain ( $S_{-min}$ ) will be at a local minimum but not usually return to its original unpoled value ( $S_{-min} \neq S_0$ ). It is also sometimes referred to as negative strain since it is lower than  $S_r$ . At the highest magnitude negative electric field ( $E_{-max}$ ) the strain ( $S_{-max}$ ) and polarisation ( $P_{-max}$ ) are reached at nearly all domains are again oriented along the new field direction.

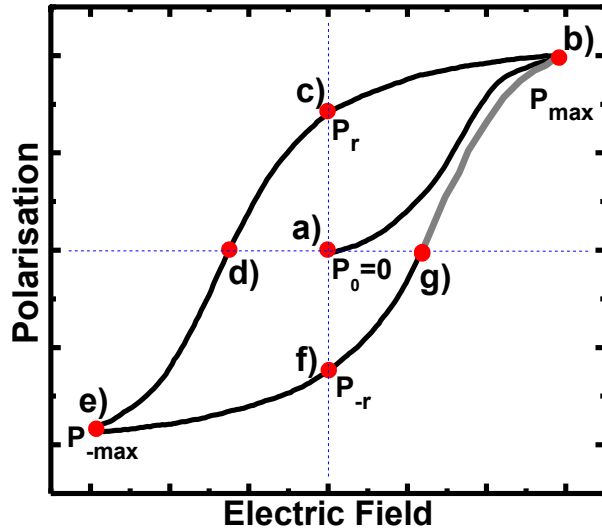


Fig 4: Polarisation vs. large electric field.

The polarisation goes from zero(a) to  $P_{max}$ (b) at  $E_{max}$  back to  $P_r$ (c) at zero field and then through zero(d) at  $E_{-c}$  and on to  $P_{-max}$ (e) at  $E_{-max}$ . It falls back to  $P_{-r}$ (f) when the field returns to zero. Once a positive field is applied again during the second cycle, the polarisation goes through zero(g) at  $E_c$  to  $P_{max}$ (b) and follows the same path again from that point onwards.

Once the field is removed, the cycle can start again but starting from  $P_{-r}$  and  $S_{-r}$  instead. In an ideal ferroelectric, the remanent polarisation ( $P_r/P_{-r}$ ) always has the same magnitude independent of the last field direction and the sign of the last applied field direction. The remanent strain is equal in magnitude and sign independent of the last field direction ( $S_r = -S_{-r}$ ). This behaviour is summarised in Fig 4 (polarisation) and Fig 5 (strain) with the corresponding electric field shown

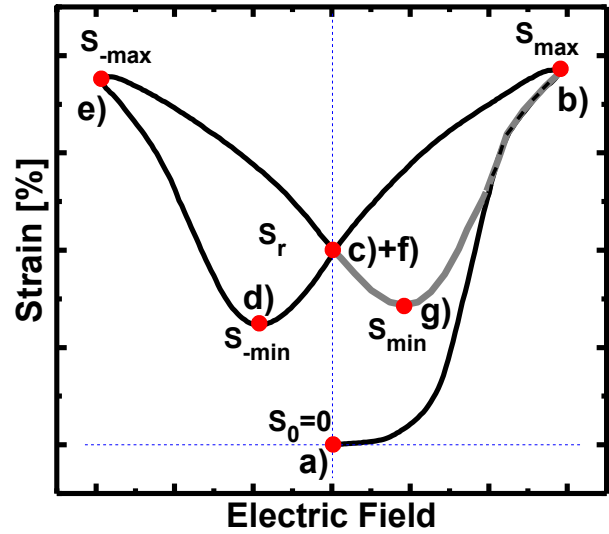


Fig 5: Strain in field direction in a large electric field as shown in Fig 3.

The strain goes from zero(a) to  $S_{max}$ (b) at  $E_{max}$  back to  $S_r$ (c) at zero field and then through  $S_{min}$ (d) at  $E_{-c}$  and on to  $S_{-max}$ (e) at  $E_{-max}$ . It falls back to  $S_{-r}$ (f) when the field returns to zero. Once a positive field is applied again during the second cycle, the polarisation goes through  $S_{-min}$ (g) at  $E_c$  to  $S_{max}$ (b) and follows the same path again from that point onwards.

in Fig 3. The typically low field linear behaviour described in the equations Eq 5 and Eq 6 to first order is found in ready-poled ferroelectrics at fields much less than the coercive field.

### 2.1.5 Relaxor Ferroelectrics

Relaxor ferroelectrics are ferroelectrics, where the Curie temperature is not clearly defined. Due to inhomogeneous composition, not all parts of the material depolarise at the same temperature. While this is usually undesirable as compositional inhomogeneities also leads to strong frequency dependence<sup>[16]</sup>, there are applications as capacitor materials since the dielectric constants and subsequently the capacitance are highest near the Curie temperature. This Curie temperature now becomes a broad temperature range. Therefore, relaxor ferroelectrics show a larger working temperature range than normal ferroelectrics in capacitive applications. The high dielectric constants over a wide range of temperatures also make these materials interesting for temperature-dependent high electrostrictive strain applications<sup>[17]</sup>.

### 2.1.6 Perovskites and Other Ferroelectric Structures

Current manufacturing techniques only allow polycrystalline materials to be considered for large-scale industrial applications. This in turn means that materials can be considered, whose polarity can be influenced by an external field<sup>[18]</sup>. Ilmenite, perovskite, tungsten bronze and bismuth-layer structure ferroelectrics are the most commonly investigated types.

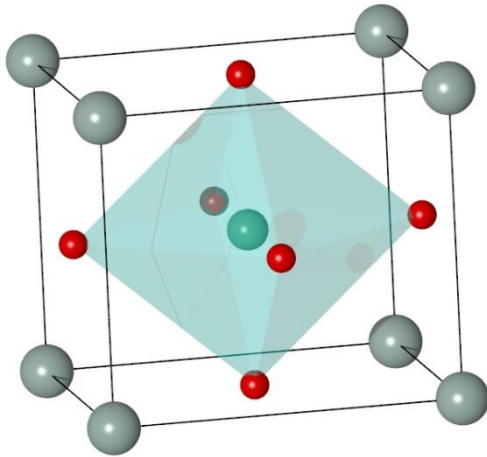


**Fig 6: Unit cell of an undistorted perovskite structure.**

**It is centred on the six-fold coordinated B-site cation (turquoise). The twelve-fold coordinated A-site cation (silver) is positioned at the corners of the cell; the six-fold coordinated oxygen anion is located at the faces of the cube (red).**

The general chemical formula for a perovskite structure is  $ABO_3$ . A and B are cations. The term complex in this context refers to structures where the A and/or B cation positions are occupied by more than one type of cation. The undistorted structure is described in Fig 6. For piezoelectric structures, non-centrosymmetric modifications of this structure are required. These modifications can for example be a deviation from right angle of the angles (rhombohedral), a change in the



cell axes in one or more directions (tetragonal and orthorhombic, respectively) or a combination of both (monoclinic,...).

$$t = \frac{R_A + R_O}{\sqrt{2}(R_B + R_O)}$$

**Eq 7: The formula of the Goldschmidt tolerance factor. The Goldschmidt tolerance factor helps predict the preferential formation of perovskite type structures over other structures by simple geometric means.  $R_A$ ,  $R_B$  and  $R_O$  are the radii of the respective ions with the coordination numbers of the undistorted structure<sup>[19]</sup>.**

Initial prediction of the stability of a perovskite structure is done using the Goldschmidt tolerance factor (Eq 7). It is a simple geometrical relationship with tolerance factor (t) equal to unity if the lattice is treated as an array of close packed spheres. Although the twelve-fold coordinated radii used technically only apply to the undistorted cubic structure, for comparability they are used for the distorted structures also<sup>[20]</sup>. Since twelve-fold coordinated radii are rarely available<sup>[21]</sup>, sometimes the nine-fold or six-fold radii are used directly or used for extrapolation<sup>[22]</sup>. The oxygen anion radius is usually taken as six-fold coordinated.

The B-side ions enclosed in the oxygen octahedra can shift their positions when an external field is applied. Each oxygen octahedron is connected to four other oxygen octahedra since each oxygen ion is shared between two octahedra. The A-side ions also have limited mobility around their average position surrounded by 12 oxygen ions, particularly, if their ionic size is small, i.e. the tolerance factor below one.

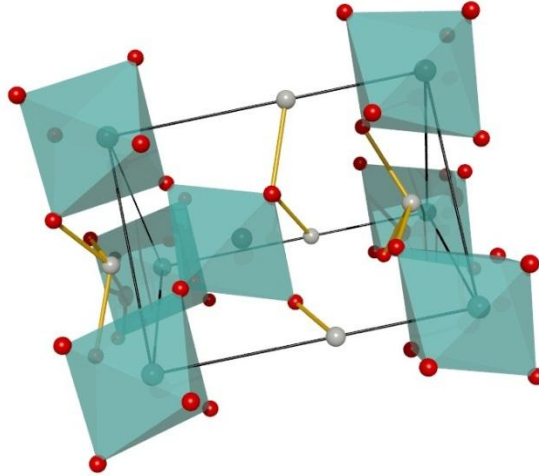


**Fig 7: The unit cell of an ilmenite structure. The example given here is lithium niobate. Lithium ions are shown as grey, niobium blue and oxygen red spheres. The oxygen octahedra are shaded in blue.**

Ilmenite has the same chemical formula as perovskite ( $\text{ABO}_3$ ) but each unit cell is much more complex as seen in Fig 7. Each unit cell consists of seven oxygen octahedra. However, not each oxygen ion is shared with a neighbouring oxygen octahedron. Therefore, the amount of oxygen octahedra per mol  $\text{ABO}_3$  (and per unit volume) is actually lower than in the case of the perovskite structure. This in turn provides fewer sites for ions within the octahedra to contribute to piezoelectric polarisation and leads to lower piezoelectric activity. Ilmenite structures form when the larger cation (the A-site ion if it was a perovskite structure) is too small to allow the formation of a perovskite structure.

Bismuth-layer structures (Fig 8) are effectively repeating units of perovskite unit cell layers. Within each layer, oxygen ions are shared between adjacent oxygen octahedra like in the standard perovskite structure. Oxygen ions are also shared between oxygen octahedra of adjacent layers. Every two to four perovskite layers there is a bismuth oxide layer, which is ferroelectrically inactive. These bismuth oxide layers help stabilising the perovskite layer structure hence leading to generally higher Curie temperatures. However, like in the case of ilmenite not all of the ions are used up in perovskite unit cells. Therefore, it is again unlikely that the perovskite layer structure ferroelectrics will ever show the same amount of ferroelectric activity as a pure perovskite structure.

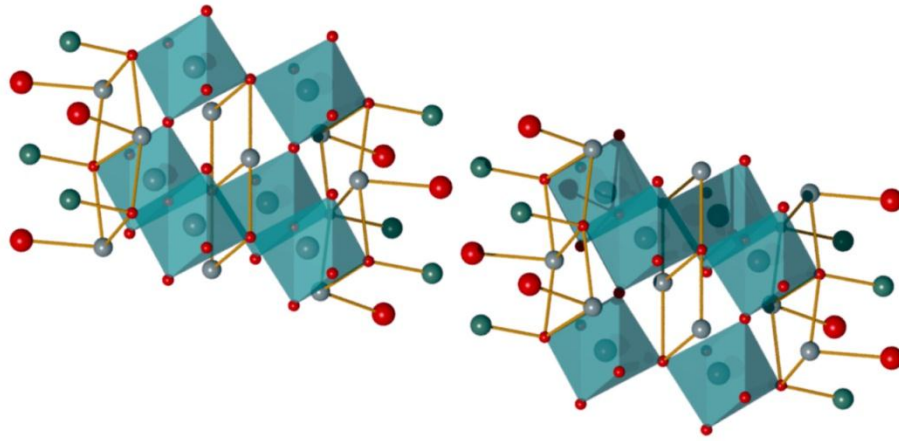


**Fig 8:** The unit cell of bismuth-layer structure with two repeating perovskite layers and the bismuth oxide layer. The example given here is  $\text{Bi}_{2-x}\text{Pb}_x\text{Sr}_{1.5}\text{Ca}_{1.5}\text{Mn}_2\text{O}_{9.8}$ . The oxygen octahedra are shaded in light blue with the oxygen ions at each corner. In the centre of each octahedron sits a manganese ion. The larger spheres represent bismuth ions, which share their crystallographic positions also with lead, strontium and calcium ions<sup>[23]</sup>.

## 2.1.7 References

- [1] A. S. Sonin and B. A. Strukow, "Einführung in die Ferroelektrizität." In *Mathematik und Physik*. Edited by G. Schmidt, Berlin, 1974.
- [2] B. Jaffe, W. R. Cook, and H. Jaffe. In *Piezoelectric Ceramics*. Academic Press, London, 1971.
- [3] B. A. Strukov and A. P. Levanyuk, "Ferroelectric Phenomena in Crystals." In. Springer-Verlag Berlin Heidelberg, Yew York, 1998.
- [4] A. J. Moulson and J. M. Herbert, "Electroceramics." In. Wiley & Sons Ltd., Chchester, 2003.
- [5] J. F. Nye. In *Physical Properties of Crystals*. Oxford Science Publications, Oxford, 1993.
- [6] R. E. Newnham. In *Properties of Materials: Anisotropy, Symmetry, Structure*. Oxford University Press, 2005.
- [7] S. E. Park and T. R. Shrout, "Ultrahigh strain and piezoelectric behavior in relaxor based ferroelectric single crystals," *Journal of Applied Physics*, **82**[4] 1804-11 (1997).
- [8] S.-E. Park, M.-J. Pan, K. Markowski, S. Yoshikawa, and L. E. Cross, "Electric field induced phase transition of antiferroelectric lead lanthanum zirconate titanate stannate ceramics," *Journal of Applied Physics*, **82**[4] 1798-803 (1997).
- [9] W. Pan, Q. Zhang, A. S. Bhalla, and L. E. Cross, "Field-forced antiferroelectric-to-ferroelectric switching in modified lead zirconate titanate stannate ceramics," *Journal of the American Ceramic Society*, **72** 7 (1989).
- [10] J. E. Daniels, W. Jo, J. Rödel, V. Honkimäki, and J. L. Jones, "Electric-field-induced phase transformation at a lead-free morphotropic phase boundary: Case study in a 93%(Bi<sub>0.5</sub>Na<sub>0.5</sub>)TiO<sub>3</sub>-7 % BaTiO<sub>3</sub> piezoelectric ceramic," *Applied Physics Letters*, **95**[3] 032904 (2009).
- [11] W. Jo, T. Granzow, E. Aulbach, J. Rödel, and D. Damjanovic, "Origin of the large strain response in (K<sub>0.5</sub>Na<sub>0.5</sub>)NbO<sub>3</sub> - modified (Bi<sub>0.5</sub>Na<sub>0.5</sub>)TiO<sub>3</sub> - BaTiO<sub>3</sub> - lead-free piezoceramics," *Journal of Applied Physics*, **105** 094102 (2009).
- [12] C. Kittel, "Theory of Antiferroelectric Crystals," *Physical Review*, **82**[5] 729 (1951).
- [13] D. Berlincourt, H. H. A. Krueger, and B. Jaffe, "Stability of phases in modified lead zirconate with variation in pressure, electric field, temperature and composition," *Journal of Physics and Chemistry of Solids*, **25**[7] 659-74 (1964).
- [14] V. Dorcet, G. Trolliard, and P. Boullay, "Reinvestigation of phase transitions in Na<sub>0.5</sub>Bi<sub>0.5</sub>TiO<sub>3</sub> by TEM. Part I: First order rhombohedral to orthorhombic phase transition," *Chemistry of Materials*, **20**[15] 5061-73 (2008).
- [15] G. Trolliard and V. Dorcet, "Reinvestigation of phase transitions in Na<sub>0.5</sub>Bi<sub>0.5</sub>TiO<sub>3</sub> by TEM. Part II: Second order orthorhombic to tetragonal phase transition," *Chemistry of Materials*, **20**[15] 5074-82 (2008).
- [16] L. E. Cross, "Relaxor Ferroelectrics," *Ferroelectrics*, **76**[3-4] 241-67 (1987).
- [17] K. T. P. Seifert, W. Jo, and J. Rödel, "Temperature-Insensitive Large Strain of (Bi<sub>1/2</sub>Na<sub>1/2</sub>)TiO<sub>3</sub>-(Bi<sub>1/2</sub>K<sub>1/2</sub>)TiO<sub>3</sub>-(K<sub>0.5</sub>Na<sub>0.5</sub>)NbO<sub>3</sub> Lead-Free Piezoceramics," *Journal of the American Ceramic Society*, **93**[5] 1392-6 (2010).
- [18] J. Rödel, W. Jo, K. Seifert, E.-M. Anton, T. Granzow, and D. Damjanovic, "Perspective on the Development of Lead-free Piezoceramics," *Journal of the American Ceramic Society*, **92**[6] 1153-77 (2009).
- [19] V. M. Goldschmidt, "Geochemische Verteilungsgesetze der Elemente. VII: Die Gesetze der Krystallochemie," *Skifter utgitt av det Norske Videnskaps-Akademi i Oslo, I. Matem.-Naturvid. Klasse*, **2** 5-116 (1926).
- [20] A. Senyshyn, H. Ehrenberg, L. Vasylechko, J. D. Gale, and U. Bismayer, "Computational study of LnGaO<sub>3</sub> (Ln = La-Gd) perovskites," *Journal of Physics-Condensed Matter*, **17**[39] 6217-34 (2005).
- [21] R. D. Shannon, "Revised effective ionic-radii and systematic studies of interatomic distances in halides and chalcogenides," *Acta Crystallographica Section A*, **32**[Sep1] 751-67 (1976).
- [22] M. W. Lufaso and P. M. Woodward, "Prediction of the crystal structures of perovskites using the software program SPuDS," *Acta Crystallographica Section B*, **57**[6].
- [23] M. Hervieu, C. Michel, D. Pelloquin, A. Maignan, and B. Raveau, "A bismuth manganite with the "2212" structure: Bi<sub>2-x</sub>Pb<sub>x</sub>Sr<sub>1.5</sub>Ca<sub>1.5</sub>Mn<sub>2</sub>O<sub>9-delta</sub>," *Journal of Solid State Chemistry*, **132**[2] 420-31 (1997).

## 2.2. Bismuth Alkali Titanates

The next two chapters will give an overview of the current state of scientific knowledge regarding lead-free piezoceramics. A number of previous reviews can be found in literature. Some cover lead-free piezoceramics in general<sup>[1-3]</sup>, others focus on specific systems or summarise a single workgroup's achievements<sup>[4-7]</sup>. While there are many types of structures (for example bismuth-layer structures such as  $\text{Bi}_4\text{Ti}_3\text{O}_{12}$ <sup>[8,9]</sup>, ilmenite such as  $\text{LiNbO}_3$ <sup>[10-12]</sup>, ...), which exhibit piezoelectricity, currently the most promising structure is of perovskite type. Within this structure type, current scientific work focuses mostly on two major groups. The first group is bismuth-alkali-titanate-based lead-free perovskites. The second is alkali-niobate-based lead-free perovskites. Tables with reported properties of pure and modified systems can be found at the end of the respective chapters due to their size.

### 2.2.1 Structure and Phase Transitions of BNT and BKT

Bismuth sodium titanate (BNT or  $\text{Bi}_{1/2}\text{Na}_{1/2}\text{TiO}_3$ ) is the building block of almost all bismuth-based lead-free perovskites. In pure BNT, half of all A-site positions are filled with bismuth (3+) ions, the other half with sodium (1+) ions. The B-site positions are filled by titanium (4+) ions. Even though bismuth and sodium have very different charges, there is only short range but no long range ordering of the A-site ions<sup>[13-15]</sup>.

Pure BNT is a relaxor-like<sup>[16]</sup> rhombohedral ferroelectric<sup>[17]</sup> at room temperature and ambient pressure. It has at least two more structural phase transitions between room temperature and its sintering temperature. However, there is not even consensus about the number of phase transitions 50 years after discovery<sup>[18]</sup>. Beginning at room temperature, the first and only undisputed phase transition temperature is 200 °C<sup>[13,17]</sup>. To avoid confusion, the transition temperature will always be referred to as  $T_d$  independent of what its true nature might be. For the Curie temperature, reported values are in the vicinity of 320 °C<sup>[13,19,20]</sup>. The gamma value<sup>1</sup> of the phase transition at  $T_C$  is reported as 1.55, which implies relaxor characteristics<sup>[21]</sup>. Above the Curie temperature, there is a tetragonal phase, which is considered either ferroelastic and/or superparaelectric<sup>[22]</sup>. At 540 °C, this phase changes to a cubic paraelectric phase<sup>[13]</sup>.

---

<sup>1</sup> The gamma value ( $\gamma$ ) of a phase transition is defined by  $1/\epsilon_r - 1/\epsilon_m = C^{-\gamma} (T - T_m)^\gamma$  where  $\gamma$  is the degree of diffuseness,  $\epsilon_m$  is the maximum dielectric constant at  $T_m$  and  $C$  is the Curie coefficient. The gamma value is 1 for ideal, normal, ferroelectrics and 2 for relaxor ferroelectrics<sup>[21]</sup>.

The phase between 200 °C and 320 °C merits more detailed discussion. Pronin et al.<sup>[23]</sup> propose that upon cooling a single crystal of BNT, smaller regions of an antiferroelectric phase appear, which grow in size and number. For energetic reasons, they also propose a paraelectric layer between differently orientated antiferroelectric regions. This theory is also supported by Sakata et al.<sup>[20]</sup>. Zvirgizds et al.<sup>[24]</sup> identify this phase as rhombohedral (pseudocubic) in a single crystal. Pseudocubic in this context means that the unit cell angles cannot be distinguished from 90° but other properties such as birefringence cannot be explained by a cubic symmetry. They find evidence, which is consistent with a ferroelectric to antiferroelectric transition but also point out that there are no superstructure reflexes indicating the doubling of the unit cell, which is required in an antiferroelectric phase. There is also a strong frequency dependence of the maximum in the dielectric constant at this phase transition, which is otherwise unknown in ferroelectric to antiferroelectric transitions. Vakhurshev et al.<sup>[13]</sup> support these results again with neutron scattering data and proposed the existence of the high-temperature non-polar phase with smaller polar regions. Polar regions in a non-polar matrix were also indicated in pyroelectric measurements. The coexistence of rhombohedral and tetragonal phases in the temperature range from 200 °C to 280 °C is suggested<sup>[18,25]</sup> and again supported through time-dependent electric permittivity measurements<sup>[26]</sup>. Ferroelastic properties in this temperature range have also been shown<sup>[27]</sup>.

Dorcet et al.<sup>[14,28]</sup> discuss previous literature and in conjunction with TEM studies and selected area electron diffraction (SAED) conclude the existence of a modulated phase (explained here<sup>[29]</sup>) where orthorhombic sheets appear in the rhombohedral ferroelectric matrix at temperatures above 200 °C. Once the amount of orthorhombic phase is sufficiently large, the polar vectors of the remaining polar regions reorient so that neighbouring regions have opposing polar vectors leading to be quasi-antiferroelectric nature of the phase. They also report the appearance of a superstructure reflex between 200 °C and 300 °C and identify the tilt systems of the oxygen octahedral in the different phases. Trolliard et al.<sup>[15]</sup> then complement this work by reporting that the second phase transition at 320 °C is from purely orthorhombic to tetragonal. Jones et al.<sup>[30]</sup> report a purely rhombohedral phase up to 255 °C using powder neutron diffraction. A rhombohedral/tetragonal mixed phase region was found at 300 °C and 320 °C. The temperature range of the rhombohedral/tetragonal mixed phase region is unclear due to incomplete data. From 400 °C to 500 °C, a purely tetragonal phase is reported. A tetragonal/cubic mixed phase region was found between 500 °C and 540 °C and above 540 °C the structure is cubic.

Pure bismuth potassium titanate (BKT or  $\text{Bi}_{1/2}\text{K}_{1/2}\text{TiO}_3$ ) was first determined to be ferroelectric by Smolenskii et al.<sup>[31]</sup> in 1961 at the same time as BNT. Its unit cell is similar to that of BNT but with all the sodium ions replaced by potassium ions. It is a tetragonal ferroelectric perovskite at room temperature with  $a=0.39313$  nm and  $c=0.3993$  nm ( $c/a=1.016$ ) and a Curie temperature of between  $380^\circ\text{C}$ <sup>[31]</sup> and  $437^\circ\text{C}$ <sup>[32]</sup>. Another report states  $a=0.3918$  nm and  $c=0.3996$  ( $c/a=1.020$ )<sup>[33]</sup>. The Curie temperature determined from dielectric measurements shows strong frequency dependence. At 10 kHz, the Curie temperature is  $415^\circ\text{C}$ , while  $425^\circ\text{C}$  and  $437^\circ\text{C}$  were measured at 100 kHz and 1 mHz, respectively. Below the Curie temperature, a frequency independent maximum of  $\tan\delta$  at  $340^\circ\text{C}$  indicates another phase transition. Above the Curie temperature BKT is cubic paraelectric<sup>[32]</sup>.

### 2.2.2 Preparation of Pure BNT and BKT

Pure BNT can be synthesised as a polycrystalline ceramic<sup>[34]</sup>, thin film<sup>[35,36]</sup> or as a single crystal<sup>[26,37]</sup>. Pure polycrystalline ceramic BNT is difficult to prepare<sup>[19,38]</sup>. When using a standard mixed oxide route, the stoichiometrically mixed and milled powders are usually calcined at around  $800^\circ\text{C}$  to  $900^\circ\text{C}$  for two to four hours<sup>[14,28,38]</sup>. Longer calcination times as well as repeated milling between multiple calcinations can improve sample quality if bismuth oxide vaporisation is prevented<sup>[30]</sup>. Thermogravimetric analysis of BNT powder has shown that bismuth oxide vaporisation occurs above  $1130^\circ\text{C}$ <sup>[38]</sup>. However, to achieve acceptable densities, sintering temperatures of at least  $1200^\circ\text{C}$  are required<sup>[5,38]</sup>, which is close to its melting point of  $1225^\circ\text{C}$ . Another report states  $1290^\circ\text{C}$  as the melting point<sup>[37]</sup>. Therefore, loss of bismuth oxide needs to be suppressed, which is described in section 4.1, or compensated and temperatures have to be well controlled<sup>[38]</sup>. BNT-based materials, which can be sintered below  $1100^\circ\text{C}$  require no suppression compensation of bismuth<sup>[39,40]</sup>. Temperature and time dependence of grain growth in BNT during sintering has been found to be relatively low<sup>[41]</sup>.

Single phase BKT powder can be produced from the mixed and milled starting powders by calcinations at  $800^\circ\text{C}$  for four hours followed by  $950^\circ\text{C}$  for two hours. Conventional sintering yields single-phase perovskite ceramics, if the temperature stays below  $1030^\circ\text{C}$ . Above  $1030^\circ\text{C}$ , impurity reflexes in x-ray diffraction are witnessed up to the melting temperature of  $1070^\circ\text{C}$ . The highest density of 93 % is achieved at  $1060^\circ\text{C}$  but conductivity is high due to secondary phases from decomposition due to potassium and bismuth loss. Hot pressing at  $1060^\circ\text{C}$  suppresses phase impurities and results in 97 % density ceramics with  $10^{13} \Omega\text{cm}$  resistivity<sup>[32]</sup>. To improve results of hot pressing, 0.6 wt.% excess bismuth oxide can be added, which reduces

microcracking. Increasing the hot-pressing time from 4 to 10 hours improves all piezoelectric and dielectric properties but simultaneously reduces  $T_d$  and  $T_C$  by up to about 20 °C. In general, for conventional sintering of pure BNT and BKT, reasonable sintering occurs only just below the melting point and well above temperatures for partial decomposition<sup>[42]</sup>. For BKT preparation via a sol-gel method, see section 2.2.8.

### 2.2.3 Properties of BNT and BKT

Smolenskii et al.<sup>[31]</sup> show graphs of the temperature dependence of the dielectric permittivity ( $\epsilon/\epsilon_0=\epsilon_r$ ), the loss tangent<sup>[31]</sup> ( $\tan\delta$ ), the linear thermal expansion coefficient ( $\alpha$ ) and the relative extension( $\Delta l/l$ ) from room temperature to 400 °C. They report having been able to pole BNT fully but not BKT although no specific field values are given. Nagata et al.<sup>[38]</sup> show a near linear increase in relative density of BNT with temperature from 90 % at 1150 °C to 98 % at 1225 °C with a sintering time of two hours. At temperatures above 1225 °C, the samples partially melted. At 1100 °C, a two-hour sintering time resulted in 87 % relative density, which can be improved to 96 % relative density after 100 hours. They also add excess bismuth oxide to BNT and report a rapid increase in Curie temperature from 332 °C in pure BNT to 351 °C with 1% excess bismuth oxide. Adding more than 1 mol% bismuth oxide does not increase the Curie temperature much further. The increase in Curie temperature is accompanied by a three order of magnitude decrease in resistivity from nearly  $10^{14}$   $\Omega\text{cm}$  to  $10^{11}$   $\Omega\text{cm}$  between 0.3 mol% and 1 mol% excess bismuth oxide. However, between zero and 0.3 mol% excess bismuth oxide, the resistivity increases from  $10^{12}$  to  $10^{14}$   $\Omega\text{cm}$ . It is therefore assumed that 0.3 mol% excess bismuth oxide exactly compensates for the loss of bismuth during sintering in this case. Suchanicz et al.<sup>[22]</sup> investigate the temperature-dependent real and imaginary parts of the dielectric constant ( $\epsilon''$  and  $\epsilon'''$ ). The real part shows a linear increase from 80 °C up to 250 °C where the slope steepens peaking at 320 °C. Roleder et al. also show the time dependence of the dielectric constant at different temperatures here<sup>[26]</sup>. Vakhurshev et al.<sup>[13]</sup> determine a depolarization temperature of 190 °C from pyroelectric current measurements during heating. Suchanicz et al.<sup>[25]</sup> find a second pyroelectric current peak at 320 °C. They also report a small but finite piezoelectric resonance above 200 °C<sup>[18]</sup>. Pure BNT has a coercive field of 7.3 kV/mm, which is higher than the usual breakdown strength in the polycrystalline ceramic and conductivity is also an issue<sup>[19]</sup>. At room temperature, dielectric constants between 408 (unpoled) and 780 (poled) are reported<sup>[21,35,43]</sup>, coercive fields vary greatly between 2 kV/mm for sol-gel derived BNT and 7.3 kV/mm for BNT prepared by a mixed oxide route. Lower values can usually be attributed to



nonstoichiometry<sup>[21,35,36,41]</sup>. The only report of fully poled BNT mentions a remanent polarisation of  $37 \mu\text{C}/\text{cm}^2$ <sup>[21]</sup>. Li et al.<sup>[44]</sup> show a hysteresis of almost fully poled BNT with  $P_r=29.0 \mu\text{C}/\text{cm}^2$  and  $E_C=6.11 \text{ kV}/\text{mm}$ . A study of the effects of sintering time and temperature variation shows only statistical fluctuations of the dielectric and piezoelectric properties as well as grain size<sup>[41]</sup>. BKT, hot-pressed at  $1080^\circ\text{C}$ , is considered slightly nonstoichiometric due to its lower  $T_C$  of  $410^\circ\text{C}$  but shows otherwise the best overall ferroelectric properties reported. Dielectric constant  $\epsilon_s$ ,  $\tan\delta$ ,  $P_r$  and  $E_C$  are 517, 7.1 %,  $22.2 \mu\text{C}/\text{cm}^2$  and  $5.25 \text{ kV}/\text{mm}$  respectively. A unipolar strain of 0.12 % at  $8 \text{ kV}/\text{mm}$  corresponds to a  $d_{33}^*$  of  $135 \text{ pC}/\text{N}$ . The „true“  $d_{33}$  is reported as  $69.8 \text{ pC}/\text{N}$ <sup>[32]</sup>. Hot-pressed BKT with excess bismuth oxide shows maximum values of 764, 0.4 and  $101 \text{ pC}/\text{N}$  for  $\epsilon_{33}$ ,  $k_{33}$  and  $d_{33}$ , respectively, and a 0.13 % maximum unipolar strain at  $8 \text{ kV}/\text{mm}$ <sup>[45]</sup>. These improved values are the results of field cooling (poling during cooling) and increased grain size due to extended sintering. Sasaki et al.<sup>[33]</sup> report  $\epsilon_{33}$  of  $\sim 800$ , a mechanical quality factor ( $Q_m$ ) of 100 as well as coupling factors  $k_p$ ,  $k_t$  and  $k_{31}$  of  $\sim 0.19$ ,  $\sim 0.38$  and  $\sim 0.11$ , respectively. The phase transition at the Curie temperature ( $T_C$ ) of BNT and BKT is identified as being of second order.

The properties of pure BNT and BKT are summarised in Tab 1 and Tab 2, which, due to their size can be found at the end of the chapter (pages 41 ff. and 45 ff.). It should, however, be noted that most of the values for both pure BNT and BKT are derived from material that was either hot-pressed or sintered with excess bismuth oxide since material derived via an unmodified mixed oxide route usually results in unacceptable quality<sup>[19,31]</sup>. Properties of the modified BNT can be found in Tab 3 (pages 48 ff.).

## 2.2.4 BNT-BT and Related Materials

Based on the knowledge that piezoelectric properties are increased at the morphotropic phase boundary between rhombohedral and tetragonal<sup>[46]</sup>, Takenaka et al.<sup>[39,40]</sup> attempted to create similar morphotropic phase boundaries between BNT and different ratios of  $\text{SrTiO}_3$ ,  $\text{PbTiO}_3$  and  $\text{CaTiO}_3$ . For several ratios of at least two of  $\text{SrTiO}_3$ ,  $\text{PbTiO}_3$  and  $\text{CaTiO}_3$  morphotropic phase boundaries between rhombohedral and tetragonal were found at 87 mol% BNT and 13 mol%  $a*\text{SrTiO}_3+b*\text{PbTiO}_3+c*\text{CaTiO}_3$  ( $a+b+c=1$ ). BNT+ $\text{CaTiO}_3$  even shows a  $10^\circ\text{C}$  increase in Curie temperature over pure BNT to  $330^\circ\text{C}$ . However, the  $d_{33}$  is low at  $50 \text{ pC}/\text{N}$ . coupling factors  $k_p$  and  $k_{33}$  of the  $\text{CaTiO}_3$  added material are also much lower than those of the other two systems. None of the systems showed sufficient potential as a replacement for PZT.

In 1991, Takenaka et al.<sup>[47]</sup> discovered the morphotropic phase boundary between BNT and tetragonal barium titanate ( $\text{BaTiO}_3$  or BT) at 6 mol% BT addition. They constructed a temperature and composition dependent phase diagram based on x-ray diffraction, dielectric and piezoelectric data up to 30 mol% barium titanate. It should be noted that the Curie temperature and depolarisation temperature of BNT in the phase diagram is reported as 25 K higher than previous reports<sup>[13,17,19,20]</sup>. At room temperature, the morphotropic phase boundary is clearly defined by a sharp increase in the dielectric constant of poled and unpoled samples to  $\sim 1600$  and  $\sim 950$ , respectively. Coupling factors  $k_p$ ,  $k_t$  and  $k_{31}$  remain relatively constant around 0.20, 0.48 and 0.15, respectively, up to 30 mol% BT addition to BNT, whereas  $k_{33}$  increases from 0.35 to above 0.50 near the MPB. For the depolarisation temperature, values between 100 °C and 130 °C are reported<sup>[43,46-49]</sup>. Preparation of BNT-BT via mixed oxide route is identical to that of BNT but achievable densification is higher<sup>[21,43,47,49]</sup>.

Ranjan et al.<sup>[50]</sup> provide a detailed powder x-ray diffraction analysis for compositions around the MPB. They show that there are no measurable tetragonal lattice distortions or tetragonal superstructure reflexes in BNT-BT between the MPB (6 mol% BT) and 10 mol% BT. They instead claim a nearly cubic phase. Xu et al.<sup>[21]</sup>, however, show clear tetragonal distortion above 6 mol% added BT.

The remanent polarisation ( $P_r$ ) peaks at the MPB at  $38.8 \mu\text{C}/\text{cm}^2$ <sup>[21]</sup>. The coercive field ( $E_c$ ) is continuously reduced with increasing BT content up to its lowest value of 3.25 kV/mm at 8 mol% BT. Compositional dependence of  $d_{33}$ ,  $k_p$ ,  $\epsilon_r$  and  $\tan\delta$  is reported up to 12 mol% BT.  $d_{33}$ ,  $k_p$  and  $\tan\delta$  show their optimum values of 155 pC/N, 36.7 %, and approximately 2.5 %, respectively, at the MPB. In contrast, the relative dielectric constant  $\epsilon_r$  peaks at 8 mol% BT with 1099<sup>[21]</sup>. This is in contradiction to the original results by Takenaka et al.<sup>[47]</sup> but no reason is evident.

Xu et al.<sup>[21]</sup> also measure the diffuseness of the phase transition at  $T_d$ . The gamma value of morphotropic BNT-BT is reported as 2.02, making it a pure relaxor, which is also reported here<sup>[51]</sup>. The relaxor nature is attributed to the A-site cation disorder of BNT-BT. Temperature-dependent  $k_p$  shows a drop around 80 °C and  $d_{33}$  and  $\tan\delta$  about 105 °C. Temperature-dependent polarisation hystereses for 0, 6 and 12 mol% BT content show a typical ferroelectric behaviour below 140 °C, 60 °C and 160 °C, respectively, with decreasing  $E_c$  when the temperature increases. Above these respective temperatures, antiferroelectric-like pinched loops or nearly double loops are found in all three compositions. The fact that there is always some small amount of hysteresis at low fields is treated as evidence that above  $T_d$  a small amount of polar

ferroelectric material remains. Qu et al.<sup>[43]</sup> introduce up to 20 % BT in BNT and show continuously improved density with BT content. They claim that there is a phase coexistence between trigonal and tetragonal above  $T_d$ . Combined with a thermal hysteresis in the dielectric constant, this is treated as evidence for the existence of polar micro-domains above  $T_d$ . Data by Oh et al.<sup>[49]</sup> suffers from experimental difficulties and should not be considered. A table (Tab 4) listing the properties reported for pure BNT-BT can be found on pages 49ff.

### 2.2.5 BNT-BKT and Related Materials

Buhrer et al.<sup>[46]</sup> first prepared BNT-BKT in 1962 and found a minimum in the depolarisation temperature at 20 mol% BKT. Since this is undesirable, it was not until 1996<sup>[33]</sup> that at first a biphasic region was first found to centre around the same composition and with 10 mol% BKT content to either side. At the same time, it was shown that the phase transition at  $T_m$  is of second order and is considered the Curie temperature ( $T_C$ ). In 1999 Sasaki et al.<sup>[52]</sup> concluded BNT-20BKT to be the morphotropic phase boundary between BNT and BKT. It should, however, be noted that dielectric and piezoelectric constants  $\epsilon_r$  and  $d_{31}$  are highest at 21 mol% BKT with 1030 and 46.9 pC/N<sup>[52]</sup>. Coupling factors  $k_t$ ,  $k_p$ , and  $k_{31}$  as well as mechanical quality factor  $Q_m$  are higher at 16 mol% BKT with 0.42, 0.31, 0.18 and 195 respectively. Remanent polarisation and coercive field are reported as 19.9  $\mu\text{C}/\text{cm}^2$  and 2.4 kV/mm<sup>[52]</sup>.

However, while there is no dispute about the existence of the enhanced dielectric and piezoelectric properties at or very near BNT-20BKT, the existence and nature of the corresponding morphotropic phase boundary at this point is disputed. Jones et al.<sup>[53]</sup> mentioned previous studies that found a phase boundary at 20 mol% BKT and another with the MPB at 14 mol% BKT<sup>[54]</sup>. Their own extensive neutron data analysis across the complete compositional range from pure BNT to pure BKT is the first to assign space groups to all compositions. They did not, however, find any room temperature MPB around 20 mol% BKT. Instead they report MPBs at 45 mol% and 70 mol% BKT. In a more recent report<sup>[55]</sup>, 16 mol% BKT has also been suggested as the composition with the best overall properties. A high temperature mixed phase of rhombohedral and tetragonal around 20 mol% BKT found by Jones et al.<sup>[53]</sup> has recently been correlated with dielectric and piezoelectric data by Hiruma et al.<sup>[56]</sup>.

Yoshii et al.<sup>[57]</sup> and Hiruma et al.<sup>[56]</sup> found an inversely linear correlation between  $d_{33}$  and  $T_d$  for BNT-BKT-based systems. Therefore, the increased piezoelectric properties around 20 mol% BKT might simply be a result of the vicinity of the second order phase transition to room temperature at that point<sup>[57,58]</sup>.

Manufacture of BNT-20BKT necessitates lower sintering temperatures<sup>[55]</sup> compared to BNT-BT due to the lower decomposition temperature and melting point of BKT<sup>[32]</sup>. The higher vapour pressure of potassium compared to barium and sodium also needs to be addressed<sup>[58]</sup> through evaporation suppression or compensation. A sintering study of BNT-BKT with 18 mol% to 22 mol% BKT shows optimum  $d_{33}$  and remanent polarisation for samples sintered at 1150 °C<sup>[59]</sup>. However, the samples with the highest piezoelectric properties do not also automatically have the highest relative density. Overall, BNT-22BKT shows the higher  $\epsilon_{33}$ ,  $P_r$  and  $k_p$  of 1007, 19.5  $\mu\text{C}/\text{cm}^2$  and 32.5 %, respectively, but BNT-20BKT the lowest  $\tan\delta$  of 1.87 %. Yang et al.<sup>[60]</sup>, focused on optimization of processing parameters, find that  $d_{33}$ ,  $\tan\delta$ ,  $\epsilon_r$  and  $k_p$  improve up to a maximum sintering temperature of 1170 °C, after which they decrease slightly. The best values were found to be 144 pC/N, 3.7 %, 893 and 0.29, respectively, at 18 mol% BKT. They also reported a doubling in grain size when increasing the sintering temperature from 1150 to 1200 °C but with an overall decrease in density. The highest  $d_{33}$  achieved so far in pure BNT-BKT is 192 pC/N. This was found at 22 mol% BKT with the loss of bismuth compensated<sup>[61]</sup>. The influence of bismuth compensation was closely investigated by Zhang et al.<sup>[62]</sup> whose results emphasize the importance of bismuth loss. Bismuth loss compensation gives 25-30 % higher remanent polarisation and  $d_{33}$ . At the same time, the compensation appears to shift the MPB towards higher BKT content. Best values for uncompensated BNT-BKT were found to be  $d_{33}=145$  pC/N,  $T_C=292$  °C and  $k_p=0.27$  at 20 mol% BKT. Bismuth loss compensated BNT-BKT has its best properties at 23 mol% BKT with  $d_{33}=207$  pC/N,  $T_C=330$  °C and  $k_p=0.30$ . Bismuth loss compensation also hinders grain growth.

Hiruma et al.<sup>[56]</sup> also demonstrated that different properties, which are usually assumed to be closely related, show optimum values at different mole percentages of BKT. More precisely at 22 mol%, BKT  $S_{\max}/E_{\max}$  (also called  $d_{33}^*$ ), unipolar strain,  $\epsilon_{33}$ ,  $E_C$  are optimal, whereas  $d_{33}$ ,  $k_{33}$  are higher at 20 mol% BKT. Yoshii et al.<sup>[57]</sup> found the  $d_{33}^*$  of BNT-22BKT and BNT-26BKT to be higher than that of BNT-20BKT, which is normally considered the MPB composition. The mechanical quality factor shows a minimum at the MPB and increases continuously with increasing BKT content on the tetragonal side of the MPB<sup>[52,62]</sup> and also on the rhombohedral side with decreasing BKT content<sup>[52]</sup>.

The inconsistencies in the reported MPB positions, as well as dielectric and piezoelectric properties and in particular the phase transition temperatures, are unique to the BNT-BKT system. They may therefore be related to potassium with its high vapour pressure and its consequent loss during sintering. A small deviation in the potassium content will result in

significant deviations of all relevant properties. Possible variations can be anticipated by considering reports of compositions close to and at the MPB<sup>[52,56,57,60,61,63]</sup>. The properties of pure BNT-BKT are summarised in Tab 6 (pages 52ff.).

### 2.2.6 BNT-BKT-BT

Having found the regions of optimal properties in both BNT-BT and BNT-BKT, the next logical step may be to create a ternary phase diagram of BNT-BKT-BT (Fig 9). In 2003 Nagata et al.<sup>[64]</sup> investigated 12 compositions along two lines in the phase diagram connecting BNT-6BT with BNT-16BKT (line A) and BNT-7BT with BNT-20BKT (line B), which are both shown with red rings in Fig 9. The starting points of both lines in the phase diagram were chosen since they mark the most likely limits of the MPB regions in the BNT-BT and BNT-BKT systems as reported in sections 2.2.4 and 2.2.5. Curie temperature, dielectric constant  $\epsilon_r$ , coupling factor  $k_{33}$  and piezoelectric constant  $d_{33}$  of line A vary almost linearly between the values of the endpoint compositions. The same holds true for Curie temperature and dielectric constant of line B. However, coupling factor and piezoelectric constant of line B compositions show a maximum at (BNT-7BT)-40(BNT-20BKT) and (BNT-7BT)-60(BNT-20-BKT) reaching 56 % and 191 pC/N, respectively. While the actual percentage increase over the highest end member compositions value is only 20 to 25 %, it comes at little to no expense to the Curie temperature or other reported properties. Preparation of BNT-BKT-BT is the same as that of BNT-BKT due to BKT, which is the limiting factor in terms of both sintering temperature and evaporation.

Wang et al.<sup>[65]</sup> investigate the line  $(1-x)\text{BNT}-x\text{BKT}-5\text{BT}$  up to  $x=0.2$  and find continuous improvement of  $T_d$ ,  $\tan\delta$ ,  $\epsilon_{33}$  and continuous worsening of  $Q_m$  with increasing  $x$ .  $k_p$  and  $d_{33}$  are highest at  $x=0.05$  and  $0.06$ , respectively, but improvements are always at the expense of some other ferroelectric properties.

Makiuchi et al.<sup>[66]</sup> introduce BT and BKT in a 4:1 and 2:1 ratio into BNT. In both cases  $d_{33}$ ,  $\epsilon_{33}$  and  $k_{33}$  increase inversely related to the depolarisation temperature while the Curie temperature remains reasonably constant. The depolarisation temperature drops suddenly from above 200 °C to around 100 °C at 25 mol% (4BT-1BKT) within a 3 mol% step and within a 6 mol% step for (2BT-BKT) indicating that BT is mainly responsible for the drop. BNT-4BKT-8BT shows a particularly stable temperature-dependent  $k_{33}$  of 0.45 right up to its depolarisation temperature of 197 °C. Li et al.<sup>[44]</sup> find their highest  $d_{33}$  at BNT-12BKT-3BT but make no mention of the corresponding  $T_d$ . Again, different dielectric and piezoelectric properties show optimum values at different, though closely grouped, (4BKT-1BT) concentrations. Chen et al.<sup>[67]</sup> compare these

results with BNT-x(2BKT-1BT) and find a similar maximum at BNT-7BKT-3.5BT. The MPB region between BNT-BT and BNT-BKT is also further refined<sup>[67]</sup>. A temperature-dependent phase diagram of BNT-x(2BKT-1BT) is presented here<sup>[68]</sup>. The BNT-x(2BKT-1BT) line intersects the MPB region suggested by Nagata et al.<sup>[64]</sup> directly. Temperature-dependent properties of BNT-x(2BKT-1BT) on the tetragonal and rhombohedral side, as well as within the MPB region, help defining the actual shape of the MPB region more precisely<sup>[4]</sup>.

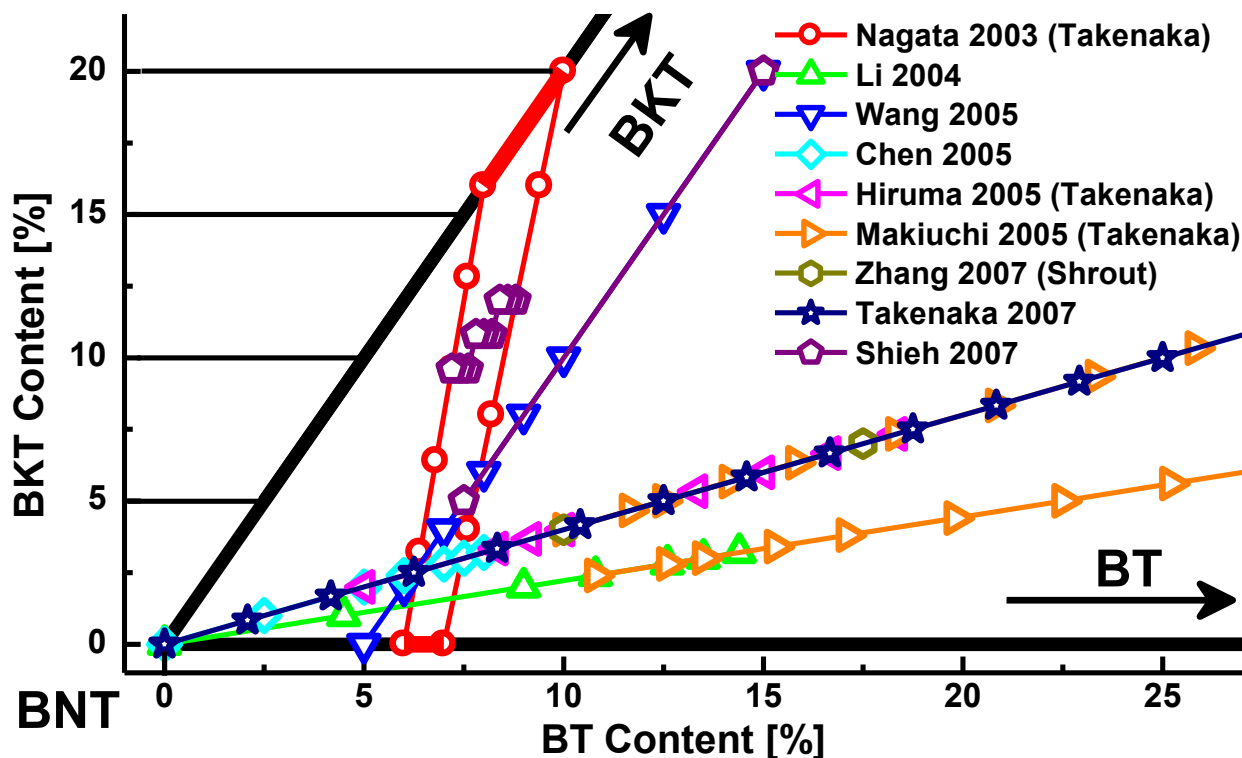


Fig 9: The BNT rich part of the BNT-BKT-BT phase diagram with all compositions reported in literature<sup>[4,44,64,66-71]</sup> sorted by their respective authors.

Shieh et al.<sup>[69]</sup> created all compositions of 60(BNT-xBKT)-40(BNT-yBT) that intersect with lines connecting BNT-BKT and BNT-BT MPB boundaries. Their highest achieved  $d_{33}$  is 295 pC/N. However, the phase diagram showing the places of the compositions is incorrect since they did not actually lie on the 6BKT-4BT line but in the positions indicated in Fig 9.

Choy et al. use BNT-5BKT-5BT in ultrasonic wire bonding applications<sup>[70]</sup> and compressive type accelerometers<sup>[71]</sup>, to demonstrate the potential usability of already known lead-free piezoceramics.

## 2.2.7 Dopants, Modification and Their Effects

It has been well established by now that most improvements of room temperature dielectric and piezoelectric properties of BNT-related materials are directly correlated with a reduction in depolarisation temperature<sup>[72]</sup>. It is therefore desirable to find dopants and modifications with

minimal influence on  $T_d$ . Reports of improved piezoelectric properties of modified BNT or BNT-BT without stated depolarisation temperatures are therefore of little use, all other reports BNT-BT listing  $d_{33}$ <sup>[65,73-83]</sup> and  $k_p$ <sup>[65,73-79,82,84]</sup>, and a corresponding  $T_d$ , are summarised in Fig 10 and Fig 11 respectively.

Strontium titanate ( $\text{SrTiO}_3$ ) was added to BNT initially in an attempt to lower the phase transition temperature  $T_d$ <sup>[20]</sup>. Its relaxor behaviour was studied<sup>[85]</sup> and it was used as a representative to investigate the influence of non-ferroelectric perovskites on BNT<sup>[85]</sup>. Hiruma et al.<sup>[86]</sup> report that 26-28 mol%  $\text{SrTiO}_3$  moves the transition temperature  $T_d$  close to room temperature. This is accompanied by a large normalised strain  $d_{33}^*$  of 488 pm/V. Other reports mention 25 mol%<sup>[87]</sup> and 26 mol%<sup>[85]</sup> as the phase boundary mixture.

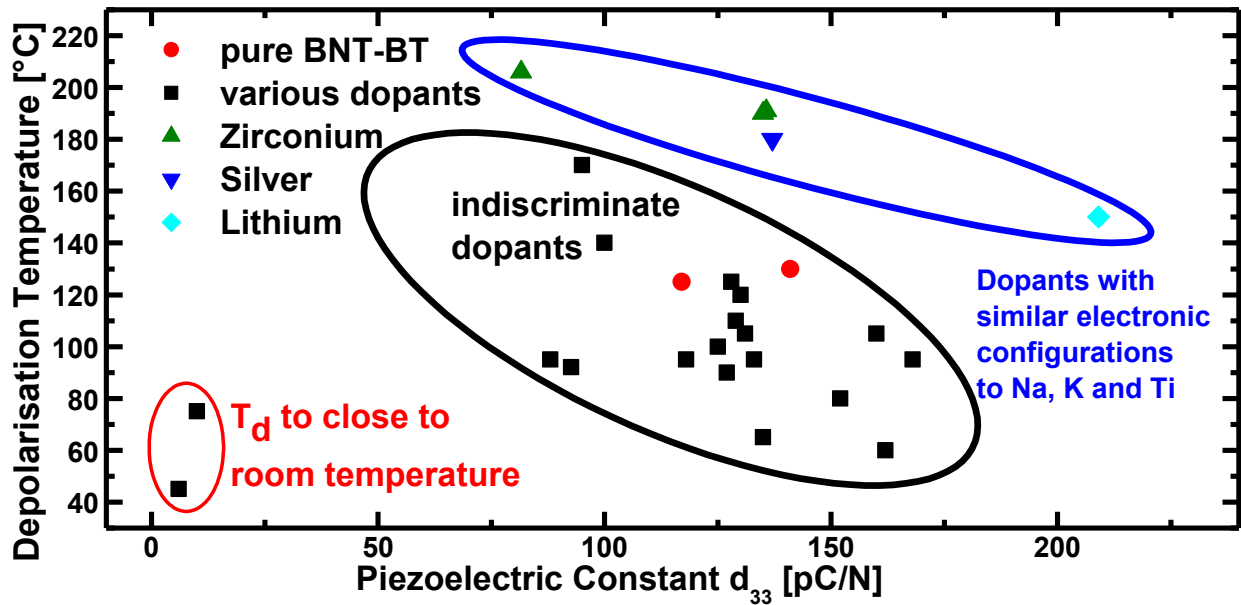


Fig 10: All known literature of modified BNT-BT, which contained  $d_{33}$  with reported  $T_d$  was compiled<sup>[65,73-83]</sup>. The inverse relationship of  $T_d$  and  $d_{33}$  is clearly visible. Notable exceptions are dopants, which replace cations with similar electronic structure i.e.  $\text{Na}^+$ ,  $\text{K}^+$  is replaced with  $\text{Li}$ <sup>[81]</sup> (and  $\text{Ag}^{+76}$ ) and also  $\text{Ti}^{4+}$  with  $\text{Zr}^{4+}$ <sup>[83]</sup>.

Manganese carbonate ( $\text{MnCO}_3$ ) addition of 0.2 wt.% reduces the Curie temperature by 25 K to 310 °C but also improves resistivity by more than three orders of magnitude to  $3 \times 10^{14} \Omega\text{m}$ <sup>[88]</sup>. Up to 20 at.% of sodium in BNT can be replaced with lithium before secondary phases appear. Resistivity is optimal at 10 at.% lithium due to the improved sinterability. Piezoelectric coefficient  $d_{33}$  as well as  $\epsilon_{33}$  and  $\tan\delta$  all increase with lithium addition until secondary phases appear while  $E_C$ ,  $k_p$  and  $Q_m$  get lower<sup>[89]</sup>. Strontium modified BNT is relevant for electrostrictive applications due to its high electrostrictive coefficient of  $0.02 \text{ m}^4\text{C}^{-2}$  and maximum strain of 0.1 %<sup>[90]</sup>, which is nearly as high as values in more complex systems<sup>[91,92]</sup>. Chu et al.<sup>[48]</sup>

investigated nonstoichiometry of BNT. Either  $(\text{Bi}_{1/2}\text{Na}_{1/2})^{2+}$  deficiency or excess improves  $d_{33}$  but also lowers  $T_d$ ,  $T_C$  and  $\epsilon_{33}$ . A graph of  $d_{33}$  versus  $T_d$  shows a clear inverse correlation of the two properties. BNT was also doped with bismuth<sup>[65]</sup>, iron<sup>[93]</sup>, cobalt<sup>[48]</sup>, niobium<sup>[48]</sup>, lanthanum<sup>[41]</sup>, manganese<sup>[88,94]</sup>,  $(2:1 \text{ Nb:Ni})$ <sup>[95]</sup> and also perovskite materials such as  $\text{NaNbO}_3$ <sup>[42,73,96-98]</sup>,  $\text{BiFeO}_3$ <sup>[99]</sup>,  $\text{BiScO}_3$ <sup>[99,100]</sup>,  $\text{NaTaO}_3$ <sup>[101]</sup>,  $\text{Ba}(\text{Cu}_{1/2}\text{W}_{1/2})\text{O}_3$ <sup>[102]</sup> and  $\text{K}_{0.5}\text{Na}_{0.5}\text{NbO}_3$ <sup>[103]</sup>. If a depolarisation temperature is reported, it is always lower than for pure BNT. In BNT, desired improvements are a lower coercive field and better sintering behaviour. None of the above modifications produce materials, which rival the piezoelectric properties of BNT-BT and BNT-BKT. This is why most current research focuses on these two BNT derivatives.

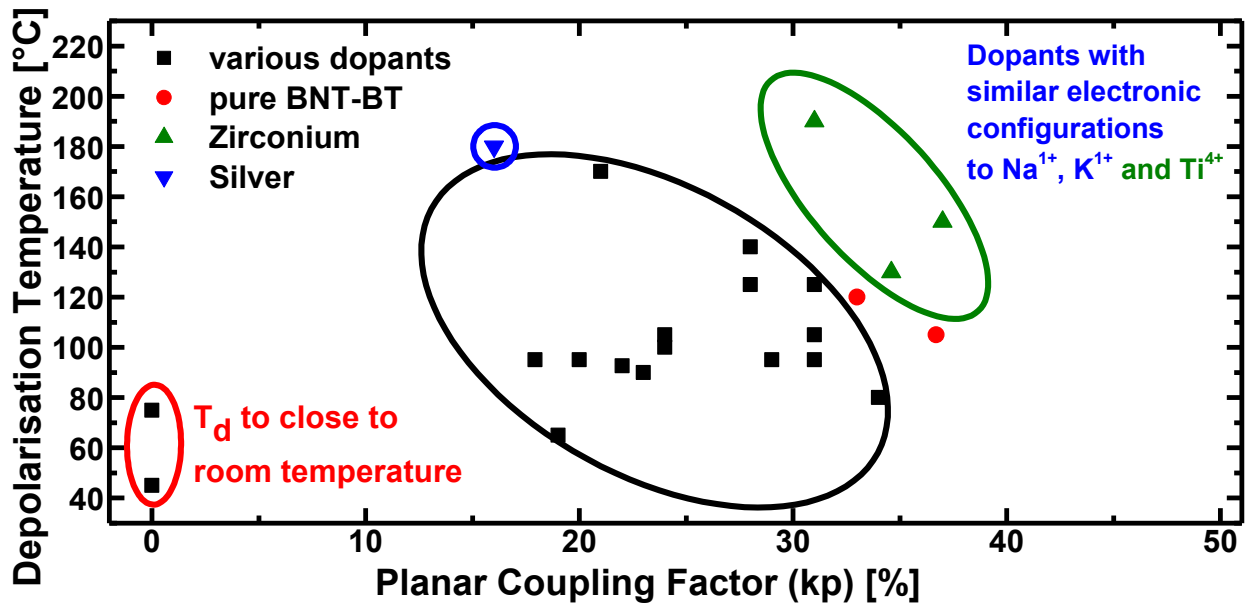


Fig 11: All known literature of modified BNT-BT, which contained  $k_p$  with reported  $T_d$  was compiled<sup>[65,73-79,82,84]</sup>. There appears to be no clear correlation between  $k_p$  and  $T_d$ , however, all modifications show lower  $k_p$  than pure BNT-BT with the exception of Zr<sup>[83]</sup>.

BNT-BT and BNT-BKT already have acceptable sintering behaviour and coercive fields that are less than half that of pure BNT but the depolarisation temperatures are already much lower than in pure BNT. Any successful doping should therefore be aimed at raising or at least maintaining  $T_d$  without compromising piezoelectric properties. An effective dopant needs to stabilise or enhance the lattice distortions that make BNT-BT and BNT-BKT a stronger ferroelectric. The stabilising effect needs to supersede the disordering effect, which any dopant possesses and which is responsible for the lowering of  $T_d$  during doping. Dopant-free modifications such as deficiency of titanium cations in BNT-BT improves  $d_{33}$ ,  $\epsilon_{33}$  and worsens  $\tan\delta$ , excess titanium cations worsen all of the afore-mentioned<sup>[74]</sup>.



Lithium doping in small quantities provides an almost constant depolarisation temperature and improved sintering and with it  $d_{33}$ ,  $\epsilon_{33}$  and other relevant quantities in BNT-BT<sup>[81,104,105]</sup>, BNT-BKT<sup>[105-110]</sup> and BNT-BKT-BT<sup>[111]</sup> but concentrations needed for optimal sintering also reduce  $T_d$ <sup>[108]</sup>. In pure BNT lithium reduces  $T_d$  and  $P_r$  continuously<sup>[89]</sup>.

Other dopants and modifications of BNT-BT include cerium<sup>[79,112,113]</sup>, lanthanum<sup>[75,77,114-116]</sup>, zirconium<sup>[82,117-119]</sup>, niobium<sup>[77,120]</sup>, tantalum<sup>[120]</sup>, antimony<sup>[120]</sup>, hafnium<sup>[83]</sup>, cobalt<sup>[77,121]</sup>, silver<sup>[76,122]</sup> and manganese<sup>[123-125]</sup>. Co-doping was done with Ce+Sn<sup>[84]</sup>, Ce+La<sup>[80]</sup>, Li+Sr<sup>[105]</sup> and Zr+Cu<sup>[126]</sup>. All improve some combination of  $d_{33}$ ,  $T_C$ ,  $\epsilon_{33}$  by improving densification and/or controlling grain size and limiting conductivity. However,  $\tan\delta$  always increases and  $T_d$ , when reported (compare Fig 10), always drops. There are so far no reports of  $k_p$  values, which are significantly higher than those of pure BNT-BT (compare Fig 11).

Mixtures with other perovskite type materials like paraelectric SrTiO<sub>3</sub><sup>[127]</sup>, antiferroelectric NaNbO<sub>3</sub><sup>[128]</sup> and ferroelectric BiFeO<sub>3</sub><sup>[129]</sup> all have equivalent effects of lowering  $T_d$ , which is surprising at least in the case of BiFeO<sub>3</sub><sup>[130]</sup>, which increases Curie temperature of BF-PT with increasing BiFeO<sub>3</sub> concentration<sup>[131]</sup>. However, at second glance, the behaviour of  $T_d$  and  $T_C$  can never be assumed to be correlated.  $T_C$  of BNT-BT-BiFeO<sub>3</sub> does in fact increase, which is, however, irrelevant, since the working temperature range is not limited by  $T_C$  but by  $T_d$ . A similar behaviour can be found in the KNN system doped with lithium (see section 2.3.5.1).

BNT-BKT has been modified with manganese<sup>[132]</sup>, strontium<sup>[133]</sup>, cerium<sup>[134]</sup> and co-doped with (Fe/Zn/Mg+Nb)<sup>[68]</sup>, Ce+Li<sup>[135]</sup>, Sr+La<sup>[136]</sup>, Li+Ag<sup>[105]</sup> and mixed with other perovskite ferroelectrics like KNbO<sub>3</sub><sup>[137]</sup> and K<sub>0.5</sub>Na<sub>0.5</sub>NbO<sub>3</sub><sup>[92]</sup>. Reports of BNT-BKT-BT with manganese<sup>[138]</sup> and cerium<sup>[139]</sup> also exist. These modifications of BNT-BKT yield no results, which are causally different from those of BNT-BT doping even though manganese may by some unverified mechanism increase  $T_d$ . Unsurprising, all introduced cations different from the already present ones increase the relaxor behaviour of BNT-based systems, since they increase disorder on their respective cation sites. High concentrations of most dopants will always without any known exception lower  $T_d$  to near or below room temperature and broaden the dielectric maximum peak at  $T_m$  to the point, where it stretches from room temperature to around 200 °C<sup>[85-87,96]</sup>. At that point, the compositions with the highest dielectric response become interesting for capacitive applications.

BNT-BT with KNN<sup>[140-142]</sup> and BNT-BKT with KNN<sup>[92]</sup> show extremely large bipolar and unipolar strain of 0.4 % to 0.45 % for compositions that have a depolarisation temperature

slightly above room temperature. The reason for this high strain is that the nearby phase transition allow for the existence of a non-polar phase within the material, which lets the material return to its unpoled state after each cycle. In the case of BNT-BT with KNN, The space group high-temperature non-polar phase has recently been identified as  $P4bm$ <sup>[143]</sup>. Each strain cycle, therefore, includes the strain, which is normally lost as remanent strain in ferroelectrics<sup>[144]</sup>. The strain response is very temperature-dependent, since it relies on the proximity of the phase transition<sup>[141]</sup> as long as the ferroelectric-to-non-polar phase transition temperature is above room temperature. Similar behaviour is also shown in BNT-SrTiO<sub>3</sub><sup>[86]</sup> and BNT-KN<sup>[145]</sup>. TEM studies of the BNT-BT-KNN system have revealed a coexistence of tetragonal ( $P4bm$ ) and rhombohedral ( $R3c$ ) space groups<sup>[146]</sup> within a single grain<sup>[147]</sup>. The tetragonal and rhombohedral distortions are attributed to octahedral tilting for both phases<sup>[148]</sup>.

Improving  $T_d$  and  $T_C$ , however unlikely, is still desirable in all of BNT-based systems preferably without having to compromise ferroelectric properties. So far, the only way to increase the depolarisation temperature of BNT-based materials is a BT content of above 8 mol%<sup>[116,149]</sup>, where there is no depolarisation temperature below the Curie temperature. Silver doping<sup>[76]</sup> might possibly stabilise the ferroelectricity of BNT-BT due to its similar electronic configuration to sodium and potassium like in the case of lithium (see above). Apart from those two methods, only zirconia doping does not reduce  $T_d$  but appears not to have any improvement effect on dielectric and piezoelectric properties<sup>[119]</sup> either unless also combined with copper<sup>[126]</sup> or unless combined with BT content higher than 6 mol%<sup>[83]</sup>. A detailed comparison between many different dopants at the same concentration intervals is so far missing in literature. Such a report would help identify the most effective dopants, which could be used in such low concentrations that their effect on the depolarisation temperature and relaxor behaviour is minimised. The complexity of BNT-BKT and BNT-BT and even BNT makes doping beyond trying to improve physical properties (microstructure, mechanical stability, atmospheric stability) difficult. Unless the mechanism behind the depolarisation temperature, which is clearly independent of the type of dopant with few exceptions, is better understood, further doping experiments will simply be random dopant testing experiments.

### 2.2.8 Sol-Gel, Orientated Grain Growth and Single Crystals Bi-Based Materials

Aside from the standard mixed oxide route, also sol-gel-type processing has been successfully applied to BNT<sup>[35,36,150-154]</sup>, BNT-BT<sup>[152,155-157]</sup>, BNT-BKT<sup>[59]</sup> and BKT<sup>[158,159]</sup>.

Nano-sized powders derived from sol-gel can be created by dissolving bismuth oxide and sodium carbonate in 70 % nitric acid. Once dissolved, ethylene glycol is added and the remaining water evaporated at 80 °C. A stoichiometric amount of titanium tetraisopropoxide is added and stirred for two hours at 70 °C. Calcination temperatures between 600 °C and 700 °C of the BNT sol for six hours lead to 100 to 200 nm sized crystals of BNT<sup>[150]</sup>. A report shows conductivity and very low remanent polarisation of 8.3  $\mu\text{C}/\text{cm}^2$  but a maximum polarisation of almost 30  $\mu\text{C}/\text{cm}^2$  together with a coercive field of about 2 kV/mm<sup>[36]</sup>. A steric acid gel synthesis route shows particle sizes of 10 to 40 nm with a calcination time of one hour at 600 °C to 800 °C<sup>[151]</sup>. Particles of 100 to 200 nm can also be prepared by hydrothermal synthesis at 200 °C for 24 hours in 12 molar sodium hydroxide<sup>[160]</sup> or potassium hydroxide<sup>[154]</sup>, both of which are also reported here<sup>[161]</sup>.

BNT-5BT<sup>[155]</sup> prepared via sol-gel shows nearly identical temperature-dependent dielectric behaviour to BNT-6BT by Takenaka et al.<sup>[47]</sup>. A 1-3 fibre epoxy composite transducer of BNT-BT made by sol-gel method can be considered a first step towards real industrial applicability since its properties approach those of PZT-based transducers<sup>[156]</sup>. A report by Zhou et al.<sup>[157]</sup> finds a  $d_{33}$  of 132 pC/N,  $\epsilon_{33}$  of 703,  $k_p$  of 0.25 and a  $\tan\delta$  of 1.9 %. With the exception of the lower planar coupling factor, these are comparable to BNT-BT prepared by a mixed oxide route. (compare Tab 4 (pages 49ff.)

Radiofrequency magnetron sputtering of BNT shows high conductivity and high dielectric losses while dielectric constants are on par with standard manufacturing techniques<sup>[35]</sup>. Conductivity and losses are attributed to oxygen vacancies. EDS<sup>2</sup> reveals an upper limit of 2 at.% deficiency of the A-site ion concentration. Chemical vapour deposition<sup>[162]</sup> produces BNT thin film of up to 162 nm thickness with dielectric constant being about half that of other fabrication techniques.

BKT prepared by sol-gel methods is preferable to solid state sintering methods since pure BKT is hard to prepare via standard mixed oxide methods at all. The small particle size allows for lower sintering temperature and hence less decomposition due to evaporation of bismuth and potassium<sup>[158,159]</sup>. Initial attempts to prepare morphotropic BNT-BKT suffer from strong

<sup>2</sup> EDAX/EDS: Energy-dispersive X-ray spectroscopy (See experimental section (4.2.2))

dependence of the material quality with BNT to BKT ratio, which prevents reliable characterisation thus far<sup>[59]</sup>.

Textured BNT ceramics can be produced by reactive-templated grain growth (RTGG) on platelets of  $\text{Bi}_4\text{Ti}_3\text{O}_{12}$ <sup>[163]</sup>. Here, 2 % excess sodium carbonate leads to a relative density of 92 % and the degree of orientation of 0.86, which was determined from XRD patterns via Lotgering's method<sup>[164]</sup>. Stoichiometric mixtures lead to a relative density of 61 % and the degree of orientation of 0.53. The excess sodium forms a liquid phase, which is responsible for the improved density. Excess bismuth oxide also improves the degree of orientation as it inhibits grain growth and leads to preferential growth on the larger template grains<sup>[163]</sup>. Templates of  $\text{Sr}_3\text{Ti}_2\text{O}_7$  and  $\text{BaBi}_2\text{Nb}_2\text{O}_9$  can be used if titanium oxide in the first case and titanium oxide and sodium carbonate in the second case are used in excess<sup>[165,166]</sup>.

Grain oriented BNT-BKT has a  $d_{33}$ ,  $Q_m$  and  $k_{31}$  of 134 pC/N, 154 and 0.31 respectively. The ferroelectric hysteresis displays too high a conductivity for polarisation values to be reliable, however. Dielectric constant parallel and perpendicular to the orientation direction are about 2500 and 4700<sup>[167]</sup>. Templated grain growth of BNT-BT shows slight improvement of  $k_{33}$  and  $\epsilon_{33}$  but also 25 % higher  $\tan\delta$ <sup>[168]</sup>. Comparison of plate and needle-like templates shows that needle-like template particles do not orient during casting and, therefore, do not produce any texturing effect<sup>[169]</sup>, which is also confirmed here<sup>[170]</sup>. A maximum degree of orientation of 0.8 for BNT-BT is achieved<sup>[171]</sup>. The influence of potassium concentration<sup>[172]</sup> and particle size of template and matrix grains has also been subject to investigation<sup>[173]</sup>.

Single crystals of BNT can be easily grown via a flux or Czochralski method<sup>[37]</sup>. The stoichiometrically weighed powders are mixed and placed in a closed platinum crucible. Spontaneous crystallisation occurs during cooling in air. Unfortunately, either the starting temperature or the cooling rate are rarely specified<sup>[17,25-27,30]</sup>. SEM and hot stage TEM investigations of BNT single crystals show domain structures up to 200 °C, which return at the same temperature upon cooling<sup>[174]</sup>. Manganese<sup>[175]</sup> doping can improve ferroelectric properties with little influence on  $T_d$ .

Single crystals of BNT-BT can be grown with BT content controllable to within 5 % of the target concentration via spontaneous nucleation during cooling of previously calcined oxide melt. The melt is held for five hours at 1350 °C and then slowly cooled at 5 °C/min. Morphotropic BNT-BT single crystals are sometimes rhombohedral and sometimes tetragonal due to minor compositional fluctuations. One single crystal of rhombohedral BNT-5.5BT showed 0.44 % strain<sup>[176]</sup> at 3 kV/mm owing to a field-induced phase transformation similar to relaxor PMN-PT.

With a bipolar electric driving field of 3.8 kV/mm a maximum strain of 0.85 % was achieved in tetragonal BNT-5.5BT<sup>[177]</sup>. Another report shows that crystals are grown via a flux or Bridgman method are 50 at.% barium deficient<sup>[178]</sup>. Crystals grown via a Bridgman method can reach several centimetres in size<sup>[179]</sup>. Inhomogeneity and compositional fluctuations can be addressed through a metal strip heated zone melting technique<sup>[180]</sup>, the detailed procedure of which is described here<sup>[181]</sup>. Inductively coupled plasma (ICP) analysis revealed fully controlled barium and titanium ion content and about 1-2 % variation in the bismuth and sodium ion content. Top-seeded solution growth of BNT-BT crystals revealed a low segregation coefficient<sup>3</sup> of barium of 0.32, which means that only 32 at.% of the barium in the melt is incorporated into the crystal<sup>[182]</sup>. A report of nanocrystalline BNT via recrystallisation requires further investigation<sup>[183]</sup>.

Unlike pure BNT, BNT-3BT and BNT-8BT single crystals did not show any domain structure in TEM and SEM investigations<sup>[174]</sup>. Cerium doping of BNT-BT single crystals is reported to increase maximum and remanent polarisation but this might also be attributed to increased conductivity<sup>[184]</sup>. BNT-BT single crystals with varying BT content and 3 at.% zirconia addition show purely electrostrictive strain of 0.3 % in the rhombohedral phase and 0.45 % in the tetragonal phase both at a field of 5.8 kV/mm<sup>[117]</sup>.

Large BNT-BKT single crystals can be prepared by top-seeded solution growth but the actual composition was not verified<sup>[185]</sup>. BNT-BKT-BT single crystals reach 0.87 % strain under 4 kV/mm bipolar load<sup>[186]</sup> and 0.24 % strain with linear behaviour<sup>[187]</sup>.

---

<sup>3</sup> The segregation coefficient is the ratio between the concentration of ions in the growing crystal and that of the melt. I.e. it is less than unity if the concentration of a type of ion is higher in the melt than the growing crystal and above unity if the reverse is true.

### 2.2.9 Other Bismuth-based Ferroelectrics

Initial attempts to prepare bismuth-based perovskite focused on  $\text{Bi}^{3+}\text{Me}^{3+}\text{O}_3$ -type structures.  $\text{Me}^{3+}$  in this case is a trivalent small metal ion such as  $\text{Cr}^{3+}$ ,  $\text{Al}^{3+}$ ,  $\text{Sc}^{3+}$  and  $\text{Fe}^{3+}$ . These do not form during pressureless sintering<sup>[46]</sup>.  $\text{Bi}_{1/2}\text{Na}_{1/2}\text{ZrO}_3$  and  $\text{Bi}_{1/2}\text{K}_{1/2}\text{ZrO}_3$  form perovskite structures<sup>[31]</sup> but there are no reports about ferroelectricity in either composition. Bismuth-layer-structured ferroelectrics like  $\text{Bi}_4\text{Ti}_3\text{O}_{12}$  are suitable for high temperature applications since the reported Curie temperatures are above 400 °C and there are no depolarisation temperatures below that<sup>[188]</sup> but  $d_{33}$  is not likely to ever reach the values of perovskite type ferroelectrics<sup>[189]</sup>.

### 2.2.10 Summary of BNT-Based Materials

In conclusion it can be said that BNT-based materials are the most promising candidates to replace PZT in many applications. Their lower sensitivity to humidity and non-stoichiometry compared to KNN will likely help consistency and reliability in industrial mass production. Currently known drawbacks include the low depolarisation temperature and the relaxor behaviour. These drawbacks cannot likely be remedied by doping. Doping to improve microstructure, density and related properties has already seen progress. BNT-BT is likely to be more reliable and reproducible than BNT-BKT due to the handling difficulties of potassium. Some current reports still include the Curie temperature and not the depolarisation temperature even though the Curie temperature of BNT-based materials is irrelevant for practical applications.

## 2.2.11 References

- [1] M. D. Maeder, D. Damjanovic, and N. Setter, "Lead free piezoelectric materials," *Journal of Electroceramics*, **13**[1-3] 385-92 (2004).
- [2] T. R. Shrout and S. J. Zhang, "Lead-free piezoelectric ceramics: Alternatives for PZT?," *Journal of Electroceramics*, **19**[1] 113-26 (2007).
- [3] S. Zhang, R. Xia, and T. Shrout, "Lead-free piezoelectric ceramics vs. PZT?," *Journal of Electroceramics*, **19**[4] 251-7 (2007).
- [4] T. Takenaka, H. Nagata, Y. Hiruma, Y. Yoshii, and K. Matumoto, "Lead-free piezoelectric ceramics based on perovskite structures," *Journal of Electroceramics*, **19**[4] 259-65 (2007).
- [5] T. Takenaka, H. Nagata, and Y. Hiruma, "Current Developments and Prospective of Lead-Free Piezoelectric Ceramics," *Japanese Journal of Applied Physics*, **47**[5] 3787-801 (2008).
- [6] T. Takenaka and H. Nagata, "Current status and prospects of lead-free piezoelectric ceramics," *Journal of the European Ceramic Society*, **25**[12] 2693-700 (2005).
- [7] W. W. Wolny, "European approach to development of new environmentally sustainable electroceramics," *Ceramics International*, **30**[7] 1079-83 (2004).
- [8] P. Popper, S. N. Ruddlesden, and T. A. Ingles, "Structure and Electrical Properties of  $\text{Bi}_4\text{Ti}_3\text{O}_{12}$  and its Application in Dielectrics," *Transactions of the British Ceramic Society*, **56** 356 (1957).
- [9] S. Ikegami and I. Ueda, "Piezoelectricity in Ceramics of Ferroelectric Bismuth Compound with Layer Structure," *Japanese Journal of Applied Physics*, **13**[10] 1572-7 (1974).
- [10] S. C. Abrahams, W. C. Hamilton, and J. M. Reddy, "Ferroelectric lithium niobate. 4. Single crystal neutron diffraction study at  $24^\circ\text{C}$ ," *Journal of Physics and Chemistry of Solids*, **27**[6-7] 1013-8 (1966).
- [11] H. D. Megaw, "A note on structure of lithium niobate  $\text{LiNbO}_3$ ," *Acta Crystallographica, Section A: Foundations of Crystallography*, **A 24** 583-8 (1968).
- [12] I. Inbar and R. E. Cohen, "Origin of ferroelectricity in  $\text{LiNbO}_3$  and  $\text{LiTaO}_3$ ," *Ferroelectrics*, **194**[1-4] 83-95 (1997).
- [13] S. B. Vakhrushev, V. A. Isupov, B. E. Kvyatkovsky, N. M. Okuneva, I. P. Pronin, G. A. Smolensky, and P. P. Syrnikov, "Phase transitions and soft modes in sodium bismuth titanate," *Ferroelectrics*, **63**[1] 153 - 60 (1985).
- [14] V. Dorcet and G. Trolliard, "A transmission electron microscopy study of the A-site disordered perovskite  $\text{Na}_{0.5}\text{Bi}_{0.5}\text{TiO}_3$ ," *Acta Materialia*, **56**[8] 1753-61 (2008).
- [15] G. Trolliard and V. Dorcet, "Reinvestigation of phase transitions in  $\text{Na}_{0.5}\text{Bi}_{0.5}\text{TiO}_3$  by TEM. Part II: Second order orthorhombic to tetragonal phase transition," *Chemistry of Materials*, **20**[15] 5074-82 (2008).
- [16] I. G. Siny, S. G. Lushnikov, C.-S. Tu, and V. H. Schmidt, "Specific features of hypersonic damping in relaxor ferroelectrics," *Ferroelectrics*, **170**[1] 197-202 (1995).
- [17] J. Suchanicz, "Investigations of the phase transitions in  $\text{Na}_{0.5}\text{Bi}_{0.5}\text{TiO}_3$ ," *Ferroelectrics*, **172**[1] 455-8 (1995).
- [18] K. Roleder, I. Franke, A. M. Glazer, P. A. Thomas, S. Miga, and J. Suchanicz, "The piezoelectric effect in  $\text{Na}_{1/2}\text{Bi}_{1/2}\text{TiO}_3$  ceramics," *Journal of Physics-Condensed Matter*, **14**[21] 5399-406 (2002).
- [19] B. Jaffe, W. R. Cook, and H. Jaffe. In *Piezoelectric Ceramics*. Academic Press, London, 1971.
- [20] K. Sakata and Y. Masuda, "Ferroelectric and antiferroelectric properties of  $(\text{Na}_{1/2}\text{Bi}_{1/2})\text{TiO}_3\text{-SrTiO}_3$  solid-solution ceramics," *Ferroelectrics*, **7**[1-4] 347-9 (1974).
- [21] C. Xu, D. Lin, and K. W. Kwok, "Structure, electrical properties and depolarization temperature of  $(\text{Bi}_{0.5}\text{Na}_{0.5})\text{TiO}_3\text{-BaTiO}_3$  lead-free piezoelectric ceramics," *Solid State Sciences*, **10**[7] 934-40 (2008).
- [22] J. Suchanicz, "Behaviour of  $\text{Na}_{0.5}\text{Bi}_{0.5}\text{TiO}_3$  ceramics in the ac electric field," *Ferroelectrics*, **209**[3-4] 561-8 (1998).
- [23] I. P. Pronin, P. P. Syrnikov, V. A. Isupov, V. M. Egorov, and N. V. Zaitseva, "Peculiarities of Phase-Transitions in Sodium-Bismuth Titanate," *Ferroelectrics*, **25**[1-4] 395-7 (1980).
- [24] J. A. Zvirgzds, P. P. Kapostin, J. V. Zvirgzde, and T. V. Kruzina, "X-ray study of phase transitions in ferroelectric  $\text{Na}_{0.5}\text{Bi}_{0.5}\text{TiO}_3$ ," *Ferroelectrics*, **40**[1] 75 - 7 (1982).
- [25] J. Suchanicz, K. Roleder, A. Kania, and J. Handerek, "Electrostrictive Strain and Pyroeffect in the Region of Phase Coexistence in  $\text{Na}_{0.5}\text{Bi}_{0.5}\text{TiO}_3$ ," *Ferroelectrics*, **77** 107-10 (1988).
- [26] K. Roleder, J. Suchanicz, and A. Kania, "Time-Dependence of Electric Permittivity in  $\text{Na}_{0.5}\text{Bi}_{0.5}\text{TiO}_3$  Single-Crystals," *Ferroelectrics*, **89** 1-5 (1989).
- [27] T. V. Kruzina, V. M. Duda, and J. Suchanicz, "Peculiarities of optical behaviour of  $\text{Na}_{0.5}\text{Bi}_{0.5}\text{TiO}_3$  single crystals," *Materials Science and Engineering B*, **87**[1] 48-52 (2001).
- [28] V. Dorcet, G. Trolliard, and P. Boullay, "Reinvestigation of phase transitions in  $\text{Na}_{0.5}\text{Bi}_{0.5}\text{TiO}_3$  by TEM. Part I: First order rhombohedral to orthorhombic phase transition," *Chemistry of Materials*, **20**[15] 5061-73 (2008).

- [29] H. Böhm, "Modulated structures at phase transitions," *American Mineralogist*, **68** 11-7 (1983).
- [30] G. O. Jones and P. A. Thomas, "Investigation of the structure and phase transitions in the novel A-site substituted distorted perovskite compound  $\text{Na}_{1/2}\text{Bi}_{1/2}\text{TiO}_3$ ," *Acta Crystallographica, Section B: Structural Science*, **58** 168-78 (2002).
- [31] G. A. Smolenskii, V. A. Isupov, A. I. Agranovskaya, and N. N. Krainik, "New Ferroelectrics of Complex Composition. IV," *Soviet Physics-Solid State*, **2**[11] 2651-4 (1961).
- [32] Y. Hiruma, R. Aoyagi, H. Nagata, and T. Takenaka, "Ferroelectric and piezoelectric properties of  $(\text{Bi}_{1/2}\text{K}_{1/2})\text{TiO}_3$  ceramics," *Japanese Journal of Applied Physics Part 1-Regular Papers Brief Communications & Review Papers*, **44**[7A] 5040-4 (2005).
- [33] O. Elkechai, M. Manier, and J. P. Mercurio, " $\text{Na}_{0.5}\text{Bi}_{0.5}\text{TiO}_3$ - $\text{K}_{0.5}\text{Bi}_{0.5}\text{TiO}_3$  (NBT-KBT) system: A structural and electrical study," *Physica Status Solidi A: Applied Research*, **157**[2] 499-506 (1996).
- [34] G. A. Smolenskii and A. I. Agranovskaya, "Dielectric Polarization of a Number of Complex Compounds," *Soviet Physics-Solid State*, **1**[10] 1429-37 (1960).
- [35] Z. H. Zhou, J. M. Xue, W. Z. Li, J. Wang, H. Zhu, and J. M. Miao, "Ferroelectric and electrical behavior of  $(\text{Na}_{0.5}\text{Bi}_{0.5})\text{TiO}_3$  thin films," *Applied Physics Letters*, **85**[5] 804-6 (2004).
- [36] T. Yu, K. W. Kwok, and H. L. W. Chan, "Preparation and properties of sol-gel-derived  $\text{Bi}_{0.5}\text{Na}_{0.5}\text{TiO}_3$  lead-free ferroelectric thin film," *Thin Solid Films*, **515**[7-8] 3563-6 (2007).
- [37] S. E. Park, S. J. Chung, I. T. Kim, and K. S. Hong, "Nonstoichiometry and the Long-Range Cation Ordering in Crystals of  $(\text{Na}_{1/2}\text{Bi}_{1/2})\text{TiO}_3$ ," *Journal of the American Ceramic Society*, **77**[10] 2641-7 (1994).
- [38] H. Nagata, T. Shinya, Y. Hiruma, and T. Takenaka, "Developments in Dielectric Materials and Electronic Devices," pp. 213-21. In *Ceramic Transactions*, Vol. 167. Edited by K. M. Nair. American Ceramic Society, Indianapolis, Indiana, USA, 2004.
- [39] T. Takenaka and K. Sakata, "Dielectric, Piezoelectric and Pyroelectric Properties of  $(\text{BiNa})_{1/2}\text{TiO}_3$ -Based Ceramics," *Ferroelectrics*, **95** 153-6 (1989).
- [40] T. Takenaka, K. Sakata, and K. Toda, "Piezoelectric Properties of  $(\text{Bi}_{1/2}\text{Na}_{1/2})\text{TiO}_3$ -Based Ceramics," *Ferroelectrics*, **106** 375-80 (1990).
- [41] A. Herabut and A. Safari, "Processing and electromechanical properties of  $(\text{Bi}_{0.5}\text{Na}_{0.5})_{(1-1.5x)}\text{La}_x\text{TiO}_3$  ceramics," *Journal of the American Ceramic Society*, **80**[11] 2954-8 (1997).
- [42] T. Wada, K. Toyoiike, Y. Imanaka, and Y. Matsuo, "Dielectric and piezoelectric properties of  $(\text{A}_{0.5}\text{Bi}_{0.5})\text{TiO}_3$ - $\text{ANbO}_3$  ( $\text{A} = \text{Na}, \text{K}$ ) systems," *Japanese Journal of Applied Physics Part 1-Regular Papers Short Notes & Review Papers*, **40**[9B] 5703-5 (2001).
- [43] Y. F. Qu, D. Shan, and J. J. Song, "Effect of A-site substitution on crystal component and dielectric properties in  $\text{Bi}_{0.5}\text{Na}_{0.5}\text{TiO}_3$  ceramics," *Materials Science & Engineering, B: Solid-State Materials for Advanced Technology*, **121**[1-2] 148-51 (2005).
- [44] Y. Li, W. Chen, Q. Xu, J. Zhou, and X. Gu, "Piezoelectric and ferroelectric properties of  $\text{Na}_{0.5}\text{Bi}_{0.5}\text{TiO}_3$ - $\text{K}_{0.5}\text{Bi}_{0.5}\text{TiO}_3$ - $\text{BaTiO}_3$  piezoelectric ceramics," *Materials Letters*, **59**[11] 1361-4 (2005).
- [45] Y. Hiruma, H. Nagata, and T. Takenaka, "Grain-size effect on electrical properties of  $(\text{Bi}_{1/2}\text{K}_{1/2})\text{TiO}_3$  ceramics," *Japanese Journal of Applied Physics Part 1-Regular Papers Brief Communications & Review Papers*, **46**[3A] 1081-4 (2007).
- [46] C. F. Bührer, "Some Properties of Bismuth Perovskites," *Journal of Chemical Physics*, **36**[3] 798-803 (1962).
- [47] T. Takenaka, K. Maruyama, and K. Sakata, " $(\text{Bi}_{1/2}\text{Na}_{1/2})\text{TiO}_3$ - $\text{BaTiO}_3$  system for lead-free piezoelectric ceramics," *Japanese Journal of Applied Physics Part 1-Regular Papers Short Notes & Review Papers*, **30**[9B] 2236-9 (1991).
- [48] B. J. Chu, D. R. Chen, G. R. Li, and Q. R. Yin, "Electrical properties of  $\text{Na}_{1/2}\text{Bi}_{1/2}\text{TiO}_3$ - $\text{BaTiO}_3$  ceramics," *Journal of the European Ceramic Society*, **22**[13] 2115-21 (2002).
- [49] T. Oh and M. H. Kim, "Phase relation and dielectric properties in  $(\text{Bi}_{1/2}\text{Na}_{1/2})_{1-x}\text{Ba}_x\text{TiO}_3$  lead-free ceramics," *Materials Science & Engineering, B: Solid-State Materials for Advanced Technology*, **132**[3] 239-46 (2006).
- [50] R. Ranjan and A. Dviwedi, "Structure and dielectric properties of  $(\text{Na}_{0.50}\text{Bi}_{0.50})(1-x)\text{Ba}_x\text{TiO}_3$ :  $0 \leq x \leq 0.10$ ," *Solid State Communications*, **135**[6] 394-9 (2005).
- [51] J. R. Gomah-Petry, S. Said, P. Marchet, and J. P. Mercurio, "Sodium-bismuth titanate based lead-free ferroelectric materials," *Journal of the European Ceramic Society*, **24**[6] 1165-9 (2004).
- [52] A. Sasaki, T. Chiba, Y. Mamiya, and E. Otsuki, "Dielectric and piezoelectric properties of  $(\text{Bi}_{1/2}\text{Na}_{1/2})\text{TiO}_3$ - $(\text{Bi}_{0.5}\text{K}_{0.5})\text{TiO}_3$  systems," *Japanese Journal of Applied Physics Part 1-Regular Papers Short Notes & Review Papers*, **38**[9B] 5564-7 (1999).
- [53] G. O. Jones, J. Kreisel, and P. A. Thomas, "A structural study of the  $(\text{Na}_{1-x}\text{K}_x)_{0.5}\text{Bi}_{0.5}\text{TiO}_3$  perovskite series as a function of substitution ( $x$ ) and temperature," *Powder Diffraction*, **17**[4] 301-19 (2002).
- [54] Y. Yamada, T. Akutsu, H. Asada, K. Nozawa, S. Hachiga, T. Kurosaki, O. Ikagawa, H. Fujiki, K. Hozumi, T. Kawamura, T. Amakawa, K. Hirota, and T. Ikeda, "Effect of B-Ions Substitution in  $[(\text{K}_{1/2}\text{Bi}_{1/2})$ -



- ( $\text{Na}_{1/2}\text{Bi}_{1/2}$ )]( $\text{Ti-B}$ ) $\text{O}_3$  System with  $\text{B}=\text{Zr}, \text{Fe}_{1/2}\text{Nb}_{1/2}, \text{Zn}_{1/3}\text{Nb}_{2/3}$  or  $\text{Mg}_{1/3}\text{Nb}_{2/3}$ ," *Japanese Journal of Applied Physics Part I-Regular Papers Short Notes & Review Papers*, **34**[9B] 5462-6 (1995).
- [55] S. C. Zhao, G. R. Li, A. L. Ding, T. B. Wang, and Q. R. Yin, "Ferroelectric and piezoelectric properties of ( $\text{Na}, \text{K}$ ) $_{0.5}\text{Bi}_{0.5}\text{TiO}_3$  lead free ceramics," *Journal of Physics D: Applied Physics*, **39**[10] 2277-81 (2006).
- [56] Y. Hiruma, K. Yoshii, H. Nagata, and T. Takenaka, "Phase transition temperature and electrical properties of ( $\text{Bi}_{1/2}\text{Na}_{1/2}$ ) $\text{TiO}_3$ -( $\text{Bi}_{1/2}\text{A}_{1/2}$ ) $\text{TiO}_3$  ( $\text{A} = \text{Li}$  and  $\text{K}$ ) lead-free ferroelectric ceramics," *Journal of Applied Physics*, **103**[8] 084121-7 (2008).
- [57] K. Yoshii, Y. Hiruma, H. Nagata, and T. Takenaka, "Electrical properties and depolarization temperature of ( $\text{Bi}_{1/2}\text{Na}_{1/2}$ ) $\text{TiO}_3$ -( $\text{Bi}_{1/2}\text{K}_{1/2}$ ) $\text{TiO}_3$  lead-free piezoelectric ceramics," *Japanese Journal of Applied Physics Part I-Regular Papers Brief Communications & Review Papers*, **45**[5B] 4493-6 (2006).
- [58] S. C. Zhao, L. N. Zhang, G. R. Li, T. B. Wang, and A. L. Ding, "Dielectric properties of  $\text{Na}_{0.25}\text{K}_{0.25}\text{Bi}_{0.5}\text{TiO}_3$  lead-free ceramics," *Physica Status Solidi A: Applied Research*, **202**[3] R22-R4 (2005).
- [59] T. Yu, K. W. Kwok, and H. L. W. Chan, "The synthesis of lead-free ferroelectric  $\text{Bi}_{0.5}\text{Na}_{0.5}\text{TiO}_3$ - $\text{Bi}_{0.5}\text{K}_{0.5}\text{TiO}_3$  thin films by sol-gel method," *Materials Letters*, **61**[10] 2117-20 (2007).
- [60] Z. Yang, B. Liu, L. Wei, and Y. Hou, "Structure and electrical properties of  $(1-x)\text{Bi}_{0.5}\text{Na}_{0.5}\text{TiO}_3$ - $x\text{Bi}_{0.5}\text{K}_{0.5}\text{TiO}_3$  ceramics near morphotropic phase boundary," *Materials Research Bulletin*, **43**[1] 81-9 (2008).
- [61] Y.-R. Zhang, J.-F. Li, and B.-P. Zhang, "Enhancing Electrical Properties in NBT-KBT Lead-Free Piezoelectric Ceramics by Optimizing Sintering Temperature," *Journal of the American Ceramic Society*, **91**[8] 2716-9 (2008).
- [62] Y. R. Zhang, J. F. Li, B. P. Zhang, and C. E. Peng, "Piezoelectric and ferroelectric properties of Bi-compensated ( $\text{Bi}_{1/2}\text{Na}_{1/2}$ ) $\text{TiO}_3$ -( $\text{Bi}_{1/2}\text{K}_{1/2}$ ) $\text{TiO}_3$  lead-free piezoelectric ceramics," *Journal of Applied Physics*, **103**[7] 074109 (2008).
- [63] T. Oh, "Dielectric relaxor properties in the system of ( $\text{Na}_{1-x}\text{K}_x$ ) $_{1/2}\text{Bi}_{1/2}\text{TiO}_3$  ceramics," *Japanese Journal of Applied Physics Part I-Regular Papers Brief Communications & Review Papers*, **45**[6A] 5138-43 (2006).
- [64] H. Nagata, M. Yoshida, Y. Makiuchi, and T. Takenaka, "Large piezoelectric constant and high Curie temperature of lead-free piezoelectric ceramic ternary system based on bismuth sodium titanate-bismuth potassium titanate-barium titanate near the morphotropic phase boundary," *Japanese Journal of Applied Physics Part I-Regular Papers Short Notes & Review Papers*, **42**[12] 7401-3 (2003).
- [65] X. X. Wang, K. W. Kwok, X. G. Tang, H. L. W. Chan, and C. L. Choy, "Electromechanical properties and dielectric behavior of ( $\text{Bi}_{1/2}\text{Na}_{1/2}$ ) $_{(1-1.5x)}\text{Bi}_x\text{TiO}_3$  lead-free piezoelectric ceramics," *Solid State Communications*, **129**[5] 319-23 (2004).
- [66] Y. Makiuchi, R. Aoyagi, Y. Hiruma, H. Nagata, and T. Takenaka, "( $\text{Bi}_{1/2}\text{Na}_{1/2}$ ) $\text{TiO}_3$ -( $\text{Bi}_{1/2}\text{K}_{1/2}$ ) $\text{TiO}_3$ - $\text{BaTiO}_3$ -Based lead-free piezoelectric ceramics," *Japanese Journal of Applied Physics Part I-Regular Papers Short Notes & Review Papers*, **44**[6B] 4350-3 (2005).
- [67] W. Chen, Y. M. Li, Q. Xu, and J. Zhou, "Electromechanical properties and morphotropic phase boundary of  $\text{Na}_{0.5}\text{Bi}_{0.5}\text{TiO}_3$ - $\text{K}_{0.5}\text{Bi}_{0.5}\text{TiO}_3$ - $\text{BaTiO}_3$  lead-free piezoelectric ceramics," *Journal of Electroceramics*, **15**[3] 229-35 (2005).
- [68] Y. Hiruma, H. Nagata, and T. Takenaka, "Phase transition temperatures and piezoelectric properties of ( $\text{Bi}_{1/2}\text{Na}_{1/2}$ ) $\text{TiO}_3$ -( $\text{Bi}_{1/2}\text{K}_{1/2}$ ) $\text{TiO}_3$ - $\text{BaTiO}_3$  lead-free piezoelectric ceramics," *Japanese Journal of Applied Physics Part I-Regular Papers Brief Communications & Review Papers*, **45**[9B] 7409-12 (2006).
- [69] J. Shieh, K. C. Wu, and C. S. Chen, "Switching characteristics of MPB compositions of ( $\text{Bi}_{0.5}\text{Na}_{0.5}$ ) $\text{TiO}_3$ - $\text{BaTiO}_3$ -( $\text{Bi}_{0.5}\text{K}_{0.5}$ ) $\text{TiO}_3$  lead-free ferroelectric ceramics," *Acta Materialia*, **55**[9] 3081-7 (2007).
- [70] S. H. Choy, X. X. Wang, C. P. Chong, H. L. W. Chan, P. C. K. Liu, and C. L. Choy, "0.90( $\text{Bi}_{1/2}\text{Na}_{1/2}$ ) $\text{TiO}_3$ -0.05( $\text{Bi}_{1/2}\text{K}_{1/2}$ ) $\text{TiO}_3$ -0.05 $\text{BaTiO}_3$  transducer for ultrasonic wirebonding applications," *Applied Physics A: Materials Science & Processing*, **84**[3] 313-6 (2006).
- [71] S. H. Choy, X. X. Wang, H. L. W. Chan, and C. L. Choy, "Study of compressive type accelerometer based on lead-free BNKBT piezoceramics," *Applied Physics A: Materials Science & Processing*, **82**[4] 715-8 (2006).
- [72] X. X. Wang, X. G. Tang, and H. L. W. Chan, "Electromechanical and ferroelectric properties of ( $\text{Bi}_{1/2}\text{Na}_{1/2}$ ) $\text{TiO}_3$ -( $\text{Bi}_{1/2}\text{K}_{1/2}$ ) $\text{TiO}_3$ - $\text{BaTiO}_3$  lead-free piezoelectric ceramics," *Applied Physics Letters*, **85**[1] 91-3 (2004).
- [73] Y. M. Li, W. Chen, J. Zhou, Q. Xu, H. Sun, and R. X. Xu, "Dielectric and piezoelectric properties of lead-free ( $\text{Na}_{0.5}\text{Bi}_{0.5}$ ) $\text{TiO}_3$ - $\text{NaNbO}_3$  ceramics," *Materials Science & Engineering, B: Solid-State Materials for Advanced Technology*, **112**[1] 5-9 (2004).
- [74] X. X. Wang, S. W. Or, X. G. Tang, H. L. W. Chan, P. K. Choy, and P. C. K. Liu, " $\text{TiO}_2$ -nonstoichiometry dependence on piezoelectric properties and depolarization temperature of ( $\text{Bi}_{1/2}\text{Na}_{1/2}$ ) $_{0.94}\text{Ba}_{0.06}\text{TiO}_3$  lead-free ceramics," *Solid State Communications*, **134**[10] 659-63 (2005).

- [75] H. D. Li, C. D. Feng, and P. H. Xiang, "Electrical properties of  $\text{La}^{3+}$ -doped  $(\text{Na}_{1/2}\text{Bi}_{1/2})_{0.94}\text{Ba}_{0.06}\text{TiO}_3$  ceramics," *Japanese Journal of Applied Physics Part 1-Regular Papers Short Notes & Review Papers*, **42**[12] 7387-91 (2003).
- [76] L. Wu, D. Q. Xiao, D. M. Lin, J. G. Zhu, and P. Yu, "Synthesis and properties of  $[\text{Bi}_{0.5}(\text{Na}_{1-x}\text{Ag}_x)_{0.5}]_{1-y}\text{Ba}_y\text{TiO}_3$  piezoelectric ceramics," *Japanese Journal of Applied Physics Part 1-Regular Papers Brief Communications & Review Papers*, **44**[12] 8515-8 (2005).
- [77] H. D. Li, C. D. Feng, and W. L. Yao, "Some effects of different additives on dielectric and piezoelectric properties of  $(\text{Bi}_{1/2}\text{Na}_{1/2})\text{TiO}_3$ - $\text{BaTiO}_3$  morphotropic-phase-boundary composition," *Materials Letters*, **58**[7-8] 1194-8 (2004).
- [78] X. X. Wang, H. L. W. Chan, and C. L. Choy, "Piezoelectric and dielectric properties of  $\text{CeO}_2$ -added  $(\text{Bi}_{1/2}\text{Na}_{1/2})_{0.94}\text{Ba}_{0.06}\text{TiO}_3$  lead-free ceramics," *Solid State Communications*, **125**[7-8] 395-9 (2003).
- [79] L. Liu, H. Fan, S. Ke, and X. Chen, "Effect of sintering temperature on the structure and properties of cerium-doped  $0.94(\text{Bi}_{0.5}\text{Na}_{0.5})\text{TiO}_3$ - $0.06\text{BaTiO}_3$  piezoelectric ceramics," *Journal of Alloys and Compounds*, **458**[1-2] 504-8 (2008).
- [80] X. X. Wang, H. L. W. Chan, and C. L. Choy, " $(\text{Bi}_{1/2}\text{Na}_{1/2})_{0.94}\text{Ba}_{0.06}\text{TiO}_3$  lead-free ceramics with simultaneous addition of  $\text{CeO}_2$  and  $\text{La}_2\text{O}_3$ ," *Applied Physics A: Materials Science & Processing*, **80**[2] 333-6 (2005).
- [81] D. M. Lin, D. Q. Xiao, J. G. Zhu, and P. Yu, "Piezoelectric and ferroelectric properties of lead-free  $[\text{Bi}_{1-y}(\text{Na}_{1-x-y}\text{Li}_x)]_{0.5}\text{Ba}_y\text{TiO}_3$  ceramics," *Journal of the European Ceramic Society*, **26**[15] 3247-51 (2006).
- [82] Y. Q. Yao, T. Y. Tseng, C. C. Chou, and H. H. D. Chen, "Phase transition and piezoelectric property of  $(\text{Bi}_{0.5}\text{Na}_{0.5})_{0.94}\text{Ba}_{0.06}\text{Zr}_y\text{Ti}_{1-y}\text{O}_3$  ( $y=0-0.04$ ) ceramics," *Journal of Applied Physics*, **102**[9] 094102 (2007).
- [83] H. Y. Tian, D. Y. Wang, D. M. Lin, J. T. Zeng, K. W. Kwok, and H. L. W. Chan, "Diffusion phase transition and dielectric characteristics of  $\text{Bi}_{1/2}\text{Na}_{1/2}\text{TiO}_3$ - $\text{Ba}(\text{Hf,Ti})\text{O}_3$  lead-free ceramics," *Solid State Communications*, **142**[1] 10-4 (2007).
- [84] L. J. Liu and H. Q. Fan, "Influence of sintering temperatures on the electrical property of bismuth sodium titanate based piezoelectric ceramics," *Journal of Electroceramics*, **16**[4] 293-6 (2006).
- [85] J. R. Gomah-Petry, P. Marchet, A. Salak, V. M. Ferreira, and J. P. Mercurio, "Electrical properties of  $\text{Na}_{0.5}\text{Bi}_{0.5}\text{TiO}_3$ - $\text{SrTiO}_3$  ceramics," *Integrated Ferroelectrics*, **61** 159-62 (2004).
- [86] Y. Hiruma, Y. Imai, Y. Watanabe, H. Nagata, and T. Takenaka, "Large electrostrain near the phase transition temperature of  $(\text{Bi}_{0.5}\text{Na}_{0.5})\text{TiO}_3$ - $\text{SrTiO}_3$  ferroelectric ceramics," *Applied Physics Letters*, **92**[26] 262904-3 (2008).
- [87] J. K. Lee, K. S. Hong, C. K. Kim, and S. E. Park, "Phase transitions and dielectric properties in A-site ion substituted  $(\text{Na}_{1/2}\text{Bi}_{1/2})\text{TiO}_3$  ceramics ( $\text{A}=\text{Pb}$  and  $\text{Sr}$ )," *Journal of Applied Physics*, **91**[7] 4538-42 (2002).
- [88] H. Nagata and T. Takenaka, "Additive effects on electrical properties of  $(\text{Bi}_{1/2}\text{Na}_{1/2})\text{TiO}_3$  ferroelectric ceramics," *Journal of the European Ceramic Society*, **21**[10-11] 1299-302 (2001).
- [89] W. Z. Lu, G. F. Fan, X. H. Wang, and F. Liang, "Dielectric and piezoelectric properties of  $[\text{Bi}_{0.5}(\text{Na}_{1-x}\text{Li}_x)_{0.5}]\text{TiO}_3$  lead-free ceramics," *Japanese Journal of Applied Physics Part 1-Regular Papers Brief Communications & Review Papers*, **45**[11] 8763-5 (2006).
- [90] C. Ang and Z. Yu, "High, purely electrostrictive strain in lead-free dielectrics," *Advanced Materials*, **18**[1] 103-6 (2006).
- [91] S.-T. Zhang, A. B. Kouna, W. Jo, C. Jamin, K. Seifert, T. Granzow, J. Rödel, and D. Damjanovic, "High-strain lead-free antiferroelectric electrostrictors," *Advanced Materials*, **21**[46] 4716 - 20 (2009).
- [92] K. T. P. Seifert, W. Jo, and J. Rödel, "Temperature-Insensitive Large Strain of  $(\text{Bi}_{1/2}\text{Na}_{1/2})\text{TiO}_3$ - $(\text{Bi}_{1/2}\text{K}_{1/2})\text{TiO}_3$ - $(\text{K}_{0.5}\text{Na}_{0.5})\text{NbO}_3$  Lead-Free Piezoceramics," *Journal of the American Ceramic Society*, **93**[5] 1392-6 (2010).
- [93] A. Watcharapasorn, S. Jiansirisomboon, and T. Tunkasiri, "Sintering of Fe-doped  $\text{Bi}_{0.5}\text{Na}_{0.5}\text{TiO}_3$  at  $< 1000^\circ\text{C}$ ," *Materials Letters*, **61**[14-15] 2986-9 (2007).
- [94] J. J. Hao, X. H. Wang, Z. L. Gui, and L. T. Li, "Effect of  $\text{MnO}_2$  on the property of bismuth sodium titanate piezoelectric ceramics," *Rare Metal Materials and Engineering*, **32** 438-40 (2003).
- [95] C. R. Zhou and X. Y. Liu, "Effect of B-site substitution by  $(\text{Ni}_{1/3}\text{Nb}_{2/3})^{4+}$  for  $\text{Ti}^{4+}$  on microstructure and piezoelectric properties in  $(\text{Bi}_{1/2}\text{Na}_{1/2})\text{TiO}_3$  piezoelectric ceramics," *Journal of Alloys and Compounds*, **466**[1-2] 563-7 (2008).
- [96] T. Takenaka, T. Okuda, and K. Takegahara, "Lead-free piezoelectric ceramics based on  $(\text{Bi}_{1/2}\text{Na}_{1/2})\text{TiO}_3$ - $\text{NaNbO}_3$ ," *Ferroelectrics*, **196**[1-4] 175-8 (1997).
- [97] S. I. Raevskaya, L. A. Reznichenko, I. P. Raevski, V. V. Titov, S. V. Titov, and J. L. Dellis, "Lead-free niobate ceramics with relaxor-like properties," *Ferroelectrics*, **340** 107-12 (2006).
- [98] Y.-M. Li, W. Chen, J. Zhou, Q. Xu, X.-Y. Gu, and R.-H. Liao, "Impedance spectroscopy and dielectric properties of  $\text{Na}_{0.5}\text{Bi}_{0.5}\text{TiO}_3$ - $\text{NaNbO}_3$  ceramics," *Physica B: Condensed Matter*, **365**[1-4] 76-81 (2005).

- [99] P. Marchet, E. Boucher, V. Dorcet, and J. P. Mercurio, "Dielectric properties of some low-lead or lead-free perovskite-derived materials:  $\text{Na}_{0.5}\text{Bi}_{0.5}\text{TiO}_3\text{-PbZrO}_3$ ,  $\text{Na}_{0.5}\text{Bi}_{0.5}\text{TiO}_3\text{-BiScO}_3$  and  $\text{Na}_{0.5}\text{Bi}_{0.5}\text{TiO}_3\text{-BiFeO}_3$  ceramics," *Journal of the European Ceramic Society*, **26**[14] 3037-41 (2006).
- [100] H. Nagata and T. Takenaka, "Lead-free piezoelectric ceramics of  $(\text{Bi}_{1/2}\text{Na}_{1/2})\text{TiO}_3\text{-}1/2(\text{Bi}_2\text{O}_3\cdot\text{Sc}_2\text{O}_3)$  system," *Japanese Journal of Applied Physics Part 1-Regular Papers Short Notes & Review Papers*, **36**[9B] 6055-7 (1997).
- [101] J. König, B. Jancar, and D. Suvorov, "New  $\text{Na}_{0.5}\text{Bi}_{0.5}\text{TiO}_3\text{-NaTaO}_3$ -Based Perovskite Ceramics," *Journal of the American Ceramic Society*, **90** 3621-7 (2007).
- [102] X. X. Wang, H. L. W. Chan, and C. L. Choy, " $(\text{Bi}_{1/2}\text{Na}_{1/2})\text{TiO}_3\text{-Ba}(\text{Cu}_{1/2}\text{W}_{1/2})\text{O}_3$  lead-free piezoelectric ceramics," *Journal of the American Ceramic Society*, **86**[10] 1809-11 (2003).
- [103] A. B. Kouniga, S.-T. Zhang, W. Jo, T. Granzow, and J. Rödel, "Morphotropic phase boundary in  $(1-x)\text{Bi}_{0.5}\text{Na}_{0.5}\text{TiO}_3\text{-}x\text{K}_{0.5}\text{Na}_{0.5}\text{NbO}_3$  lead-free piezoceramics," *Applied Physics Letters*, **92**[22] 222902-3 (2008).
- [104] D. Lin, K. W. Kwok, and H. L. W. Chan, "Structure and electrical properties of  $\text{Bi}_{0.5}\text{Na}_{0.5}\text{TiO}_3\text{-BaTiO}_3\text{-Bi}_{0.5}\text{Li}_{0.5}\text{TiO}_3$  lead-free piezoelectric ceramics," *Solid State Ionics*, **178**[37-38] 1930-7 (2008).
- [105] D. Q. Xiao, D. M. Lin, J. G. Zhu, and P. Yu, "Investigation on the design and synthesis of new systems of BNT-based lead-free piezoelectric ceramics," *Journal of Electroceramics*, **16**[4] 271-5 (2006).
- [106] Y. Hiruma, H. Nagata, and T. Takenaka, "Phase-transition temperatures and piezoelectric properties of  $(\text{Bi}_{1/2}\text{Na}_{1/2})\text{TiO}_3\text{-(Bi}_{1/2}\text{Li}_{1/2})\text{TiO}_3\text{-(Bi}_{1/2}\text{K}_{1/2})\text{TiO}_3$  lead-free ferroelectric ceramics," *IEEE Transactions on Ultrasonics Ferroelectrics and Frequency Control*, **54**[12] 2493-9 (2007).
- [107] Y. Yuan, S. R. Zhang, X. H. Zhou, and J. S. Liu, "Phase transition and temperature dependences of electrical properties of  $[\text{Bi}_{0.5}\text{Na}_{1-x-y}\text{K}_x\text{Li}_y]_{0.5}\text{TiO}_3$  ceramics," *Japanese Journal of Applied Physics Part 1-Regular Papers Brief Communications & Review Papers*, **45**[2A] 831-4 (2006).
- [108] D. M. Lin, D. Q. Xiao, J. G. Zhu, and P. Yu, "Piezoelectric and ferroelectric properties of  $[\text{Bi}_{0.5}(\text{Na}_{1-x-y}\text{K}_x\text{Li}_y)]_{0.5}\text{TiO}_3$  lead-free piezoelectric ceramics," *Applied Physics Letters*, **88**[6] 062901 (2006).
- [109] D. M. Lin, D. Q. Xiao, J. G. Zhu, P. Yu, H. J. Yan, and L. Z. Li, "Synthesis and piezoelectric properties of lead-free piezoelectric  $[\text{Bi}_{0.5}(\text{Na}_{1-x-y}\text{K}_x\text{Li}_y)]_{0.5}\text{TiO}_3$  ceramics," *Materials Letters*, **58**[5] 615-8 (2004).
- [110] D. M. Lin, D. Q. Xiao, J. G. Zhu, P. Yu, H. J. Yan, L. Z. Li, and W. Zhang, "The relations of sintering conditions and microstructures of  $[\text{Bi}_{0.5}(\text{Na}_{1-x-y}\text{K}_x\text{Li}_y)]_{0.5}\text{TiO}_3$  piezoelectric ceramics," *Crystal Research and Technology*, **39**[1] 30-3 (2004).
- [111] D. M. Lin, D. Q. Xiao, J. G. Zhu, and P. Yu, "Electrical properties of  $[\text{Bi}_{1-z}(\text{Na}_{1-x-y-z}\text{K}_x\text{Li}_y)]_{0.5}\text{Ba}_z\text{TiO}_3$  multi-component lead-free piezoelectric ceramics," *Physica Status Solidi A: Applications and Materials Science*, **202**[9] R89-R91 (2005).
- [112] D. Shan, Y. F. Qu, and J. J. Song, "Ionic doping effects on crystal structure and relaxation character in  $\text{Bi}_{0.5}\text{Na}_{0.5}\text{TiO}_3$  ferroelectric ceramics," *Journal of Materials Research*, **22**[3] 730-4 (2007).
- [113] J. Shi and W. Yang, "Piezoelectric and dielectric properties of  $\text{CeO}_2$ -doped  $(\text{Bi}_{0.5}\text{Na}_{0.5})_{0.94}\text{Ba}_{0.06}\text{TiO}_3$  lead-free ceramics," *Journal of Alloys and Compounds*, **472** 267-70 (2009).
- [114] H. D. Li, C. D. Feng, and P. H. Xiang, "Dielectric behavior and piezoelectric properties of  $\text{La}^{3+}$ -doping  $0.94(\text{Na}_{1/2}\text{Bi}_{1/2})\text{TiO}_3\text{-}0.06\text{BaTiO}_3$  ceramics," *Journal of Inorganic Materials*, **19**[3] 579-85 (2004).
- [115] Y. J. Son, Y. G. Choi, J. C. Kwon, K. W. Cho, Y. M. Kim, S. Y. Kweon, T. H. Hong, Y. G. Lee, S. L. Ryu, M. S. Yoon, and S. C. Ur, "Effects of  $\text{La}_2\text{O}_3$  on the piezoelectric properties of lead-free  $(\text{Bi}_{0.5}\text{Na}_{0.5})(0.94)\text{Ba}_{0.06}\text{TiO}_3$  piezoelectric ceramics," *Eco-Materials Processing & Design VII*, **510-511** 538-41 (2006).
- [116] K. Pengpat, S. Hanphimol, S. Eitssayeam, U. Intatha, G. Rujijanagul, and T. Tunkasiri, "Morphotropic phase boundary and electrical properties of lead-free bismuth sodium lanthanum titanate-barium titanate ceramics," *Journal of Electroceramics*, **16**[4] 301-5 (2006).
- [117] S. A. Sheets, A. N. Soukhovjak, N. Ohashi, and Y.-M. Chiang, "Relaxor single crystals in the  $(\text{Bi}_{1/2}\text{Na}_{1/2})_{1-x}\text{Ba}_x\text{Zr}_y\text{Ti}_{1-y}\text{O}_3$  system exhibiting high electrostrictive strain," *Journal of Applied Physics*, **90**[10] 5287-95 (2001).
- [118] Z. W. Chen, A. Shui, Z. Y. Lu, and P. G. Liu, "Piezoelectric and dielectric properties of  $(\text{Bi}_{0.5}\text{Na}_{0.5})\text{TiO}_3\text{-Ba}(\text{Zr}_{0.04}\text{Ti}_{0.96})\text{O}_3$  lead-free piezoelectric ceramics," *Journal of the Ceramic Society of Japan*, **114**[1334] 857-60 (2006).
- [119] C. Peng, J.-F. Li, and W. Gong, "Preparation and properties of  $(\text{Bi}_{1/2}\text{Na}_{1/2})\text{TiO}_3\text{-Ba}(\text{Ti},\text{Zr})\text{O}_3$  lead-free piezoelectric ceramics," *Materials Letters*, **59**[12] 1576-80 (2005).
- [120] Z. Yu, V. D. Krstic, and B. K. Mukherjee, "Microstructure and properties of lead-free  $(\text{Bi}_{0.5}\text{Na}_{0.5})\text{TiO}_3$ ," *Journal of Material Science*, **42** 3544-51 (2007).
- [121] Q. Xu, M. Chen, W. Chen, H.-X. Liu, B.-H. Kim, and B.-K. Ahn, "Effect of  $\text{CoO}$  additive on structure and electrical properties of  $(\text{Na}_{0.5}\text{Bi}_{0.5})_{0.93}\text{Ba}_{0.07}\text{TiO}_3$  ceramics prepared by the citrate method," *Acta Materialia*, **56**[3] 642-50 (2008).

- [122] L. Wu, D. Q. Xiao, D. M. Lin, J. U. Zhu, P. Yu, and X. Li, "Temperature dependence of electric properties of  $[\text{Bi}_{0.5}(\text{Na}_{1-x}\text{Ag}_x)_{0.5}](1-y)\text{Ba}_y\text{TiO}_3$  ceramics," *Japanese Journal of Applied Physics Part 1-Regular Papers Brief Communications & Review Papers*, **46**[11] 7382-7 (2007).
- [123] G. F. Fan, W. Z. Lu, X. H. Wang, and F. Liang, "Effects of manganese additive on piezoelectric properties of  $(\text{Bi}_{1/2}\text{Na}_{1/2})\text{TiO}_3\text{-BaTiO}_3$  ferroelectric ceramics," *Journal of Materials Science*, **42**[2] 472-6 (2007).
- [124] X. Y. Zhou, H. S. Gu, Y. Wang, W. Li, and T. S. Zhou, "Piezoelectric properties of Mn-doped  $(\text{Na}_{0.5}\text{Bi}_{0.5})_{0.92}\text{Ba}_{0.08}\text{TiO}_3$  ceramics," *Materials Letters*, **59**[13] 1649-52 (2005).
- [125] M. Zhu, L. Liu, Y. Hou, H. Wang, and H. Yan, "Microstructure and Electrical Properties of MnO-Doped  $(\text{Na}_{0.5}\text{Bi}_{0.5})_{0.92}\text{Ba}_{0.08}\text{TiO}_3$  Lead-Free Piezoceramics," *Journal of the American Ceramic Society*, **90**[1] 120-4 (2007).
- [126] H. Tian, K. Kwok, H. Chan, and C. Buckley, "The effects of CuO-doping on dielectric and piezoelectric properties of  $\text{Bi}_{0.5}\text{Na}_{0.5}\text{TiO}_3\text{-Ba}(\text{Zr},\text{Ti})\text{O}_3$  lead-free ceramics," *Journal of Materials Science*, **42**[23] 9750-5 (2007).
- [127] K. Kusumoto, "Dielectric and piezoelectric properties of  $\text{KNbO}_3\text{-NaNbO}_3\text{-LiNbO}_3\text{-SrTiO}_3$  ceramics," *Japanese Journal of Applied Physics Part 1-Regular Papers Brief Communications & Review Papers*, **45**[9B] 7440-3 (2006).
- [128] Y. G. Wu, H. L. Zhang, Y. Zhang, J. Y. Ma, and D. H. Xie, "Lead-free piezoelectric ceramics with composition of  $(0.97-x)\text{Na}_{1/2}\text{Bi}_{1/2}\text{TiO}_3\text{-}0.03\text{NaNbO}_3\text{-xBaTiO}_3$ ," *Journal of Materials Science*, **38**[5] 987-94 (2003).
- [129] H. Nagata, N. Koizumi, N. Kuroda, I. Igarashi, and T. Takenaka, "Lead-free piezoelectric ceramics of  $(\text{Bi}_{1/2}\text{Na}_{1/2})\text{TiO}_3\text{-BaTiO}_3\text{-BiFeO}_3$  system," *Ferroelectrics*, **229**[1-4] 273-8 (1999).
- [130] S. A. Fedulov, "Determination of Curie Temperature for  $\text{BiFeO}_3$  Ferroelectric," *Doklady Akademii Nauk Sssr*, **139**[6] 1345-& (1961).
- [131] S. A. Fedulov and P. B. Ladyzhinskii, "Complete phase diagram of the  $\text{PbTiO}_3\text{-BiFeO}_3$  system," *Soviet Physics-Solid State*, **6** 375-7 (1964).
- [132] X. P. Jiang, L. Z. Li, M. Zeng, and H. L. W. Chan, "Dielectric properties of Mn-doped  $(\text{Na}_{0.8}\text{K}_{0.2})_{0.5}\text{Bi}_{0.5}\text{TiO}_3$  ceramics," *Materials Letters*, **60**[15] 1786-90 (2006).
- [133] J. Yoo, D. Oh, Y. Jeong, J. Hong, and M. Jung, "Dielectric and piezoelectric characteristics of lead-free  $\text{Bi}_{0.5}(\text{Na}_{0.84}\text{K}_{0.16})_{0.5}\text{TiO}_3$  ceramics substituted with Sr," *Materials Letters*, **58**[29] 3831-5 (2004).
- [134] Y. Li, W. Chen, Q. Xu, J. Zhou, Y. Wang, and H. Sun, "Piezoelectric and dielectric properties of  $\text{CeO}_2$ -doped  $\text{Bi}_{0.5}\text{Na}_{0.44}\text{K}_{0.06}\text{TiO}_3$  lead-free ceramics," *Ceramics International*, **33**[1] 95-9 (2007).
- [135] Y. Liao, D. Xiao, D. Lin, J. Zhu, P. Yu, L. Wu, and X. Wang, "The effects of  $\text{CeO}_2$ -doping on piezoelectric and dielectric properties of  $\text{Bi}_{0.5}(\text{Na}_{1-x-y}\text{K}_x\text{Li}_y)_{0.5}\text{TiO}_3$  piezoelectric ceramics," *Materials Science and Engineering: B*, **133**[1-3] 172-6 (2006).
- [136] J. Yoo, J. Hong, H. Lee, Y. Jeong, B. Lee, H. Song, and J. Kwon, "Piezoelectric and dielectric properties of  $\text{La}_2\text{O}_3$  added  $\text{Bi}(\text{Na},\text{K})\text{TiO}_3\text{-SrTiO}_3$  ceramics for pressure sensor application," *Sensors and Actuators A: Physical*, **126**[1] 41-7 (2006).
- [137] G. F. Fan, W. Z. Lu, X. H. Wang, and F. Liang, "Morphotropic phase boundary and piezoelectric properties of  $(\text{Bi}_{1/2}\text{Na}_{1/2})\text{TiO}_3\text{-(Bi}_{1/2}\text{K}_{1/2})\text{TiO}_3\text{-KNbO}_3$  lead-free piezoelectric ceramics," *Applied Physics Letters*, **91**[20] - (2007).
- [138] J. H. Chen, S. B. Qu, K. H. Gao, Z. B. Pei, and L. H. Zhu, "Effect of Mn doping on dielectric and piezoelectric properties of  $(\text{Na}_{0.5}\text{Bi}_{0.5})\text{TiO}_3\text{-}0.1\text{BaTiO}_3\text{-}0.1(\text{K}_{0.5}\text{Bi}_{0.5})\text{TiO}_3$  ceramics," *Rare Metal Materials and Engineering*, **35**[11] 1704-7 (2006).
- [139] S. H. Choy, X. X. Wang, H. L. W. Chan, and C. L. Choy, " $0.75(\text{Bi}_{1/2}\text{Na}_{1/2})\text{TiO}_3\text{-}0.20(\text{Bi}_{1/2}\text{K}_{1/2})\text{TiO}_3\text{-}0.05\text{BaTiO}_3$  lead-free ceramics with addition of  $\text{CeO}_2$ ," *Ferroelectrics*, **336** 69-79 (2006).
- [140] S.-T. Zhang, A. B. Kounga, E. Aulbach, H. Ehrenberg, and J. Rödel, "Giant strain in lead-free piezoceramics  $\text{Bi}_{0.5}\text{Na}_{0.5}\text{TiO}_3\text{-BaTiO}_3\text{-K}_{0.5}\text{Na}_{0.5}\text{NbO}_3$  system," *Applied Physics Letters*, **91**[11] 112906-3 (2007).
- [141] S. T. Zhang, A. B. Kounga, E. Aulbach, W. Jo, T. Granzow, H. Ehrenberg, and J. Rödel, "Lead-free piezoceramics with giant strain in the system  $\text{Bi}_{0.5}\text{Na}_{0.5}\text{TiO}_3\text{-BaTiO}_3\text{-K}_{0.5}\text{Na}_{0.5}\text{NbO}_3$ . II. Temperature dependent properties," *Journal of Applied Physics*, **103**[3] 034108 (2008).
- [142] S. T. Zhang, A. B. Kounga, E. Aulbach, T. Granzow, W. Jo, H. J. Kleebe, and J. Rödel, "Lead-free piezoceramics with giant strain in the system  $\text{Bi}_{0.5}\text{Na}_{0.5}\text{TiO}_3\text{-BaTiO}_3\text{-K}_{0.5}\text{Na}_{0.5}\text{NbO}_3$ . I. Structure and room temperature properties," *Journal of Applied Physics*, **103**[3] 034107 (2008).
- [143] M. Hinterstein, M. Knapp, M. Hölzel, W. Jo, A. Cervellino, H. Ehrenberg, and H. Fuess, "Field induced phase transition in lead-free  $0.92\text{BNT}\text{-}0.06\text{BT}\text{-}0.02\text{KNN}$ ," *Journal of Applied Crystallography*[in press] (2010).
- [144] W. Jo, T. Granzow, E. Aulbach, J. Rödel, and D. Damjanovic, "Origin of the large strain response in  $(\text{K}_{0.5}\text{Na}_{0.5})\text{NbO}_3$  - modified  $(\text{Bi}_{0.5}\text{Na}_{0.5})\text{TiO}_3$  -  $\text{BaTiO}_3$  - lead-free piezoceramics," *Journal of Applied Physics*, **105** 094102 (2009).

- [145] Y. Hiruma, H. Nagata, and T. Takenaka, "Phase diagrams and electrical properties of  $(\text{Bi}_{1/2}\text{Na}_{1/2})\text{TiO}_3$ -based solid solutions," *Journal of Applied Physics*, **104**[12] 124106 (2008).
- [146] L. A. Schmitt, M. Hinterstein, H. J. Kleebe, and H. Fuess, "Comparative study of two lead-free piezoceramics using diffraction techniques," *Journal of Applied Crystallography*, **43** 805-10 (2010).
- [147] L. A. Schmitt and H. J. Kleebe, "Single Grains Hosting two Space Groups - A Transmission Electron Microscopy Study of a Lead-Free Ferroelectric," *Functional Materials Letters*, **3**[1] 55-8 (2010).
- [148] J. Kling, X. Tan, W. Jo, H. J. Kleebe, H. Fuess, and J. Rödel, "In Situ Transmission Electron Microscopy of Electric Field-Triggered Reversible Domain Formation in Bi-Based Lead-Free Piezoceramics," *Journal of the American Ceramic Society*, **93**[9] 2452-5 (2010).
- [149] J. Suchanicz, J. Kusz, H. Bohm, H. Duda, J. P. Mercurio, and K. Konieczny, "Structural and dielectric properties of  $(\text{Na}_{0.5}\text{Bi}_{0.5})_{0.70}\text{Ba}_{0.30}\text{TiO}_3$  ceramics," *Journal of the European Ceramic Society*, **23**[10] 1559-64 (2003).
- [150] C. Y. Kim, T. Sekino, and K. Niihara, "Synthesis of Bismuth Sodium Titanate Nanosized Powders by Solution/Sol-Gel Process," *Journal of the American Ceramic Society*, **86**[9] 1464-7 (2003).
- [151] J. J. Hao, X. H. Wang, R. Z. Chen, and L. T. Li, "Synthesis of  $(\text{Bi}_{0.5}\text{Na}_{0.5})\text{TiO}_3$  nanocrystalline powders by stearic acid gel method," *Materials Chemistry and Physics*, **90**[2-3] 282-5 (2005).
- [152] Q. Xu, X. Chen, W. Chen, S. Chen, B. Kim, and J. Lee, "Synthesis, ferroelectric and piezoelectric properties of some  $(\text{Na}_{0.5}\text{Bi}_{0.5})\text{TiO}_3$  system compositions," *Materials Letters*, **59**[19-20] 2437-41 (2005).
- [153] C. Y. Kim, T. Sekino, Y. Yamamoto, and K. Niihara, "The synthesis of lead-free ferroelectric  $\text{Bi}_{1/2}\text{Na}_{1/2}\text{TiO}_3$  thin film by solution-sol-gel method," *Journal of Sol-Gel Science and Technology*, **33**[3] 307-14 (2005).
- [154] Y. J. Ma, J. H. Cho, Y. H. Lee, and B. I. Kim, "Hydrothermal synthesis of  $(\text{Bi}_{1/2}\text{Na}_{1/2})\text{TiO}_3$  piezoelectric ceramics," *Materials Chemistry and Physics*, **98**[1] 5-8 (2006).
- [155] D. L. West and D. A. Payne, "Preparation of  $0.95\text{Bi}_{1/2}\text{Na}_{1/2}\text{TiO}_3$ - $0.05\text{BaTiO}_3$  Ceramics by an Aqueous Citrate-Gel Route," *Journal of the American Ceramic Society*, **86**[1] 192-4 (2003).
- [156] D. Y. Wang, K. Li, and H. L. W. Chan, "High frequency 1-3 composite transducer fabricated using sol-gel derived lead-free BNT fibers," *Sensors and Actuators A: Physical*, **114**[1] 1-6 (2004).
- [157] D. Zhou, H. Li, S. Gong, Y. Hu, and K. Han, "Sodium Bismuth Titanate-Based Lead-Free Piezoceramics Prepared by Aqueous Gelcasting," *Journal of the American Ceramic Society*, **91**[9] 2792-6 (2008).
- [158] T. Wada, A. Fukui, and Y. Matsuo, "Preparation of  $(\text{K}_{1/2}\text{Bi}_{1/2})\text{TiO}_3$  ceramics by polymerized complex method and their properties," *Japanese Journal of Applied Physics Part 1-Regular Papers Short Notes & Review Papers*, **41**[11B] 7025-8 (2002).
- [159] M. K. Zhu, L. Hou, Y. D. Hou, J. B. Liu, H. Wang, and H. Yan, "Lead-free  $(\text{K}_{0.5}\text{Bi}_{0.5})\text{TiO}_3$  powders and ceramics prepared by a sol-gel method," *Materials Chemistry and Physics*, **99**[2-3] 329-32 (2006).
- [160] P. Pookmanee, G. Rujijanagul, S. Ananta, R. B. Heimann, and S. Phanichphant, "Effect of sintering temperature on microstructure of hydrothermally prepared bismuth sodium titanate ceramics," *Journal of the European Ceramic Society*, **24**[2] 517-20 (2004).
- [161] J. H. Cho, Y. J. Ma, Y. H. Lee, M. P. Chun, and B. I. Kim, "Piezoelectric ceramic powder synthesis of bismuth-sodium titanate by a hydrothermal process," *Journal of Ceramic Processing Research*, **7**[2] 91-4 (2006).
- [162] B. H. Kim, S. H. Kim, J. H. Kim, K. J. Lee, Y. H. Choa, Y. K. Choi, and S. S. Kim, "Synthesis and electrical properties of  $(\text{Bi}_{1/2}\text{Na}_{1/2})\text{TiO}_3$  (BNT) ferroelectric thin films by liquid sprayed mist chemical vapor deposition technique," *Journal of Nanoscience and Nanotechnology*, **6**[11] 3479-82 (2006).
- [163] T. Kimura, E. Fukuchi, and T. Tani, "Fabrication of textured bismuth sodium titanate using excess bismuth oxide," *Japanese Journal of Applied Physics Part 1-Regular Papers Brief Communications & Review Papers*, **44**[11] 8055-61 (2005).
- [164] F. K. Lotgering, "Topotactical reactions with ferrimagnetic oxides having hexagonal crystal structures--I," *Journal of Inorganic and Nuclear Chemistry*, **9**[2] 113-23 (1959).
- [165] D. L. West and D. A. Payne, "Microstructure development in reactive-templated grain growth of  $\text{Bi}_{1/2}\text{Na}_{1/2}\text{TiO}_3$ -based ceramics: Template and formulation effects," *Journal of the American Ceramic Society*, **86**[5] 769-74 (2003).
- [166] D. L. West and D. A. Payne, "Reactive-Templated Grain Growth of  $\text{Bi}_{1/2}(\text{Na},\text{K})_{1/2}\text{TiO}_3$ : Effects of Formulation on Texture Development," *Journal of the American Ceramic Society*, **86**[7] 1132-7 (2003).
- [167] F. Gao, C.-S. Zhang, X.-C. Liu, L.-H. Cheng, and C.-S. Tian, "Microstructure and piezoelectric properties of textured  $(\text{Na}_{0.84}\text{K}_{0.16})_{0.5}\text{Bi}_{0.5}\text{TiO}_3$  lead-free ceramics," *Journal of the European Ceramic Society*, **27**[12] 3453-8 (2007).
- [168] D. S. Lee, S. J. Jeong, E. C. Park, and J. S. Song, "Characteristic of grain oriented  $(\text{Bi}_{0.5}\text{Na}_{0.5})\text{TiO}_3$ - $\text{BaTiO}_3$  ceramics," *Journal of Electroceramics*, **17**[2-4] 505-8 (2006).

- [169] F. Gao, R.-Z. Hong, J.-J. Liu, Y.-H. Yao, and C.-S. Tian, "Effect of different templates on microstructure of textured  $\text{Na}_{0.5}\text{Bi}_{0.5}\text{TiO}_3\text{-BaTiO}_3$  ceramics with RTGG method," *Journal of the European Ceramic Society*, **28**[10] 2063-70 (2008).
- [170] X. Z. Jing, Y. X. Li, Q. B. Yang, J. T. Zeng, and Q. R. Yin, "Influence of different templates on the textured  $\text{Bi}_{0.5}(\text{Na}_{1-x}\text{K}_x)_{0.5}\text{TiO}_3$  piezoelectric ceramics by the reactive templated grain growth process," *Ceramics International*, **30**[7] 1889-93 (2004).
- [171] T. Kimura, T. Takahashi, T. Tani, and Y. Saito, "Preparation of crystallographically textured  $\text{Bi}_{1/2}\text{Na}_{1/2}\text{TiO}_3\text{-BaTiO}_3$  ceramics by reactive-templated grain growth method," *Ceramics International*, **30**[7] 1161-7 (2004).
- [172] E. Fukuchi, T. Kimura, T. Tani, T. Takeuchi, and Y. Saito, "Effect of potassium concentration on the grain orientation in bismuth sodium potassium titanate," *Journal of the American Ceramic Society*, **85**[6] 1461-6 (2002).
- [173] K. Fuse and T. Kimura, "Effect of particle sizes of starting materials on microstructure development in textured  $\text{Bi}_{0.5}(\text{Na}_{0.5}\text{K}_{0.5})_{0.5}\text{TiO}_3$ ," *Journal of the American Ceramic Society*, **89**[6] 1957-64 (2006).
- [174] A. N. Soukhovjak, H. Wang, G. W. Farrey, and Y. M. Chiang, "Superlattice in single crystal barium-doped sodium bismuth titanate," *Journal of Physics and Chemistry of Solids*, **61**[2] 301-4 (2000).
- [175] H. Liu, W. Ge, X. Jiang, X. Zhao, and H. Luo, "Growth and characterization of Mn-doped  $\text{Na}_{1/2}\text{Bi}_{1/2}\text{TiO}_3$  lead-free ferroelectric single crystal," *Materials Letters*, **62**[17-18] 2721-4 (2008).
- [176] S. E. Park and T. R. Shrout, "Ultrahigh strain and piezoelectric behavior in relaxor based ferroelectric single crystals," *Journal of Applied Physics*, **82**[4] 1804-11 (1997).
- [177] Y. M. Chiang, G. W. Farrey, and A. N. Soukhovjak, "Lead-free high-strain single-crystal piezoelectrics in the alkaline-bismuth-titanate perovskite family," *Applied Physics Letters*, **73**[25] 3683-5 (1998).
- [178] Y. Hosono, K. Harada, and Y. Yamashita, "Crystal growth and electrical properties of lead-free piezoelectric material  $(\text{Na}_{1/2}\text{Bi}_{1/2})\text{TiO}_3\text{-BaTiO}_3$ ," *Japanese Journal of Applied Physics Part 1-Regular Papers Short Notes & Review Papers*, **40**[9B] 5722-6 (2001).
- [179] G. Xu, Z. Duan, X. Wang, and D. Yang, "Growth and some electrical properties of lead-free piezoelectric crystals  $(\text{Na}_{1/2}\text{Bi}_{1/2})\text{TiO}_3$  and  $(\text{Na}_{1/2}\text{Bi}_{1/2})\text{TiO}_3\text{-BaTiO}_3$  prepared by a Bridgman method," *Journal of Crystal Growth*, **275**[1-2] 113-9 (2005).
- [180] J. Bubesh Babu, G. Madeswaran, M. He, D. F. Zhang, X. L. Chen, and R. Dhanasekaran, "Inhomogeneity issues in the growth of  $\text{Na}_{1/2}\text{Bi}_{1/2}\text{TiO}_3\text{-BaTiO}_3$  single crystals," *Journal of Crystal Growth*, **310**[2] 467-72 (2008).
- [181] D. Q. Ni, W. Y. Wang, D. F. Zhang, X. Wu, X. L. Chen, and K. Q. Lu, "Near-stoichiometric  $\text{LiNbO}_3$  single-crystal growth by metal strip-heated zone melting technique," *Journal of Crystal Growth*, **263**[1-4] 421-6 (2004).
- [182] W. Ge, H. Liu, X. Zhao, X. Pan, T. He, D. Lin, H. Xu, and H. Luo, "Growth and characterization of  $\text{Na}_{0.5}\text{Bi}_{0.5}\text{TiO}_3\text{-BaTiO}_3$  lead-free piezoelectric crystal by the TSSG method," *Journal of Alloys and Compounds*, **456**[1-2] 503-7 (2008).
- [183] P. Setasuwon, N. Vaneesorn, S. Kijamnajsuk, and A. Thanaboonsombut, "Nanocrystallization of  $\text{Bi}_{0.5}\text{Na}_{0.5}\text{TiO}_3$  piezoelectric material," *Science and Technology of Advanced Materials*, **6**[3-4] 278-81 (2005).
- [184] J. Bubesh Babu, M. He, D. F. Zhang, X. L. Chen, and R. Dhanasekaran, "Enhancement of ferroelectric properties of  $\text{Na}_{1/2}\text{Bi}_{1/2}\text{TiO}_3\text{-BaTiO}_3$  single crystals by Ce dopings," *Applied Physics Letters*, **90**[10] 102901-3 (2007).
- [185] X. Yi, H. Chen, W. Cao, M. Zhao, D. Yang, G. Ma, C. Yang, and J. Han, "Flux growth and characterization of lead-free piezoelectric single crystal  $[\text{Bi}_{0.5}(\text{Na}_{1-x}\text{K}_x)_{0.5}]\text{TiO}_3$ ," *Journal of Crystal Growth*, **281**[2-4] 364-9 (2005).
- [186] S. Teranishi, M. Suzuki, Y. Noguchi, M. Miyayama, C. Moriyoshi, Y. Kuroiwa, K. Tawa, and S. Mori, "Giant strain in lead-free  $(\text{Bi}_{0.5}\text{Na}_{0.5})\text{TiO}_3$ -based single crystals," *Applied Physics Letters*, **92**[18] 182905-3 (2008).
- [187] M. Izumi, K. Yamamoto, M. Suzuki, Y. Noguchi, and M. Miyayama, "Large electric-field-induced strain in  $\text{Bi}_{0.5}\text{Na}_{0.5}\text{TiO}_3\text{-Bi}_{0.5}\text{K}_{0.5}\text{TiO}_3$  solid solution single crystals," *Applied Physics Letters*, **93**[24] 242903 (2008).
- [188] S. Ehara, K. Muramatsu, M. Shimazu, J. Tanaka, M. Tsukioka, Y. Mori, T. Hattori, and H. Tamura, "Dielectric-properties of  $\text{Bi}_4\text{Ti}_3\text{O}_{12}$  below the Curie-temperature," *Japanese Journal of Applied Physics*, **20**[5] 877-81 (1981).
- [189] S. Y. Lee, C. W. Ahn, H. J. Lee, S. H. Kang, J. S. Kim, I. W. Kim, and K. S. Lee, "Dielectric and ferroelectric properties of La, Nd and V substituted  $\text{Bi}_4\text{Ti}_3\text{O}_{12}$  ceramics," *Journal of the Korean Physical Society*, **46**[1] 337-40 (2005).

## 2.2.12 Tables of Properties of BNT-Based Materials

### 2.2.12.1 BNT (Pure)

Tab 1: Properties of  $\text{Bi}_{1/2}\text{Na}_{1/2}\text{TiO}_3$  (Unmodified)

Piezoelectric coefficients ( $d_{33}$ [pC/N])			
	Value	Chemical Composition	Reference
	93.4	BNT+Bi <sup>4</sup>	[1]
	97.5	BNT (HP <sup>5</sup> : 200kg/cm <sup>2</sup> )	
	47-58	BNT	[2]
	70	BNT	[3]

Piezoelectric Voltage Coefficient ( $g_{33}$ [mV*m/N])			
	Value	Chemical Composition	Reference
	22-27	BNT	[2]

Calcination Temperatures ([°C]) / Sintering Times ([h, min])			
	Value	Chemical Composition	Reference
	800 for 2 h	BNT+Bi/ BNT (HP <sup>5</sup> : 200kg/cm <sup>2</sup> )	[1]
	900 for 4 h	BNT	[4-6]
	800-900 for 2 h – 5 h	BNT	[2]

Sintering Temperatures ([°C]) / Sintering Times ([h, min])			
	Value	Chemical Composition	Reference
	1050-1225 for 5 min-100 h	BNT+Bi <sup>4</sup>	[1]
	1100/30 min	BNT (HP <sup>5</sup> : 200kg/cm <sup>2</sup> )	[1]
	1120 for 1 h	BNT	[4-6]
	1120-1140 °C for 0.5-2 h	BNT	[7]
	1050-1200 for 1 h – 4 h	BNT	[2]

<sup>4</sup> It is assumed that the purpose of excess bismuth oxide is solely to replace bismuth oxide which evaporated during sintering.

<sup>5</sup> Material was hot-pressed, not conventionally sintered.

Phase transition temperatures ( $T_{O-T}$ <sup>6</sup> / $T_d$ <sup>7</sup> / $T_c$ [°C])			
	Value	Chemical Composition	Reference
	320 ( $T_c$ )	BNT	[7-9]
	200 ( $T_d$ )	BNT	[7,8]
	168 ( $T_d$ )	BNT	[10]
	200-230 (start modulated phase) 300-320 (end of modulated phase)	BNT	[4]
	520 ( $T_{T-C}$ )	BNT	[8]
	337 ( $T_c$ )	BNT+Bi <sup>4</sup>	[1]
	314 ( $T_c$ )	BNT	[11]
	360 ( $T_c$ )	BNT	[10]
	200 ( $T_{R-(R+T)}$ ) <sup>8</sup> 340 ( $T_{(R+T)-T}$ ) <sup>8</sup> 540 ( $T_{T-C}$ ) <sup>8</sup>	BNT	[12,13]
	-268 ( $T_{?-R}$ ) <sup>8</sup> 255 ( $T_{R-R+T}$ ) <sup>8</sup> 400 ( $T_{((R+T)-T)}$ ) <sup>8</sup> 500 ( $T_{T-(T+C)}$ ) <sup>8</sup> 540 ( $T_{(C+T)-C}$ ) <sup>8</sup>	BNT	[14]
	220 ( $T_d$ ) 320 ( $T_c$ )	BNT	[15]

Relative Dielectric Constant ( $\epsilon$ [no units])			
	Value	Chemical Composition	Reference
	~780 ( $\epsilon_{33}$ )	BNT	[15]
	408	BNT	[10]
	470-650	BNT (magn. sput.)	[16]
	240-245	BNT	[2]
	475 ( $\epsilon_{33}$ )	BNT	[17]

Degree of diffuseness $\gamma$ ([no units])			
	Value	Chemical Composition	Reference
	1.55	BNT	[10]

<sup>6</sup>  $T_{O-T}$ : refers to the phase transition between orthorhombic and tetragonal in alkali niobate-based systems.

<sup>7</sup>  $T_d$ : refers to the phase transition between room temperature ferroelectric phase and a high temperature phase in BNT-based materials, which is commonly regarded as antiferroelectric or non-polar.

<sup>8</sup>  $T_{R-(R+T)}$ : refers to the transition temperature between phase A and mixed phase A+B where A and B can be R(rhombohedral), T(tetragonal) and C(Cubic).



Coercive Field ( $E_c$ [kV/mm])			
	Value	Chemical Composition	Reference
	1.4 (T=116 °C)	BNT	[7]
	5.69	BNT	[10]
	6.11	BNT	[17]
	7.3	BNT	[2]
	2	BNT (sol-gel)	[18]
	3.79	BNT (magn. sput.)	[16]

Lattice Constants (a, c [nm])			
	Value	Chemical Composition	Reference
	38.8 (cubic)	BNT	[7]
	38.995 (rhomb)	BNT	[2]

Resistivity ( $\Omega$ m)			
	Value	Chemical Composition	Reference
	$10^{12}$	BNT+Bi <sup>4</sup>	[1]

Loss Tangent ( $\tan\delta$ [%])			
	Value	Chemical Composition	Reference
	2.65	BNT	[10]
	4	BNT	[17]

Electromechanical coupling factor ( $k_{33}$ [no units])			
	Value	Chemical Composition	Reference
	0.43-0.47	BNT+Bi <sup>4</sup>	[1]
	0.48	BNT (HP <sup>5</sup> : 200kg/cm <sup>2</sup> )	

Electromechanical coupling factor ( $k_p$ [no units])			
	Value	Chemical Composition	Reference
	0.159	BNT	[10]
	0.11-0.12	BNT	[2]
	0.12	BNT	[3]

Electromechanical coupling factor ( $k_t$ [no units])			
	Value	Chemical Composition	Reference
	0.43-0.47	BNT	[2]

Relative Density ([no units])			
	Value	Chemical Composition	Reference
	0.87-0.98	BNT+Bi <sup>4</sup>	[1]
	0.99	BNT (HP <sup>5</sup> : 200kg/cm <sup>2</sup> )	[1]
	0.925	BNT	[15]
	0.94-0.95	BNT	[2]

Remanent Polarisation (P <sub>R</sub> [μC/cm <sup>2</sup> ])			
	Value	Chemical Composition	Reference
	8.0 (T=116 °C)	BNT	[7]
	22 (T=190 °C, estimate)	BNT	[19]
	37	BNT	[10]
	8.3	BNT (sol-gel)	[18]
	11.9	BNT (magn. sput.)	[16]
	29.0	BNT	[17]

Relative Density ([no units])			
	Value	Chemical Composition	Reference
	0.87-98 (1100 °C – 1225 °C)	BNT+Bi <sup>4</sup>	[1]
	0.99	BNT (HP <sup>5</sup> : 200kg/cm <sup>2</sup> )	[1]

Mechanical Quality Factor (Q <sub>m</sub> [no units])			
	Value	Chemical Composition	Reference
	85	BNT+Bi <sup>4</sup>	[1]
	80	BNT (HP <sup>5</sup> : 200kg/cm <sup>2</sup> )	[1]
	140	BNT	[17]

Elastic Constant (s <sub>33</sub> <sup>E</sup> [pm <sup>2</sup> /N])			
	Value	Chemical Composition	Reference
	10.5	BNT+Bi <sup>4</sup>	[1]
	10	BNT (HP <sup>5</sup> : 200kg/cm <sup>2</sup> )	[1]

**2.2.12.2 BKT (Pure)****Tab 2: Properties of  $\text{Bi}_{1/2}\text{K}_{1/2}\text{TiO}_3$  (Unmodified)**

Piezoelectric coefficients ( $d_{33}$ [pC/N])			
	Value	Chemical Composition	Reference
	69.8	BKT (HP)	[20]
	135 ( $d_{33}^*$ )	BKT (HP)	[20]

Piezoelectric coefficients ( $d_{31}$ [pC/N])			
	Value	Chemical Composition	Reference
	26	BKT	[21]

c/a-Ratio			
	Value	Chemical Composition	Reference
	1.016	BKT	[20]
	1.020	BKT	[3]
	1.02	BKT	[22]

Loss Tangent ( $\tan\delta$ [%])			
	Value	Chemical Composition	Reference
	49.0	BKT	[23]
	4.3-6.4	BKT (sol-gel)	[23]
	6.8-7.1	BKT (HP)	[20]

Coercive Field ( $E_c$ [kV/mm])			
	Value	Chemical Composition	Reference
	4.72-5.25	BKT (HP)	[20]
	2.07	BKT (sol-gel)	[23]

Calcination Temperatures ( $^{\circ}\text{C}$ )			
	Value	Chemical Composition	Reference
	1060 for 0.5-2 h	BKT	[7]
	1050 for 4 h	BKT	[9]

Sintering Temperatures ( $^{\circ}\text{C}$ )			
	Value	Chemical Composition	Reference
	1000 for 4 h and 100 h	BKT	[9]

Relative Density ([no units])			
	Value	Chemical Composition	Reference
	0.93	BKT	[20]
	0.97	BKT (HP)	[20]

Electromechanical coupling factor ( $k_p$ [no units])			
	Value	Chemical Composition	Reference
	0.152	BKT	[23]
	0.091-0.177	BKT (sol-gel)	[23]
	0.15	BKT	[24]
	~0.19	BKT	[21]

Electromechanical coupling factor ( $k_{33}$ [no units])			
	Value	Chemical Composition	Reference
	0.28	BKT (HP)	[20]

Electromechanical coupling factor ( $k_{31}$ [no units])			
	Value	Chemical Composition	Reference
	~0.11	BKT	[21]

Electromechanical coupling factor ( $k_t$ [no units])			
	Value	Chemical Composition	Reference
	0.38	BKT	[21]

Dielectric Constants			
	Value	Chemical Composition	Reference
	625-682	BKT	[23]
	683	BKT (sol-gel)	[23]
	517-524	BKT (HP)	[20]
	~660	BKT	[24]
	~800	BKT	[21]

Phase transition temperatures( $T_{O-T}/T_{FE-AFE}^9/T_d/T_c$ [°C])			
	Value	Chemical Composition	Reference
	380( $T_C$ )	BKT	[7,9]
	340 ( $T_2$ )	BKT (HP)	[20]
	415-437 ( $T_C$ )	BKT (HP)	[20]
	315 ( $T_d$ )	BKT (HP)	[25]

Resistivity ( $[\Omega m]$ )			
	Value	Chemical Composition	Reference
	$10^{13}$	BKT (HP)	[20]

<sup>9</sup>  $T_{O-T}$ : refers to the phase transition between orthorhombic and tetragonal in alkali niobate-based systems.

$T_{FE-AFE}$ : refers to the phase transition between room temperature ferroelectric phase and a high temperature phase in BNT-based materials, which is commonly regarded as antiferroelectric.

<b>Remanent Polarisation(<math>P_R</math>[])</b>			
	<b>Value</b>	<b>Chemical Composition</b>	<b>Reference</b>
	14.2-22.2	BKT (HP)	[20]
	5.4	BKT (sol-gel)	[23]

<b>Unipolar strain (<math>S_{max}</math>[%])</b>			
	<b>Value</b>	<b>Chemical Composition</b>	<b>Reference</b>
	0.12 (8 kV)	BKT (HP)	[20]
	0.13 (8 kV)	BKT (HP+Bi)	[26]

<b>Mechanical Quality Factor (<math>Q_m</math>[no units])</b>			
	<b>Value</b>	<b>Chemical Composition</b>	<b>Reference</b>
	100	BKT	[21]

### 2.2.12.3 BNT (Doped)

**Tab 3: Properties of  $\text{Bi}_{1/2}\text{Na}_{1/2}\text{TiO}_3$  (Modified)**

Curie Temperature ( $T_C$ [°C])			
	Value	Chemical Composition	Reference
	268	BNT+Sr+Pb	[11,27]
	268	BNT+Pb+Ca	
	330	BNT+Ca	

Depolarisation Temperature ( $T_d$ [°C])			
	Value	Chemical Composition	Reference
	Non reported		

Piezoelectric Constant ( $d_{33}$ [pm/V])			
	Value	Chemical Composition	Reference
	82.2	BNT+Sr+Pb	[11,27]
	71.6	BNT+Pb+Ca	
	50.0	BNT+Ca	

Planar Coupling Factor ( $k_p$ [%])			
	Value	Chemical Composition	Reference
	20.3	BNT+Sr+Pb	[11,27]
	17.0	BNT+Pb+Ca	
	13.8	BNT+Ca	

Coupling Factor ( $k_t$ [%])			
	Value	Chemical Composition	Reference
	44.9	BNT+Sr+Pb	[11,27]
	58.5	BNT+Pb+Ca	
	51.3	BNT+Ca	

Coupling Factor ( $k_{33}$ [%])			
	Value	Chemical Composition	Reference
	50.6	BNT+Sr+Pb	[11,27]
	47.6	BNT+Pb+Ca	
	37.1	BNT+Ca	

**2.2.12.4 BNT-BT (Pure)****Tab 4: Properties of  $94(\text{Bi}_{1/2}\text{Na}_{1/2}\text{TiO}_3)\text{-}6(\text{BaTiO}_3)$** 

Calcination Temperatures ( $^{\circ}\text{C}$ ) / Sintering Times ([h, min])			
	Value	Chemical Composition	Reference
	800 for 1 h	BNT-BT	[28]
	800 for 3 h	BNT-BT	[29]
	850 for 1 h	BNT-BT	[15]
	850 for 2 h	BNT-BT	[10]

Sintering Temperatures ( $^{\circ}\text{C}$ ) / Sintering Times ([h, min])			
	Value	Chemical Composition	Reference
	1200 for 2 h	BNT-BT	[28]
	1150 for 2 h	BNT-BT	[29]
	1180 for 2 h	BNT-BT	[15]
	1200 for 2 h	BNT-BT	[10]

Phase transition temperatures( $T_{\text{O-T}}^{10}/T_{\text{d}}^{11}/T_{\text{c}}[^{\circ}\text{C}]$ )			
	Value	Chemical Composition	Reference
	288 ( $T_{\text{c}}$ )	BNT-BT	[28]
	$\sim 120$ ( $T_{\text{d}}$ , read of graph)	BNT-BT	[28]
	100	BNT-BT	[30]
	$130^{12}$	BNT-BT	[29]
	80-105 ( $T_{\text{d}}$ )	BNT-BT	[10]
	288 ( $T_{\text{c}}$ )	BNT-BT	[10]

Dielectric Constants ( $\epsilon$ [no units])			
	Value	Chemical Composition	Reference
	1580 ( $\epsilon_{33}$ )	BNT-BT	[28]
	$\sim 850$	BNT-BT	[28]
	601	BNT-BT	[30]
	$\sim 1650$ ( $\epsilon_{33}$ )	BNT-BT	[15]
	826	BNT-BT	[10]
	704	BNT-BT (sol-gel)	[31]

Coercive Field ( $E_{\text{c}}$ [kV/mm])			
	Value	Chemical Composition	Reference
	$2^{13}$	BNT-BT	[29]
	3.41	BNT-BT	[10]

<sup>10</sup>  $T_{\text{O-T}}$ : refers to the phase transition between orthorhombic and tetragonal in alkali niobate-based systems.

<sup>11</sup>  $T_{\text{d}}$ : refers to the phase transition between room temperature ferroelectric phase and a high temperature phase in BNT-based materials, which is commonly regarded as antiferroelectric or non-polar.

<sup>12</sup> Results questionable

<sup>13</sup> Results questionable

Piezoelectric coefficients ( $d_{33}$ [pC/N])			
	Value	Chemical Composition	Reference
	125	BNT-BT	[28]
	155	BNT-BT	[10]
	112	BNT-BT	[30]
	132	BNT-BT (sol-gel)	[31]

Degree of diffuseness ( $\gamma$ [no units])			
	Value	Chemical Composition	Reference
	2.02	BNT-BT	[10]

Electromechanical coupling factor ( $k_{33}$ [%])			
	Value	Chemical Composition	Reference
	55.0	BNT-BT	[28]

Electromechanical coupling factor ( $k_p$ [%])			
	Value	Chemical Composition	Reference
	36.7	BNT-BT	[10]
	25	BNT-BT (sol-gel)	[31]

Relative Density ([no units])			
	Value	Chemical Composition	Reference
	0.939	BNT	[15]

Remanent Polarisation( $P_R$ [ $\mu C/cm^2$ ])			
	Value	Chemical Composition	Reference
	20	BNT-BT	[28]
	$2^{13}$		[29]
	38.8	BNT-BT	[10]

Elastic Constant ( $s_{33}^E$ [ $pm^2/N$ ])			
	Value	Chemical Composition	Reference
	10	BNT-BT	[28]

Loss Tangent ( $\tan\delta$ [%])			
	Value	Chemical Composition	Reference
	1.3	BNT-BT	[28]
	1.79	BNT-BT	[30]
	4	BNT-BT	[15]
	2.5	BNT-BT	[10]
	1.9	BNT-BT (sol-gel)	[31]



**2.2.12.5 BNT-BT (Doped)****Tab 5: Properties of Doped BNT-BT**

<b>Piezoelectric Constant <math>d_{33}</math></b>			
	<b>Value</b>	<b>Chemical Composition</b>	<b>Reference</b>
	140	BNT-BT (-BiNa)	[30]
	125	BNT-BT (+BiNa)	[30]
	149	BNT-BT+Nb	[30]
	108	BNT-BT+Co	[30]

<b>Relative Dielectric Constant (<math>\epsilon_{33}</math>[no units])</b>			
	<b>Value</b>	<b>Chemical Composition</b>	<b>Reference</b>
	870	BNT-BT (-BiNa)	[30]
	740	BNT-BT (+BiNa)	[30]
	1230	BNT-BT+Nb	[30]
	450	BNT-BT+Co	[30]

<b>Loss Tangent (<math>\tan\delta</math>[%])</b>			
	<b>Value</b>	<b>Chemical Composition</b>	<b>Reference</b>
	2.81	BNT-BT (-BiNa)	[30]
	2.12	BNT-BT (+BiNa)	[30]
	3.9	BNT-BT+Nb	[30]
	1.5	BNT-BT+Co	[30]

<b>Depolarisation Temperature (<math>T_d</math>) [°C]</b>			
	<b>Value</b>	<b>Chemical Composition</b>	<b>Reference</b>
	125	BNT-BT (-BiNa)	[30]
	135	BNT-BT (+BiNa)	[30]
	70	BNT-BT+Nb	[30]
	155	BNT-BT+Co	[30]

<b>Curie Temperature (<math>T_C</math>) [°C]</b>			
	<b>Value</b>	<b>Chemical Composition</b>	<b>Reference</b>
	210	BNT-BT (-BiNa)	[30]
	215	BNT-BT (+BiNa)	[30]
	250	BNT-BT+Nb	[30]
	245	BNT-BT+Co	[30]

### 2.2.12.6 BNT-BKT (Pure)

**Tab 6: Properties of Pure BNT-BKT**

Calcination Temperatures (°C) / Sintering Times ([h, min])			
	Value	Chemical Composition	Reference
	880-950 for 20 h	BNT-BKT	[3]
	800 for 1 h	BNT-BKT	[21]
	600 for 5 h + 850 for 4 h	BNT-BKT	[25]
	850 for 4 h	BNT-BKT	[22]
	850 for 3 h	BNT-22BKT+Bi	[32]

Sintering Temperatures (°C) / Sintering Times ([h, min])			
	Value	Chemical Composition	Reference
	1070-1190 for 30 min	BNT-BKT	[3]
	1100-1200 for 2 h	BNT-BKT	[21]
	1100-1200 for 2 h	BNT-BKT	[25]
	1150 for 3 h	BNT-22BKT+Bi	[32]

Phase transition temperatures ( $T_{O-T}^{14}/T_d^{15}/T_c$ [°C])			
	Value	Chemical Composition	Reference
	174 ( $T_d$ )	BNT-BKT	[25]
	130 ( $T_d$ )	BNT-18BKT	[33]
	292 ( $T_c$ )	BNT-BKT	[34]
	289 ( $T_c$ )	BNT-BKT+Bi	[34]
	330 ( $T_c$ )	BNT-23BKT+Bi	[34]

MPB Position [BNT-xBKT]			
	Value	Chemical Composition	Reference
	0.16-0.2	BNT-BKT	[21]
	0.1-0.3	BNT-BKT	[3]
	0.45, 0.7	BNT-BKT	[35]
	0.18-0.2	BNT-BKT	[25]
	0.16	BNT-BKT	[22]
	0.14-0.2	BNT-BKT	[36]
	0.2	BNT-BKT	[34]
	0.23	BNT-BKT+Bi	[34]

Coercive Field ( $E_c$ [kV/mm])			
	Value	Chemical Composition	Reference
	~3.5	BNT-BKT	[25]
	4.9	BNT-16BKT	[22]

<sup>14</sup>  $T_{O-T}$ : refers to the phase transition between orthorhombic and tetragonal in alkali niobate-based systems.

<sup>15</sup>  $T_d$ : refers to the phase transition between room temperature ferroelectric phase and a high temperature phase in BNT-based materials, which is commonly regarded as antiferroelectric or non-polar.

Piezoelectric coefficients ( $d_{33}$ [pC/N])			
	Value	Chemical Composition	Reference
	240* <sup>16</sup>	BNT-26BKT	[25]
	291*	BNT-22BKT	[25]
	~290	BNT-22BKT	[33]
	157	BNT-BKT	[25]
	112	BNT-16BKT	[22]
	150	BNT-50BKT	[22]
	159	BNT-BKT	[36]
	190	BNT-BKT+Bi	[32]
	192	BNT-22BKT+Bi	[32]
	145	BNT-BKT	[34]
	190	BNT-BKT+Bi	[34]
	207	BNT-23BKT+Bi	[34]

Remanent Polarisation( $P_R$ [ $\mu\text{C}/\text{cm}^2$ ])			
	Value	Chemical Composition	Reference
	19.5	BNT-BKT	[21]
	38.4	BNT-BKT	[25]
	66.8	BNT-16BKT	[22]
	19.5	BNT-22BKT+Bi	[32]
	10.3	BNT-BKT	[34]
	13	BNT-BKT+Bi	[34]
	21	BNT-23BKT+Bi	[34]

Dielectric Constants ( $\epsilon$ [no units])			
	Value	Chemical Composition	Reference
	1030 ( $\epsilon_{33}$ )	BNT-BKT	[21]
	945 ( $\epsilon_{33}$ )	BNT-22BKT+Bi	[32]
	635 ( $\epsilon_r$ )	BNT-16BKT	[21]
	630 ( $\epsilon_r$ )	BNT-16BKT	[22]
	891 ( $\epsilon_{33}$ )	BNT-BKT	[34]
	945 ( $\epsilon_{33}$ )	BNT-BKT+Bi	[34]
	1261 ( $\epsilon_{33}$ )	BNT-23BKT+Bi	[34]

Degree of diffuseness ( $\gamma$ [no units])			
	Value	Chemical Composition	Reference
	1.97	BNT-12BKT	[37]
	1.88	BNT-16BKT	[37]
	1.90	BNT-18BKT	[37]
	1.84	BNT-20BKT	[37]

<sup>16</sup> \*: large-signal  $d_{33}$  value

Electromechanical coupling factor ( $k_{33}$ [no units])			
	Value	Chemical Composition	Reference
	0.56	BNT-BKT	[33]

Electromechanical coupling factor ( $k_p$ [no units])			
	Value	Chemical Composition	Reference
	0.314	BNT-16BKT	[21]
	0.270	BNT-BKT	[21]
	0.25	BNT-16BKT	[22]
	0.30	BNT-BKT	[36]
	0.35	BNT-22BKT+Bi	[32]
	0.27	BNT-BKT	[34]
	0.35	BNT-BKT+Bi	[34]
	0.30	BNT-23BKT+Bi	[34]

Electromechanical coupling factor ( $k_t$ [no units])			
	Value	Chemical Composition	Reference
	0.423	BNT-16BKT	[21]
	0.418	BNT-BKT	[21]

Relative Density ([no units])			
	Value	Chemical Composition	Reference
	0.90-0.95	BNT-BKT	[3]
	0.96	BNT-BKT	[25]
	~0.98	BNT-22BKT+Bi	[32]

Mechanical Quality Factor ( $Q_m$ [no units])			
	Value	Chemical Composition	Reference
	195	BNT-16BKT	[21]
	109	BNT-BKT	[21]
	171	BNT-16BKT	[22]

Loss Tangent ( $\tan\delta$ [%])			
	Value	Chemical Composition	Reference
	2.77	BNT-16BKT	[22]
	1.865	BNT-22BKT+Bi	[32]
	4.1	BNT-BKT	[34]
	4.0	BNT-BKT+Bi	[34]
	5.1	BNT-23BKT+Bi	[34]

**2.2.12.7 BNT-BKT-BT****Tab 7: Properties of BNT-BKT-BT**

<b>Piezoelectric coefficients (<math>d_{33}</math>[pC/N])</b>			
	<b>Value</b>	<b>Chemical Composition</b>	<b>Reference</b>
	191	BNT-12BKT-2.8BT	[38]
	148	BNT-xBKT-5BT	[39]
	134	BNT-25(4BKT-BT)	[40]
	191	BNT-14.8(4BKT-BT)	[40]
	135	BNT-22(2BKT-BT)	[40]
	149	BNT-3(4BKT-BT)	[17]

<b>Remanent Polarisation (<math>P_R</math>[<math>\mu\text{C}/\text{cm}^2</math>])</b>			
	<b>Value</b>	<b>Chemical Composition</b>	<b>Reference</b>
	35.9	BNT-xBKT-5BT	[39]
	31.4	BNT-3(4BKT-BT)	[17]

<b>Phase transition temperatures (<math>T_{O-T}</math><sup>17</sup>/<math>T_d</math><sup>18</sup>/<math>T_c</math>[<math>^{\circ}\text{C}</math>])</b>			
	<b>Value</b>	<b>Chemical Composition</b>	<b>Reference</b>
	301 ( $T_c$ )	BNT-12BKT-2.8BT	[38]
	135-200 ( $T_d$ )	BNT-xBKT-5BT	[39]
	295 ( $T_c$ )	BNT-25(4BKT-BT)	[40]
	214 ( $T_d$ )	BNT-25(4BKT-BT)	[40]
	301 ( $T_c$ )	BNT-14.8(4BKT-BT)	[40]
	115 ( $T_d$ )	BNT-14.8(4BKT-BT)	[40]
	197	BNT-22(2BKT-BT)	[40]
	290	BNT-22(2BKT-BT)	[40]

<b>Loss Tangent (<math>\tan\delta</math>[%])</b>			
	<b>Value</b>	<b>Chemical Composition</b>	<b>Reference</b>
	2	BNT-xBKT-5BT	[39]
	4.2	BNT-3(4BKT-BT)	[17]

<sup>17</sup>  $T_{O-T}$ : refers to the phase transition between orthorhombic and tetragonal in alkali niobate-based systems.

<sup>18</sup>  $T_d$ : refers to the phase transition between room temperature ferroelectric phase and a high temperature phase in BNT-based materials, which is commonly regarded as antiferroelectric or non-polar.

Mechanical Quality Factor ( $Q_m$ [no units])			
	Value	Chemical Composition	Reference
	84	BNT-12BKT-2.8BT	[38]

Electromechanical coupling factor ( $k_p$ [no units])			
	Value	Chemical Composition	Reference
	0.33	BNT-12BKT-2.8BT	[38]
	0.34	BNT-xBKT-5BT	[39]
	0.28	BNT-3(4BKT-BT)	[17]

Dielectric Constants			
	Value	Chemical Composition	Reference
	1141	BNT-12BKT-2.8BT	[38]
	700	BNT-xBKT-5BT	[39]
	843	BNT-25(4BKT-BT)	[40]
	1141	BNT-14.8(4BKT-BT)	[40]
	850	BNT-22(2BKT-BT)	[40]
	1150	BNT-3(4BKT-BT)	[17]

### 2.2.12.8 References

- [1] H. Nagata, T. Shinya, Y. Hiruma, and T. Takenaka, "Developments in Dielectric Materials and Electronic Devices," pp. 213-21. In *Ceramic Transactions*, **Vol. 167**. Edited by K. M. Nair. American Ceramic Society, Indianapolis, Indiana, USA, 2004.
- [2] A. Herabut and A. Safari, "Processing and electromechanical properties of  $(\text{Bi}_{0.5}\text{Na}_{0.5})_{(1-1.5x)}\text{La}_x\text{TiO}_3$  ceramics," *Journal of the American Ceramic Society*, **80**[11] 2954-8 (1997).
- [3] O. Elkechai, M. Manier, and J. P. Mercurio, " $\text{Na}_{0.5}\text{Bi}_{0.5}\text{TiO}_3$ - $\text{K}_{0.5}\text{Bi}_{0.5}\text{TiO}_3$  (NBT-KBT) system: A structural and electrical study," *Physica Status Solidi A: Applied Research*, **157**[2] 499-506 (1996).
- [4] V. Dorcet, G. Trolliard, and P. Boullay, "Reinvestigation of phase transitions in  $\text{Na}_{0.5}\text{Bi}_{0.5}\text{TiO}_3$  by TEM. Part I: First order rhombohedral to orthorhombic phase transition," *Chemistry of Materials*, **20**[15] 5061-73 (2008).
- [5] V. Dorcet and G. Trolliard, "A transmission electron microscopy study of the A-site disordered perovskite  $\text{Na}_{0.5}\text{Bi}_{0.5}\text{TiO}_3$ ," *Acta Materialia*, **56**[8] 1753-61 (2008).
- [6] G. Trolliard and V. Dorcet, "Reinvestigation of phase transitions in  $\text{Na}_{0.5}\text{Bi}_{0.5}\text{TiO}_3$  by TEM. Part II: Second order orthorhombic to tetragonal phase transition," *Chemistry of Materials*, **20**[15] 5074-82 (2008).
- [7] G. A. Smolenskii, V. A. Isupov, A. I. Agranovskaya, and N. N. Krainik, "New Ferroelectrics of Complex Composition. IV," *Soviet Physics-Solid State*, **2**[11] 2651-4 (1961).
- [8] I. P. Pronin, P. P. Syrnikov, V. A. Isupov, V. M. Egorov, and N. V. Zaitseva, "Peculiarities of Phase-Transitions in Sodium-Bismuth Titanate," *Ferroelectrics*, **25**[1-4] 395-7 (1980).
- [9] C. F. Buhner, "Some Properties of Bismuth Perovskites," *Journal of Chemical Physics*, **36**[3] 798-803 (1962).
- [10] C. Xu, D. Lin, and K. W. Kwok, "Structure, electrical properties and depolarization temperature of  $(\text{Bi}_{0.5}\text{Na}_{0.5})\text{TiO}_3$ - $\text{BaTiO}_3$  lead-free piezoelectric ceramics," *Solid State Sciences*, **10**[7] 934-40 (2008).
- [11] T. Takenaka and K. Sakata, "Dielectric, Piezoelectric and Pyroelectric Properties of  $(\text{BiNa})_{1/2}\text{TiO}_3$ -Based Ceramics," *Ferroelectrics*, **95** 153-6 (1989).
- [12] K. Roleder, J. Suchanicz, and A. Kania, "Time-Dependence of Electric Permittivity in  $\text{Na}_{0.5}\text{Bi}_{0.5}\text{TiO}_3$  Single-Crystals," *Ferroelectrics*, **89** 1-5 (1989).
- [13] J. Suchanicz, "Investigations of the phase transitions in  $\text{Na}_{0.5}\text{Bi}_{0.5}\text{TiO}_3$ ," *Ferroelectrics*, **172**[1] 455-8 (1995).
- [14] G. O. Jones and P. A. Thomas, "Investigation of the structure and phase transitions in the novel A-site substituted distorted perovskite compound  $\text{Na}_{1/2}\text{Bi}_{1/2}\text{TiO}_3$ ," *Acta Crystallographica, Section B: Structural Science*, **58** 168-78 (2002).
- [15] Y. F. Qu, D. Shan, and J. J. Song, "Effect of A-site substitution on crystal component and dielectric properties in  $\text{Bi}_{0.5}\text{Na}_{0.5}\text{TiO}_3$  ceramics," *Materials Science & Engineering, B: Solid-State Materials for Advanced Technology*, **121**[1-2] 148-51 (2005).
- [16] Z. H. Zhou, J. M. Xue, W. Z. Li, J. Wang, H. Zhu, and J. M. Miao, "Ferroelectric and electrical behavior of  $(\text{Na}_{0.5}\text{Bi}_{0.5})\text{TiO}_3$  thin films," *Applied Physics Letters*, **85**[5] 804-6 (2004).
- [17] Y. Li, W. Chen, Q. Xu, J. Zhou, and X. Gu, "Piezoelectric and ferroelectric properties of  $\text{Na}_{0.5}\text{Bi}_{0.5}\text{TiO}_3$ - $\text{K}_{0.5}\text{Bi}_{0.5}\text{TiO}_3$ - $\text{BaTiO}_3$  piezoelectric ceramics," *Materials Letters*, **59**[11] 1361-4 (2005).
- [18] T. Yu, K. W. Kwok, and H. L. W. Chan, "Preparation and properties of sol-gel-derived  $\text{Bi}_{0.5}\text{Na}_{0.5}\text{TiO}_3$  lead-free piezoelectric thin film," *Thin Solid Films*, **515**[7-8] 3563-6 (2007).
- [19] J. Suchanicz, "Behaviour of  $\text{Na}_{0.5}\text{Bi}_{0.5}\text{TiO}_3$  ceramics in the ac electric field," *Ferroelectrics*, **209**[3-4] 561-8 (1998).
- [20] Y. Hiruma, R. Aoyagi, H. Nagata, and T. Takenaka, "Ferroelectric and piezoelectric properties of  $(\text{Bi}_{1/2}\text{K}_{1/2})\text{TiO}_3$  ceramics," *Japanese Journal of Applied Physics Part 1-Regular Papers Brief Communications & Review Papers*, **44**[7A] 5040-4 (2005).
- [21] A. Sasaki, T. Chiba, Y. Mamiya, and E. Otsuki, "Dielectric and piezoelectric properties of  $(\text{Bi}_{1/2}\text{Na}_{1/2})\text{TiO}_3$ - $(\text{Bi}_{0.5}\text{K}_{0.5})\text{TiO}_3$  systems," *Japanese Journal of Applied Physics Part 1-Regular Papers Short Notes & Review Papers*, **38**[9B] 5564-7 (1999).
- [22] S. C. Zhao, G. R. Li, A. L. Ding, T. B. Wang, and Q. R. Yin, "Ferroelectric and piezoelectric properties of  $(\text{Na}, \text{K})_{0.5}\text{Bi}_{0.5}\text{TiO}_3$  lead free ceramics," *Journal of Physics D: Applied Physics*, **39**[10] 2277-81 (2006).
- [23] T. Wada, A. Fukui, and Y. Matsuo, "Preparation of  $(\text{K}_{1/2}\text{Bi}_{1/2})\text{TiO}_3$  ceramics by polymerized complex method and their properties," *Japanese Journal of Applied Physics Part 1-Regular Papers Short Notes & Review Papers*, **41**[11B] 7025-8 (2002).
- [24] T. Wada, K. Toyoiike, Y. Imanaka, and Y. Matsuo, "Dielectric and piezoelectric properties of  $(\text{A}_{0.5}\text{Bi}_{0.5})\text{TiO}_3$ - $\text{ANbO}_3$  ( $\text{A} = \text{Na}, \text{K}$ ) systems," *Japanese Journal of Applied Physics Part 1-Regular Papers Short Notes & Review Papers*, **40**[9B] 5703-5 (2001).

- [25] K. Yoshii, Y. Hiruma, H. Nagata, and T. Takenaka, "Electrical properties and depolarization temperature of  $(\text{Bi}_{1/2}\text{Na}_{1/2})\text{TiO}_3$ - $(\text{Bi}_{1/2}\text{K}_{1/2})\text{TiO}_3$  lead-free piezoelectric ceramics," *Japanese Journal of Applied Physics Part 1-Regular Papers Brief Communications & Review Papers*, **45**[5B] 4493-6 (2006).
- [26] Y. Hiruma, H. Nagata, and T. Takenaka, "Grain-size effect on electrical properties of  $(\text{Bi}_{1/2}\text{K}_{1/2})\text{TiO}_3$  ceramics," *Japanese Journal of Applied Physics Part 1-Regular Papers Brief Communications & Review Papers*, **46**[3A] 1081-4 (2007).
- [27] T. Takenaka, K. Sakata, and K. Toda, "Piezoelectric Properties of  $(\text{Bi}_{1/2}\text{Na}_{1/2})\text{TiO}_3$ -Based Ceramics," *Ferroelectrics*, **106** 375-80 (1990).
- [28] T. Takenaka, K. Maruyama, and K. Sakata, " $(\text{Bi}_{1/2}\text{Na}_{1/2})\text{TiO}_3$ - $\text{BaTiO}_3$  system for lead-free piezoelectric ceramics," *Japanese Journal of Applied Physics Part 1-Regular Papers Short Notes & Review Papers*, **30**[9B] 2236-9 (1991).
- [29] T. Oh and M. H. Kim, "Phase relation and dielectric properties in  $(\text{Bi}_{1/2}\text{Na}_{1/2})_{1-x}\text{Ba}_x\text{TiO}_3$  lead-free ceramics," *Materials Science & Engineering, B: Solid-State Materials for Advanced Technology*, **132**[3] 239-46 (2006).
- [30] B. J. Chu, D. R. Chen, G. R. Li, and Q. R. Yin, "Electrical properties of  $\text{Na}_{1/2}\text{Bi}_{1/2}\text{TiO}_3$ - $\text{BaTiO}_3$  ceramics," *Journal of the European Ceramic Society*, **22**[13] 2115-21 (2002).
- [31] D. Zhou, H. Li, S. Gong, Y. Hu, and K. Han, "Sodium Bismuth Titanate-Based Lead-Free Piezoceramics Prepared by Aqueous Gelcasting," *Journal of the American Ceramic Society*, **91**[9] 2792-6 (2008).
- [32] Y.-R. Zhang, J.-F. Li, and B.-P. Zhang, "Enhancing Electrical Properties in NBT-KBT Lead-Free Piezoelectric Ceramics by Optimizing Sintering Temperature," *Journal of the American Ceramic Society*, **91**[8] 2716-9 (2008).
- [33] Y. Hiruma, H. Nagata, and T. Takenaka, "Phase transition temperatures and piezoelectric properties of  $(\text{Bi}_{1/2}\text{Na}_{1/2})\text{TiO}_3$ - $(\text{Bi}_{1/2}\text{K}_{1/2})\text{TiO}_3$ - $\text{BaTiO}_3$  lead-free piezoelectric ceramics," *Japanese Journal of Applied Physics Part 1-Regular Papers Brief Communications & Review Papers*, **45**[9B] 7409-12 (2006).
- [34] Y. R. Zhang, J. F. Li, B. P. Zhang, and C. E. Peng, "Piezoelectric and ferroelectric properties of Bi-compensated  $(\text{Bi}_{1/2}\text{Na}_{1/2})\text{TiO}_3$ - $(\text{Bi}_{1/2}\text{K}_{1/2})\text{TiO}_3$  lead-free piezoelectric ceramics," *Journal of Applied Physics*, **103**[7] 074109 (2008).
- [35] G. O. Jones, J. Kreisel, and P. A. Thomas, "A structural study of the  $(\text{Na}_{1-x}\text{K}_x)_{0.5}\text{Bi}_{0.5}\text{TiO}_3$  perovskite series as a function of substitution (x) and temperature," *Powder Diffraction*, **17**[4] 301-19 (2002).
- [36] T. Oh, "Dielectric relaxor properties in the system of  $(\text{Na}_{1-x}\text{K}_x)_{1/2}\text{Bi}_{1/2}\text{TiO}_3$  ceramics," *Japanese Journal of Applied Physics Part 1-Regular Papers Brief Communications & Review Papers*, **45**[6A] 5138-43 (2006).
- [37] Z. Yang, B. Liu, L. Wei, and Y. Hou, "Structure and electrical properties of  $(1-x)\text{Bi}_{0.5}\text{Na}_{0.5}\text{TiO}_3$ - $x\text{Bi}_{0.5}\text{K}_{0.5}\text{TiO}_3$  ceramics near morphotropic phase boundary," *Materials Research Bulletin*, **43**[1] 81-9 (2008).
- [38] H. Nagata, M. Yoshida, Y. Makiuchi, and T. Takenaka, "Large piezoelectric constant and high Curie temperature of lead-free piezoelectric ceramic ternary system based on bismuth sodium titanate-bismuth potassium titanate-barium titanate near the morphotropic phase boundary," *Japanese Journal of Applied Physics Part 1-Regular Papers Short Notes & Review Papers*, **42**[12] 7401-3 (2003).
- [39] X. X. Wang, X. G. Tang, and H. L. W. Chan, "Electromechanical and ferroelectric properties of  $(\text{Bi}_{1/2}\text{Na}_{1/2})\text{TiO}_3$ - $(\text{Bi}_{1/2}\text{K}_{1/2})\text{TiO}_3$ - $\text{BaTiO}_3$  lead-free piezoelectric ceramics," *Applied Physics Letters*, **85**[1] 91-3 (2004).
- [40] Y. Makiuchi, R. Aoyagi, Y. Hiruma, H. Nagata, and T. Takenaka, " $(\text{Bi}_{1/2}\text{Na}_{1/2})\text{TiO}_3$ - $(\text{Bi}_{1/2}\text{K}_{1/2})\text{TiO}_3$ - $\text{BaTiO}_3$ -Based lead-free piezoelectric ceramics," *Japanese Journal of Applied Physics Part 1-Regular Papers Short Notes & Review Papers*, **44**[6B] 4350-3 (2005).



## 2.3. Potassium Sodium Niobates

### 2.3.1 Introduction

Potassium sodium niobate (KNN) is the second of the two most commonly investigated lead-free ferroelectric systems today, the other first one being bismuth sodium titanate-barium titanate (BNT-BT). KNN is the only known lead-free system with a perovskite structure, which has a higher Curie temperature than the commonly used lead zirconate titanate (PZT) and piezoelectric properties of the same order of magnitude. High chemical inertness and compatibility with human tissue allow for medical uses as well. Its high electromechanical coupling factor and low dielectric constant make it interesting for ultrasonic applications<sup>[1]</sup>. Following the work of Saito et al.<sup>[2,3]</sup>, the research effort into KNN-based materials in fact surpassed that of BNT-based materials in 2005 (Fig 1, p. 2).

A few drawbacks, however, still prevent wide scale industrial use today. KNN is made from volatile alkali metal compounds, which require carefully controlled manufacturing conditions and low reaction temperatures. Furthermore, KNN exhibits poor densification behaviour in pressureless sintering conditions. There is also a phase transition between two ferroelectric phases above room temperature. Heating above this transition temperature causes accelerated aging.

### 2.3.2 The Structure of KNN

Potassium sodium niobate (KNN) is a ferroelectric system with a complex perovskite structure. Complex in this case refers to the fact that the A-site is shared by more than one type of ion. KNN is a mixed system of orthorhombic ferroelectric potassium niobate (KN) displaying similar phase transitions (see Fig 14) to barium titanate but at higher temperatures<sup>[4,5]</sup> and orthorhombic sodium niobate (NN), which was originally reported as ferroelectric<sup>[6]</sup> but is in fact antiferroelectric<sup>[7]</sup>. KNN was first reported as ferroelectric by Shirane et al.<sup>[4]</sup>, though without identifying the enhanced properties at the 50/50 potassium to sodium ratio. Egerton et al.<sup>[8]</sup> reported the first piezoelectric data and identified enhanced ferroelectric properties at the 50 % potassium niobate composition.

$K_xNa_{1-x}NbO_3$  is a complex system with several thermally induced phase transitions and morphotropic phase boundaries (MPBs) summarised by Ahtee et al.<sup>[9,10]</sup> as displayed in Fig 12. At room temperature, MPBs lie at 17.5 %, 32.5 % and 47.5 % NN content. Notable is the almost composition independent phase transition temperature between ferroelectric phases at ~200 °C

and between ferroelectric and paraelectric phases at  $\sim 400$  °C. Only small substitutions of sodium for potassium in  $\text{NaNbO}_3$  cause a transition to ferroelectric (Region Q) from the pure antiferroelectric sodium niobate (Region P).

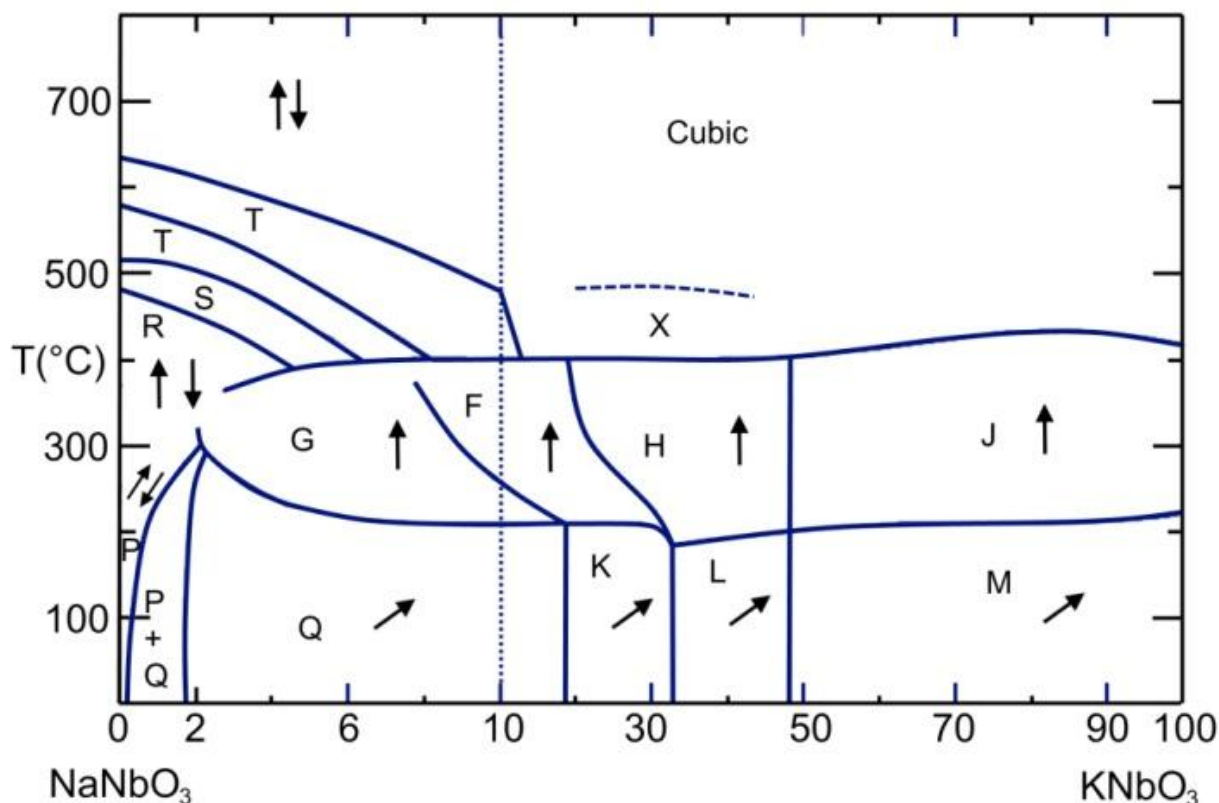


**Fig 12:** Phase diagram of  $\text{K}_x\text{Na}_{(1-x)}\text{NbO}_3$ . Regions labelled with Q, K, and L are monoclinic (or orthorhombic in most literature) ferroelectric, M, G is orthorhombic ferroelectric; F, H and J are tetragonal ferroelectric. Region P is orthorhombic antiferroelectric<sup>[9]</sup>.

### 2.3.3 First Reported Results

Egerton et al.<sup>[8]</sup> used a standard mixed oxide method for preparation of pure KNN. They calcined the powder at temperatures of 900 °C to 950 °C and sintered it at 1050 °C to 1325 °C. Achieved relative densities were between 94 % and 97 %.

**Tab 8:** Some Properties of Potassium Niobate (KN) and of Sodium Niobate (NN)

Property	KN	NN
Dielectric constant	$\sim 430$	$\sim 160$
Density	4.15-4.20g/cm <sup>3</sup>	4.38-4.40g/cm <sup>3</sup>
Phase transitions	220 °C, 420 °C	350 °C, 480 °C, 640 °C

**Some properties of the end members KN and NN. The morphotropic phase boundary (MPB) composition KNN is summarised in Tab 9 (pages 79ff.).**

The best piezoelectric properties were achieved using a sintering temperature of 1054 °C for the morphotropic phase boundary (MPB) 50/50 potassium sodium niobate composition. Tab 8 shows

some properties of the end members KN and NN. The morphotropic phase boundary (MPB) composition KNN is summarised in Tab 9 (pages 79ff.) due to its size.

## 2.3.4 Processing

### 2.3.4.1 Powder Processing

Due to the low melting point as well as agglomeration and solubility concerns of potassium oxide on the one hand and the difficult densification on the other, the mixed oxide route requires a much higher degree of optimization of the processing conditions than PZT or BNT-BT<sup>[11,12]</sup>. In conventional mixed oxide processing of KNN, desirable for industrial applications, four critical issues are currently known. They are volatility of alkali oxides<sup>[13,14]</sup>, compositional inhomogeneity for example when tantalum is introduced<sup>[15]</sup>, phase stability at high temperatures<sup>[16]</sup>, and most significantly poor densification<sup>[11]</sup>. The volatility can be addressed by introducing excess alkali metal oxides<sup>[17]</sup> and also through calcination and sintering in atmospheric powder<sup>[18]</sup> in sealed crucibles, where mass loss becomes negligible<sup>[16]</sup>. Carbonates<sup>[1,8,11,19-62]</sup> are the usual starting materials for the compounds containing alkali and alkali-earth metal cations since they are cheapest and available in relatively higher purity grades than the oxide counterparts; they completely decompose into the oxides and carbon dioxide during calcination. However, one of the major disadvantages is the hygroscopic nature<sup>[63]</sup> of the oxides and also of the corresponding carbonates<sup>[64]</sup>, which makes their storage difficult and hinders exact determination of molar ratios during mixing. In the meantime, due to similar size of the anion, elements that form carbonates can also form nitrates. The nitrates normally have lower solubilities in water and can therefore be used in conjunction with water during milling. They can be also used for chemical evaporation mixing<sup>[65]</sup>. The transition metallic elements and rare earths elements are usually present as oxides since most do not form stable carbonates. Conventional ball milling of KNN is typically done in ethanol<sup>[18,20,21,26,31,34,36,41,42,47,48,51,52,58,66-86]</sup> or acetone<sup>[1,12,19,26,35,39,56,87-90]</sup>. Ethanol is most commonly used since it combines a reasonable price with low solubility of ionic materials such as oxides, carbonates and nitrates. Higher-order alcohols can be used to increase the viscosity and therefore reduce wear of the containers and milling balls, which in turn reduces contamination. Isopropanol<sup>[50,61]</sup> is slightly less expensive and also does not contain denaturing<sup>19</sup> chemicals, whereas ethanol always contains 1 % unspecified denaturing chemical if sold in the EU. Isopropanol and acetone are, however, more toxic to the environment, specifically water organisms. Water is not suitable for alkali metal

---

<sup>19</sup> German translation: Vergällung

oxides and carbonates due to high solubility<sup>[12]</sup>. Methanol<sup>[12]</sup> is very toxic when it comes in contact with skin or when inhaled as fumes.

The KNN powders are sensitive to stoichiometry and slight deviations in stoichiometry lead to many non-perovskite secondary phases. These are frequently hygroscopic, which leads to quick disintegration of fired samples<sup>[63]</sup>. This can be prevented by dissolving the non-perovskite phases with 2 % potassium carbonate solution after calcination. The perovskite phase is insoluble in most solvents<sup>[91]</sup>.

Mechanically activated powders of NN do not form with grinding times of up to 30 days with a Fritsch Pulverisette 0 (Vibration mill) but only the carbonate decomposes<sup>[55]</sup>. A lowered calcination temperature of 600 °C compared to originally 750 °C to complete the reaction is possible, however.

Rojac et al.<sup>[92]</sup> reported the formation of NN via mechanical activation in a Retch PM 400 (planetary ball mill) with yttria-stabilised zirconia milling balls. Milling ball to powder weight ratio was 25:1. After five hours of milling partial conversion of the starting materials was seen. After milling for 20 hours complete conversion was reached but contamination with zirconia from the milling containers and balls is seen in the XRD pattern. Formation of KN and KNN via the same method did not occur.

Attrition milling was reported to be more effective in improving density of KNN than planetary milling. By the use of attrition milling, 98.5 % of the theoretical density was obtained compared to a maximum of 94 % for planetary milling<sup>[82]</sup>. Rubio-Marcos et al. also used attrition milling but since the KNN was modified with LiTaO<sub>3</sub> results are not directly comparable<sup>[84]</sup>.

After calcination, a leaching process, where the reacted material was washed with a potassium carbonate solution followed by a rinsing step with water, was able to improve the physical and electrical properties by removing unwanted secondary phases<sup>[8]</sup>. A calcination temperature of 600 °C for mechanically activated powder is amongst the lowest reported calcination temperatures for the KNN system<sup>[92]</sup>. Only hydrated potassium carbonate and niobium oxide allow an even lower temperature of 500 °C when mixed with 200 mol% urea (CO(NH<sub>2</sub>)<sub>2</sub>). For comparison standard calcination temperature commonly lies between 800 °C<sup>[1]</sup> and 900 °C<sup>[8]</sup>.

#### 2.3.4.2 Sintering

Conventional sintering is in general the preferred manufacturing route<sup>[4,8,93]</sup> due to its simplicity and its readiness for commercial mass production in industry. Especially when it comes to device-oriented applications such as multilayer actuators, conventional sintering technique is the

only option as hot pressing<sup>[37,38,64,94]</sup> and spark plasma sintering<sup>[34,95]</sup> damage or completely diffuse the electrodes of multilayer actuators.

KNN has a melting point of approximately 1120 °C, which limits the sintering temperature since abnormal grain growth and inhomogeneous melting, i.e. melting of potassium rich regions, occurs near the melting point<sup>[18]</sup>. Furthermore, the heating rate has a strong influence on the densification and planar coupling factor of KNN, which can be seen in Fig 13. Under their conditions, optimum properties including the highest reported theoretical density of conventionally sintered pure KNN at 97.6 % is achieved at a heating rate of five degrees per minute<sup>[11]</sup>. This is, however, a parameter that will have to be re-established for each new particle size and dopant choice. Commonly 94 % to 96 % of theoretical density is achieved in pure KNN<sup>[1,8,82]</sup>.

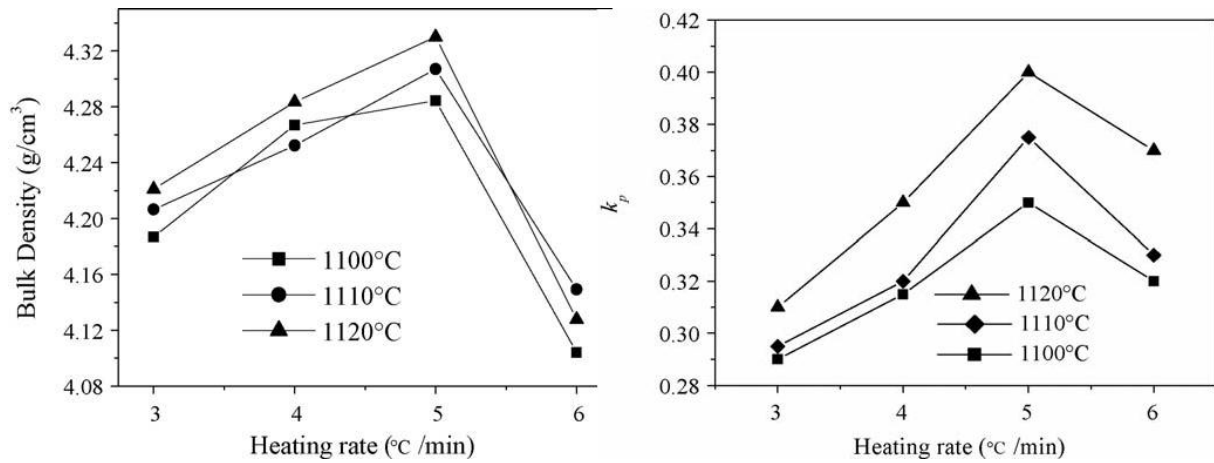


**Fig 13: Density and  $k_p$  of KNN ceramics as a function of heating rate and sintering temperature<sup>[11]</sup>**

Hot pressing is used to overcome the poor densification of usually less than 96 % theoretical density of KNN<sup>[1,11,64]</sup>. Egerton et al.<sup>[38]</sup> and Jaeger et al.<sup>[37]</sup> reported that hot isostatic pressing of KNN is usually so effective that it yields densities of above 99 % theoretical density and a finer grained microstructure compared to conventional sintering although only graphic evidence was given. Improvements of the radial coupling coefficient  $k_r$  from 0.32 to 0.48, dielectric constant from 290 to 420, piezoelectric constant  $d_{33}$  from 80 pC/N to 160 pC/N as well as mechanical quality factors  $Q_m$ <sup>20</sup> increased from 130 to 240 are the most notable. On the other hand, electrical quality factor, resistivity, frequency constant<sup>21</sup> and Young's modulus remain unaffected or only marginally improved. A coercive field of 0.47 kV/mm and a maximum remanent polarisation  $P_r$  of 33  $\mu\text{C}/\text{cm}^2$  and a  $\epsilon_r$  of 550 is reported<sup>[94]</sup>. The coercive field is drastically lower than

<sup>20</sup>The mechanical quality factor is defined as:  $2\pi \cdot \text{Energy stored} / \text{Energy lost per cycle}$

<sup>21</sup>The frequency constant is defined as: resonant frequency \* length of object

1.04 kV/mm<sup>[95]</sup> and 2 kV/mm<sup>[1]</sup> for conventionally sintered material while the remanent polarisation stays the same.

Spark plasma sintering (SPS) is highly effective in enhancing sinterability of materials, i.e. better densification with minimised grain growth. It was shown that this also holds for KNN. More than 99 % of theoretical density and grain sizes between 200 nm and 500 nm were reported<sup>[34]</sup>. Furthermore, the piezoelectric constant  $d_{33}$  of 148 pC/N is comparable to the results obtained by hot pressing. However, one drawback is that annealing at 900 °C for several hours is needed to decrease leakage currents to an acceptable level in order to fully pole the sample. Liquid phase sintering can produce single crystals of KNN derivatives<sup>[88]</sup> using potassium copper niobate to create the liquid phase. Cadmium oxide also creates a liquid phase during sintering but cannot be used under the regulations of RoHS or comparable regulations outside the EU<sup>[82]</sup>.

#### **2.3.4.3 Single Crystals, Sol-Gel and Texturing of KNN**

Single Crystals of KN and NN with low concentrations of potassium are relatively easily created from flux of Na<sub>2</sub>O, K<sub>2</sub>O, Nb<sub>2</sub>O<sub>5</sub> and NaF<sup>[4,6,96]</sup> or NaBO<sub>2</sub><sup>[97]</sup> as solvents. KN crystals are grown from melt of K<sub>2</sub>O and Nb<sub>2</sub>O<sub>5</sub> by spontaneous nucleation<sup>[98]</sup>. However, these methods are reported as unsuitable for growing K<sub>0.5</sub>Na<sub>0.5</sub>NbO<sub>3</sub> crystals of reasonable quality<sup>[9]</sup>. Recently, KNN crystals with sodium/potassium ratios near 1:1 have been grown via self-flux method from KNN powder in eutectic NaF/KF flux<sup>[99]</sup>. KNN<sup>[88]</sup> and Li and Ta modified KNN<sup>[88]</sup> single crystals were grown by solid-state crystal growth using KTaO<sub>3</sub> seed crystals with K<sub>4</sub>CuNb<sub>8</sub>O<sub>23</sub> as a sintering aid. This method overcomes difficulties in fabricating crystals with precisely controlled compositions. These crystals, while with controlled composition, were not of full density. Hot pressing instead of conventional sintering can reduce the porosity of the grown crystals<sup>[100]</sup>. The only piezoelectric properties for single crystal KNN currently reported are those of KNN with 5 % LiTaO<sub>3</sub> grown by the Bridgman method. Here, a Curie temperature of 426 °C and  $d_{33}$  value of 405 pC/N<sup>[101]</sup>, about 100 pC/N higher than comparable randomly oriented ceramics, were found.

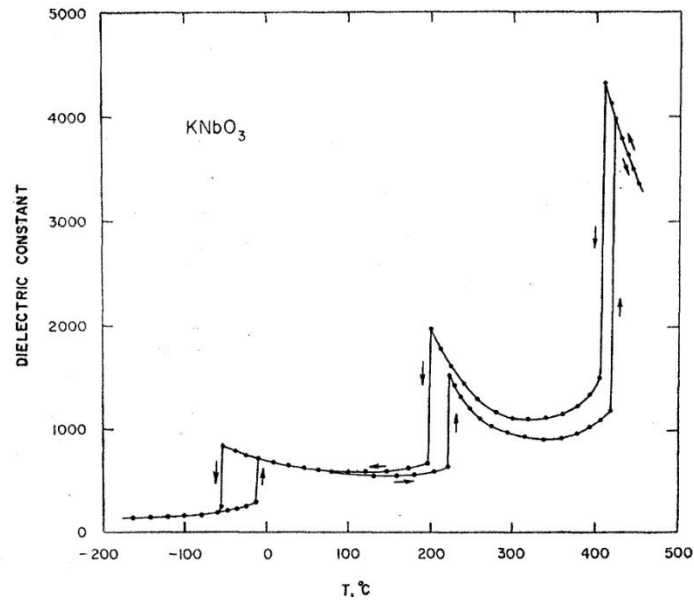


**Fig 14: Dielectric constant versus temperature for a single crystal of  $\text{KNbO}_3$ <sup>[5]</sup>. This shows clearly the three phase transitions relevant for most piezoelectric applications. Dopants can cause the transition at 200 °C to shift towards common operating temperatures where it might result in increased thermally induced aging<sup>[61]</sup>. PZT has no comparable phase transition between room temperature and its Curie temperature<sup>[102]</sup>.**

Radio frequency magnetron sputtering with  $\text{K}_{1/2}\text{Na}_{1/2}\text{NbO}_3$  targets onto a  $\text{Pt}_{0.8}\text{Ir}_{0.2}$  substrate yields single-phase perovskite thin films with about 30 at.% deficiency in the alkali metal oxides while it was attempted to reduce pressure and temperature of the manufacturing process. It is concluded that the loss is not a result of the heat treatment but the sputtering process<sup>[103]</sup>. Dielectric constants of about 500 are reported<sup>[104]</sup>. Films of non-alkali deficient KNN can be achieved by a compositionally compensated target with K:Na:Nb ratio of 1.5:1.5:1. As a drawback of alkali compensation, however, long term stability and resistance to humidity are adversely affected<sup>[105]</sup>. Pulsed laser deposition onto  $\text{SrTiO}_3$  substrate, on the other hand, can give thin films of KNN with near stoichiometric composition. Sodium-rich compositions are, however, still better quality than potassium-rich ones<sup>[106]</sup>. Cho et al., in fact, report that high gas pressures during pulsed laser deposition is required to achieve thermalisation of the heavier Nb ions to produce stoichiometric KNN. They also report a remanent and spontaneous polarization of  $10 \mu\text{C}/\text{cm}^2$  and  $17.5 \mu\text{C}/\text{cm}^2$ , respectively, a loss tangent of 2.5 %, coercive field of 2 kV/mm and a resistivity of about  $10^{12} \Omega\text{m}$ <sup>[107]</sup>, which is the same as the reported bulk resistivity<sup>[8]</sup>. Conductivity of (Li, Ta, Sb) modified KNN thin films can be reduced by three orders of magnitude with manganese doping<sup>[108]</sup>. Early attempts to prepare KNN via three different sol-gel routes, alkoxide route, oxalate and Pechini method, did not result in single-phase perovskite films

even at sintering temperatures of 900 °C. Stability of the precursor solutions and porosity are also an issue<sup>[109]</sup>. Takana et al.<sup>[110]</sup> further investigated the alkoxide route and fabricated single-phase perovskite films. Films by chemical solution deposition need 15 mol% to 50 mol% excess alkali metal oxide to form single phase material and result in dielectric constants up to 900<sup>[111]</sup>. Chemical vapour deposition is also usable to create single phase films, however, currently with niobium deficiency<sup>[112]</sup>.



### 2.3.5 Influence of Dopants

The chemical modifications of KNN can generally be divided into two groups. The first group attempts to improve the sintering behaviour of KNN while keeping its inherent structure and phase diagram unaffected. It is aimed at improving specific properties like piezoelectric or coupling constants. The second group utilizes shifting the orthorhombic-to-tetragonal phase transition found in pure KNN at 200 °C<sup>[9,10]</sup> to near or below room temperature (compare also phase transitions of pure KN in Fig 14). It is interesting to note that Ringgaard et al.<sup>[64]</sup> concluded from the investigation of various dopants<sup>[19]</sup> that processing conditions have comparable influence on the piezoelectric and mechanical properties of KNN to doping. This is also voiced by Tashiro et al.<sup>[12]</sup> and Du et al.<sup>[11]</sup>. A summary of the properties reported for modified KNN can be found in Tab 10 (pages 82ff.).

#### 2.3.5.1 Lithium-Modified KNN

Modifications of KNN exploiting the O-T phase transition similar to Saito et al.<sup>[2]</sup>, who use KNN + Li, Ta and Sb and report piezoelectric constants  $d_{33}$  of >300 pC/N (not textured) to >400 pC/N (textured) and a Curie temperature of 253 °C, have seen considerable interest<sup>[46,49,80,84,113-121]</sup>. Before Saito et al. there were only two reports of lithium doped KNN<sup>[41,53]</sup>. Later reports usually investigated phase changes during minor changes in composition or tried to optimize processing conditions. Commonly  $d_{33}$  values of around 200 pC/N, with a few reaching 300 pC/N<sup>[115]</sup>, and Curie temperatures of about 350 °C are reported. A gain of 100 pC/N in the piezoelectric constant normally comes with an about 100 K penalty in Curie temperature. Related sub-systems with variations in  $\text{LiTaO}_3$ <sup>[15,16,18,41,50,70,89,122-125]</sup>,  $\text{LiNbO}_3$ <sup>[18,29,40,45,50,53,61,69,124,126-130]</sup>,  $\text{LiSbO}_3$ <sup>[47,59,66,71,78,131-134]</sup> or just Ta<sup>[51,135,136]</sup> have been investigated in great detail regarding microstructure, sintering conditions and phase transition. Pure  $\text{Sb}_2\text{O}_3$  doping of KNN has not yet been reported. The effects of the constituents originally used by Saito et al.<sup>[2]</sup> can be generalised as follows: Tantalum doping hinders abnormal grain growth and decreases  $T_C$  and the O-T transition temperature. Lithium decreases the O-T transition temperature to room temperature at about 6 at.% A-site substitution and increased  $T_C$  whilst also improving densification. It is possible to reach 300 pC/N and Curie temperatures above 350 °C by lithium doping only<sup>[127]</sup>. The effect of  $\text{LiSbO}_3$  is similar to that of  $\text{LiNbO}_3$ , except 1 mol% less is required to shift the O-T transition to room temperature<sup>[47,131]</sup>. While Saito et al.'s results<sup>[2]</sup> are encouraging, there are discrepancies regarding the MPB of KNN with  $\text{LiTaO}_3$  (LT), originally reported at 5 mol% LT, now reported at 6-7 mol% LT<sup>[41,50]</sup>. The so-called MPB between ilmenite  $\text{LiTaO}_3$  and perovskite

KNN is often stated in literature owing to the initial report<sup>[2]</sup>. However, this is technically not correct since this phase boundary would have to be between the ilmenite structure of  $\text{LiTaO}_3$  and the perovskite structure of KNN. Technically, what is commonly called the solubility limit of  $\text{LiTaO}_3$  in KNN is the actual LT-KNN MPB. However, there is no improvement of properties at that point<sup>[122]</sup>.

It has become apparent that other issues, such as temperature stability of polarisation and piezoelectric properties<sup>[61,126]</sup>, processing difficulties and the cost of tantalum will impede large scale industrial application. Hollenstein et al.<sup>[61]</sup> showed that thermal cycling across the O-T transition causes up to 30 % reduction of piezoelectric properties. 140 °C is needed for sterilisation of medical equipment. Addition of up to 6 at.% lithium decreases the temperature for the phase transition<sup>[69]</sup>, making the problem more and more relevant. At 7 at.% lithium the transition temperature drops below room temperature eliminating the associated thermal reduction of properties. However, at that point, the lithium addition has already reduced the piezoelectric properties to the same level as cycling through the O-T phase transition does. Considering that the Curie temperature is also increased to 480 °C by the addition of 7 at.% lithium, this is then a material with no unwanted phase transitions over a wider range than PZT<sup>[45]</sup>. For vehicular applications, thermal stability down to -45 °C is needed, which is not yet possible in Li-doped KNN. Hollenstein et al.<sup>[50]</sup> find unipolar strain values of lithium and tantalum modified KNN similar to PZT. They also attempt to reproduce the high  $d_{33}$  reported by Saito et al. But, like Guo et al.<sup>[41]</sup>, this has not been possible so far.

KNN with a wide range of lithium and tantalum additions is investigated thoroughly, reporting optimum sintering temperatures, Curie temperatures, dielectric constants, dielectric losses, resistivities,  $d_{31}$  coefficients, coupling coefficients  $k_{31}$  and  $k_p$ , Young's moduli, elastic compliances, electromechanical quality factor and Poisson's ratios of 48 different compositions in these systems. The aging related changes of the dielectric losses are also reported for up to 7 years<sup>[89]</sup>.

### 2.3.5.2 Copper

Copper has been discovered as an effective sintering aid in form of  $\text{K}_4\text{Cu}(\text{Nb}/\text{Ta})_8\text{O}_{23}$ <sup>[81]</sup> giving 97.5 % relative density and unipolar strain of 0.09 % at 4 kV/mm<sup>[48]</sup>. The percentage of sintering aid should remain below 0.5 %, otherwise piezoelectric properties degrade<sup>[137]</sup>. Sintering temperatures as low as 950 °C are possible<sup>[138,139]</sup>. Copper sintering aids have since been added to various more complex KNN-based systems with equivalent effect<sup>[140,141]</sup>. In required concentrations, the influence of CuO on  $T_C$  and  $T_{O-T}$  is to decrease both<sup>[83]</sup>.

Copper improves sinterability by creating a liquid phase during sintering. Matsubara et al.<sup>[81,83]</sup> report  $d_{33}$  coefficients of 180 pC/N for KNN while  $T_{O-T}$  drops from 204 °C to 170 °C, 200 pC/N for lithium doped KNN<sup>[69]</sup> and 270 pC/N for 30 % tantalum added KNN<sup>[85]</sup> using various copper containing alkali niobate and tantalate derivatives.

### 2.3.5.3 $\text{CaTiO}_3$ and $\text{SrTiO}_3$ in KNN

$\text{CaTiO}_3$  has been shown to make electrical fatigue in  $\text{LiSbO}_3$  modified KNN almost undetectable<sup>[142]</sup>. It also reduces the temperature dependence of the piezoelectric properties<sup>[143]</sup> and improves resistance to humidity when used in small quantities<sup>[72]</sup>.

$\text{SrTiO}_3$  doping to KNN produces relaxor behaviour<sup>[32,33,36,41,43]</sup> with dielectric constants reaching up to 3000 and 5000 with  $\text{SrZrO}_3$ . At the same time these ceramics provide better cycling stability than lanthanum doped PZT<sup>[54]</sup>. The results were nearly the same in KNN with  $\text{BiScO}_3$ <sup>[144]</sup>. This relaxor effect is much less pronounced when using  $\text{CaTiO}_3$ <sup>[72]</sup>, where  $\epsilon_r$  was only about 1000.

A morphotropic phase boundary between orthorhombic and tetragonal at 4 % strontium titanate is reported by Guo et al.<sup>[23]</sup>. They also find  $d_{33}$  values below 100 and coupling factors  $k_p$  between 0.266 and 0.325 as well as a fast dropping Curie temperature with increasing strontium titanate content. The results are later confirmed by Wang et al.<sup>[145]</sup>. Kusumoto et al.<sup>[22]</sup> add strontium titanate ( $\text{SrTiO}_3$ ) to 6 % lithium modified KNN. Significantly reduced  $d_{33}$  and Curie temperatures are observed. Chang et al.<sup>[72]</sup> report on 0.5 %  $\text{SrTiO}_3$  added KNN. While the relative density is a high 98.4 %,  $P_r$ ,  $k_p$ ,  $T_c$  and  $d_{33}$  are all reduced by between 5 % and 15 %.

Purely electrostrictive behaviour is reported for 15 % strontium titanate addition and above<sup>[33]</sup>. Electro-optical properties of KNN with 20 % strontium titanate are measured by Kroupa et al.<sup>[32]</sup>. This has a pseudo-cubic structure and relaxor behaviour<sup>[43]</sup>. Mixing with up to 33 % strontium zirconate forms single phase relaxor ferroelectrics<sup>[54]</sup>.

### 2.3.5.4 Mixture with BNT, BT and Other Titanate-Based Systems

KNN forms orthorhombic to tetragonal MPBs with lead, barium and strontium titanate at around 5 % of the ternary titanium oxide. KNN with barium titanate (BT) is also investigated<sup>[60]</sup>. The MPB was found at 6 % barium titanate. Solid solubility up to 20 % BT was shown. Piezoelectric properties decrease with increasing BT content. Improved density and decreased grain size for the same system are reported<sup>[146]</sup> and confirmed<sup>[147]</sup> but at the same time contradicted<sup>[27]</sup>.

Bismuth sodium titanate (BNT) mixed KNN systems are orthorhombic up to 2 % BNT, tetragonal up to 9 % BNT and cubic thereafter. At the 2 % BNT MPB, a  $d_{33}$  of 195 pC/N and a

Curie temperature of 395 °C was reported<sup>[79]</sup>. BNT gave relaxor behaviour with a less temperature stable dielectric constant<sup>[148]</sup>.

Most reports focus on NN or KN only, which are mixed with BNT, BT or BKT. Coupling factors of 0.15 and depolarisation temperatures of 100 °C or less are common<sup>[20,149,150]</sup>. Addition of bismuth and scandium oxide forms a pseudo-ternary system but the depolarisation temperature stays near 200 °C as the coercive field is increased<sup>[151]</sup>. KN-BT shows relaxor behaviour<sup>[152]</sup>.

5 mol% BaTiO<sub>3</sub> is reported to form an MPB with KNN<sup>[60]</sup> but it appears to be just another way to move the O-T transition (PPT<sup>22</sup>) to room temperature. Sintering is improved by formation of a liquid phase above 1060 °C<sup>[58]</sup> but also causing abnormal grain growth<sup>[147]</sup>. Mixtures with other ferroelectric systems in low concentrations like BiFeO<sub>3</sub><sup>[153]</sup>, Bi<sub>1/2</sub>K<sub>1/2</sub>TiO<sub>3</sub><sup>[154]</sup>, BNT<sup>[79]</sup> or BNT-BT<sup>[155]</sup> also produce O-T PPT type behaviour and not MPBs as stated.

### 2.3.5.5 Other Dopants of KNN

Silver oxide, also in the form of Ag(Nb/Ta)O<sub>3</sub>, increases the Curie temperature of Li, Ta and Sb modified KNN more strongly than LiNbO<sub>3</sub> whilst dropping the O-T transition temperature<sup>[121,156,157]</sup>. Replacing niobium in KNN with 30 at.% tantalum increases the electrostrictive effect and gives 0.11 % unipolar strain at 4 kV/mm. Manganese lowers losses and  $\epsilon_r$ <sup>[27]</sup> and improves  $Q_m$  and  $k_p$ <sup>[158]</sup>.

A study of 0.5 mol% alkali-earth doping showed that strontium, calcium improves sintering, and magnesium oxide hinders it. All decrease O-T phase transition temperatures. Barium oxide leads to formation of secondary phases. Magnesium reduces the relative density most out of all investigated dopants<sup>[19]</sup>.

ZnO and SnO<sub>2</sub> improve sintering. WO<sub>3</sub>, SnO<sub>2</sub>, Sc<sub>2</sub>O<sub>3</sub> and CeO<sub>2</sub> hinder grain growth. All but SnO<sub>2</sub> also hinder densification<sup>[82]</sup>. However, another report shows that zinc oxide helps densification and prevents commonly occurring disintegration of KNN<sup>[159]</sup>. Zirconia impedes grain growth<sup>[160]</sup>. Bi<sub>2</sub>O<sub>3</sub> appears to improve phase stability of KNN at high temperatures<sup>[161]</sup>, but raises sintering temperatures as well. Iron oxide or lanthanum ferrite are used to lower sintering temperatures of pure KN<sup>[35,39,87]</sup>.

<sup>22</sup> PPT: polymorphic phase transition: a phase transition, which is composition and temperature dependent unlike an MPB which is independent of temperature.

### 2.3.6 Summary

In summary, so far there are no methods for raising the O-T transition to higher temperatures, all dopants had the opposite effect. Few, in particular  $\text{LiNbO}_3$  and  $\text{AgNbO}_3$ , increased  $T_C$  allowing for purely tetragonal material from room temperature to beyond 400 °C but with the inherently lower piezoelectric properties of the tetragonal phase. Fig 15 shows the influence of the O-T phase transition onto  $d_{33}$ . The highest piezoelectric properties are found when optimally sintered material and the O-T phase transition temperature of about 30-50 K above the working temperature is maintained. Mixtures with other ferroelectric systems have also not yielded temperature independent mixed phase regions. Texturing is currently the only way to avoid this complication and increase the piezoelectric properties of KNN at the same time.

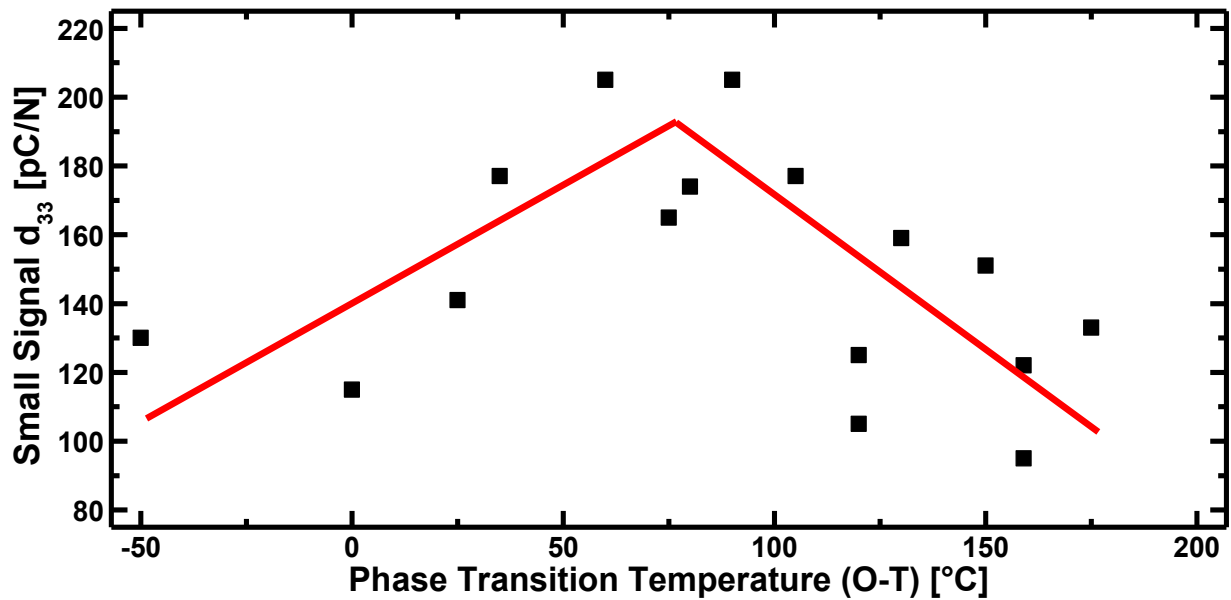


Fig 15: The piezoelectric constant  $d_{33}$  is plotted against the temperature of the O-T phase transition for some Li-doped KNN systems<sup>[124,136]</sup>. The highest room temperature  $d_{33}$  values are found between 55 and 70 °C. Also, on the tetragonal side of the phase transition, the  $d_{33}$  coefficient drops faster with temperature than on the orthorhombic side. The large spread is due to the fact that the values were mostly read of graphs in the reports and also the temperature of the reported “room temperature” values were presumably taken at 17-30 °C depending on laboratory conditions around the world.

## 2.3.7 References

- [1] H. Birol, D. Damjanovic, and N. Setter, "Preparation and characterization of  $(K_{0.5}Na_{0.5})NbO_3$  ceramics," *Journal of the European Ceramic Society*, **26**[6] 861-6 (2006).
- [2] Y. Saito, H. Takao, T. Tani, T. Nonoyama, K. Takatori, T. Homma, T. Nagaya, and M. Nakamura, "Lead-free piezoceramics," *Nature*, **432**[7013] 84-7 (2004).
- [3] I. Fuyuno, "Toyota's production line leads from lab to road," *Nature*, **435**[7045] 1026-7 (2005).
- [4] G. Shirane, R. Newnham, and R. Pepinsky, "Dielectric properties and phase transitions of  $NaNbO_3$  and  $(Na,K)NbO_3$ ," *Physical Review*, **96**[3] 581-8 (1954).
- [5] G. Shirane, H. Danner, A. Pavlovic, and R. Pepinsky, "Phase Transitions in Ferroelectric  $KNbO_3$ ," *Physical Review*, **93**[4] 672-3 (1954).
- [6] B. T. Matthias and J. P. Remeika, "Dielectric properties of sodium and potassium niobates," *Physical Review*, **82**[5] 727-9 (1951).
- [7] E. A. Wood, "Polymorphism in potassium niobate, sodium niobate, and other  $ABO_3$  Compounds," *Acta Crystallographica*, **4**[4] 353-62 (1951).
- [8] L. Egerton and D. M. Dillon, "Piezoelectric and dielectric properties of ceramics in the system potassium sodium niobate," *Journal of the American Ceramic Society*, **42**[9] 438-42 (1959).
- [9] M. Ahtee and A. M. Glazer, "Lattice parameters and tilted octahedra in sodium-potassium niobate solid solutions," *Acta Crystallographica, Section A: Foundations of Crystallography*, **32** 434-45 (1976).
- [10] M. Ahtee and A. W. Hewat, "Structural phase-transitions in sodium-potassium niobate solid-solutions by neutron powder diffraction," *Acta Crystallographica, Section A: Foundations of Crystallography*, **34**[Mar] 309-17 (1978).
- [11] H. L. Du, Z. M. Li, F. S. Tang, S. B. Qu, Z. B. Pei, and W. C. Zhou, "Preparation and piezoelectric properties of  $(K_{0.5}Na_{0.5})NbO_3$  lead-free piezoelectric ceramics with pressure-less sintering," *Materials Science & Engineering, B: Solid-State Materials for Advanced Technology*, **131**[1-3] 83-7 (2006).
- [12] S. Tashiro and K. Nagata, "Influence of mixing condition and nonstoichiometry on piezoelectric properties of  $(K, Na, Pb)NbO_3$  ceramics," *Japanese Journal of Applied Physics Part 1-Regular Papers Short Notes & Review Papers*, **43**[9B] 6711-5 (2004).
- [13] P. Dubernet and J. Ravez, "Dielectric study of  $KNbO_3$  ceramics over a large range of frequency ( $10^2$  -  $10^9$  Hz) and temperature (300 - 800 K)," *Ferroelectrics*, **211**[1-4] 51-66 (1998).
- [14] T. A. Skidmore and S. J. Milne, "Phase development during mixed-oxide processing of a  $[Na_{0.5}K_{0.5}NbO_3]_{(1-x)}[LiTaO_3]_x$  powder," *Journal of Materials Research*, **22**[8] 2265-72 (2007).
- [15] Y. Wang, D. Damjanovic, N. Klein, E. Hollenstein, and N. Setter, "Compositional inhomogeneity in Li- and Ta-modified  $(K,Na)NbO_3$  ceramics," *Journal of the American Ceramic Society*, **90**[11] 3485-9 (2007).
- [16] Y. Wang, D. Damjanovic, N. Klein, and N. Setter, "High-Temperature Instability of Li- and Ta-Modified  $(K,Na)NbO_3$  Piezoceramics," *Journal of the American Ceramic Society*, **91**[6] 1962-70 (2008).
- [17] P. Zhao, B.-P. Zhang, and J.-F. Li, "Enhanced dielectric and piezoelectric properties in  $LiTaO_3$ -doped lead-free  $(K,Na)NbO_3$  ceramics by optimizing sintering temperature," *Scripta Materialia*, **58**[6] 429-32 (2008).
- [18] Y. H. Zhen and J. F. Li, "Normal sintering of  $(K,Na)NbO_3$ -based ceramics: Influence of sintering temperature on densification, microstructure, and electrical properties," *Journal of the American Ceramic Society*, **89**[12] 3669-75 (2006).
- [19] B. Malic, J. Bernard, J. Holc, D. Jenko, and M. Kosec, "Alkaline-earth doping in  $(K,Na)NbO_3$  based piezoceramics," *Journal of the European Ceramic Society*, **25**[12] 2707-11 (2005).
- [20] Y. M. Li, W. Chen, J. Zhou, Q. Xu, H. Sun, and R. X. Xu, "Dielectric and piezoelectric properties of lead-free  $(Na_{0.5}Bi_{0.5})TiO_3$ - $NaNbO_3$  ceramics," *Materials Science & Engineering, B: Solid-State Materials for Advanced Technology*, **112**[1] 5-9 (2004).
- [21] Y. F. Chang, Z. P. Yang, X. L. Chao, R. Zhang, and X. R. Li, "Dielectric and piezoelectric properties of alkaline-earth titanate doped  $(K_{0.5}Na_{0.5})NbO_3$  ceramics," *Materials Letters*, **61**[3] 785-9 (2007).
- [22] K. Kusumoto, "Dielectric and piezoelectric properties of  $KNbO_3$ - $NaNbO_3$ - $LiNbO_3$ - $SrTiO_3$  ceramics," *Japanese Journal of Applied Physics Part 1-Regular Papers Brief Communications & Review Papers*, **45**[9B] 7440-3 (2006).
- [23] Y. Guo, K.-i. Kakimoto, and H. Ohsato, "Dielectric and piezoelectric properties of lead-free  $(Na_{0.5}K_{0.5})NbO_3$ - $SrTiO_3$  ceramics," *Solid State Communications*, **129**[5] 279-84 (2004).
- [24] T. Liu, A. L. Ding, X. Y. He, X. S. Zheng, P. S. Qiu, W. X. Cheng, and X. Zeng, "Dielectric and piezoelectric properties of Mn doped  $(K,Na)_{0.96}Sr_{0.02}NbO_3$  ceramics," *Integrated Ferroelectrics*, **85** 3-12 (2006).

- [25] T. Liu, A. L. Ding, X. Y. He, X. S. Zheng, P. S. Qiu, and W. X. Cheng, "Dielectric and piezoelectric properties of Mn-doped  $(\text{K},\text{Na})_{0.96}\text{Sr}_{0.02}\text{NbO}_3$  ceramics," *Physica Status Solidi A: Applications and Materials Science*, **203**[15] 3861-7 (2006).
- [26] B. Hilczer, J. Kulek, M. Polomska, M. Kosec, B. Malic, and L. Kepinski, "Dielectric relaxation in  $\text{K}_{0.5}\text{Na}_{0.5}\text{NbO}_3$ -PVDF composites," *Ferroelectrics*, **338** 159-70 (2006).
- [27] C. W. Ahn, H. C. Song, S. Nahm, S. H. Park, K. Uchino, S. Priya, H. G. Lee, and N. K. Kang, "Effect of  $\text{MnO}_2$  on the piezoelectric properties of  $(1-x)(\text{Na}_{0.5}\text{K}_{0.5})\text{NbO}_3$ - $x\text{BaTiO}_3$  ceramics," *Japanese Journal of Applied Physics, Part 2: Letters & Express Letters*, **44**[42-45] L1361-4 (2005).
- [28] H. L. Du, F. S. Tang, Z. M. Li, W. C. Zhou, S. B. Qu, and Z. B. Pei, "Effect of poling condition on piezoelectric properties of  $(\text{K}_{0.5}\text{Na}_{0.5})\text{NbO}_3$  ceramics," *Transactions of Nonferrous Metals Society of China*, **16** S462-S5 (2006).
- [29] H. L. Du, F. S. Tang, F. Luo, W. C. Zhou, S. B. Qu, and Z. B. Pei, "Effect of poling condition on piezoelectric properties of  $(\text{K}_{0.5}\text{Na}_{0.5})\text{NbO}_3$ - $\text{LiNbO}_3$  lead-free piezoelectric ceramics," *Materials Science and Engineering B-Solid State Materials for Advanced Technology*, **137**[1-3] 175-9 (2007).
- [30] R.-C. Chang, S.-Y. Chu, Y.-P. Wong, C.-S. Hong, and H.-H. Huang, "The effects of sintering temperature on the properties of lead-free  $(\text{Na}_{0.5}\text{K}_{0.5})\text{NbO}_3$ - $\text{SrTiO}_3$  ceramics," *Journal of Alloys and Compounds*, **456**[1-2] 308-12 (2008).
- [31] M. Ichiki, L. Zhang, M. Tanaka, and R. Maeda, "Electrical properties of piezoelectric sodium-potassium niobate," *Journal of the European Ceramic Society*, **24**[6] 1693-7 (2004).
- [32] J. Kroupa, J. Petzelt, B. Malic, and M. Kosec, "Electro-optic properties of KNN-STO lead-free ceramics," *Journal of Physics D-Applied Physics*, **38**[5] 679-81 (2005).
- [33] V. Bobnar, B. Malic, J. Holc, M. Kosec, R. Steinhausen, and H. Beige, "Electrostrictive effect in lead-free relaxor  $\text{K}_{0.5}\text{Na}_{0.5}\text{NbO}_3$ - $\text{SrTiO}_3$  ceramic system," *Journal of Applied Physics*, **98**[2] 024113 (2005).
- [34] J. F. Li, K. Wang, B. P. Zhang, and L. M. Zhang, "Ferroelectric and piezoelectric properties of fine-grained  $\text{Na}_{0.5}\text{K}_{0.5}\text{NbO}_3$  lead-free piezoelectric ceramics prepared by spark plasma sintering," *Journal of the American Ceramic Society*, **89**[2] 706-9 (2006).
- [35] K. Kakimoto, I. Masuda, and H. Ohsato, "Ferroelectric and piezoelectric properties of  $\text{KNbO}_3$  ceramics containing small amounts of  $\text{LaFeO}_3$ ," *Japanese Journal of Applied Physics Part 1-Regular Papers Short Notes & Review Papers*, **42**[9B] 6102-5 (2003).
- [36] Y. P. Guo, K. Kakimoto, and H. Ohsato, "Ferroelectric-relaxor behavior of  $(\text{Na}_{0.5}\text{K}_{0.5})\text{NbO}_3$ -based ceramics," *Journal of Physics and Chemistry of Solids*, **65**[11] 1831-5 (2004).
- [37] R. E. Jaeger and L. Egerton, "Hot pressing of potassium-sodium niobates," *Journal of the American Ceramic Society*, **45**[5] 209-13 (1962).
- [38] L. Egerton and C. A. Bieling, "Isostatically hot-pressed sodium-potassium niobate transducer material for ultrasonic devices," *American Ceramic Society Bulletin*, **47**[12] 1151-6 (1968).
- [39] K. Kakimoto, I. Masuda, and H. Ohsato, "Lead-free  $\text{KNbO}_3$  piezoceramics synthesized by pressure-less sintering," *Journal of the European Ceramic Society*, **25**[12] 2719-22 (2005).
- [40] H. L. Du, F. S. Tang, D. J. Liu, D. M. Zhu, W. C. Zhou, and S. B. Qu, "The microstructure and ferroelectric properties of  $(\text{K}_{0.5}\text{Na}_{0.5})\text{NbO}_3$ - $\text{LiNbO}_3$  lead-free piezoelectric ceramics," *Materials Science and Engineering B-Solid State Materials for Advanced Technology*, **136**[2-3] 165-9 (2007).
- [41] Y. P. Guo, K. Kakimoto, and H. Ohsato, " $(\text{Na}_{0.5}\text{K}_{0.5})\text{NbO}_3$ - $\text{LiTaO}_3$  lead-free piezoelectric ceramics," *Materials Letters*, **59**[2-3] 241-4 (2005).
- [42] A. Aydi, H. Khemakhem, C. Boudaya, R. Von der Muhll, and A. Simon, "New ferroelectric and relaxor ceramics in the mixed oxide system  $\text{NaNbO}_3$ - $\text{BaSnO}_3$ ," *Solid State Sciences*, **6**[4] 333-7 (2004).
- [43] M. Kosec, V. Bobnar, M. Hrovat, J. Bernard, B. Malic, and J. Holc, "New lead-free relaxors based on the  $\text{K}_{0.5}\text{Na}_{0.5}\text{Nb}_{0.3}\text{SrTi}_{0.3}$  solid solution," *Journal of Materials Research*, **19**[6] 1849-54 (2004).
- [44] Y. D. Juang, "Phase transition of lithium potassium niobate ceramics," *Solid State Communications*, **120**[1] 25-8 (2001).
- [45] Y. P. Guo, K. Kakimoto, and H. Ohsato, "Phase transitional behavior and piezoelectric properties of  $(\text{Na}_{0.5}\text{K}_{0.5})\text{NbO}_3$ - $\text{LiNbO}_3$  ceramics," *Applied Physics Letters*, **85**[18] 4121-3 (2004).
- [46] J. Yoo, K. Lee, K. Chung, S. Lee, K. Kim, J. Hong, S. Ryu, and C. Lhee, "Piezoelectric and dielectric properties of  $(\text{LiNaK})(\text{NbTaSb})\text{O}_3$  ceramics with variation in poling temperature," *Japanese Journal of Applied Physics, Part 1: Regular Papers, Short Notes & Review Papers*, **45**[9B] 7444-8 (2006).
- [47] S. Zhang, R. Xia, T. R. Shrout, G. Zang, and J. Wang, "Piezoelectric properties in perovskite  $0.948(\text{K}_{0.5}\text{Na}_{0.5})\text{NbO}_3$ - $0.052\text{LiSbO}_3$  lead-free ceramics," *Journal of Applied Physics*, **100**[10] 104108-6 (2006).
- [48] M. Matsubara, K. Kikuta, and S. Hirano, "Piezoelectric properties of  $(\text{K}_{0.5}\text{Na}_{0.5})(\text{Nb}_{1-x}\text{Ta}_x)\text{O}_3$ - $\text{K}_{5.4}\text{CuTa}_{10}\text{O}_{29}$  ceramics," *Journal of Applied Physics*, **97**[11] 114105 (2005).
- [49] B. Q. Ming, J. F. Wang, P. Qi, and G. Z. Zang, "Piezoelectric properties of  $(\text{Li}, \text{Sb}, \text{Ta})$  modified  $(\text{Na},\text{K})\text{NbO}_3$  lead-free ceramics," *Journal of Applied Physics*, **101**[5] 054103 (2007).

- [50] E. Hollenstein, M. Davis, D. Damjanovic, and N. Setter, "Piezoelectric properties of Li- and Ta-modified  $(K_{0.5}Na_{0.5})NbO_3$  ceramics," *Applied Physics Letters*, **87**[18] 182905 (2005).
- [51] M. Matsubara, T. Yamaguchi, W. Sakamoto, K. Kikuta, T. Yogo, and S. Hirano, "Processing and piezoelectric properties of lead-free (K,Na) (Nb,Ta)  $O_3$  ceramics," *Journal of the American Ceramic Society*, **88**[5] 1190-6 (2005).
- [52] R.-C. Chang, S.-Y. Chu, Y.-P. Wong, Y.-F. Lin, and C.-S. Hong, "Properties of  $(Na_{0.5}K_{0.5})NbO_3$ - $SrTiO_3$  based lead-free ceramics and surface acoustic wave devices," *Sensors and Actuators A: Physical*, **136**[1] 267-72 (2007).
- [53] S. Y. Chu, W. Water, Y. D. Juang, and J. T. Liaw, "Properties of  $(Na, K)NbO_3$  and  $(Li, Na, K)NbO_3$  ceramic mixed systems," *Ferroelectrics*, **287** 23-33 (2003).
- [54] V. Bobnar, J. Holc, M. Hrovat, and M. Kosec, "Relaxorlike dielectric dynamics in the lead-free  $K_{0.5}Na_{0.5}NbO_3$ - $SrZrO_3$  ceramic system," *Journal of Applied Physics*, **101**[7] 074103-4 (2007).
- [55] A. Castro, B. Jimenez, T. Hungria, A. Moure, and L. Pardo, "Sodium niobate ceramics prepared by mechanical activation assisted methods," *Journal of the European Ceramic Society*, **24**[6] 941-5 (2004).
- [56] K. Kakimoto, I. Masuda, and H. Ohsato, "Solid-solution structure and piezoelectric property of  $KNbO_3$  ceramics doped with small amounts of elements," *Japanese Journal of Applied Physics Part 1-Regular Papers Short Notes & Review Papers*, **43**[9B] 6706-10 (2004).
- [57] J. S. de Andrade, A. G. Pinheiro, I. F. Vasconcelos, M. A. B. de Araujo, M. A. Valente, and A. S. B. Sombra, "Structural studies of  $KNbO_3$  in niobate glass-ceramics," *Journal of Physics and Chemistry of Solids*, **61**[6] 899-906 (2000).
- [58] C.-W. Ahn, H.-Y. Park, S. Nahm, K. Uchino, H.-G. Lee, and H.-J. Lee, "Structural variation and piezoelectric properties of  $0.95(Na_{0.5}K_{0.5})NbO_3$ - $0.05BaTiO_3$  ceramics," *Sensors and Actuators A: Physical*, **136**[1] 255-60 (2007).
- [59] L. Dunmin, K. W. Kwok, K. H. Lam, and H. L. W. Chan, "Structure and electrical properties of  $K_{0.5}Na_{0.5}NbO_3$ - $LiSbO_3$  lead-free piezoelectric ceramics," *Journal of Applied Physics*, **101**[7] 074111 (2007).
- [60] Y. P. Guo, K. Kakimoto, and H. Ohsato, "Structure and electrical properties of lead-free  $(Na_{0.5}K_{0.5})NbO_3$ - $BaTiO_3$  ceramics," *Japanese Journal of Applied Physics Part 1-Regular Papers Short Notes & Review Papers*, **43**[9B] 6662-6 (2004).
- [61] E. Hollenstein, D. Damjanovic, and N. Setter, "Temperature stability of the piezoelectric properties of Li-modified KNN ceramics," *Journal of the European Ceramic Society*, **27**[13-15] 4093-7 (2007).
- [62] P. Ben Ishai, C. E. M. de Oliveira, Y. Ryabov, A. J. Agranat, and Y. Feldman, "Unusual glass-like systems - relaxation dynamics of  $Cu^+$  ions in ferroelectric KTN crystals," *Journal of Non-Crystalline Solids*, **351**[33-36] 2786-92 (2005).
- [63] A. Reisman, F. Holtzberg, and M. Berkenblit, "Metastability in niobate systems," *Journal of the American Chemical Society*, **81**[6] 1292-5 (1959).
- [64] E. Ringgaard, T. Wurlitzer, and W. W. Wolny, "Properties of lead-free piezoceramics based on alkali niobates," *Ferroelectrics*, **319** 323-33 (2005).
- [65] S. Lanfredi, L. Dessemond, and A. C. Martins Rodrigues, "Dense ceramics of  $NaNbO_3$  produced from powders prepared by a new chemical route," *Journal of the European Ceramic Society*, **20**[7] 983-90 (2000).
- [66] S. J. Zhang, R. Xia, T. R. Shrout, G. Z. Zang, and J. F. Wang, "Characterization of lead free  $(K_{0.5}Na_{0.5})NbO_3$ - $LiSbO_3$  piezoceramic," *Solid State Communications*, **141**[12] 675-9 (2007).
- [67] J. Xu, D. Xue, and C. Yan, "Chemical synthesis of  $NaTaO_3$  powder at low-temperature," *Materials Letters*, **59**[23] 2920-2 (2005).
- [68] B. P. Zhang, J. F. Li, K. Wang, and H. L. Zhang, "Compositional dependence of piezoelectric properties in  $Na_xK_{1-x}NbO_3$  lead-free ceramics prepared by spark plasma sintering," *Journal of the American Ceramic Society*, **89**[5] 1605-9 (2006).
- [69] M. Matsubara, T. Yamaguchi, K. Kikuta, and S. Hirano, "Effect of Li substitution on the piezoelectric properties of potassium sodium niobate ceramics," *Japanese Journal of Applied Physics, Part 1: Regular Papers, Short Notes & Review Papers*, **44**[8] 6136-42 (2005).
- [70] M.-S. Kim, D.-S. Lee, E.-C. Park, S.-J. Jeong, and J.-S. Song, "Effect of  $Na_2O$  additions on the sinterability and piezoelectric properties of lead-free  $95(Na_{0.5}K_{0.5})NbO_3$ - $5LiTaO_3$  ceramics," *Journal of the European Ceramic Society*, **27**[13-15] 4121-4 (2007).
- [71] Z. Yang, Y. F. Chang, B. Liu, and L. L. Wei, "Effects of composition on phase structure, microstructure and electrical properties of  $(K_{0.5}Na_{0.5})NbO_3$ - $LiSbO_3$  ceramics," *Materials Science & Engineering, A: Structural Materials: Properties, Microstructure and Processing*, **432**[1-2] 292-8 (2006).
- [72] R.-C. Chang, S.-Y. Chu, Y.-F. Lin, C.-S. Hong, and Y.-P. Wong, "An investigation of  $(Na_{0.5}K_{0.5})NbO_3$ - $CaTiO_3$  based lead-free ceramics and surface acoustic wave devices," *Journal of the European Ceramic Society*, **27**[16] 4453-60 (2007).



- [73] A. Saito, S. Uraki, H. Kakemoto, T. Tsurumi, and S. Wada, "Growth of lithium doped silver niobate single crystals and their piezoelectric properties," *Materials Science and Engineering B-Solid State Materials for Advanced Technology*, **120**[1-3] 166-9 (2005).
- [74] W. You-Bao, Y. Pei-Zhi, W. Yu-Rong, Z. Hai-Bing, T. Jia, and Y. Hui, "The influence of composition on optical properties of ferroelectric potassium lithium niobate single crystals," *Optical Materials*, **29**[12] 1746-50 (2007).
- [75] H. Takao, Y. Saito, Y. Aoki, and K. Horibuchi, "Microstructural evolution of crystalline-oriented  $(K_{0.5}Na_{0.5})NbO_3$  piezoelectric ceramics with a sintering aid of  $CuO$ ," *Journal of the American Ceramic Society*, **89**[6] 1951-6 (2006).
- [76] K. H. Ryu, J. A. Cho, T. K. Song, M. H. Kim, S. S. Kim, H. S. Lee, S. J. Jeong, J. S. Song, and K. S. Choi, "Microstructure and piezoelectric properties of lead-free niobate ceramics," *Ferroelectrics*, **338** 1473-9 (2006).
- [77] V. Lingwal and N. S. Panwar, "Morphotropic phase transitions in mixed sodium-potassium niobate system," *Ferroelectrics*, **300** 3-14 (2004).
- [78] G. Z. Zang, J. F. Wang, H. C. Chen, W. B. Su, C. M. Wang, P. Qi, B. Q. Ming, J. Du, and L. M. Zheng, "Perovskite  $(Na_{0.5}K_{0.5})_{1-x}(LiSb)_xNb_{1-x}O_3$  lead-free piezoceramics," *Applied Physics Letters*, **88**[21] 212908 (2006).
- [79] R. Zuo, X. Fang, and C. Ye, "Phase structures and electrical properties of new lead-free  $(Na_{0.5}K_{0.5})NbO_3-(Bi_{0.5}Na_{0.5})TiO_3$  ceramics," *Applied Physics Letters*, **90**[9] 092904-3 (2007).
- [80] Z. P. Yang, Y. F. Chang, and L. L. Wei, "Phase transitional behavior and electrical properties of lead-free  $(K_{0.44}Na_{0.52}Li_{0.04})(Nb_{0.96-x}Ta_xSb_{0.04})O_3$  piezoelectric ceramics," *Applied Physics Letters*, **90**[4] 042911 (2007).
- [81] M. Matsubara, T. Yamaguchi, K. Kikuta, and S. Hirano, "Sinterability and piezoelectric properties of  $(K,Na)NbO_3$  ceramics with novel sintering aid," *Japanese Journal of Applied Physics Part 1-Regular Papers Brief Communications & Review Papers*, **43**[10] 7159-63 (2004).
- [82] R. Z. Zuo, J. Rödel, R. Z. Chen, and L. T. Li, "Sintering and electrical properties of lead-free  $Na_{0.5}K_{0.5}NbO_3$  piezoelectric ceramics," *Journal of the American Ceramic Society*, **89**[6] 2010-5 (2006).
- [83] M. Matsubara, T. Yamaguchi, K. Kikuta, and S. Hirano, "Sintering and piezoelectric properties of potassium sodium niobate ceramics with newly developed sintering aid," *Japanese Journal of Applied Physics Part 1-Regular Papers Short Notes & Review Papers*, **44**[1A] 258-63 (2005).
- [84] F. Rubio-Marcos, P. Ochoa, and J. F. Fernandez, "Sintering and properties of lead-free  $(K,Na,Li)(Nb,Ta,Sb)O_3$  ceramics," *Journal of the European Ceramic Society*, **27**[13-15] 4125-9 (2007).
- [85] M. Matsubara, T. Yamaguchi, K. Kikuta, and S. Hirano, "Synthesis and characterization of  $(K_{0.5}Na_{0.5})(Nb_{0.7}Ta_{0.3})O_3$  piezoelectric ceramics sintered with sintering aid  $K_{5.4}Cu_{1.3}Ta_{10}O_{29}$ ," *Japanese Journal of Applied Physics Part 1-Regular Papers Brief Communications & Review Papers*, **44**[9A] 6618-23 (2005).
- [86] A. Aydi, H. Khemakhem, C. Boudaya, A. Simon, and R. Von der Muhll, "X-ray and dielectric studies of ferroelectric or relaxor phases in the  $Ca_{1-x}Na_xSn_{1-x}Nb_xO_3$  system," *Solid State Sciences*, **7**[3] 249-55 (2005).
- [87] I. Masuda, K. I. Kakimoto, and H. Ohsato, "Ferroelectric property and crystal structure of  $KNbO_3$  based ceramics," *Journal of Electroceramics*, **13**[1-3] 555-9 (2004).
- [88] J. G. Fisher, A. Bencan, J. Bernard, J. Holc, M. Kosec, S. Vernay, and D. Rytz, "Growth of  $(Na, K, Li)(Nb, Ta)O_3$  single crystals by solid state crystal growth," *Journal of the European Ceramic Society*, **27**[13-15] 4103-6 (2007).
- [89] Y. Saito and H. Takao, "High performance lead-free piezoelectric ceramics in the  $(K,Na)NbO_3-LiTaO_3$  solid solution system," *Ferroelectrics*, **338** 1433-48 (2006).
- [90] B. Malic, J. Bernard, J. Holc, and M. Kosec, "Strontium doped  $K_{0.5}M_{0.5}NbO_3$  based piezoceramics," *Ferroelectrics*, **314** 149-56 (2005).
- [91] A. Reisman, F. Holtzberg, S. Triebwasser, and M. Berkenblit, "Preparation of pure potassium metaniobate," *Journal of the American Chemical Society*, **78**[4] 719-20 (1956).
- [92] T. Rojac, M. Kosec, B. Malic, and J. Holc, "Mechanochemical synthesis of  $NaNbO_3$ ,  $KNbO_3$  and  $K_{0.5}Na_{0.5}NbO_3$ ," *Science of Sintering*, **37**[1] 61-7 (2005).
- [93] S. C. Abrahams, W. C. Hamilton, and J. M. Reddy, "Ferroelectric lithium niobate. 4. Single crystal neutron diffraction study at  $24^\circ C$ ," *Journal of Physics and Chemistry of Solids*, **27**[6-7] 1013-8 (1966).
- [94] G. H. Haertling, "Properties of hot-pressed ferroelectric alkali niobate ceramics," *Journal of the American Ceramic Society*, **50**[6] 329-30 (1967).
- [95] R. P. Wang, R. J. Xie, T. Sekiya, and Y. Shimojo, "Fabrication and characterization of potassium-sodium niobate piezoelectric ceramics by spark-plasma-sintering method," *Materials Research Bulletin*, **39**[11] 1709-15 (2004).
- [96] L. E. Cross, "Electric Double Hysteresis in  $(K_xNa_{1-x})NbO_3$  Single Crystals," *Nature*, **181**[4603] 178-9 (1958).

- [97] I. P. Raevskii, L. A. Reznichenko, M. P. Ivliev, V. G. Smotrakov, V. V. Eremkin, M. A. Malitskaya, L. A. Shilkina, S. I. Shevtsova, and A. V. Borodin, "Growth and study of single crystals of (Na, K)NbO<sub>3</sub> solid solutions," *Crystallography Reports*, **48**[3] 486-90 (2003).
- [98] R. Ilangoan, S. Balakumar, and C. Subramanian, "Growth and characterisation of KNbO<sub>3</sub> single crystals," *Materials Science and Technology*, **15**[2] 132-6 (1999).
- [99] Y. Kizaki, Y. Noguchi, and M. Miyayama, "Defect control for low leakage current in K<sub>0.5</sub>Na<sub>0.5</sub>NbO<sub>3</sub> single crystals," *Applied Physics Letters*, **89**[14] 142910 (2006).
- [100] J. G. Fisher, A. Bencan, M. Kosec, S. Vernay, and D. Rytz, "Growth of dense single crystals of potassium sodium niobate by a combination of solid-state crystal growth and hot pressing," *Journal of the American Ceramic Society*, **91**[5] 1503-7 (2008).
- [101] K. Chen, G. S. Xu, D. F. Yang, X. F. Wang, and J. B. Li, "Dielectric and piezoelectric properties of lead-free 0.95(K<sub>0.5</sub>Na<sub>0.5</sub>)NbO<sub>3</sub>-0.05LiNbO<sub>3</sub> crystals grown by the Bridgman method," *Journal of Applied Physics*, **101**[4] - (2007).
- [102] T. Yamazaki, A. Onodera, H. Fujishita, Y. Ishikawa, and M. Tanaka, "Thermal Behavior and phase transition in PZT near the morphotropic phase boundary," *Ferroelectrics*, **266** 139-51 (2002).
- [103] V. M. Kugler, F. Söderlind, D. Music, U. Helmersson, J. Andreasson, and T. Lindbäck, "Low temperature growth and characterization of (Na,K)NbO<sub>x</sub> thin films," *Journal of Crystal Growth*, **254**[3-4] 400-4 (2003).
- [104] V. M. Kugler, F. Söderlind, D. Music, U. Helmersson, J. Andreasson, and T. Lindbäck, "Microstructure/dielectric property relationship of low temperature synthesised (Na,K)NbO<sub>x</sub> thin films," *Journal of Crystal Growth*, **262**[1-4] 322-6 (2004).
- [105] X. Wang, S. Olafsson, L. D. Madsen, S. Rudner, I. P. Ivanov, A. Grishin, and U. Helmersson, "Growth and characterization of Na<sub>0.5</sub>K<sub>0.5</sub>NbO<sub>3</sub> thin films on polycrystalline Pt<sub>80</sub>Ir<sub>20</sub> substrates," *Journal of Materials Research*, **17**[5] 1183-91 (2002).
- [106] T. Saito, T. Wada, H. Adachi, and I. Kanno, "Pulsed laser deposition of high-quality (K,Na)NbO<sub>3</sub> thin films on SrTiO<sub>3</sub> substrate using high-density ceramic targets," *Japanese Journal of Applied Physics Part 1- Regular Papers Short Notes & Review Papers*, **43**[9B] 6627-31 (2004).
- [107] C.-R. Cho and A. Grishin, "Self-assembling ferroelectric Na<sub>0.5</sub>K<sub>0.5</sub>NbO<sub>3</sub> thin films by pulsed-laser deposition," *Applied Physics Letters*, **75**[2] 268-70 (1999).
- [108] M. Abazari, E. K. Akdogan, and A. Safari, "Effect of manganese doping on remnant polarization and leakage current in (K<sub>0.44</sub>Na<sub>0.52</sub>Li<sub>0.04</sub>)(Nb<sub>0.84</sub>Ta<sub>0.10</sub>Sb<sub>0.06</sub>)O<sub>3</sub> epitaxial thin films on SrTiO<sub>3</sub>," *Applied Physics Letters*, **92**[21] 212903-3 (2008).
- [109] F. Söderlind, P.-O. Käll, and U. Helmersson, "Sol-gel synthesis and characterization of Na<sub>0.5</sub>K<sub>0.5</sub>NbO<sub>3</sub> thin films," *Journal of Crystal Growth*, **281**[2-4] 468-74 (2005).
- [110] K. Tanaka, K.-I. Kakimoto, and H. Ohsato, "Fabrication of highly oriented lead-free (Na, K)NbO<sub>3</sub> thin films at low temperature by Sol-Gel process," *Journal of Crystal Growth*, **294**[2] 209-13 (2006).
- [111] C. Schroeter, B. Wessler, and L. M. Eng, "High throughput method for K<sub>0.5</sub>Na<sub>0.5</sub>NbO<sub>3</sub> thin films preparation by chemical solution deposition," *Journal of the European Ceramic Society*, **27**[13-15] 3785-8 (2007).
- [112] C.-R. Cho, "C-Axis oriented (Na,K)NbO<sub>3</sub> thin films on Si substrates using metalorganic chemical vapor deposition," *Materials Letters*, **57**[4] 781-6 (2002).
- [113] P. Zhao and B.-P. Zhang, "High Piezoelectric d<sub>33</sub> Coefficient in Li/Ta/Sb-Codoped Lead-Free (Na,K)NbO<sub>3</sub> Ceramics Sintered at Optimal Temperature," *Journal of the American Ceramic Society*, **91**[9] 3078-81 (2008).
- [114] E. K. Akdogan, K. Kerman, M. Abazari, and A. Safari, "Origin of high piezoelectric activity in ferroelectric (K<sub>0.44</sub>Na<sub>0.52</sub>Li<sub>0.04</sub>) - (Nb<sub>0.84</sub>Ta<sub>0.10</sub>Sb<sub>0.06</sub>)O<sub>3</sub> ceramics," *Applied Physics Letters*, **92**[11] 112908-3 (2008).
- [115] J. G. Wu, D. Q. Xiaob, Y. Y. Wang, J. G. Zhu, L. Wu, and Y. H. Jiang, "Effects of K/Na ratio on the phase structure and electrical properties of (K<sub>x</sub>Na<sub>0.96-x</sub>Li<sub>0.04</sub>)(Nb<sub>0.91</sub>Ta<sub>0.05</sub>Sb<sub>0.04</sub>)O<sub>3</sub> lead-free ceramics," *Applied Physics Letters*, **91**[25] 252907 (2007).
- [116] J. Wu, D. Xiao, Y. Wang, W. Wu, B. Zhang, and J. Zhu, "Improved temperature stability of CaTiO<sub>3</sub>-modified [(K<sub>0.5</sub>Na<sub>0.5</sub>)<sub>0.96</sub>Li<sub>0.04</sub>](Nb<sub>0.91</sub>Sb<sub>0.05</sub>Ta<sub>0.04</sub>)O<sub>3</sub> lead-free piezoelectric ceramics," *Journal of Applied Physics*, **104**[2] 024102-4 (2008).
- [117] R. Zuo, Z. Xu, and L. Li, "Dielectric and piezoelectric properties of Fe<sub>2</sub>O<sub>3</sub>-doped (Na<sub>0.5</sub>K<sub>0.5</sub>)<sub>0.96</sub>Li<sub>0.04</sub>Nb<sub>0.86</sub>Ta<sub>0.1</sub>Sb<sub>0.04</sub>O<sub>3</sub> lead-free ceramics," *Journal of Physics and Chemistry of Solids*, **69**[7] 1728-32 (2008).
- [118] J. G. Wu, T. Peng, Y. Y. Wang, D. Q. Xiao, J. M. Zhu, Y. Jin, J. Zhu, P. Yu, L. Wu, and Y. H. Jiang, "Phase structure and electrical properties of (K<sub>0.48</sub>Na<sub>0.52</sub>)(Nb<sub>0.95</sub>Ta<sub>0.05</sub>)O<sub>3</sub>-LiSbO<sub>3</sub> lead-free piezoelectric ceramics," *Journal of the American Ceramic Society*, **91**[1] 319-21 (2008).
- [119] Y. F. Chang, Z. P. Yang, and L. L. Wei, "Microstructure, density, and dielectric properties of lead-free (K<sub>0.44</sub>Na<sub>0.52</sub>Li<sub>0.04</sub>)(Nb<sub>0.96-x</sub>Ta<sub>x</sub>Sb<sub>0.04</sub>)O<sub>3</sub> piezoelectric ceramics," *Journal of the American Ceramic Society*, **90**[5] 1656-8 (2007).

- [120] Y. F. Chang, Z. P. Yang, Y. T. Hou, Z. H. Liu, and Z. L. Wang, "Effects of Li content on the phase structure and electrical properties of lead-free  $(K_{0.46-x/2}Na_{0.54-x/2}Li_x)(Nb_{0.76}Ta_{0.20}Sb_{0.04})O_3$  ceramics," *Applied Physics Letters*, **90**[23] 232905 (2007).
- [121] J. Wu, Y. Wang, D. Xiao, J. Zhu, and Z. Pu, "Effects of Ag content on the phase structure and piezoelectric properties of  $(K_{0.44-x}Na_{0.52}Li_{0.04}Ag_x)(Nb_{0.91}Ta_{0.05}Sb_{0.04})O_3$  lead-free ceramics," *Applied Physics Letters*, **91**[13] 132914-3 (2007).
- [122] Y. Dai, X. Zhang, and G. Zhou, "Phase transitional behavior in  $K_{0.5}Na_{0.5}NbO_3$ -LiTaO<sub>3</sub> ceramics," *Applied Physics Letters*, **90**[26] 262903-3 (2007).
- [123] P. Bomlai, P. Sinsap, S. Muensit, and S. J. Milne, "Effect of MnO on the Phase Development, Microstructures, and Dielectric Properties of  $0.95Na_{0.5}K_{0.5}NbO_3$ -0.05LiTaO<sub>3</sub> Ceramics," *Journal of the American Ceramic Society*, **91**[2] 624-7 (2008).
- [124] D. Lin, K. W. Kwok, and H. L. W. Chan, "Microstructure, phase transition, and electrical properties of  $(K_{0.5}Na_{0.5})_{1-x}Li_x(Nb_{1-y}Ta_y)O_3$  lead-free piezoelectric ceramics," *Journal of Applied Physics*, **102**[3] 034102-7 (2007).
- [125] Y. Chang, Z.-P. Yang, D. Ma, Z. Liu, and Z. Wang, "Phase transitional behavior, microstructure, and electrical properties in Ta-modified  $[(K_{0.458}Na_{0.542})_{0.96}Li_{0.04}]NbO_3$  lead-free piezoelectric ceramics," *Journal of Applied Physics*, **104**[2] 024109-8 (2008).
- [126] K. Higashide, K.-I. Kakimoto, and H. Ohsato, "Temperature dependence on the piezoelectric property of  $(1-x)(Na_{0.5}K_{0.5})NbO_3$ -xLiNbO<sub>3</sub> ceramics," *Journal of the European Ceramic Society*, **27**[13-15] 4107-10 (2007).
- [127] P. Zhao, B.-P. Zhang, and J.-F. Li, "High piezoelectric  $d_{33}$  coefficient in Li-modified lead-free  $(Na,K)NbO_3$  ceramics sintered at optimal temperature," *Applied Physics Letters*, **90**[24] 242909-3 (2007).
- [128] H. L. Du, W. C. Zhou, F. Luo, D. M. Zhu, S. B. Qu, and Z. B. Pei, "An approach to further improve piezoelectric properties of  $(K_{0.5}Na_{0.5})NbO_3$ -based lead-free ceramics," *Applied Physics Letters*, **91**[20] 202907 (2007).
- [129] X. K. Niu, J. L. Zhang, L. Wu, P. Zheng, M. L. Zhao, and C. L. Wang, "Crystalline structural phase boundaries in  $(K,Na,Li)NbO_3$  ceramics," *Solid State Communications*, **146**[9-10] 395-8 (2008).
- [130] H. C. Song, K. H. Cho, H. Y. Park, C. W. Ahn, S. Nahm, K. Uchino, S. H. Park, and H. G. Lee, "Microstructure and piezoelectric properties of  $(1-x)(Na_{0.5}K_{0.5})NbO_3$ -xLiNbO<sub>3</sub> ceramics," *Journal of the American Ceramic Society*, **90**[6] 1812-6 (2007).
- [131] J. G. Wu, Y. Y. Wang, D. Q. Xiao, J. U. Zhu, P. Yu, L. Wu, and W. J. Wu, "Piezoelectric properties of LiSbO<sub>3</sub>-Modified  $(K_{0.48}Na_{0.52})NbO_3$  lead-free ceramics," *Japanese Journal of Applied Physics Part 1- Regular Papers Brief Communications & Review Papers*, **46**[11] 7375-7 (2007).
- [132] J. G. Wu, D. Q. Xiao, Y. Y. Wang, J. G. Zhu, and P. Yu, "Effects of K content on the dielectric, piezoelectric, and ferroelectric properties of  $0.95(K_xNa_{1-x})NbO_3$ -0.05LiSbO<sub>3</sub> lead-free ceramics," *Journal of Applied Physics*, **103**[2] 024102 (2008).
- [133] J. Wu, D. Xiao, Y. Wang, W. Wu, B. Zhang, J. Li, and J. Zhu, "CaTiO<sub>3</sub>-modified  $[(K_{0.5}Na_{0.5})_{0.94}Li_{0.06}](Nb_{0.94}Sb_{0.06})O_3$  lead-free piezoelectric ceramics with improved temperature stability," *Scripta Materialia*, **59**[7] 750-2 (2008).
- [134] L. Wu, D. Xiao, J. Wu, Y. Sun, D. Lin, J. Zhu, P. Yu, Y. Zhuang, and Q. Wei, "Good temperature stability of  $K_{0.5}Na_{0.5}NbO_3$  based lead-free ceramics and their applications in buzzers," *Journal of the European Ceramic Society*, **28**[15] 2963-8 (2008).
- [135] Y. G. Lv, C. L. Wang, J. L. Zhang, M. L. Zhao, M. K. Li, and H. C. Wang, "Modified  $(K_{0.5}Na_{0.5})(Nb_{0.9}Ta_{0.1})O_3$  ceramics with high  $Q_m$ ," *Materials Letters*, **62**[19] 3425-7 (2008).
- [136] Y. G. Lv, C. L. Wang, J. L. Zhang, L. Wu, M. L. Zhao, and J. P. Xu, "Tantalum influence on physical properties of  $(K_{0.5}Na_{0.5})(Nb_{1-x}Ta_x)O_3$  ceramics," *Materials Research Bulletin*, **44**[2] 284-7 (2009).
- [137] Q. Chen, L. Chen, Q. Li, X. Yue, D. Xiao, J. Zhu, X. Shi, and Z. Liu, "Piezoelectric properties of  $K_4CuNb_8O_{23}$  modified  $(Na_{0.5}K_{0.5})NbO_3$  lead-free piezoceramics," *Journal of Applied Physics*, **102**[10] 104109-4 (2007).
- [138] S.-J. Park, H.-Y. Park, K.-H. Cho, S. Nahm, H.-G. Lee, D.-H. Kim, and B.-H. Choi, "Effect of CuO on the sintering temperature and piezoelectric properties of lead-free  $0.95(Na_{0.5}K_{0.5})NbO_3$ -0.05CaTiO<sub>3</sub> ceramics," *Materials Research Bulletin*, **43**[12] 3580-6 (2008).
- [139] H.-Y. Park, C.-W. Ahn, K.-H. Cho, S. Nahm, H.-G. Lee, H.-W. Kang, D.-H. Kim, and K.-S. Park, "Low-Temperature Sintering and Piezoelectric Properties of CuO-Added  $0.95(Na_{0.5}K_{0.5})NbO_3$ -0.05BaTiO<sub>3</sub> Ceramics," *Journal of the American Ceramic Society*, **90**[12] 4066-9 (2007).
- [140] D. Lin, K. W. Kwok, and H. L. W. Chan, "Structure, dielectric, and piezoelectric properties of CuO-doped  $K_{0.5}Na_{0.5}NbO_3$ -BaTiO<sub>3</sub> lead-free ceramics," *Journal of Applied Physics*, **102**[7] 074113 (2007).
- [141] E. Li, H. Kakimoto, S. Wada, and T. Tsurumi, "Influence of CuO on the structure and piezoelectric properties of the alkaline niobate-based lead-free ceramics," *Journal of the American Ceramic Society*, **90**[6] 1787-91 (2007).

- [142] S. Zhang, R. Xia, H. Hao, H. Liu, and T. R. Shrout, "Mitigation of thermal and fatigue behavior in  $K_{0.5}Na_{0.5}NbO_3$ -based lead free piezoceramics," *Applied Physics Letters*, **92**[15] 152904-3 (2008).
- [143] S. Zhang, R. Xia, and T. R. Shrout, "Modified  $(K_{0.5}Na_{0.5})NbO_3$  based lead-free piezoelectrics with broad temperature usage range," *Applied Physics Letters*, **91**[13] 132913-3 (2007).
- [144] H. L. Du, W. C. Zhou, F. Luo, D. M. Zhu, S. B. Qu, Y. Li, and Z. B. Pei, "Design and electrical properties' investigation of  $(K_{0.5}Na_{0.5})NbO_3$ -BiMeO<sub>3</sub> lead-free piezoelectric ceramics," *Journal of Applied Physics*, **104**[3] (2008).
- [145] R. P. Wang, R. J. Xie, K. Hanada, K. Matsusaki, H. Bando, and M. Itoh, "Phase diagram and enhanced piezoelectricity in the strontium titanate doped potassium-sodium niobate solid solution," *Physica Status Solidi a-Applications and Materials Science*, **202**[6] R57-R9 (2005).
- [146] I. Pibosic, D. Makovec, and M. Drofenik, "Electrical properties of  $KNbO_3$ -BaTiO<sub>3</sub> ceramics," *Euro Ceramics VII, Pt 1-3*, **206-2** 1401-4 (2002).
- [147] H. Y. Park, C. W. Ahn, H. C. Song, J. H. Lee, S. Nahm, K. Uchino, H. G. Lee, and H. J. Lee, "Microstructure and piezoelectric properties of  $0.95(Na_{0.5}K_{0.5})NbO_3$ -0.05BaTiO<sub>3</sub> ceramics," *Applied Physics Letters*, **89**[6] - (2006).
- [148] H. Du, W. Zhou, D. Zhu, L. Fa, S. Qu, Y. Li, and Z. Pei, "Sintering Characteristic, Microstructure, and Dielectric Relaxor Behavior of  $(K_{0.5}Na_{0.5})NbO_3$ -( $Bi_{0.5}Na_{0.5}$ )TiO<sub>3</sub> Lead-Free Ceramics," *Journal of the American Ceramic Society*, **91**[9] 2903-9 (2008).
- [149] T. Wada, K. Toyoiike, Y. Imanaka, and Y. Matsuo, "Dielectric and piezoelectric properties of  $(A_{0.5}Bi_{0.5})TiO_3$ -ANbO<sub>3</sub> (A = Na, K) systems," *Japanese Journal of Applied Physics Part 1-Regular Papers Short Notes & Review Papers*, **40**[9B] 5703-5 (2001).
- [150] T. Takenaka, T. Okuda, and K. Takegahara, "Lead-free piezoelectric ceramics based on  $(Bi_{1/2}Na_{1/2})TiO_3$ -NaNbO<sub>3</sub>," *Ferroelectrics*, **196**[1-4] 175-8 (1997).
- [151] H. Nagata and T. Takenaka, "Lead-free piezoelectric ceramics of  $(Bi_{1/2}Na_{1/2})TiO_3$ -KNbO<sub>3</sub>-1/2( $Bi_2O_3$ .Sc<sub>2</sub>O<sub>3</sub>) system," *Japanese Journal of Applied Physics Part 1-Regular Papers Short Notes & Review Papers*, **37**[9B] 5311-4 (1998).
- [152] J. Ravez and A. Simon, "Relaxor ferroelectricity in ceramics with composition  $Ba_{1-x}K_x(Ti_{1-x}Nb_x)O_3$ ," *Materials Letters*, **36**[1-4] 81-4 (1998).
- [153] R. Zuo, C. Ye, and X. Fang, " $Na_{0.5}K_{0.5}NbO_3$ -BiFeO<sub>3</sub> lead-free piezoelectric ceramics," *Journal of Physics and Chemistry of Solids*, **69**[1] 230-5 (2008).
- [154] R. Z. Zuo, X. S. Fang, C. Ye, and L. T. Li, "Phase transitional behavior and piezoelectric properties of lead-free  $(Na_{0.5}K_{0.5})NbO_3$ -( $Bi_{0.5}K_{0.5}$ )TiO<sub>3</sub> ceramics," *Journal of the American Ceramic Society*, **90**[8] 2424-8 (2007).
- [155] Y. Dai and X. Zhang, "Phase transition behavior and electrical properties of lead-free  $(1-x)(0.98K_{0.5}Na_{0.5}NbO_3$ -0.02LiTaO<sub>3</sub>)-x(0.96Bi<sub>0.5</sub>Na<sub>0.5</sub>TiO<sub>3</sub>-0.04BaTiO<sub>3</sub>) piezoelectric ceramics," *Journal of the European Ceramic Society*, **28**[16] 3193-8.
- [156] Y. Wang, J. Wu, D. Xiao, W. Wu, B. Zhang, J. Zhu, P. Yu, and L. Wu, "High Curie temperature of (Li, K, Ag)-modified  $(K_{0.50}Na_{0.50})NbO_3$  lead-free piezoelectric ceramics," *Journal of Alloys and Compounds*, **472** L6-L8 (2009).
- [157] Y. W. Wang, Jiagang; Xiao, Dingquan; Wu, Wenjuan; Zhang, Bing; Wu, Lang; Zhu, Jianguo "Microstructure and Electrical Properties of  $[(K_{0.50}Na_{0.50})0.95-xLi_{0.05}Ag_x](Nb_{0.95}Ta_{0.05})O_3$  Lead-Free Ceramics," *Journal of the American Ceramic Society*, **91**[8] 2772-5 (2008).
- [158] D. Lin, K. W. Kwok, and H. L. W. Chan, "Piezoelectric and ferroelectric properties of  $K_xNa_{1-x}NbO_3$  lead-free ceramics with MnO<sub>2</sub> and CuO doping," *Journal of Alloys and Compounds*, **461**[1-2] 273-8 (2008).
- [159] S. H. Park, C. W. Ahn, S. Nahm, and J. S. Song, "Microstructure and piezoelectric properties of ZnO-added  $(Na_{0.5}K_{0.5})NbO_3$  ceramics," *Japanese Journal of Applied Physics Part 2-Letters & Express Letters*, **43**[8B] L1072-L4 (2004).
- [160] B. Malic, J. Bernard, A. Bencan, and M. Kosec, "Influence of zirconia addition on the microstructure of  $K_{0.5}Na_{0.5}NbO_3$  ceramics," *Journal of the European Ceramic Society*, **28**[6] 1191-6 (2008).
- [161] H. Du, D. Liu, F. Tang, D. Zhu, W. Zhou, and S. Qu, "Microstructure, Piezoelectric, and Ferroelectric Properties of Bi<sub>2</sub>O<sub>3</sub>-Added  $(K_{0.5}Na_{0.5})NbO_3$  Lead-Free Ceramics," *Journal of the American Ceramic Society*, **90**[9] 2824-9 (2007).

## 2.3.8 Tables of Properties of KNN-Based Materials

### 2.3.8.1 KNN (Pure)

Tab 9: Properties of  $K_{0.5}Na_{0.5}NbO_3$  (unmodified)

Piezoelectric coefficients ( $d_{33}$ [pC/N])			
	Value	Chemical Composition	Reference
	80	KNN	[1]
	120	KNN	[2]
	115	KNN	[3]
	98	KNN	[4]
	70	KNN	[5]
	97	KNN	[6]
	100	KNN	[7]

Piezoelectric Voltage Coefficient [mV*m/N])			
	Value	Chemical Composition	Reference
	12.6 (g31)	KNN	[1]
	31.5 (g33)	KNN	[1]

Poisson's Ratio [no units]			
	Value	Chemical Composition	Reference
	0.27	KNN	[1]
	0.27	KNN	[8]

Phase transition temperatures( $T_{O-T}$ <sup>23</sup> / $T_d$ <sup>24</sup> / $T_c$ [°C])			
	Value	Chemical Composition	Reference
	410 ( $T_c$ )	KNN	[1]
	400 ( $T_c$ )	KNN	[2]
	420 ( $T_c$ )	KNN	[4]

Young's modulus [N/m <sup>2</sup> ]			
	Value	Chemical Composition	Reference
	$1.04 \times 10^{11}$	KNN	[1]

<sup>23</sup>  $T_{O-T}$ : refers to the phase transition between orthorhombic and tetragonal in alkali niobate-based systems.

<sup>24</sup>  $T_d$ : refers to the phase transition between room temperature ferroelectric phase and a high temperature phase in BNT-based materials, which is commonly regarded as antiferroelectric or non-polar.

Relative Dielectric Constant ( $\epsilon$ [no units])			
	Value	Chemical Composition	Reference
	290	KNN	[1]
	230	KNN	[9]
	475	KNN	[3]
	450	KNN	[10]
	470	KNN	[9]
	402	KNN	[6]
	420	KNN (HP)	[11]
	400	KNN	[5]

Coercive Field ( $E_C$ [kV/mm])			
	Value	Chemical Composition	Reference
	1.2 (150 °C)	KNN	[3]
	1.4 (150 °C)	KNN	[12]
	1.0-1.3	KNN	[13]
	0.4	KNN (HP)	[14]
	1.0	KNN	[13]

Resistivity ( $[\Omega m]$ )			
	Value	Chemical Composition	Reference
	$10^{12}$	KNN	[1]

Frequency Constant ( $[Hz \cdot m]$ )			
	Value	Chemical Composition	Reference
	1.67	KNN	[1]

Loss Tangent ( $\tan\delta$ [%])			
	Value	Chemical Composition	Reference
	4	KNN	[1]
	1.9	KNN	[9]
	6.8	KNN	[15]
	2	KNN	[5]
	5	KNN	[7]

Electromechanical coupling factor ( $k_{33}$ [no units])			
	Value	Chemical Composition	Reference
	0.51	KNN	[8]
	0.55	KNN	[8]

Electromechanical coupling factor ( $k_p$ [no units])			
	Value	Chemical Composition	Reference
	0.34-0.39	KNN	[1]
	0.4	KNN	[2]
	0.38	KNN	[3]
	0.36-0.45	KNN	[8]
	0.45	KNN	[14]
	0.295	KNN	[4]
	0.25	KNN	[5]

Electromechanical coupling factor ( $k_t$ [no units])			
	Value	Chemical Composition	Reference
	0.41	KNN	[15]
	0.38	KNN	[5]

Relative Density ([no units])			
	Value	Chemical Composition	Reference
	94-97	KNN	[1]
	97.6	KNN	[2]
	98.8-99.8	KNN (HP)	[14]
	97.6	KNN	[3]
	95	KNN	[16]

Remanent Polarisation ( $P_r$ [ $\mu\text{C}/\text{cm}^2$ ])			
	Value	Chemical Composition	Reference
	12,5 (150°C/60Hz)	KNN	[3]
	32	KNN	[14]
	14-21	KNN	[13]
	8-16	KNN	[7]

Piezoelectric charge coefficient $d_{31}$ [pC/N]			
	Value	Chemical Composition	Reference
	32	KNN	[1]
	31	KNN	[5]

Mechanical Quality Factor ( $Q_m$ [no units])			
	Value	Chemical Composition	Reference
	210	KNN	[2]
	270	KNN	[3]
	130-240	KNN	[8]

### 2.3.8.2 KNN (modified)

**Tab 10: Properties of  $K_{0.5}Na_{0.5}NbO_3$  (Modified)**

Piezoelectric coefficients ( $d_{33}$ [pC/N])			
	Value	Chemical Composition	Reference
	115	KNN100-97,CT0-3	[3]
	230	KNN95, LT5, Na0-2	[17]
	54	(K44Na52Li4)(Nb86Ta10Sb4)O3	[18]
	103	(K44Na52Li4)(Nb86Ta10Sb4)O3	[18]
	170	(K38Na52Li4)(Nb86Ta10Sb4)O3	[18]
	195	(K38Na52Li4)(Nb86Ta10Sb4)O3	[18]
	104	KNN98-BT2	[15]
	82 - 235	Li0-7KN100-93NbO3	[6]
	30-97	KNN90-100-ST 0-10	[6]
	90	KNN99.5 - Sr0.5	[5]
	110	KNN99 - Sr1	[5]
	~100-123	KNN91-100 – ZnO0-9	[7]
	416 (textured)	(K44Na52Li4)(Nb84Ta10Sb6)	[19]
	97	KNN+Cu	[20]
	180 ( $d_{33}^*$ )	KNN+Cu	[13]
	200	KNN+Cu	[21]
	193	KNN-BT+Cu	[22]
	105-108	KNN+Mn+Cu	[23]
	194	KNN-BT+Mn	[24]
	121	KNN+Sr+Mn	[25]

Phase transition temperatures( $T_{O-T}^{25}/T_d^{26}/T_c[^\circ C]$ )			
	Value	Chemical Composition	Reference
	400	KNN100-97,CT0-3	[3]
	410	KNN99.5,ST0,05	[12]
	200	(K44Na52Li4)(Nb86Ta10Sb4)O3	[18]
	278	(K44Na52Li4)(Nb86Ta10Sb4)O3	[18]
	270	(K38Na52Li4)(Nb86Ta10Sb4)O3	[18]
	276	(K38Na52Li4)(Nb86Ta10Sb4)O3	[18]
	300	K10N90N	[10]
	358	KNN98-BT2	[4]
	420-480	Li0-7KN100-93NbO3	[6]
	253	(K44Na52Li4)(Nb84Ta10Sb6)	[19]
	170 ( $T_{O-T}$ )	KNN+Cu	[13]

<sup>25</sup>  $T_{O-T}$ : refers to the phase transition between orthorhombic and tetragonal in alkali niobate-based systems.

<sup>26</sup>  $T_d$ : refers to the phase transition between room temperature ferroelectric phase and a high temperature phase in BNT-based materials, which is commonly regarded as antiferroelectric or non-polar.



Relative Dielectric Constant ( $\epsilon$ [no units])			
	Value	Chemical Composition	Reference
	475-675	KNN100-97,CT0-3	[3]
	760	KNN97-93, Li3-7	[26]
	470	KNN95, LT5, Na0-2	[17]
	~430	K10N90N	[10]
	260-800	KNN (whole comp. range)	[14]
	45.47 [at 1MHz, 35°C]	K90N10N	[9]
	113.18 [at 1MHz, 35°C]	K80N20N	[9]
	264.77 [at 1MHz, 35°C]	K60N40N	[9]
	~4700-5700	Li0-7KN100-93NbO3	[4]
	402 – 1448 [at 1kHz]	KNN90-100-ST 0-10	[6]
	576	KNN99-Cu1	[11]
	968	KNN99-Ta1	[11]
	994	KNN99-Al1	[11]
	330	KNN99.5 - Sr0.5	[5]
	500	KNN99 - Sr1	[5]
	580	KNN99 - Ba1	[5]
	~200-310	KNN98-100 – KCN0-2	[13]
	~300-500 [at RT]	KNN91-100 – ZnO0-9	[7]
	1570 [at 253°C]	(K44Na52Li4)(Nb84Ta10Sb6)	[19]
	1173	KNN+CaTiO3+Cu	[21]
	800	KNN-BT+Mn	[24]
	479	KNN+Sr+Mn	[25]

Coercive Field ( $E_c$ [kV/mm])			
	Value	Chemical Composition	Reference
	~0.9 (120 °C/50 Hz)	KNN97-Pb03	[27]
	1.2 (150°C/60Hz)	KNN100-97,CT0-3	[3]
	1.4 (150°C/60Hz)	KNN99.5,ST0,05	[12]
	1.18	KNN95, LT5, Na0-2	[17]
	1.1	(K44Na52Li4)(Nb86Ta10Sb4)O3	[18]
	1.6	(K44Na52Li4)(Nb86Ta10Sb4)O3	[18]
	1.7	(K38Na52Li4)(Nb86Ta10Sb4)O3	[18]
	2.0	(K38Na52Li4)(Nb86Ta10Sb4)O3	[18]
	0.4-2.0	KNN (whole comp. range)	[14]
	1.0-1.3	KNN99-100 – KCN0-1	[13]
	2.0	KNN+Cu	[20]
	0.77	KNN+Mn+Cu	[23]

Loss Tangent ( $\tan\delta$ [%])			
	Value	Chemical Composition	Reference
	1.5 [at 1MHz, 35°C]	K90N10N	[9]
	1.7 [at 1MHz, 35°C]	K80N20N	[9]
	2.2 [at 1MHz, 35°C]	K60N40N	[9]
	3.9	KNN98-BT2	[15]
	2	KNN	[5]
	4	KNN99.5 - Sr0.5	[5]
	5	KNN99 - Sr1	[5]
	3.5	KNN99 - Ba1	[5]
	~5 – 9	KNN91-100 – ZnO0-9	[7]
	0.5	KNN-BT+Cu	[22]
	1.6	KNN+Sr+Mn	[25]

Electromechanical coupling factor ( $k_p$ [no units])			
	Value	Chemical Composition	Reference
	0.38	KNN+Li	[28]
	0.375	KNN100-97,CT0-3	[12]
	0.52	KNN99.5,ST0,05	[26]
	0.43	KNN97-93, Li3-7	[17]
	0.10	KNN95, LT5, Na0-2	[18]
	0.23	(K44Na52Li4)(Nb86Ta10Sb4)O3	[18]
	0.33	(K44Na52Li4)(Nb86Ta10Sb4)O3	[18]
	0.37	(K38Na52Li4)(Nb86Ta10Sb4)O3	[18]
	0.29	(K38Na52Li4)(Nb86Ta10Sb4)O3	[18]
	0.21-0.44	KNN98-BT2	[6]
	0.162-0.325	Li0-7KN100-93NbO3	[6]
	0.27	KNN90-100-ST 0-10	[5]
	0.35	KNN99.5 - Sr0.5	[5]
	0.32	KNN99 - Sr1	[5]
	~0.15-0.4	KNN99 - Ba1	[13]
	~0.31-0.4	KNN98-100 – KCN0-2	[7]
	0.61	KNN91-100 – ZnO0-9	[19]
	0.37	KNN+CaTiO3+Cu	[21]
	0.43	KNN-BT+Cu	[22]
	0.43-0.47	KNN+Mn+Cu	[23]
	0.31	KNN-BT+Mn	[24]
	0.41	KNN+Sr+Mn	[25]

<b>Electromechanical coupling factor (<math>k_t</math>[no units])</b>			
	<b>Value</b>	<b>Chemical Composition</b>	<b>Reference</b>
	0.425	KNN100-97,CT0-3	[3]
	0.425	KNN99.5,ST0,05	[12]
	0.38	KNN98-BT2	[15]
	0.32-0.48	Li0-7KN100-93NbO3	[6]
	0.21-0.41	KNN90-100-ST 0-10	[6]
	0.4	KNN99.5 - Sr0.5	[5]
	0.39	KNN99 - Sr1	[5]
	0.39	KNN99 - Ba1	[5]
	0.4	KNN-BT+Cu	[22]
	0.46-0.48	KNN+Mn+Cu	[23]

<b>Relative Density ([no units])</b>			
	<b>Value</b>	<b>Chemical Composition</b>	<b>Reference</b>
	97.8	KNN97-Pb03	[27]
	97.6	KNN100-97,CT0-3	[3]
	98	KNN+Cu	[20]
	97.2	KNN99.5,ST0,05	[12]
	98.8-99.8	KNN (HP)	[14]
	95-96.8	Li0-7KN100-93NbO3	[16]

<b>Remanent Polarisation (<math>P_r</math>[<math>\mu\text{C}/\text{cm}^2</math>])</b>			
	<b>Value</b>	<b>Chemical Composition</b>	<b>Reference</b>
	~10 (120 °C/50 Hz)	KNN97-Pb03	[27]
	12,5 (150°C/60Hz)	KNN100-97,CT0-3	[3]
	12.7(150°C/60Hz)	KNN99.5,ST0.05	[12]
	11.7 (150°C/60Hz)	KNN95, LT5, Na0-2	[17]
	6	(K44Na52Li4)(Nb86Ta10Sb4)O3	[18]
	11	(K44Na52Li4)(Nb86Ta10Sb4)O3	[18]
	15.5	(K38Na52Li4)(Nb86Ta10Sb4)O3	[18]
	17	(K38Na52Li4)(Nb86Ta10Sb4)O3	[18]
	15-32	KNN (whole comp. range)	[14]
	14-21	KNN98-100 – KCN0-2	[13]
	8-16	KNN91-100 – ZnO0-9	[7]
	19.6	KNN+Cu	[20]

Piezoelectric charge coefficient $d_{31}$ [pC/N]			
	Value	Chemical Composition	Reference
	-76	KNN97-93, Li3-7	[26]
	16.8	(K44Na52Li4)(Nb86Ta10Sb4)O3	[18]
	39.3	(K44Na52Li4)(Nb86Ta10Sb4)O3	[18]
	57.3	(K38Na52Li4)(Nb86Ta10Sb4)O3	[18]
	62.1	(K38Na52Li4)(Nb86Ta10Sb4)O3	[18]
	30	KNN99.5 - Sr0.5	[5]
	43	KNN99 - Sr1	[5]
	43	KNN99 - Ba1	[5]
	152	(K44Na52Li4)(Nb84Ta10Sb6)	[19]

Mechanical Quality Factor ( $Q_m$ [no units])			
	Value	Chemical Composition	Reference
	~270	KNN100-97,CT0-3	[3]
	~50-1250	KNN98-100 – KCN0-2	[13]
	~100-210	KNN91-100 – ZnO0-9	[7]
	1155	KNN+Cu	[20]
	1940	KNN-BT+Cu	[22]
	1205	KNN+Mn+Cu	[23]
	298	KNN+Sr+Mn	[25]

### 2.3.8.3 References

- [1] L. Egerton and D. M. Dillon, "Piezoelectric and dielectric properties of ceramics in the system potassium sodium niobate," *Journal of the American Ceramic Society*, **42**[9] 438-42 (1959).
- [2] H. L. Du, Z. M. Li, F. S. Tang, S. B. Qu, Z. B. Pei, and W. C. Zhou, "Preparation and piezoelectric properties of  $(K_{0.5}Na_{0.5})NbO_3$  lead-free piezoelectric ceramics with pressure-less sintering," *Materials Science & Engineering, B: Solid-State Materials for Advanced Technology*, **131**[1-3] 83-7 (2006).
- [3] R.-C. Chang, S.-Y. Chu, Y.-F. Lin, C.-S. Hong, and Y.-P. Wong, "An investigation of  $(Na_{0.5}K_{0.5})NbO_3$ - $CaTiO_3$  based lead-free ceramics and surface acoustic wave devices," *Journal of the European Ceramic Society*, **27**[16] 4453-60 (2007).
- [4] Y. P. Guo, K. Kakimoto, and H. Ohsato, "Ferroelectric-relaxor behavior of  $(Na_{0.5}K_{0.5})NbO_3$ -based ceramics," *Journal of Physics and Chemistry of Solids*, **65**[11] 1831-5 (2004).
- [5] M. D. Maeder, D. Damjanovic, and N. Setter, "Lead free piezoelectric materials," *Journal of Electroceramics*, **13**[1-3] 385-92 (2004).
- [6] Y. P. Guo, K. Kakimoto, and H. Ohsato, "Phase transitional behavior and piezoelectric properties of  $(Na_{0.5}K_{0.5})NbO_3$ - $LiNbO_3$  ceramics," *Applied Physics Letters*, **85**[18] 4121-3 (2004).
- [7] S. H. Park, C. W. Ahn, S. Nahm, and J. S. Song, "Microstructure and piezoelectric properties of ZnO-added  $(Na_{0.5}K_{0.5})NbO_3$  ceramics," *Japanese Journal of Applied Physics Part 2-Letters & Express Letters*, **43**[8B] L1072-L4 (2004).
- [8] R. E. Jaeger and L. Egerton, "Hot pressing of potassium-sodium niobates," *Journal of the American Ceramic Society*, **45**[5] 209-13 (1962).
- [9] K. Singh, V. Lingwal, S. C. Bhatt, N. S. Panwar, and B. S. Semwal, "Dielectric properties of potassium sodium niobate mixed system," *Materials Research Bulletin*, **36**[13-14] 2365-74 (2001).
- [10] G. Shirane, R. Newnham, and R. Pepinsky, "Dielectric properties and phase transitions of  $NaNbO_3$  and  $(Na,K)NbO_3$ ," *Physical Review*, **96**[3] 581-8 (1954).
- [11] M. Ichiki, L. Zhang, M. Tanaka, and R. Maeda, "Electrical properties of piezoelectric sodium-potassium niobate," *Journal of the European Ceramic Society*, **24**[6] 1693-7 (2004).
- [12] R.-C. Chang, S.-Y. Chu, Y.-P. Wong, Y.-F. Lin, and C.-S. Hong, "Properties of  $(Na_{0.5}K_{0.5})NbO_3$ - $SrTiO_3$  based lead-free ceramics and surface acoustic wave devices," *Sensors and Actuators A: Physical*, **136**[1] 267-72 (2007).
- [13] M. Matsubara, T. Yamaguchi, K. Kikuta, and S. Hirano, "Sinterability and piezoelectric properties of  $(K,Na)NbO_3$  ceramics with novel sintering aid," *Japanese Journal of Applied Physics Part 1-Regular Papers Brief Communications & Review Papers*, **43**[10] 7159-63 (2004).
- [14] G. H. Haertling, "Properties of hot-pressed ferroelectric alkali niobate ceramics," *Journal of the American Ceramic Society*, **50**[6] 329-30 (1967).
- [15] Y. P. Guo, K. Kakimoto, and H. Ohsato, "Structure and electrical properties of lead-free  $(Na_{0.5}K_{0.5})NbO_3$ - $BaTiO_3$  ceramics," *Japanese Journal of Applied Physics Part 1-Regular Papers Short Notes & Review Papers*, **43**[9B] 6662-6 (2004).
- [16] M. Kosec, V. Bobnar, M. Hrovat, J. Bernard, B. Malic, and J. Holc, "New lead-free relaxors based on the  $K_{0.5}Na_{0.5}Nb_{0.3}SrTi_{0.3}$  solid solution," *Journal of Materials Research*, **19**[6] 1849-54 (2004).
- [17] M.-S. Kim, D.-S. Lee, E.-C. Park, S.-J. Jeong, and J.-S. Song, "Effect of  $Na_2O$  additions on the sinterability and piezoelectric properties of lead-free  $95(Na_{0.5}K_{0.5})NbO_3$ - $5LiTaO_3$  ceramics," *Journal of the European Ceramic Society*, **27**[13-15] 4121-4 (2007).
- [18] F. Rubio-Marcos, P. Ochoa, and J. F. Fernandez, "Sintering and properties of lead-free  $(K,Na,Li)(Nb,Ta,Sb)O_3$  ceramics," *Journal of the European Ceramic Society*, **27**[13-15] 4125-9 (2007).
- [19] Y. Saito, H. Takao, T. Tani, T. Nonoyama, K. Takatori, T. Homma, T. Nagaya, and M. Nakamura, "Lead-free piezoceramics," *Nature*, **432**[7013] 84-7 (2004).
- [20] Q. Chen, L. Chen, Q. Li, X. Yue, D. Xiao, J. Zhu, X. Shi, and Z. Liu, "Piezoelectric properties of  $K_4CuNb_8O_{23}$  modified  $(Na_{0.5}K_{0.5})NbO_3$  lead-free piezoceramics," *Journal of Applied Physics*, **102**[10] 104109-4 (2007).
- [21] H. Y. Park, C. W. Ahn, H. C. Song, J. H. Lee, S. Nahm, K. Uchino, H. G. Lee, and H. J. Lee, "Microstructure and piezoelectric properties of  $0.95(Na_{0.5}K_{0.5})NbO_3$ - $0.05BaTiO_3$  ceramics," *Applied Physics Letters*, **89**[6] - (2006).
- [22] D. Lin, K. W. Kwok, and H. L. W. Chan, "Structure, dielectric, and piezoelectric properties of CuO-doped  $K_{0.5}Na_{0.5}NbO_3$ - $BaTiO_3$  lead-free ceramics," *Journal of Applied Physics*, **102**[7] 074113 (2007).
- [23] D. Lin, K. W. Kwok, and H. L. W. Chan, "Piezoelectric and ferroelectric properties of  $K_xNa_{1-x}NbO_3$  lead-free ceramics with  $MnO_2$  and CuO doping," *Journal of Alloys and Compounds*, **461**[1-2] 273-8 (2008).
- [24] C. W. Ahn, H. C. Song, S. Nahm, S. H. Park, K. Uchino, S. Priya, H. G. Lee, and N. K. Kang, "Effect of  $MnO_2$  on the piezoelectric properties of  $(1-x)(Na_{0.5}K_{0.5})NbO_3$ - $xBaTiO_3$  ceramics," *Japanese Journal of Applied Physics, Part 2: Letters & Express Letters*, **44**[42-45] L1361-4 (2005).

- [25] T. Liu, A. L. Ding, X. Y. He, X. S. Zheng, P. S. Qiu, and W. X. Cheng, "Dielectric and piezoelectric properties of Mn-doped  $(\text{K}, \text{Na})_{0.96}\text{Sr}_{0.02}\text{NbO}_3$  ceramics," *Physica Status Solidi A: Applications and Materials Science*, **203**[15] 3861-7 (2006).
- [26] E. Hollenstein, D. Damjanovic, and N. Setter, "Temperature stability of the piezoelectric properties of Li-modified KNN ceramics," *Journal of the European Ceramic Society*, **27**[13-15] 4093-7 (2007).
- [27] S. Tashiro and K. Nagata, "Influence of mixing condition and nonstoichiometry on piezoelectric properties of  $(\text{K}, \text{Na}, \text{Pb})\text{NbO}_3$  ceramics," *Japanese Journal of Applied Physics Part 1-Regular Papers Short Notes & Review Papers*, **43**[9B] 6711-5 (2004).
- [28] K. Higashide, K.-I. Kakimoto, and H. Ohsato, "Temperature dependence on the piezoelectric property of  $(1-x)(\text{Na}_{0.5}\text{K}_{0.5})\text{NbO}_3$ - $x\text{LiNbO}_3$  ceramics," *Journal of the European Ceramic Society*, **27**[13-15] 4107-10 (2007).

## 3. Concepts and Required Properties

### 3.1. Element Selection

The replacement for PZT, more precisely the lead in PZT, has to satisfy a minimum number of conditions in order to be considered as a viable alternative:

1. Toxicity
2. Price
3. Availability of materials
4. Performance
5. Durability

Points one through five are briefly discussed in section 3.1.1 and 3.1.2 and the reader is also referred to Rödel et al.<sup>[1]</sup> for another similar discussion with a slightly different focus. It was attempted to minimise the overlaps in contents with Rödel et al.. This chapter is focussed more towards providing new and different avenues to explore in the search for alternatives to PZT.

#### 3.1.1 Toxicity, Price and Availability

Non-toxicity and environmental friendliness are obviously the main reasons, why new lead-free piezoceramics are being developed. Though those two reasons are not mutually exclusive, they are not the same, either. This can easily be demonstrated at the example of CFCs<sup>27</sup>, which showed little or no toxicity but were later found to be devastating to the environment<sup>[2]</sup>. While the toxicity of lead<sup>[3]</sup> has been well established, the health and environmental safety of many other elements and compounds is less clear. It is for example commonly assumed that bismuth, being a heavy metal, is toxic. Several studies so far have shown that these concerns are unwarranted<sup>[4,5]</sup>.

Environmental friendliness of a substance is not restricted to its impact when released into the environment during or after use. First, one would have to consider the origin of the base materials used. If a substance is not commonly available, mining or otherwise retrieving it might impact the local environment like in the case of lignite<sup>28</sup>. During production, the refinement or separation from the ore might require large amounts of energy or the use of other hazardous chemicals. Two examples would be aluminium, whose electrolytic separation from bauxite ore costs large amounts of energy. Gold, in itself not toxic, is separated from rock using toxic liquid

---

<sup>27</sup> German: FCKW

<sup>28</sup> German: Braunkohle

mercury. Materials with similar mining history should obviously be avoided. During the product life cycle, accidental destruction and improper use scenarios have to be considered, for example flammability, chemical reactivity and potentially toxic fumes during fires. Improper disposal, like waste incineration, could also lead to the release of toxic fumes. Finally, the (environmental) cost of recycling should be taken into account.

Beyond environmental and health issues, the cost is an important factor to be considered when replacing PZT. The final cost will be determined amongst other factors by the total amount of available substance, ease of access to the substance and the simplicity of purification. The prize development will also be influenced by unpredictable factors such as previously unknown uses. Two prime examples for this case would be indium, which is used in liquid crystal displays. More importantly in the case of lead-free piezoceramics, lithium, which is required in large quantities for lithium ion rechargeable batteries and potentially in fusion reactors. The total amount of lithium available on earth is estimated to be  $\sim 14$  million metric tons<sup>[6]</sup>, which is only enough for a few tens of millions of electric cars for example. An overview of the costs per kilogram of 99.5 % pure oxides or carbonates is given in Fig 16.

Material safety data sheets of elements, their oxides and carbonates in their usual valence state provided online by Alfa Aesar were used to compile a periodic table (Fig 16) indicating their toxicity. Though the final structure may not be toxic even if produced from toxic elements (like in the case of PZT), toxic elements may be released during manufacturing, improper use and so on as mentioned above. Therefore, elements indicated as toxic in the periodic table will be excluded from further consideration.



	1	2	3	4	5	6	7	8	9	10	11	12	13	14	15	16	17	18
	1a																	VIIla
1 (K)	H	IIa											IIIa	IVa	Va	VIa	VIIa	He
2 (L)	Li	Be											B	C	N	O	F	Ne
3 (M)	Na	Mg	IIIb	IVb	Vb	VIb	VIIb		VIII		IIb	IIIb	Al	Si	P	S	Cl	Ar
4 (N)	K	Ca	Sc	Ti	V	Cr	Mn	Fe	Co	Ni	Cu	Zn	Ga	Ge	As	Se	Br	Kr
5 (O)	Rb	Sr	Y	Zr	Nb	Mo	Tc	Ru	Rh	Pd	Ag	Cd	In	Sn	Sb	Te	I	Xe
6 (P)	Cs	Ba	La	Hf	Ta	W	Re	Os	Ir	Pt	Au	Hg	Tl	Pb	Bi	Po	At	Rn
7 (Q)	Fr	Ra	Ac	Rf	Db	Sg	Bh	Hs	Mt	Ds	Rg	Uub	Uut	Uuq	Uup	Uuh	Uus	Uuo
Lanthanoide			58	59	60	61	62	63	64	65	66	67	68	69	70	71		
			Ce	Pr	Nd	Pm	Sm	Eu	Gd	Tb	Dy	Ho	Er	Tm	Yb	Lu		
Actinoide			90	91	92	93	94	95	96	97	98	99	100	101	102	103		
			Th	Pa	U	Np	Pu	Am	Cm	Bk	Cf	Es	Fm	Md	No	Lr		

	<b>Cost</b>		< 500€/kg		> 500; <1000€/kg		>1000€/kg
	<b>Toxicity</b>		not toxic		slightly toxic		toxic

Fig 16: All potentially relevant elements in the search for new piezoelectric materials sorted into A-site and B-site positions.

The triangle on the top of each element box indicated the current approximate cost as listed in the legend. The right triangle shows the likely toxicity of the element. The information was collected from the Alfa Aesar website.

### 3.1.2 Required Properties

A detailed account of required piezoelectric properties for different applications is beyond the scope of this work. Furthermore, at the current level of development in lead-free ceramics, speaking of required properties in terms of numbers and limits, is probably not appropriate. Our ability to shape currently available lead-free systems to specific requirements is still rudimentary. There may be little use in creating an arbitrary list of criteria to be achieved by lead-free ceramics, since no one can predict the speed and destination of scientific progress. If these criteria cannot be achieved, alternate solutions may still be found. Besides that, any requirements will always be severely biased towards numbers required by currently available designs developed for PZT-based materials. The use of lead-free materials will require adaptations of current designs and components. Sometimes a new solution possibly without any piezoelectric

elements may even prove more suitable. A detailed discussion of required properties for current PZT-based designs is given in Rödel et al.<sup>[1]</sup>

Even before piezoelectric properties can be established, more basic factors have to be considered, which will also influence the choice of elements used. Some elements such as iron (and other transition metal ions) may result in increased conductivity especially at elevated temperatures.

Small amounts of copper (2+) for example normally do not result in increased conductivity<sup>[7-9]</sup>, but a small percentage may be reduced to copper (1+) during sintering, which causes increased conductivity in the case of for example  $\text{Ba}(\text{Cu}_{1/3}\text{Nb}_{2/3})\text{O}_3$ <sup>[10,11]</sup> and  $\text{Ba}(\text{Cu}_{1/2}\text{W}_{1/2})\text{O}_3$ <sup>[12]</sup>.

Somewhat closely related is the sinterability of the developed material itself, which has a direct impact on the conductivity and dielectric strength of the ceramic. Again,  $\text{Ba}(\text{Cu}_{1/2}\text{W}_{1/2})\text{O}_3$  and  $\text{Ba}(\text{Cu}_{1/3}\text{Nb}_{2/3})\text{O}_3$  may be taken as an example since both structures show potential, if it was not for the poor sintering behaviour. However, for sintering and conductivity issues there might be solutions through doping, which has not yet been exploited.

## 3.2. Search Concepts

It should be evident from the review of the literature and particularly the basics of ferroelectrics (chapters 2.1.6, 2.2 and 2.3) that any replacement would have to be of perovskite structure. The elements listed in Fig 16 need to be separated into three groups now before any further consideration is justified, namely their potential crystallographic positions in the perovskite structure.

	1	2	3	4	5	6	7	8	9	10	11	12	13	14	15	16	17	18
	1a																	VIIa
1 (K)	<sup>1</sup> H	IIa											IIIa	IVa	Va	VIa	VIIa	<sup>2</sup> He
2 (L)	<sup>3</sup> Li	<sup>4</sup> Be											<sup>5</sup> B	<sup>6</sup> C	<sup>7</sup> N	<sup>8</sup> O	<sup>9</sup> F	<sup>10</sup> Ne
3 (M)	<sup>11</sup> Na	<sup>12</sup> Mg	IIIb	IVb	Vb	VIb	VIIb		VIII		IIb		<sup>13</sup> Al	<sup>14</sup> Si	<sup>15</sup> P	<sup>16</sup> S	<sup>17</sup> Cl	<sup>18</sup> Ar
4 (N)	<sup>19</sup> K	<sup>20</sup> Ca	<sup>21</sup> Sc	<sup>22</sup> Ti	<sup>23</sup> V	<sup>24</sup> Cr	<sup>25</sup> Mn	<sup>26</sup> Fe	<sup>27</sup> Co	<sup>28</sup> Ni	<sup>29</sup> Cu	<sup>30</sup> Zn	<sup>31</sup> Ga	<sup>32</sup> Ge	<sup>33</sup> As	<sup>34</sup> Se	<sup>35</sup> Br	<sup>36</sup> Kr
5 (O)	<sup>37</sup> Rb	<sup>38</sup> Sr	<sup>39</sup> Y	<sup>40</sup> Zr	<sup>41</sup> Nb	<sup>42</sup> Mo	<sup>43</sup> Tc	<sup>44</sup> Ru	<sup>45</sup> Rh	<sup>46</sup> Pd	<sup>47</sup> Ag	<sup>48</sup> Cd	<sup>49</sup> In	<sup>50</sup> Sn	<sup>51</sup> Sb	<sup>52</sup> Te	<sup>53</sup> I	<sup>54</sup> Xe
6 (P)	<sup>55</sup> Cs	<sup>56</sup> Ba	<sup>57</sup> La	<sup>72</sup> Hf	<sup>73</sup> Ta	<sup>74</sup> W	<sup>75</sup> Re	<sup>76</sup> Os	<sup>77</sup> Ir	<sup>78</sup> Pt	<sup>79</sup> Au	<sup>80</sup> Hg	<sup>81</sup> Tl	<sup>82</sup> Pb	<sup>83</sup> Bi	<sup>84</sup> Po	<sup>85</sup> At	<sup>86</sup> Rn
7 (Q)	<sup>87</sup> Fr	<sup>88</sup> Ra	<sup>89</sup> Ac	<sup>104</sup> Rf	<sup>105</sup> Db	<sup>106</sup> Sg	<sup>107</sup> Bh	<sup>108</sup> Hs	<sup>109</sup> Mt	<sup>110</sup> Ds	<sup>111</sup> Rg	<sup>112</sup> Uub	<sup>113</sup> Uut	<sup>114</sup> Uuq	<sup>115</sup> Uup	<sup>116</sup> Uuh	<sup>117</sup> Uus	<sup>118</sup> Uuo
Lanthanoide			<sup>58</sup> Ce	<sup>59</sup> Pr	<sup>60</sup> Nd	<sup>61</sup> Pm	<sup>62</sup> Sm	<sup>63</sup> Eu	<sup>64</sup> Gd	<sup>65</sup> Tb	<sup>66</sup> Dy	<sup>67</sup> Ho	<sup>68</sup> Er	<sup>69</sup> Tm	<sup>70</sup> Yb	<sup>71</sup> Lu		
Actinoide			<sup>90</sup> Th	<sup>91</sup> Pa	<sup>92</sup> U	<sup>93</sup> Np	<sup>94</sup> Pu	<sup>95</sup> Am	<sup>96</sup> Cm	<sup>97</sup> Bk	<sup>98</sup> Cf	<sup>99</sup> Es	<sup>100</sup> Fm	<sup>101</sup> Md	<sup>102</sup> No	<sup>103</sup> Lr		

Fig 17: The ionic radii<sup>[13,14]</sup> of the selected elements as well as reports of known perovskite structures<sup>[15]</sup>. The A-site, B-site and oxygen site ions are coloured as indicated in the legend. Some can be placed on either A- or B-site. Replacing oxygen is complex and sometimes dangerous and the release of halogen gas when incinerated not desirable.

Looking at the periodic table in Fig 17, an initial list of usable elements can be created (Tab 11 and Tab 12). Some elements can quickly be excluded. All actinoids are radioactive, so are Technetium and Polonium. Also all toxic elements (Fig 16) are excluded. Price issues will be disregarded until later. Precious metals (Pt, Au, Pd, Ir, Ru, Rh) are unreactive. A-site lanthanoids generally produce orthorhombic, centrosymmetric  $A^{3+}B^{3+}O_3$  perovskites; there are so far no reports of ferroelectric activity.

Choosing the right coordination number for the ions in a perovskite structure is always an issue<sup>[16]</sup>. In a cubic undistorted perovskite, the coordination numbers (CN) of the crystallographic positions are 12 for the A-site, 6 for the B-site and 6 for the oxygen site. However, often 9-coordinated (CN9) radii are used for the A-site ions and equations adjusted<sup>[17]</sup>, since 12-coordinated radii are rarely reported. More fundamentally, the coordination numbers obviously depend on the distortion of the perovskite unit cell. Since the type of distortion (rhombohedral, tetragonal or orthorhombic) cannot be known in advance, its strong influence on coordination number and, therefore, ionic radius cannot factor into the prediction of new structures. The values in Tab 11 are all 9-coordinated due to lack of data availability of the 12-coordinated radii.

**Tab 11: Potential A-site ions, Standard Charge and Ionic Radii.**

Element	Charge	IR [CN9]
Li	1+	~1.0
Na	1+	1.24
K	1+	1.55
Rb	1+	1.63
Cs	1+	1.78
Ca	2+	1.18
Sr	2+	1.31
Ba	2+	1.47
La	3+	1.22
Ln <sup>29</sup>	2+ <sup>30</sup> , 3+, 4+30	~1.0-1.2
Ag	1+	1.42
Bi	3+	~1.21
NH <sup>4+</sup>	1+	~1.35

**Tab 12: All Potential B-site ions, Standard Charge and Ionic Radii**

Element	Charge	IR [CN6]
Li	1+	0.76
Mg	2+	0.72
Al	3+	0.535
Bi	5+	0.76
Cr	3+	0.615
Co	2+	0.65-0.75
Cu	2+	0.73
Zn	2+	0.74
Fe	3+	0.55-0.64
Ga	3+	0.62
Ge	2+, 4+	0.73, 0.53
Hf	4+	0.71
Ti	4+	0.605
Zr	4+	0.72
Mn	3+	0.58-0.65
V	3+	0.64
Nb	5+	0.64
Ta	5+	0.64
Ni	2+	0.69
Sc	3+	0.75
Sn	4+	0.69
W	6+	0.6
Mo	6+	0.59

A number of attempts to predict new perovskite structures beyond the use of the Goldschmidt tolerance factor have already been made. Li et al.<sup>[18]</sup> tried to define the area of formability for perovskite by investigating 197 ternary oxides. Two issues make the usability of this data difficult. Due to the previously mentioned lack of availability of 12-coordinated radii, they use 6-

<sup>29</sup> Ln: All Lanthanoides excluding La will be treated as one.

<sup>30</sup> Unlikely to be the final charge state during pressureless calcination/sintering.

coordinated radii for the A-site. Also their choice of oxygen ion radius of 1.25 Å is unclear since the correct CN6 value is 1.38 Å. Still, their argument for an upper and lower limit for the B-site ions based on limited size inside the oxygen octahedron seems valid. The upper limit is dependent on the choice of A-site ion and its radius. However, the lower limit is fixed at 0.53 Å (CN6, ionic radius, corrected value). Lufaso et al.<sup>[19]</sup> have created a structure prediction diagnostic software (SPuDS), which attempts to predict the structural distortion of perovskites. However, it does not predict the likelihood of a perovskite structure actually forming in the first place. A large database of investigated perovskite structures and their ferroelectric activity is listed in “Ferroelectrics and Related Materials”<sup>[15]</sup> (translated from Russian), which, even though not current any more, can help identify likely and unlikely candidates. Ab initio density functional theory is still not reliable enough for regular use<sup>[20]</sup> though the scientific progress is rapid. Unfortunately, the relativistic nature of the electron orbitals of heavy elements still prevents precise calculations. Yan et al.<sup>[21]</sup> propose a dimensionless factor containing differences in electronegativity, mass and radius of replacing ions that corresponds with improved  $k_p$  and  $k_{33}$ .

### 3.2.1 High Temperature BiMeO<sub>3</sub>-PbTiO<sub>3</sub> Analogue

The Curie temperature of lead titanate (PbTiO<sub>3</sub>, PT) has been shown to increase when mixed with Bi<sup>3+</sup>(Me<sup>3+</sup>)O<sub>3</sub> where Me is a single or a combination of at least two ions occupying the B-site with overall average +3 charge<sup>[22,23]</sup>. The effect of BiMeO<sub>3</sub> is to further distort the tetragonal structure of PT, if Me contains a Jahn-Teller (JT) active ion<sup>[24]</sup> like for example Fe<sup>[25]</sup> or Zn<sup>[26-28]</sup> as opposed to non-JT active Mg<sup>[26,29]</sup>. Unfortunately, this distortive effect of BiMeO<sub>3</sub> appears limited to PT, likely due to the electronic similarity of Pb<sup>2+</sup> and Bi<sup>3+</sup>, which might further favour distortions. In own experiments using Bi(Zn<sub>1/2</sub>Ti<sub>1/2</sub>)O<sub>3</sub> and Bi(Zn<sub>2/3</sub>Nb<sub>1/3</sub>)O<sub>3</sub> (Zn: JT active) combined with barium titanate, only continuous reduction in ferroelectric properties with increasing BiMeO<sub>3</sub> content was discovered. No relevant difference compared to Bi(X,Y)O<sub>3</sub>-BT where X is Mg or Li (both not JT active) and Y is Ti, Zr, Ta and Nb was found.

The region of stability of the single phase perovskite structure was also limited to 20-30 % BiMeO<sub>3</sub> addition unlike in BiMeO<sub>3</sub>-PT. Results were generally equivalent to the ones reported here<sup>[30,31]</sup>. The region of stability appears much larger in the case of BiFeO<sub>3</sub>-BT<sup>[32]</sup>.

Bi(X,Y)O<sub>3</sub> with orthorhombic KNbO<sub>3</sub>, tetragonal Ba(Cu<sub>1/2</sub>W<sub>1/2</sub>)O<sub>3</sub><sup>[12]</sup>, Ba(Cu<sub>1/3</sub>Nb<sub>2/3</sub>)O<sub>3</sub><sup>[10,11]</sup> and Ba(Cu<sub>1/3</sub>Ta<sub>2/3</sub>)O<sub>3</sub> did not form single phase perovskites at any mixture during own experiments, likely because BaWO<sub>4</sub> and Bi<sub>2</sub>NbO<sub>5</sub> are more favourable structures. It may still be possible to

stabilise the  $\text{BiMeO}_3$ -BT structures by replacing some of the  $\text{Bi}^{3+}$  ions with  $\text{La}^{3+}$  ions, which have a larger ionic radius. It will have to be determined, which of the effects of lanthanum will dominate. Its ability to stabilise the perovskite structure of  $\text{BiMeO}_3$ <sup>[33]</sup> on the one hand competes with its negative impact on tetragonality<sup>[34]</sup>. Furthermore, a multistep calcination process of the precursor materials with similar reactivity could reduce the formation of unwanted phases.

Considering the discussion above, there are still a few roads to be explored. As a direct equivalent to  $\text{BiFeO}_3$ - $\text{PbTiO}_3$ ,  $\text{Ba}(\text{Fe}_{1/2}\text{Nb}_{1/2})\text{O}_3$ , containing JT-active iron and ferroelectrically active niobium, might be added to  $\text{BaTiO}_3$  to increase the tetragonality of  $\text{BaTiO}_3$  and subsequently raising its Curie temperature without the instability introduced by the bismuth ions (Fig 20). Targeting BKT instead of BT as a tetragonal starting material may also be possible analogous to  $\text{BiMeO}_3$ -PT. The compositions shown in Fig 18 may be used to increase the Curie-temperature of BKT and maintain its tetragonal structure.

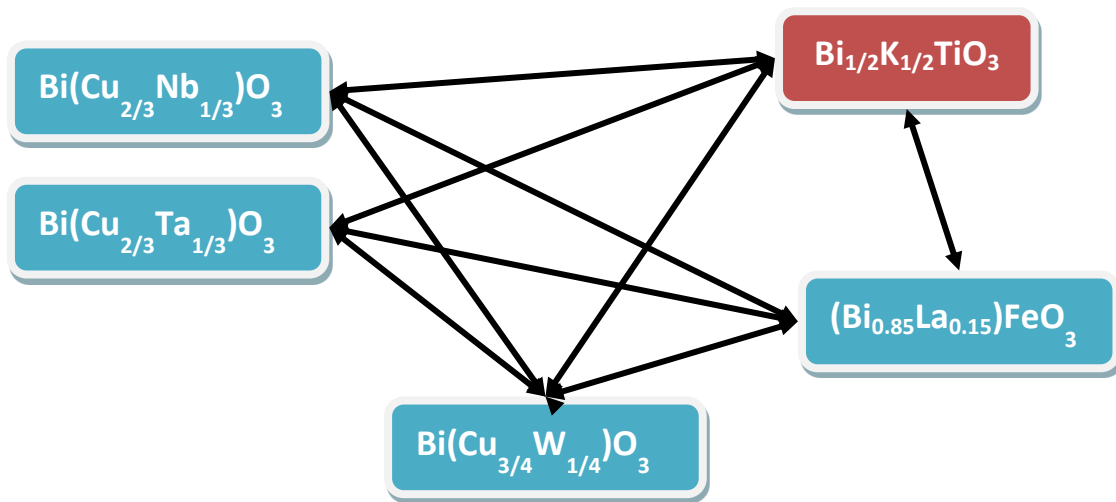


**Fig 18:** The  $\text{Bi}(\text{Cu},\text{Y})\text{O}_3$  structures are analogues to  $\text{Ba}(\text{Cu},\text{Y})\text{O}_3$ . They can be combined with BKT and  $(\text{Bi}_{0.85}\text{La}_{0.15})\text{FeO}_3$  as shown.

There are as of now no reports about these structures.  $(\text{Bi}_{0.85}\text{La}_{0.15})\text{FeO}_3$  is reported as a single phase ferroelectric producible by a standard mixed oxide route with pressureless sintering<sup>[35]</sup>.

All structures with Jahn-Teller active ions will always have a potential for increased conductivity due to usual multitude of oxidation states of transition metals. However, their potential for increasing unit cell distortions may outweigh this drawback since tetragonal non-centrosymmetric (Pb-containing) perovskites with  $c/a$  ratios of 1.23 have been reported<sup>[36]</sup>.



### 3.2.2 Barium Copper Tungstenate

$\text{Ba}(\text{Cu}_{1/2}\text{W}_{1/2})\text{O}_3$ <sup>[12]</sup> is a barium perovskite with a very high tetragonality with a reported  $c/a$  ratio of 1.11<sup>31</sup>. Its high tetragonality is a result of the copper (see section 3.2.1). It can be seen in Fig 19 that the tungsten ion in  $\text{Ba}(\text{Cu}_{1/2}\text{W}_{1/2})\text{O}_3$  sits in an undistorted oxygen octahedron.

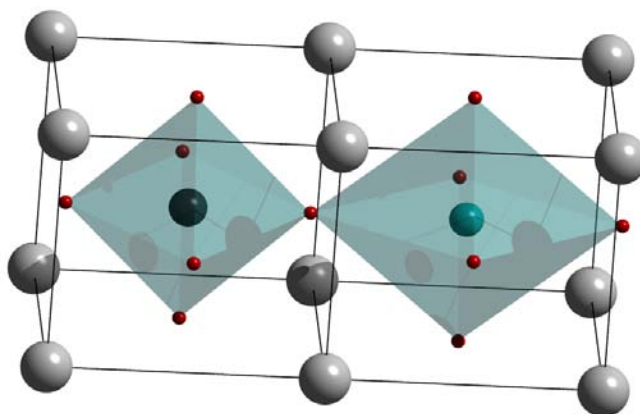


**Fig 19: 3D crystal structure of  $\text{Ba}(\text{Cu}_{1/2}\text{W}_{1/2})\text{O}_3$  generated with Diamond 3.2a and POV-Ray from powder diffraction data. The Barium atoms are white, Oxygen red, tungsten black and copper blue. The oxygen octahedra are highlighted. The 18 % longer diagonal of the copper oxygen octahedron compared to the other two directions can be seen. The oxygen octahedron around tungsten is undistorted.**

There are, as of now, no reports about possible ferroelectric activity since the material cannot be sintered and its conductivity is too high. However, similar materials like  $\text{Ba}(\text{Cu}_{1/3}\text{Nb}_{2/3})\text{O}_3$ <sup>[10,11]</sup> and likely  $\text{Ba}(\text{Cu}_{1/3}\text{Ta}_{2/3})\text{O}_3$  have been shown to possess (minor) ferroelectric activity and conductivity can be addressed with the sintering temperature and sintering aids<sup>[37]</sup>. The low ferroelectric activity may be attributed mostly to the almost undistorted niobium/tungsten environment as most of the distortion arises from the  $\text{Cu}^{2+}$  oxygen octahedron. Since all  $\text{Ba}(\text{Cu},\text{Y})\text{O}_3$  materials consist of repeating layers of undistorted and distorted octahedra, higher ferroelectric activity may be induced by introducing ferroelectrically active ions (Nb, Ti, Ni) into the distorted layers normally occupied only by copper. Due to the periodicity of the structure, the octahedra would remain partially distorted assuming a single-phase structure can be achieved. The compositions in Fig 20 may be used in the combinations indicated by the arrows. Each combination utilises the tetragonal distortion of at least one of the end members and introduces ferroelectrically active ions into the JT-distorted environment of the other end member.

<sup>31</sup> Own reproduced value:  $c/a=1.09$

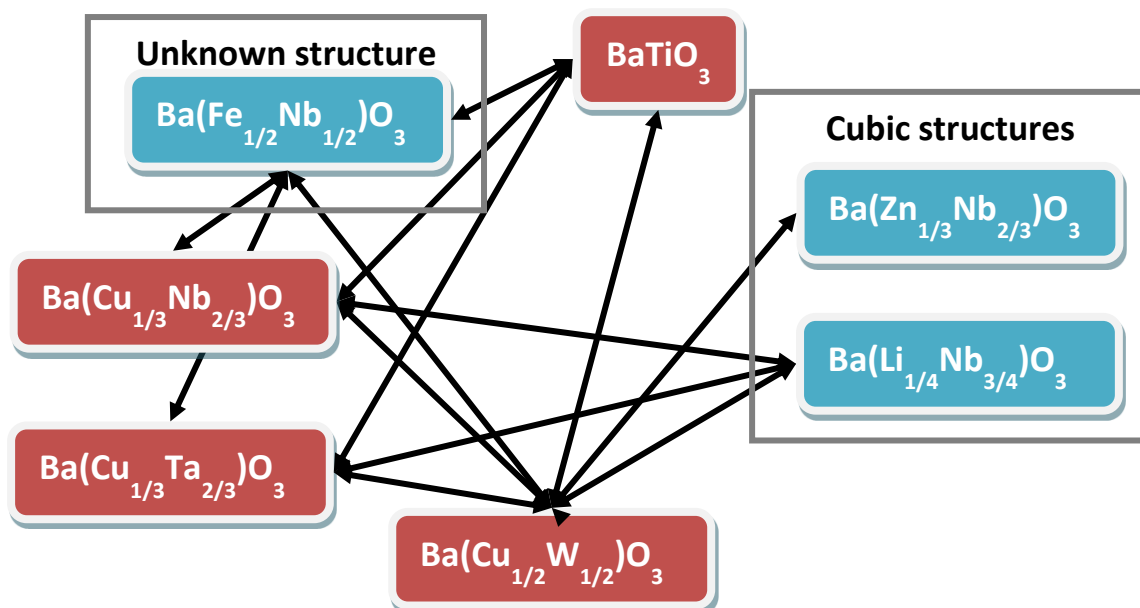


**Fig 20: Possible combinations of materials that force ferroelectrically active ions into distorted octahedra of tetragonal crystal systems due to mismatch of the B-site ion ratios.**

The structure of  $\text{BaFe}_{1/2}\text{Nb}_{1/2}\text{O}_3$  is not reported in literature but will likely form a perovskite structure. The cubic structures<sup>[38]</sup> show no JT-distortion but contain only ferroelectrically active ions.

Due to the likelihood of undesired phases becoming dominant, the attempt was made to separate bismuth (Fig 18) and barium (Fig 20) containing materials<sup>32</sup>. Minimising the number of different ions used will increase the chances of successfully preparing single-phase materials. Limiting the number of ions also reduces the frequency dependence.

<sup>32</sup> Own experiments showed that mixing  $\text{Ba}(\text{Cu}_{1/2}\text{W}_{1/2})\text{O}_3$  with  $\text{Bi}(\text{Cu}_{2/3}\text{W}_{1/3})\text{O}_3$  does not produce single-phase materials at any ratio.



### 3.2.3 Ion Replacement in Known Systems

Some known lead-free ferroelectric systems like  $(\text{Bi}_{1/2}\text{Na}_{1/2})\text{TiO}_3$  and  $(\text{Bi}_{1/2}\text{K}_{1/2})\text{TiO}_3$  were logically derived from existing systems like  $\text{PbTiO}_3$  or  $\text{BaTiO}_3$  proving the successfulness of replacing a single ion with a combination of two or more ions with an equal average charge<sup>[39]</sup>.

There are still multitudes of systems that remain unexplored or unreported (Fig 21).

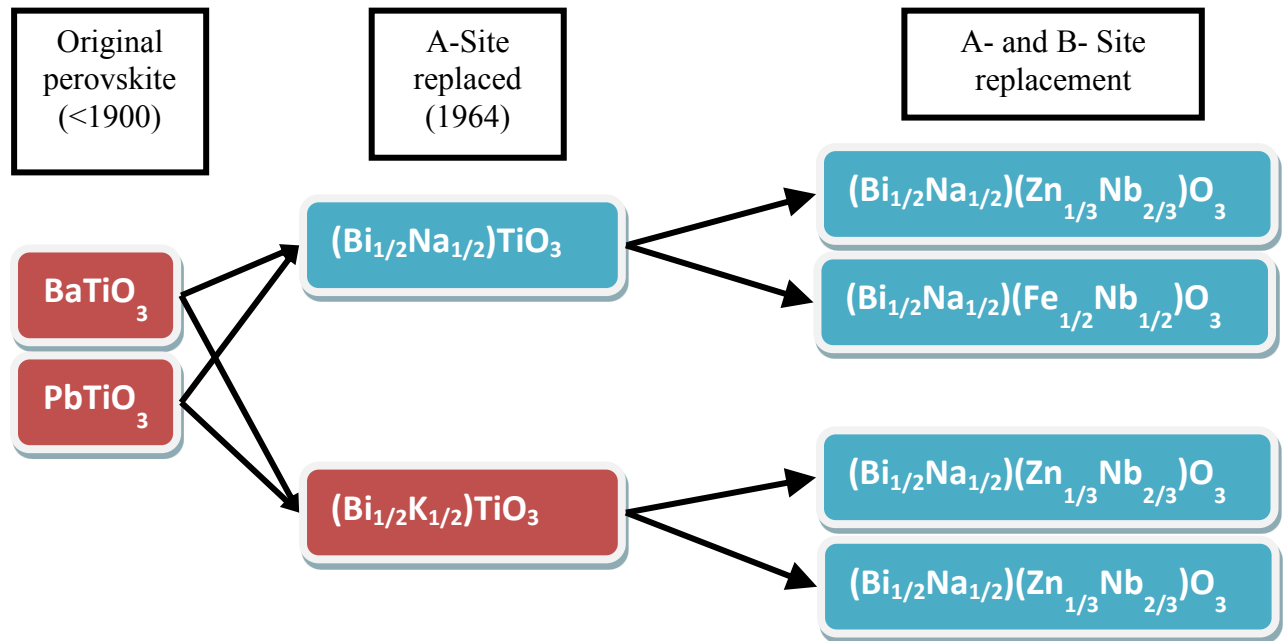


**Fig 21: Materials based on ion replacement of currently known ferroelectric systems.**

The original of perovskite (left) were known since before 1900. Replacement of the A-site cation led to the discovery of BNT and BKT (centre) in 1964. Similar substitution of the B-site cation may produce further ferroelectric materials (right).

While any combination of ions with the average charge of the ion to be replaced would possibly form a perovskite structure, some are known for their ferroelectric activity, which is likely linked to their polarisabilities<sup>[40]</sup>. The reported polarisabilities are restricted to the dielectric case but their values suggest, which ions are easily shifted off-centre from their B-site positions. The best candidates are highlighted in red in Tab 12. The second most relevant parameter is the average B-site ion radius (T-factor with constant A-site ion radius)

To verify this concept, the niobium in  $\text{KNbO}_3$  was replaced giving  $\text{K(X,Y)O}_3$  where X is  $\text{Ti}^{4+}$  and  $\text{Zr}^{4+}$  and Y is  $\text{W}^{6+}$  and  $\text{Mo}^{6+}$ . Under standard calcination conditions (800°C/3h) none formed perovskite structures in own investigations. This failure can be attributed to the low reactivity of tungsten, the high vapour pressure of Molybdenum and the generally high tolerance factor of 1.04 of these systems ( $\text{KNbO}_3=1.05$ ) since pure  $\text{KNbO}_3$  is difficult to prepare as a single-phase material. It is therefore proposed that the same concept should be explored with  $\text{K}_{0.5}\text{Na}_{0.5}\text{NbO}_3$

and  $\text{NaNbO}_3$  (Fig 22). The following steps might improve chances for success: unwanted secondary structures need to be identified. If they are the result of preferential reaction of two or more compounds, precursors can be prepared and a two-step calcination process may improve phase purity. The sodium to potassium ratio can be varied continuously and lower potassium content may increase the chance for successful sintering/densification and generally promote a more stable perovskite structure.

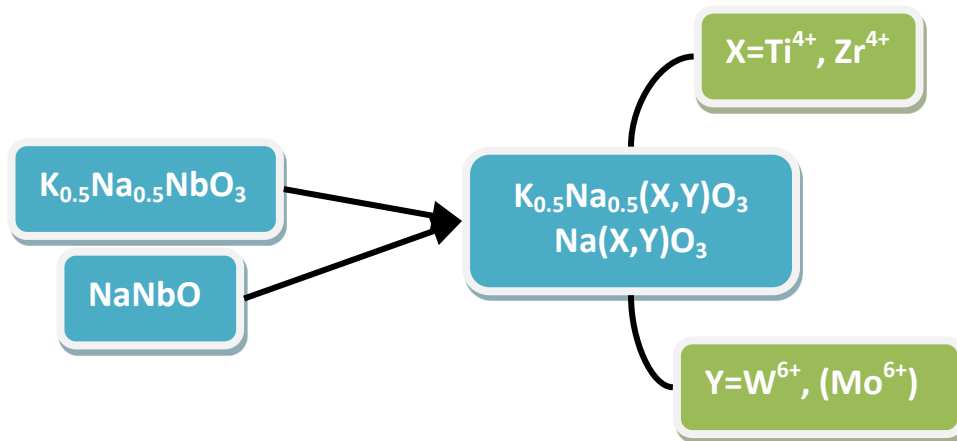


**Fig 22: Proposed replacement of  $\text{Nb}^{5+}$  in KNN with a combination of  $\text{Ti}^{4+}$ ,  $\text{Zr}^{4+}$  and  $\text{W}^{6+}$ ,  $\text{Mo}^{6+}$ . Molybdenum may be unsuitable for conventional sintering due to its high vapour pressure.**

### 3.2.4 Doping to Raise Phase Transition Temperatures

The effect of doping to improve sintering and conductivity is already covered in the respective chapters of the literature reviews of KNN (section 2.3.5) and BNT (section 2.2.7). However, some elements have thus far been mostly ignored. Silver is clearly too expensive to be used as a primary A-site ion but as a dopant its role should be further investigated since it is besides lithium the only element, where increased Curie/depolarisation temperatures are reported in BNT.

A conclusion from the literature review of BNT and KNN was that in order to increase the Curie temperature of BNT- and KNN-based materials, ions with similar electronic structures need to be used. In the case of  $\text{K}^+$  and  $\text{Na}^+$ , Ag and Li were already mentioned but rubidium and caesium have not been reported. Both are highly reactive and must be handled with caution. Their ionic radii are too large to form perovskite structures with B-site niobium. However, small amounts may be incorporated into KNN- and BNT-based materials to promote structural distortions.

Furthermore, since the upper limit of the A-site ion is dependent on the size of the B-site ion<sup>[15]</sup>, previously disregarded ions can now be considered as B-site ions. In particular  $\text{Bi}^{5+}$  may be stable in this environment due to the reactivity of rubidium and caesium. The Goldschmidt

tolerance factors of  $\text{CsBiO}_3$  and  $\text{RbBiO}_3$  would be 1.07 and 1.02 respectively.  $\text{CsBiO}_3$  may have to be modified with  $\text{K}^+$  or  $\text{Rb}^+$  to improve formability.

Finally,  $\text{NH}_4^+$  has an ionic radius between  $\text{K}^+$  and  $\text{Na}^+$  but since it cannot be used in conjunction with a standard mixed oxide route, there are no reports thus far.

Similarly,  $\text{Sn}^{4+}$  may replace  $\text{Zr}^{4+}$  and  $\text{Ti}^{4+}$  with ionic radius directly between  $\text{Ti}^{4+}$  and  $\text{Zr}^{4+}$  and close to the much more expensive  $\text{Hf}^{4+}$ .

### 3.2.5 Broadening of the Phase Regions and Transition in BNT

In Zhang et al.<sup>[41]</sup> it has been shown that high strain electrostrictors may be an alternative to ferroelectrics in some situations where non-linearity is less important and energy dissipation has to be minimal. A very good starting point for high strain electrostrictors appears to be the non-polar phase of BNT-based systems. Further broadening may be achieved by introducing a larger variety of ions partially replacing the KNN-BKT. Influence of A-site doping on this broadening is not reported but  $\text{Zr}^{4+}$  and  $\text{Ta}^{5+}$  could partially replace  $\text{Ti}^{4+}$  and  $\text{Nb}^{5+}$  though  $\text{Nb}_2\text{O}_5$  and  $\text{Ta}_2\text{O}_5$  should be pre-reacted<sup>[42]</sup>.

Similarly, a large strain was reported in the region of the ferroelectric-to-non-polar transition. To make it more useful, the transitional region between the ferroelectric and non-polar phase has to be extended from below room temperature to the desired working temperature. KNN-BKT doping has already been shown to be a first step in approaching this goal<sup>[43]</sup>. Analogous to the increased temperature range of the electrostrictive phase, the broadening of the transitional region may also be achieved by making the material even more heterogeneous through the introduction of small concentrations of a number of different ions.

### 3.2.6 Morphotropic Phase Boundaries

From Rödel et al.<sup>[11]</sup> it is clear that once suitable rhombohedral, tetragonal and orthorhombic end members have been identified, an MPB compositions of two of them might further improve the ferroelectric properties.

Most of the bismuth containing materials proposed in sections 3.2.1 and 3.2.3 are likely to be rhombohedral or monoclinic due to the small ionic radius of bismuth. The barium-containing compositions in Fig 20 have a high chance of being tetragonal. The structure of the KNN and BNT/BKT derived systems in section 3.2.3 are anyone's guess. If not all suggested systems prove to be single-phase perovskites, however, this does not rule them out entirely since compositions containing BKT, KN and  $\text{BiFeO}_3$  have shown that the MPB materials often prove

more stable than their respective end members do. This is not surprising simply because the tolerance factors of the MPB compositions are nearer to one than either end members.

Once a few new materials have been developed and their room temperature phases and phase transitions have been identified, different crystal structures may be combined to find morphotropic phase boundaries. It should, however, be noted that the actual properties of pure new end members cannot be estimated at all if mixed with large quantities of known ferroelectric end members. For example mixing the  $\text{Bi}(\text{X},\text{Y})\text{O}_3$  systems into BNT is likely only to reduce the properties of BNT as described in the literature review of bismuth alkali titanates and will tell nothing about  $\text{Bi}(\text{X},\text{Y})\text{O}_3$ . This is already reported for  $\text{BiFeO}_3\text{-BT}^{[32]}$ , which also shows clearly that  $\text{BiFeO}_3\text{-BT}$  shows no linear trend of the properties between  $\text{BiFeO}_3$  and BT. It will have to be determined on a case by case basis, whether a morphotropic phase boundary is identified first or the sinterability and conductivity of the end members addressed with doping first. Combining more than two different crystal structures is discussed in section 3.2.7.

### 3.2.7 Combining Bismuth Alkali Titanates and Alkali Niobates

BNT-BT, BNT-BKT and KNN are all materials, which likely owe their properties to the morphotropic phase boundary. In BNT-BT and BNT-BKT the phase boundary is between rhombohedral BNT and tetragonal BT or BKT. KNN consists of orthorhombic KN and orthorhombic NN. Combining the rhombohedral, tetragonal and orthorhombic systems may further increase lattice instability and hence further maximise the effect of the MPB on ferroelectric properties. The quasi-ternary phase diagrams of BNT-BT-KNN and BNT-BKT-KNN are shown in Fig 23 with all reported MPB marked. This concept already exists and is discussed in the literature review in section 2.2.7 and 2.3.5.4.

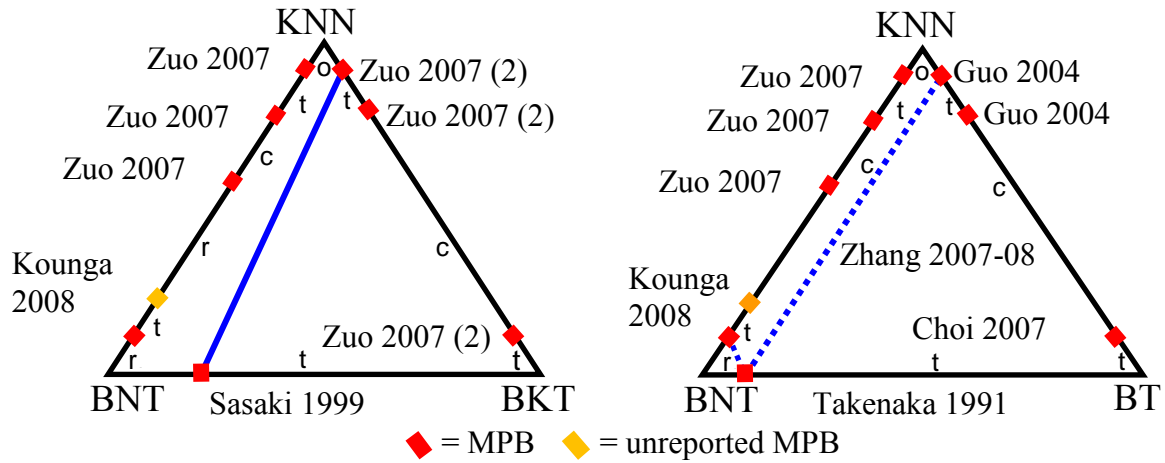


**Fig 23:** The two quasi-ternary phase diagrams of BNT-BKT-KNN are shown on the left and BNT-BT-KNN on the right. All reported MPBs (Takenaka 1991<sup>[44]</sup>, Sasaki 1999<sup>[45]</sup>, Guo 2004<sup>[46]</sup>, Choi 2007<sup>[47]</sup>, Zuo 2007<sup>[48]</sup>, Zuo 2007 (2)<sup>[49]</sup>, Zhang 2007-08<sup>[41,50-52]</sup> and Kounaga 2008<sup>[53]</sup>) are marked in red. The unreported phase transition, which is necessary to complete the picture, is marked in yellow. Previous in-group work is marked as dotted lines<sup>[41,50-53]</sup>. The investigation of this work is marked in blue connecting BNT-20BKT<sup>[45]</sup> and KNN-3BKT<sup>[49]</sup>. The letters o, r, t and c denote the orthorhombic, rhombohedral, tetragonal and cubic phase regions between MPBs.

### 3.3. Summary

This chapter provides a few currently unexplored avenues to finding new ferroelectrics with little relation to BNT and KNN-based systems. To overcome some of the drawbacks of current systems, doping with elements with related electronic structures is likely the only way to increase phase transition temperatures while maintaining the ferroelectric properties. The Jahn-Teller effect is used to provide highly distorted crystal structures, Also, the usage of ferroelectrically active ions was maximised wherever possible. It is always important to remember that the number of different ions determines the frequency dependence of the material. On the other hand under the right circumstances a larger number of different ions may actually be desired. If properties found only near the transitions need to be accessed over a wider range of temperatures, broadening/smearing out the phase transition may be desirable. Morphotropic phase boundaries of three or known ferroelectrics with three different crystal structures (rhombohedral, tetragonal and orthorhombic) are proposed to further maximise the phase instabilities and, therefore, ferroelectric properties at that triple point. The search for this triple point should be found somewhere along the line connecting two MPB between the three compositions in the phase diagram as indicated in Fig 23. This last idea was investigated in the experimental part of this thesis.

## 3.4. References

- [1] J. Rödel, W. Jo, K. Seifert, E.-M. Anton, T. Granzow, and D. Damjanovic, "Perspective on the Development of Lead-free Piezoceramics," *Journal of the American Ceramic Society*, **92**[6] 1153-77 (2009).
- [2] J. C. Laube and A. Engel, "First atmospheric observations of three chlorofluorocarbons," *Atmos. Chem. Phys. Discuss.*, **8**[2] 6683-95 (2008).
- [3] "Safety Data Sheet, Lead (II) oxide," *Alpha Aesar*.
- [4] M. F. Gordon, R. I. Abrams, D. B. Rubin, W. B. Barr, and D. D. Correa, "Bismuth toxicity," *Neurology*, **44**[12] 2418- (1994).
- [5] R. D. Brown, "Bismuth." In *Minerals Yearbook, Vol. I, Metals & Minerals*. accessed October 7, 2008, <http://minerals.usgs.gov/minerals/pubs/commodity/bismuth/110496.pdf>.
- [6] D. Fasel and M. Q. Tran, "Availability of lithium in the context of future D-T fusion reactors," *Fusion Engineering and Design*, **75-79** 1163-8 (2005).
- [7] M. Matsubara, K. Kikuta, and S. Hirano, "Piezoelectric properties of  $(K_{0.5}Na_{0.5})(Nb_{1-x}Ta_x)O_3$ - $K_{5.4}CuTa_{10}O_{29}$  ceramics," *Journal of Applied Physics*, **97**[11] 114105 (2005).
- [8] M. Matsubara, T. Yamaguchi, K. Kikuta, and S. Hirano, "Synthesis and characterization of  $(K_{0.5}Na_{0.5})(Nb_{0.7}Ta_{0.3})O_3$  piezoelectric ceramics sintered with sintering aid  $K_{5.4}Cu_{1.3}Ta_{10}O_{29}$ ," *Japanese Journal of Applied Physics Part 1-Regular Papers Brief Communications & Review Papers*, **44**[9A] 6618-23 (2005).
- [9] M. Matsubara, T. Yamaguchi, K. Kikuta, and S. Hirano, "Sintering and piezoelectric properties of potassium sodium niobate ceramics with newly developed sintering aid," *Japanese Journal of Applied Physics Part 1-Regular Papers Short Notes & Review Papers*, **44**[1A] 258-63 (2005).
- [10] W. Zhang, N. Kumada, Y. Yonesaki, T. Takei, N. Kinomura, T. Hayashi, M. Azuma, and M. Takano, "Ferroelectric perovskite-type barium copper niobate:  $BaCu_{1/3}Nb_{2/3}O_3$ ," *Journal of Solid State Chemistry*, **179**[12] 4052-5 (2006).
- [11] S. Priya, A. Ando, and Y. Sakabe, "Nonlead perovskite materials:  $Ba(Li_{1/4}Nb_{3/4})O_3$  and  $Ba(Cu_{1/3}Nb_{2/3})O_3$ ," *Journal of Applied Physics*, **94**[2] 1171-7 (2003).
- [12] D. Iwanaga, Y. Inaguma, and M. Itoh, "Crystal structure and magnetic properties of B-site ordered perovskite-type oxides  $A_2CuB'O_6$  ( $A = Ba, Sr$ ;  $B' = W, Te$ )," *Journal of Solid State Chemistry*, **147**[1] 291-5 (1999).
- [13] R. D. Shannon and C. T. Prewitt, "Effective ionic radii in oxides and fluorides," *Acta crystallographica section B: structural crystallography and crystal chemistry*, **B 25** 925-& (1969).
- [14] R. D. Shannon, "Revised effective ionic-radii and systematic studies of interatomic distances in halides and chalcogenides," *Acta Crystallographica Section A*, **32**[Sep1] 751-67 (1976).
- [15] G. A. Smolenskii, V. A. Bobkov, V. A. Isupov, N. N. Krainik, R. E. Pasynkow, and A. I. Sokolov, "Ferroelectrics and Related Materials." In *Ferroelectricity and related phenomena*. Edited by G. W. Taylor. Gordon and Breach Science Publishers, New York, 1984.
- [16] L. M. Rodriguez-Martinez, H. Ehrenberg, and J. P. Attfield, "Cation size variance effects in high-tolerance factor  $Ln_{0.7}M_{0.3}MnO_3$  perovskites," *Journal of Solid State Chemistry*, **148**[1] 20-5 (1999).
- [17] A. Senyshyn, H. Ehrenberg, L. Vasylychko, J. D. Gale, and U. Bismayer, "Computational study of  $LnGaO_3$  ( $Ln = La-Gd$ ) perovskites," *Journal of Physics-Condensed Matter*, **17**[39] 6217-34 (2005).
- [18] C. Li, K. C. K. Soh, and P. Wu, "Formability of  $ABO_3$  perovskites," *Journal of Alloys and Compounds*, **372**[1-2] 40-8 (2004).
- [19] M. W. Lufaso, P. W. Barnes, and P. M. Woodward, "Structure prediction of ordered and disordered multiple octahedral cation perovskites using SPuDS," *Acta Crystallographica Section B-Structural Science*, **62** 397-410 (2006).
- [20] D. D. Khalyavin, A. N. Salak, N. P. Vyshatko, A. B. Lopes, N. M. Olekhovich, A. V. Pushkarev, I. I. Maroz, and Y. V. Radyush, "Crystal structure of metastable perovskite  $Bi(Mg_{1/2}Ti_{1/2})O_3$ : Bi-based structural analogue of antiferroelectric  $PbZrO_3$ ," *Chemistry of Materials*, **18**[21] 5104-10 (2006).
- [21] H. J. Yan, D. Q. Xiao, P. Yu, J. G. Zhu, D. M. Lin, and G. Y. Li, "The dependence of the piezoelectric properties on the differences of the A-site and B-site ions for  $(Bi_{1-x}Na_x)TiO_3$ -based ceramics," *Materials & Design*, **26**[5] 474-8 (2005).
- [22] C. A. Randall, R. Eitel, B. Jones, T. R. Shrout, D. I. Woodward, and I. M. Reaney, "Investigation of a high  $T_C$  piezoelectric system:  $(1-x)Bi(Mg_{1/2}Ti_{1/2})O_3$ -(x) $PbTiO_3$ ," *Journal of Applied Physics*, **95**[7] 3633-9 (2004).
- [23] S. J. Zhang, C. Stringer, R. Xia, S. M. Choi, C. A. Randall, and T. R. Shrout, "Investigation of bismuth-based perovskite system:  $(1-x)Bi(Ni_{2/3}Nb_{1/3})O_3$ -(x) $PbTiO_3$ ," *Journal of Applied Physics*, **98**[3] - (2005).

- [24] M. W. Lufaso and P. M. Woodward, "Jahn-Teller distortions, cation ordering and octahedral tilting in perovskites," *Acta Crystallographica Section B-Structural Science*, **60** 10-20 (2004).
- [25] S. A. Fedulov and P. B. Ladyzhinskii, "Complete phase diagram of the  $\text{PbTiO}_3$ - $\text{BiFeO}_3$  system," *Soviet Physics-Solid State*, **6** 375-7 (1964).
- [26] S. Nomura, K. Kaneta, J. Kuwata, and K. Uchino, "Phase-transition in the  $\text{PbTiO}_3$  -  $\text{a}(\text{B}_{2/3}\text{Nb}_{1/3})_2\text{O}_3$  ( $\text{a}=\text{La}, \text{Bi}$ ;  $\text{B}=\text{Zn}, \text{Mg}$ ) solid-solutions," *Materials Research Bulletin*, **17**[12] 1471-5 (1982).
- [27] I. Grinberg, M. R. Suchomel, W. Dmowski, S. E. Mason, H. Wu, P. K. Davies, and A. M. Rappe, "Structure and polarization in the high T-c ferroelectric  $\text{Bi}(\text{Zn}, \text{Ti})\text{O}_3$ - $\text{PbTiO}_3$  solid solutions," *Physical Review Letters*, **98**[10] 4 (2007).
- [28] M. R. Suchomel and P. K. Davies, "Enhanced tetragonality in  $(x)\text{PbTiO}_3$ -(1-x) $\text{Bi}(\text{Zn}_{1/2}\text{Ti}_{1/2})\text{O}_3$  and related solid solution systems," *Applied Physics Letters*, **86**[26] - (2005).
- [29] A. Munpakdee, K. Pengpat, J. Tontrakoon, and T. Tunkasiri, "The study of dielectric diffuseness in the  $\text{Ba}(\text{Mg}_{1/3}\text{Nb}_{2/3})\text{O}_3$ - $\text{BaTiO}_3$  ceramic system," *Smart Materials & Structures*, **15**[5] 1255-9 (2006).
- [30] C.-C. Huang and D. P. Cann, "Phase transitions and dielectric properties in  $\text{Bi}(\text{Zn}_{1/2}\text{Ti}_{1/2})\text{O}_3$  -  $\text{BaTiO}_3$  perovskite solid solutions," *Journal of Applied Physics*, **104**[2] 024117-4 (2008).
- [31] C.-C. Huang, D. P. Cann, X. Tan, and N. Vittayakorn, "Phase transitions and ferroelectric properties in  $\text{BiScO}_3$ - $\text{Bi}(\text{Zn}_{1/2}\text{Ti}_{1/2})\text{O}_3$ - $\text{BaTiO}_3$  solid solutions," *Journal of Applied Physics*, **102**[4] 044103-5 (2007).
- [32] M. M. Kumar, A. Srinivas, and S. V. Suryanarayana, "Structure property relations in  $\text{BiFeO}_3$ / $\text{BaTiO}_3$  solid solutions," *Journal of Applied Physics*, **87**[2] 855-62 (2000).
- [33] A. N. Salak, V. M. Ferreira, J. L. Ribeiro, L. G. Vieira, R. C. Pullar, and N. M. Alford, "Bismuth-induced dielectric relaxation in the  $(1-x)\text{La}(\text{Mg}_{1/2}\text{Ti}_{1/2})\text{O}_3$ - $x\text{Bi}(\text{Mg}_{1/2}\text{Ti}_{1/2})\text{O}_3$  perovskite system," *Journal of Applied Physics*, **104**[1] 014105-10 (2008).
- [34] T. Leist, W. Jo, T. Comyn, and A. Bell, "Shift in Morphotropic Phase Boundary in La-Doped  $\text{BiFeO}_3$ - $\text{PbTiO}_3$  Piezoceramics," *Japanese Journal of Applied Physics*, **48** 120205 (2009).
- [35] G. L. Yuan, K. Z. Baba-Kishi, J. M. Liu, S. W. Or, Y. P. Wang, and Z. G. Liu, "Multiferroic properties of single-phase  $\text{Bi}_{0.85}\text{La}_{0.15}\text{FeO}_3$  lead-free ceramics," *Journal of the American Ceramic Society*, **89**[10] 3136-9 (2006).
- [36] K. Oka, I. Yamada, M. Azuma, S. Takeshita, K. H. Satoh, A. Koda, R. Kadono, M. Takano, and Y. Shimakawa, "Magnetic Ground-State of Perovskite  $\text{PbVO}_3$  with Large Tetragonal Distortion," *Inorganic Chemistry*, **47**[16] 7355-9 (2008).
- [37] S. Priya, C. W. Ahn, and S. Nahm, "Dielectric Properties of  $(\text{Ba}_{0.6}\text{Sr}_{0.4})(\text{Cu}_{1/3}\text{Nb}_{2/3})\text{O}_3$  system," *Ferroelectrics*, **322** 75-82 (2005).
- [38] M. Barwick, F. Azough, and R. Freer, "Structure and dielectric properties of perovskite ceramics in the system  $\text{Ba}(\text{Ni}_{1/3}\text{Nb}_{2/3})\text{O}_3$ - $\text{Ba}(\text{Zn}_{1/3}\text{Nb}_{2/3})\text{O}_3$ ," *Journal of the European Ceramic Society*, **26**[10-11] 1767-73 (2006).
- [39] C. F. Buhrer, "Some Properties of Bismuth Perovskites," *Journal of Chemical Physics*, **36**[3] 798-803 (1962).
- [40] R. D. Shannon, "Dielectric Polarizabilities of Ions in Oxides and Fluorides," *Journal of Applied Physics*, **73**[1] 348-66 (1993).
- [41] S.-T. Zhang, A. B. Kouna, W. Jo, C. Jamin, K. Seifert, T. Granzow, J. Rödel, and D. Damjanovic, "High-strain lead-free antiferroelectric electrostrictors," *Advanced Materials*, **21**[46] 4716 - 20 (2009).
- [42] Y. Wang, D. Damjanovic, N. Klein, E. Hollenstein, and N. Setter, "Compositional inhomogeneity in Li- and Ta-modified  $(\text{K}, \text{Na})\text{NbO}_3$  ceramics," *Journal of the American Ceramic Society*, **90**[11] 3485-9 (2007).
- [43] K. T. P. Seifert, W. Jo, and J. Rödel, "Temperature-Insensitive Large Strain of  $(\text{Bi}_{1/2}\text{Na}_{1/2})\text{TiO}_3$ - $(\text{Bi}_{1/2}\text{K}_{1/2})\text{TiO}_3$ -( $\text{K}_{0.5}\text{Na}_{0.5}$ ) $\text{NbO}_3$  Lead-Free Piezoceramics," *Journal of the American Ceramic Society*, **93**[5] 1392-6 (2010).
- [44] T. Takenaka, K. Maruyama, and K. Sakata, " $(\text{Bi}_{1/2}\text{Na}_{1/2})\text{TiO}_3$ - $\text{BaTiO}_3$  system for lead-free piezoelectric ceramics," *Japanese Journal of Applied Physics Part 1-Regular Papers Short Notes & Review Papers*, **30**[9B] 2236-9 (1991).
- [45] A. Sasaki, T. Chiba, Y. Mamiya, and E. Otsuki, "Dielectric and piezoelectric properties of  $(\text{Bi}_{1/2}\text{Na}_{1/2})\text{TiO}_3$ -( $\text{Bi}_{0.5}\text{K}_{0.5}$ ) $\text{TiO}_3$  systems," *Japanese Journal of Applied Physics Part 1-Regular Papers Short Notes & Review Papers*, **38**[9B] 5564-7 (1999).
- [46] Y. P. Guo, K. Kakimoto, and H. Ohsato, "Structure and electrical properties of lead-free  $(\text{Na}_{0.5}\text{K}_{0.5})\text{NbO}_3$ - $\text{BaTiO}_3$  ceramics," *Japanese Journal of Applied Physics Part 1-Regular Papers Short Notes & Review Papers*, **43**[9B] 6662-6 (2004).
- [47] C.-H. Choi, C.-W. Ahn, S. Nahm, J.-O. Hong, and J.-S. Lee, " $(1-x)\text{BaTiO}_3$  -  $x(\text{Na}_{0.5}\text{K}_{0.5})\text{NbO}_3$  ceramics for multilayer ceramic capacitors," *Applied Physics Letters*, **90**[13] 132905-3 (2007).
- [48] R. Zuo, X. Fang, and C. Ye, "Phase structures and electrical properties of new lead-free  $(\text{Na}_{0.5}\text{K}_{0.5})\text{NbO}_3$ -( $\text{Bi}_{0.5}\text{Na}_{0.5}$ ) $\text{TiO}_3$  ceramics," *Applied Physics Letters*, **90**[9] 092904-3 (2007).

- [49] R. Zuo, X. Fang, C. Ye, and L. Li, "Phase Transitional Behavior and Piezoelectric Properties of Lead-Free  $(\text{Na}_{0.5}\text{K}_{0.5})\text{NbO}_3$ - $(\text{Bi}_{0.5}\text{K}_{0.5})\text{TiO}_3$  Ceramics," *Journal of the American Ceramic Society*, **90**[8] 2424-8 (2007).
- [50] S.-T. Zhang, A. B. Kounga, E. Aulbach, H. Ehrenberg, and J. Rödel, "Giant strain in lead-free piezoceramics  $\text{Bi}_{0.5}\text{Na}_{0.5}\text{TiO}_3$ - $\text{BaTiO}_3$ - $\text{K}_{0.5}\text{Na}_{0.5}\text{NbO}_3$  system," *Applied Physics Letters*, **91**[11] 112906-3 (2007).
- [51] S. T. Zhang, A. B. Kounga, E. Aulbach, T. Granzow, W. Jo, H. J. Kleebe, and J. Rödel, "Lead-free piezoceramics with giant strain in the system  $\text{Bi}_{0.5}\text{Na}_{0.5}\text{TiO}_3$ - $\text{BaTiO}_3$ - $\text{K}_{0.5}\text{Na}_{0.5}\text{NbO}_3$ . I. Structure and room temperature properties," *Journal of Applied Physics*, **103**[3] 034107 (2008).
- [52] S. T. Zhang, A. B. Kounga, E. Aulbach, W. Jo, T. Granzow, H. Ehrenberg, and J. Rödel, "Lead-free piezoceramics with giant strain in the system  $\text{Bi}_{0.5}\text{Na}_{0.5}\text{TiO}_3$ - $\text{BaTiO}_3$ - $\text{K}_{0.5}\text{Na}_{0.5}\text{NbO}_3$ . II. Temperature dependent properties," *Journal of Applied Physics*, **103**[3] 034108 (2008).
- [53] A. B. Kounga, S.-T. Zhang, W. Jo, T. Granzow, and J. Rödel, "Morphotropic phase boundary in  $(1-x)\text{Bi}_{0.5}\text{Na}_{0.5}\text{TiO}_3$ - $x\text{K}_{0.5}\text{Na}_{0.5}\text{NbO}_3$  lead-free piezoceramics," *Applied Physics Letters*, **92**[22] 222902-3 (2008).



## 4. Experimental Techniques

### 4.1. Powder and Ceramic Processing:

The ceramic powders were prepared by weighing the stoichiometric amount of the oxides or carbonates of the constituent elements. All powders were ordered from Alfa Aesar GmbH und Co. KG, Karlsruhe, Germany. Tab 13 shows the type of powder used for each element as well as purity and order code. One hundred per cent purity of the powders was assumed when calculating the required weight of the powders used to prepare the 40 g batches of the desired composition. Compensating for different degrees of purity would lead to excess ions intended for either the A-site or the B-site of the perovskite structure. A SBC 32 balance (Scaltec, Göttingen, Germany) was used to weigh the powders to the nearest milligram.

**Tab 13: Chemicals Used in Ceramic Processing**

Element	Chem. formula	Purity [%]	order code
Bi	Bi <sub>2</sub> O <sub>3</sub>	99.98	44657
K	K <sub>2</sub> CO <sub>3</sub>	99.00	12609
Na	Na <sub>2</sub> CO <sub>3</sub>	99.50	11552
Ti	TiO <sub>2</sub>	99.90	39953
Nb	Nb <sub>2</sub> O <sub>5</sub>	99.90	11366

The weighed-in powders were placed in milling containers cut from a block of Nylon 6-6 together with a 1:2:2 weight ratio of 10 mm, 5 mm and 3 mm diameter yttria-stabilised zirconia milling balls (Mühlmeier GmbH, Bärnau, Germany). The milling ball to powder ratio was always 10:1 in weight. The powders were milled in a planetary ball mill (Pulverisette 5, Fritsch GmbH, Idar-Oberstein, Germany) with 99 % pure naturalised ethanol as the milling medium for 24 hours at 180 rpm. Even though the wear of the nylon milling containers is much higher than of comparable stabilised zirconia containers, it is assumed that the worn off container material is purely organic and will burn off during calcination and sintering, respectively. It should therefore not contaminate the powders.

Afterwards the powder was separated from the milling balls and dried at 90 °C for 24 hours. They were then homogenised in an agate mortar (Carl Roth GmbH, Karlsruhe, Germany) and placed in an alumina crucibles with 99.8 % alumina phase. The high alumina content of the crucible is important since sodium and potassium ions readily infiltrate the silicate glass phase used during the sintering of the crucible and lower the glass transition temperature below the required calcination or sintering temperature. The crucibles were covered with close fitting

alumina plates. All alumina-based lab equipment was ordered from Buntenkötter Technische Keramik GmbH, Neuss, Germany.

The powders were calcined in covered alumina crucibles with a heating rate of 5 K per minute and a holding time of three hours at 800 °C in a furnace (L9/KM, Naberterm GmbH, Lilienthal, Germany). They were allowed to cool naturally in the furnace afterwards.

The second 24-hour milling step at 250 rpm was done in 30-minute intervals with a 10-minute break between each interval to prevent overheating of the milling containers due to friction.

After a second drying and homogenisation step, disk shaped samples of 10 mm diameter weighing approximately 0.33 g each were hand-pressed in a custom-made pressing die. Then they were vacuum-sealed in flexible latex rubber protective bags to protect against contamination from mineral oil of the cold isostatic press (KIP100, Paul-Otto Weber GmbH, Remshalden, Germany) with a 50 mm pressing stamp. 700 kN of force translating to a pressure of 356 MPa was exerted for 90 seconds and then manually released over a period of 90 seconds.

The samples were then placed in a self-made sintering setup. The sintering setup, which can be seen in Fig 24, comprises of a polished and lapped thick alumina plate, approximately 1 cm high alumina pipes of 12 mm inner diameter with polished and lapped rims and heavy polished and lapped alumina lids. The lapped contact surfaces provide a tight fit between the separate parts and are intended to minimise the evaporation of bismuth and potassium during sintering. Five disk shaped green bodies of equal composition were stacked on top of each other inside the alumina pipes on the alumina plate. The green bodies were separated by a thin layer of calcined and milled powder of the same composition. The whole stack of disks inside the pipes was also surrounded on all sides by a large quantity of calcined and milled powder of the same composition, also called atmospheric or sacrificial powder. The purpose of this powder is to saturate the atmosphere inside the sintering setup with the correct concentration of elements and hence prevent the evaporation of elements from the pressed green bodies themselves. The self-made sintering setup required only about 30 % of the atmospheric powder compared to the smallest commercially available crucible and sealed more tightly. The so-arranged samples were sintered in another furnace (L16/14, Naberterm GmbH, Lilienthal, Germany) at 1100 °C for three hours with a 5 K per minute heating and cooling rate.

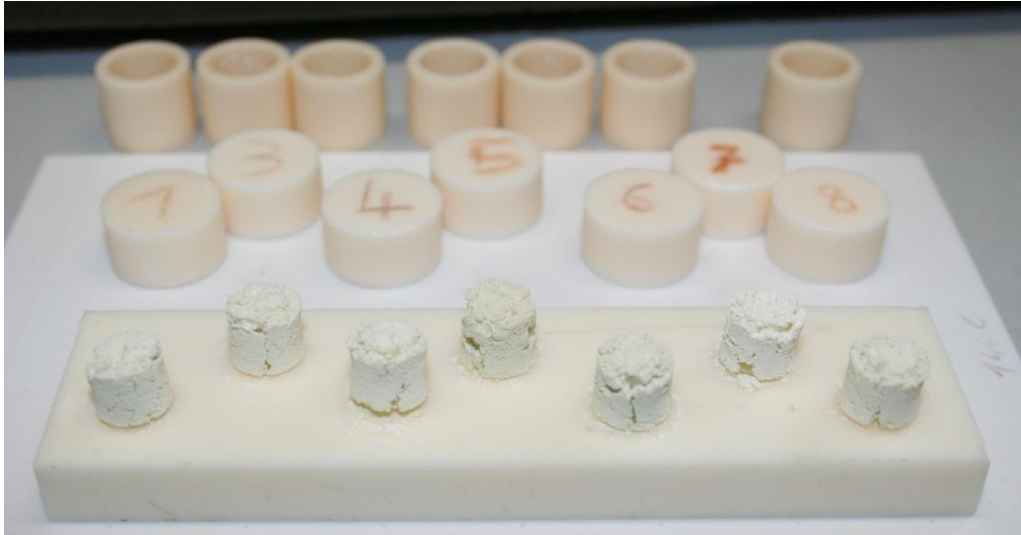


**Fig 24: The self-made sintering setup, comprising of the alumina plate, alumina pipes and alumina lids, is shown in its disassembled state. All contact surfaces were lapped and polished to minimize the gaps at the contact surfaces. The stacked samples that are baked into the atmospheric powder after sintering can also be seen at the front.**

After the atmospheric powder was removed, the samples were manually ground using silicon carbide abrasive powder of 320, 600 and 1000 grid used consecutively as needed. The final thickness was always between 0.6 mm and 0.7 mm.

The samples were then polished in a twin wheel polishing machine, (Phoenix 4000 DUO, Jean Wirtz GmbH (now Buehler GmbH), Düsseldorf, Germany) at 180 rpm with diamond polishing paste of 15 and 6 micron particle size if used for Sawyer tower type strain and polarisation measurements, reflex geometry x-ray diffraction or density determination. Samples used in high frequency dielectric measurements were polished down to 1  $\mu\text{m}$  particle size and samples used for high-resolution electron microscopy were polished to 0.25  $\mu\text{m}$ . Afterwards the samples were cleaned in an ultrasonic bath inside a beaker filled with pure acetone and then again in isopropanol.

Pure silver electrodes were created with a sputtering device (SCD 040, Balzers Union, Balzers, Liechtenstein) using a 60 mA current for 210 seconds. Electrode materials sputtered on to the edge of the sample were removed by hand using 1000 grid sandpaper.

## **4.2. Structure and Microstructure**

### **4.2.1 Density**

Based on the ASTM standard C20-00 (2005)<sup>[1]</sup>, the samples were placed in distilled water and then a vacuum was drawn for about 15 to 30 minutes to remove air from the surface of the sample. Modified Sartorius Basic analysis scales allow weighing the samples in water and in air without having to reset the scale. An analogue thermometer was used to record the temperature of the distilled water each time. Deviation from the ASTM C20-00 (2005) was necessary because the samples are water sensitive, which prevented normally required boiling for the 2 hours and submersion in water for 12 hours.

The relative density was calculated by dividing the actual density by the theoretical density. The theoretical density of each composition is the average mass per unit cell divided by the unit cell volume as determined from x-ray powder diffraction (section 4.2.3).

### **4.2.2 High-Resolution Electron Microscopy**

Samples used for high-resolution electron microscopy (HREM) investigations of the microstructure were polished to 0.25 micron. To expose the microstructure, thermal etching at 900 °C for 30 minutes or chemical etching was done. The etching medium in the second case was concentrated hydrochloric acid with 3 to 5 drops of hydrofluoric acid per 500 ml. The etching times were determined for each sample individually by inspecting the etched surface with an optical microscope. Samples for fracture surface inspection were prepared by cutting a small notch into the edge of the disk shaped samples with a razor blade. A crack was then allowed to grow slowly starting from the notch by putting the sample under tension.

The samples were then glued onto the aluminium sample holders with double-sided conductive carbon sticky tape and sputtered with gold-palladium for 60 seconds with a 60 mA current.

The electron microscope used for HREM investigations was a XL30 FEG (FEI/Phillips, Eindhoven, Netherlands) with backscattered electron (BSE) and energy-dispersive x-ray modules and controller software version 7.0 released 14.12.2004.

Pictures of the etched microstructure were loaded into Lince (version 2.4.2b)<sup>[2]</sup> to measure the average grain size and standard deviation of the grain size. After setting the scale accurately, lines are drawn randomly across the microstructure image and then the types of boundaries (e.g. grain boundary, triple boundary, pore boundary,...) are marked along these lines. Using the data of at least 200 grains, the program can then calculate the desired grain size parameter.

The back scattered electron modus was used to enhance visibility of the microstructure and to scan for compositional inhomogeneity. The EDS module was used to validate the approximate composition of the samples to check against errors during powder processing. Its absolute compositional accuracy of about 5 % is lower than the compositional variations between samples. It is, therefore, not exact enough to determine evaporation losses or similar systematic errors in composition.

### 4.2.3 X-Ray Diffraction

X-ray powder diffraction in transmission geometry was done on the calcined and milled powders and on fully sintered samples. The sintered samples were crushed into powder in agate mortar. An old damaged mortar was used since crushing sintered samples might damage the polished surface of the mortar. The powder was held in the sample holder between two sheets of amorphous organic film and glued with non-crystallising glue to prevent diffraction reflexes from anything but the powder sample. The powder x-ray machine (Stadi P, Stoe & Cie GmbH, Darmstadt, Germany) was set to an angular resolution of  $0.03^\circ$  and the scanning range was set from  $10^\circ$  to  $90^\circ$  using  $\text{Cu}_{K\alpha 1}$  radiation. The exposure time per sample was 4 hours, which was divided into two distinct scans to identify occasional variations in background intensity arising from the machine.

X-ray diffraction in reflective geometry of poled samples was done using a D8 Advanced (Bruker AXS GmbH, Karlsruhe, Germany) running DIFFRACplus software version 2.4. To avoid back switching due to mechanical pressure, the sputtered silver electrodes were not removed with sandpaper and the ultrasonic bath was not used for removing the silicon oil after poling. The oil was instead removed by washing the samples in fresh isopropanol repeatedly. It was then let dry without wiping the surface with a cloth. Using the penetration depth of  $\text{Cu}_{K\alpha 1}$  radiation into metallic silver and the estimated sputtered thickness, it was estimated that the signal contributions from the silver electrode and the sample itself would be at most equal in magnitude. Diffraction reflexes from the silver could therefore be eliminated from the diffraction profile at a later stage. This, however, proved unnecessary due to the small contribution from silver.

The resulting patterns were refined with the „GSAS“ x-ray pattern refinement software (released 20.04.2006)<sup>[3]</sup> using the „EXPGUI“ (version 1.8, released 30.04.2006) graphical user interface<sup>[4]</sup>. The wavelength of the  $\text{Cu}_{K\alpha 1}$  radiation was always taken to be 1.54056 Å.

In order to avoid “runaway” of single types of ions from their crystallographic sites, the displacement of A-site ions ( $K^{1+}$ ,  $Na^{1+}$  and  $Bi^{3+}$ ) from their A-site centre position was limited to concurrent and equal displacement of these ions. The B-site ions ( $Ti^{4+}$  and  $Nb^{5+}$ ) were constrained in a similar manner.

#### **4.2.4 Transmission Electron Microscopy**

All the transmission electron microscopy studies were carried out by Ljuba Schmitt in the workgroup of Joachim Kleebe (Geomaterialwissenschaften, Material- und Geowissenschaften, TU Darmstadt, Germany).

Sintered samples were polished down to a thickness of 120  $\mu m$ . Then disks of approximately 3 mm were drilled out. Afterwards a dimple grinding step (Mod. 656, Gatan GmbH, München, Germany) down to 15  $\mu m$  was followed by an ion beam milling step (Mod. 600, Gatan GmbH, München, Germany) resulting in a final thickness of approximately 10-100 nm. Sputtered carbon was used to provide a conductive layer against static electricity build-up under the incident electron beam.

### 4.3. Large-Signal Electrical Measurements

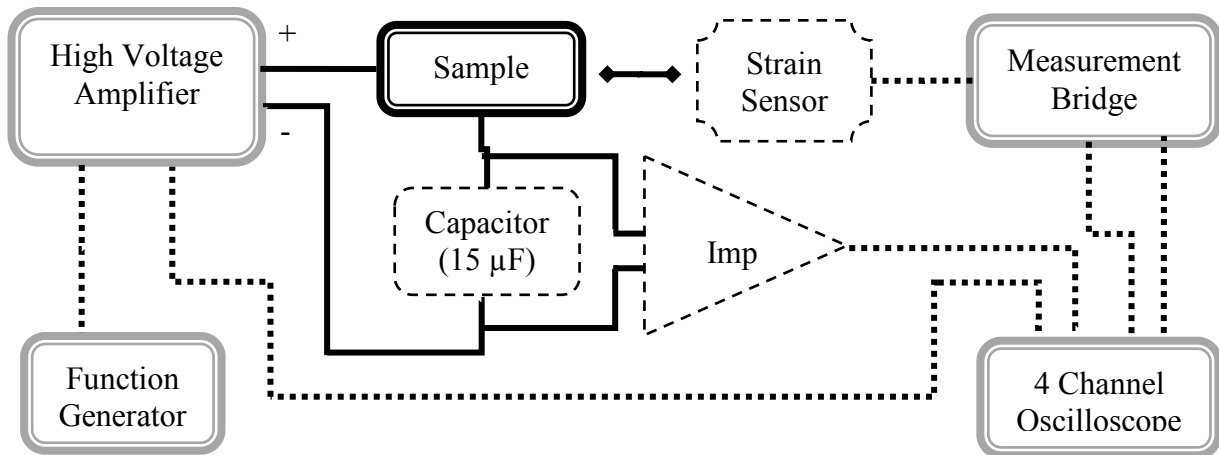


**Fig 25:** Diagram showing the extended Sawyer-Tower setup used for large-signal electrical characterisation.

Grey frames are parts that require user input during setup. The dotted frames show parts that are not modified during the experiment. Black lines are high voltage wires, dotted lines are signal carrying wires. The high voltage amplifier provides a scaled down reference output signal to the first channel of the oscilloscope, the measurement bridge supplies the axial strain signal into channel 3 and the radial signal into channel 4. Channel 2 records the voltage drop across the measurement capacitor.

The Sawyer-Tower circuit (Fig 25) is essentially a voltage source connected across two capacitors in series, the sample and the 15 μF measuring capacitor. Since the capacitance of the sample is much smaller than that of the measuring capacitor and the charge transfer onto both capacitive elements is equal, the actual voltage drop across the measuring capacitor is minimal and can be measured safely. The capacitance of the samples can then be calculated using Eq 8, which in turn gives the polarisation of the sample according to Eq 9. An impedance converter is connected between the capacitor and the oscilloscope. In the event of an electric breakdown of the sample, the impedance converter protects the expensive oscilloscope from the high voltage then applied fully across the measuring capacitor.

$$C_{sample} = C_{capacitor} * \frac{V_{capacitor}}{V_{sample}} = C_{capacitor} * \frac{V_{capacitor}}{V_{total}}$$

Eq 8

$$P_{sample} = C_{sample} * V_{total} / A_{sample} = C_{capacitor} * V_{capacitor} / A_{sample}$$

Eq 9

The electrical measurements were all done on disk shaped samples with a thickness to diameter ratio of 1:10 or less, so that the edge effect of the electric field can be neglected and the samples can hence be assumed to be parallel plate capacitors. The sample is always submerged in silicon oil (AK35 or AK150, Wacker-Chemie GmbH, München, Germany) with a breakdown strength of above 15 kV/mm under optimal conditions. AK35 was used whenever possible due to its lower viscosity but AK150 was required for temperatures above 200 °C because AK35 would decompose within minutes releasing toxic fumes in the process. Temperature-dependent measurements were done in a heated oil bath (Proline P8, Lauda GmbH & Co. KG, Lauda-Königshofen, Germany).

Strain sensors extend the Sawyer-Tower setup. Three different configurations of strain sensors were used. For temperature-dependent measurements a linear variable differential transformer (LVDT) strain sensor with 20 nm resolution (Mod W1T3 or equivalent, Hottinger Baldwin Messtechnik GmbH, Darmstadt, Germany) in conjunction with a two channel measurement bridge (AB12 or equivalent, Hottinger Baldwin Messtechnik GmbH, Darmstadt, Germany) was used. Volume changes during a measurement cycle at room temperature were done using two additional radially attached LVDT sensors concurrently with the axial sensor. The radial setup is shown in Fig 26.



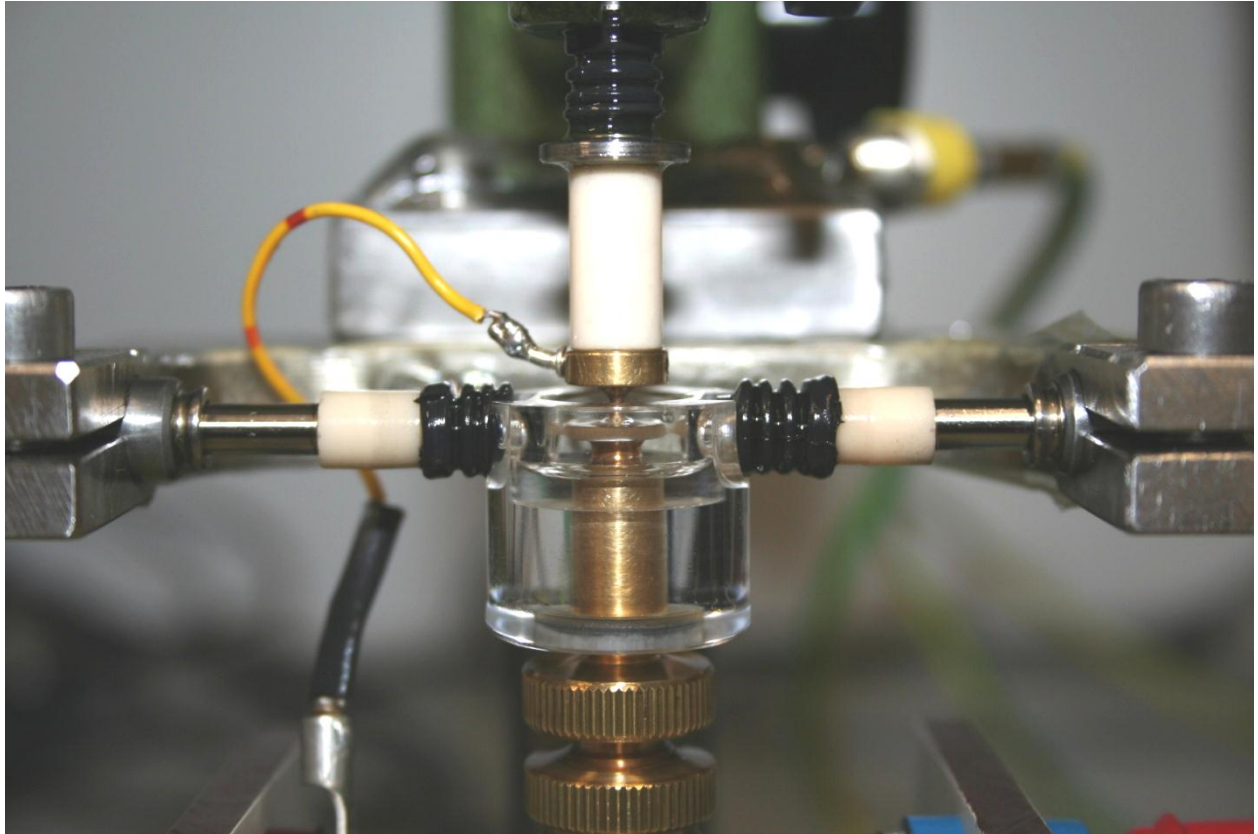


**Fig 26: Picture of the radial strain setup build in-group by Emil Aulbach.**

Similar to all strain sensor setups, the top electrode (cathode) is connected to the axial strain sensor and electrically insulated by a few centimetres of alumina. The radial sensors have to touch the middle of the edge of the sample. The height of the bottom electrode (anode) can be adjusted accordingly. The sample is held in place by the axial strain sensor in the centre of the disk-shaped sample. The two radial strain sensors each record the strain from the centre of the sample to the edge. The average of the two radial signals was used to calculate the radial strain across the diameter of the sample in per cent. The axial sensor signal is used to determine the axial strain across the thickness of the sample in per cent. The sum of the two signals, therefore, gives the absolute volume change in per cent.

At room temperature, an optical non-contact displacement sensor and analogue output (D63+A1+H+LN PQ, Philtec, Inc. Annapolis, MD, USA) in axial (33) direction was used since it provides the best resolution of 4 nm to 15 nm depending on conditions.

The natural frequency of the optical setup was experimentally found to be about 3 kHz. For this, a standard PZT samples was driven with a single rectangular pulse. The wave-like overshooting signal can then be easily read off at the beginning of the peak of the pulse and its frequency determined. Reliable large-signal strain measurements should hence be possible up to about one order of magnitude less. The LVDT sensors in comparison were limited to about 100 mHz due to

contamination with silicon oil as well as its higher measurement tip weight coupled with a weaker preload spring.

All Sawyer-Tower circuits were driven by a function generator (33220A, Technologies Deutschland GmbH, Böblingen, Germany) whose signal is amplified 2000 times by a high voltage amplifier (20/20C, TREK Inc., Medina, NY, USA), which provides a maximum output voltage of 20 kV and a maximum output current of 20 mA and a slew rate<sup>33</sup> of 450 V/ $\mu$ s. All data was recorded with an oscilloscope (DS06014A, Agilent Technologies Deutschland GmbH, Böblingen, Germany).

The applied signal for unipolar and bipolar measurements was in each case saw-tooth shaped as shown in Fig 27 and the amplitude adjusted to the thickness of the sample to give the desired maximum electric field ( $E_{\max}$ ).

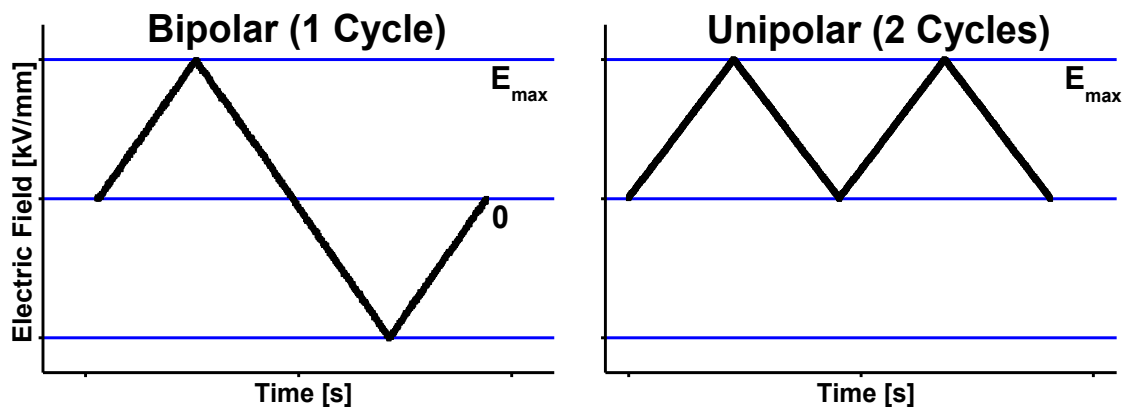


**Fig 27: Typical zigzag or saw tooth shaped voltage signal used in bipolar (a) and unipolar (b) large field characterisation.**

**a) The applied electric field goes linearly from zero to  $E_{\max}$ , back through zero(c) to  $E_{-\max}$  and back to zero again where the cycle can begin again. In a large-signal characterisation, this cycle is repeated at least twice and the second cycle, therefore, starts with the samples poled in the opposite direction. b) The unipolar signal is a phase-shifted version of the bipolar cycle by  $270^\circ$ , offset by  $\frac{1}{2} E_{\max}$ , with half the peak to peak amplitude and twice the frequency. The frequency doubling is required so that the signal ramps are the same.**

<sup>33</sup> The „slew rate,, is the highest rate of change of voltage with time achievable by the amplifier

All recorded data was imported from the oscilloscope into OriginPro 7.5 SR6 and converted according to the following equations:

$$E_{sample} [kV/mm] = f_{HV} * CH1[V]/d [mm]$$

Eq 10

$$P_{sample} [\mu C/cm^2] = C_{capacitor} [\mu F] * CH2[V] / (A_{sample} [mm^2] / 100)$$

Eq 11

$$S_{sample} [\%] = CH3[V] * 100 * f_{MB} [V/mm] / d [mm]$$

Eq 12

$$S_{Rsample} [\%] = CH4[V] * 100 * f_{MB} [V/mm] / w [mm]$$

Eq 13

The symbols mean the following: E=electric field, P=polarisation, S and S<sub>R</sub> are axial and radial strain, C=capacitance, CH1-4 are the oscilloscope channels. A, d and w are area, thickness and diameter of the sample and f<sub>MB</sub> and f<sub>HV</sub> are the conversion factors of the measurement bridge and the high-voltage amplifier, respectively. The units are given in the brackets.

The energy content of a unipolar or bipolar cycle was determined by integrating the area of the polarisation versus electric field hysteresis using origin.

In order to extend the range of frequencies achievable by the high voltage amplifier, the sample diameter was reduced to ~3.8 mm by drilling out disk shaped pieces from the original samples. Since this reduces the ratio of diameter to thickness and damage on the edges of the electrodes and samples, the polarisation values can only be compared for different frequencies of the same sample.

## 4.4. Small-Signal Electrical Measurements

### 4.4.1 Small-Signal Piezoelectric Constant

All reported small-signal  $d_{33}$  values were measured with a piezoelectric ceramic  $d_{33}$  calibrator (YE2730, Sinoceramics, State College, PA, USA) with 5 % accuracy, 110 Hz and 0.25N force. Unless stated otherwise, values were taken 24 h after poling.

### 4.4.2 Temperature-Dependent Impedance Spectroscopy

Temperature-dependent impedance spectroscopy was done between room temperature and 500 °C<sup>34</sup> in a custom built vacuum temperature control chamber (Internal design number: 7505-06, Cryovac GmbH und Co. KG, Troisdorf, Germany) with a temperature range from room temperature to 1100 °C and an achievable vacuum of 10<sup>-09</sup> bar . Two LCR<sup>35</sup> meters (4284A and 4285A, Hewlett-Packard GmbH, Böblingen, Germany) covering the frequency ranges 20 Hz to 75 kHz and 75 kHz to 20 MHz respectively were used as measurement bridges. These devices were set to measure the capacitance (C) and loss ( $\delta$ ). Starting from 100 Hz readings were taken every order of magnitude up to 1 MHz every 1 K. The recording software was programmed with Lab View (National Instruments Germany GmbH, München, Germany) in-group by Gundel Fliß. If the sample is purely capacitive (not inductive, not conductive), which is the case for piezoelectric ceramics at the measured frequencies,  $\tan\delta$  is equal to  $\delta$  for small losses.

The relative dielectric constant ( $\epsilon_r$ ) is calculated using Eq 14:

$$\epsilon_r = \frac{C_{sample} * d}{\epsilon_0 A}$$

Eq 14

Where  $\epsilon_0$  is the permittivity of free space and equals to 8.85x10<sup>-12</sup>F/m. d and A are thickness and area of the sample.

<sup>34</sup> At the time of measurement, the accuracy of the temperature sensor had not yet been verified. With a temperature sensor in place of the sample, it was later found that the sample temperature was in fact lower and the temperature difference highly dependent on the vacuum pressure. The approximate gradient between real and recorded temperature was ~1/1.25 starting at room temperature. The peak temperature of 500 °C was therefore actually more or less 400 °C.

<sup>35</sup> LCR meters measured the complex impedance of a material, the name is derived from the inductance (L), capacitance (C) and resistance (R) that make up the complex impedance.

### **4.4.3 Low Frequency Impedance Spectroscopy**

A low frequency impedance spectrometer (1260A, Solatron Analytical, AMETEK GmbH, Meerbusch, Germany) was used at the same frequencies used during frequency-dependent large-signal measurements to record the dielectric constants.

## 4.5. Ferroelastic Measurements

### 4.5.1 Sample Preparation

8 to 9 g of calcined and milled powder were hand-pressed in a pressing die with 2.5 cm diameter and isostatically pressed for three minutes with an offloading ramp of three minutes. Preparation was otherwise as described in section 4.1. The resulting cylinder with about 14 mm diameter was ground, polished and lapped down to 6 mm height with a maximum surface parallelity deviation of 0.5 %. Then, cylindrical samples of 5.88 mm diameter were drilled out of the large cylinder with a diamond drip tip. To minimise damage to sample edges, the sample was glued to a glass plate with resin and a microscope glass slide was glued onto the top surface. The drilling progress was manually kept below 0.2 mm/min and further reduced at the glass-to-ceramic interfaces. However, only 1 in 3 samples survived the drilling process with sufficient quality sample edges.

### 4.5.2 Measurement Procedure

The temperature-dependent differential dilatometer for ferroelectric testing was custom-built in-group by Emil Aulbach. The sample-testing environment is diagrammed and described in Fig 28. The force onto the setup is provided by a 10 kN (max) screw-driven load frame (Z010, Zwick GmbH und Co. KG, Ulm, Germany) via the alumina tubes on each end. The load frame can be either of load or displacement controlled. The alumina rods connected to the LVDT were pressed to their respective tungsten carbide surfaces by leaf springs with the force of less than 1 N.

The precise measurement procedure for each sample begins by annealing the sample at 450 °C for 15 minutes. Afterwards the sample was allowed to cool to room temperature, and then cleaned in an ultrasonic bath in isopropanol. The tungsten carbide surfaces and the sample surfaces were carefully cleaned with an air duster. After placing the sample in the machine and aligning it with an alumina fixture<sup>36</sup>, a pre-load of less than 10 N was set. The setup was then carefully tapped to allow all pieces to settle into their final positions. Heating was done under a preload of 15 N at a rate of 2 K/min. 15min holding time at the desired temperature still under preload was necessary to wait out thermal drift. Beginning at 100N, the load was increased to 10.32 kN at the rate of 100 N/s and decreased at the same rate down to 100 N again. This cycle was repeated twice more. The results were recorded by the testing machine software (TestXpert 9.01, Zwick GmbH und Co KG, Ulm, Germany).

---

<sup>36</sup> Since the setup was at an early stage of development when the readings were taken, there is an increased error due to the risk of misalignment.

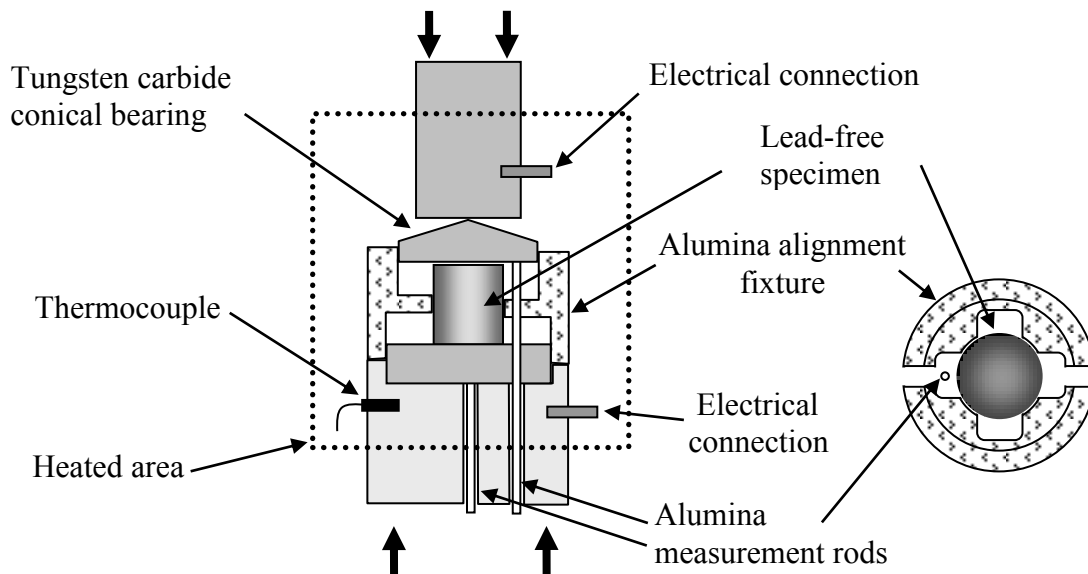


**Fig 28: Schematic drawing of the ferroelastic testing setup<sup>[5]</sup>.**

The sample rests on a lapped tungsten carbide disk with a thermocouple directly beneath. The disc is in direct contact with an alumina measurement rod connected to an LVDT sensor. On top of the sample a tungsten carbide conical bearing is placed to compensate for the possibly non-parallel sample surfaces due to the polishing process. The bottom of the conical bearing is also in direct contact with an alumina measurement rod connected to an LVDT sensor. This whole setup is centred, aligned and held in place by an alumina alignment fixture. When axial compressive stress is exerted onto the whole setup, the difference of the two LVDT sensor readings is used to calculate the strain of the sample. The top and bottom electrical connection were connected to allow charge transfer. The setup was heated by a split furnace (TL800, Thermal Technologies GmbH, Bayreuth, Germany) as shown above. The arrows show, where force was applied via hollow alumina rods (22 mm/19 mm outer/inner diameter).

Measurements were done in 25 K steps starting at 25 °C up to 150 °C, 200 °C was also recorded. The same sample was reused each time for consistency and a room temperature cycle at the beginning and end of use of the sample was taken to check for degradation. At each temperature step, the whole measuring cycle was run also without a sample. This gives the contribution to the dilation inherent in the setup. It was found to be purely linear and without hysteresis across the entire measured temperature range.

## 4.6. References

- [1] "Standard Test Methods for Apparent Porosity, Water Absorption, Apparent Specific Gravity and Bulk Density of Burned Refractory Brick and Shapes by Boiling Water," *Annual Book of ASTM Standards*, **C20-00** (2005).
- [2] S. L. dos Santo e Lucato, "Lince v2.4-Linear Intercept," *Department of Materials Science* (1999).
- [3] A. C. Larson and R. B. Von Dreele, "General Structure Analysis System (GSAS)," *Los Alamos National Laboratory Report No. LAUR 86-748* (1994).
- [4] B. Toby, "EXPGUI, a graphical user interface for GSAS," *Journal of Applied Crystallography*, **34**[2] 210-3 (2001).
- [5] K. G. Webber, E. Aulbach, T. Key, M. Marsilius, T. Granzow, and J. Rödel, "Temperature-dependent ferroelastic switching of soft lead zirconate titanate," *Acta Materialia*, **57**[15] 4614-23 (2009).



## 5. Experimental Results

### 5.1. Nomenclature

The produced materials were mixtures of two reported MPB compositions in the BNT-BKT-KNN phase diagram, 80BNT-20BKT<sup>[2]</sup> and 97KNN-3BKT<sup>[4]</sup>. 79BNT-21BKT and 81BNT-19BKT were also mixed with KNN-3BKT to investigate ,off-MPB,, behaviour. The following formula describes the prepared compositions:

$$(1 - \frac{Y}{100})[(1 - \frac{X}{100})BNT + \frac{X}{100}BKT] + \frac{Y}{100}[0.97KNN + 0.03BKT]$$

Eq 15

Where X was either 19, 20 or 21 and Y is varied between 0 and 100 in different step sizes. The mixtures are written as X;Y. Therefore, 80BNT-20BKT for example is 20;0, 97KNN-03BKT is 20;100 and 81BNT-19BKT-2(97KNN-03BKT) is 19;2.

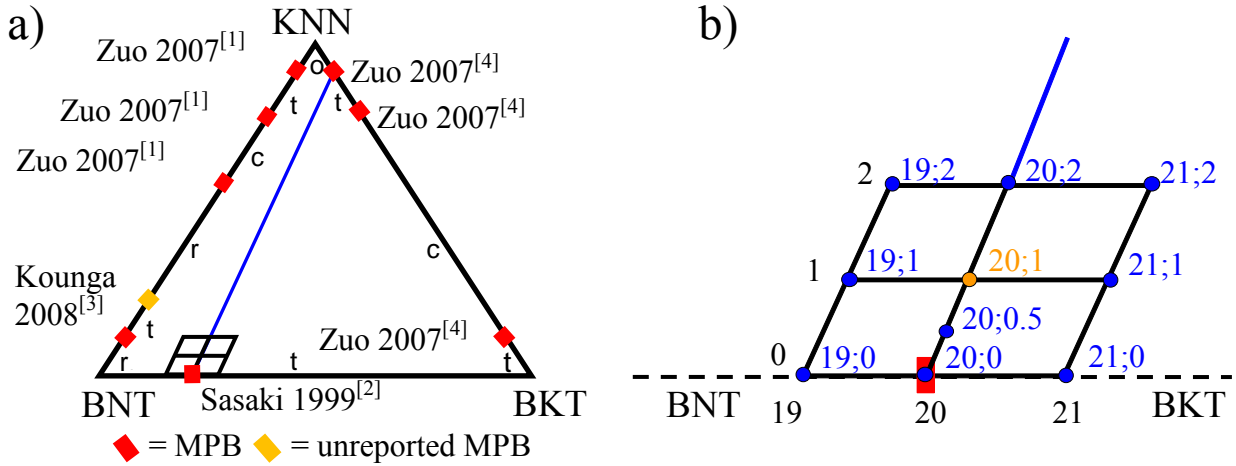


**Fig 29: The BNT-BKT-KNN phase diagram (a) with the investigated line of compositions highlighted in blue. On the right (b), the matrix of investigated compositions near the BNT-BKT MPB is displayed with position and nomenclature. The MPBs are marked in red, one unreported MPB is marked in yellow.**

As a result of the first experiments (chapter 5.2), the line shown in Fig 29, the line was extended to a 10 composition matrix (3 x 3 +20;0.5) at the BNT-BKT rich end of the line to investigate the properties of the compositions surrounding 20;1. For the remainder of this work, these 10 compositions will be referred to as the “matrix compositions” or “all compositions” since the remaining compositions were not investigated beyond their density and preliminary large and small-signal strain and polarisation.

## 5.2. Broad Composition Search

Initially, two lines of compositions were investigated, the first one connecting BNT-20BKT with KNN, the second one connecting BNT-BKT with KNN-BKT. The first line proved to have poor sintering behaviour for >50 mol% KNN. Since the difference between both lines diminishes with proximity to the BNT-20BKT, the first line was dropped from the investigation. The result of the search by use of bipolar large-signal and small-signal properties is shown in Fig 30. The region 20;0-20;10 is magnified in Fig 31, where unipolar large-signal data is also included.

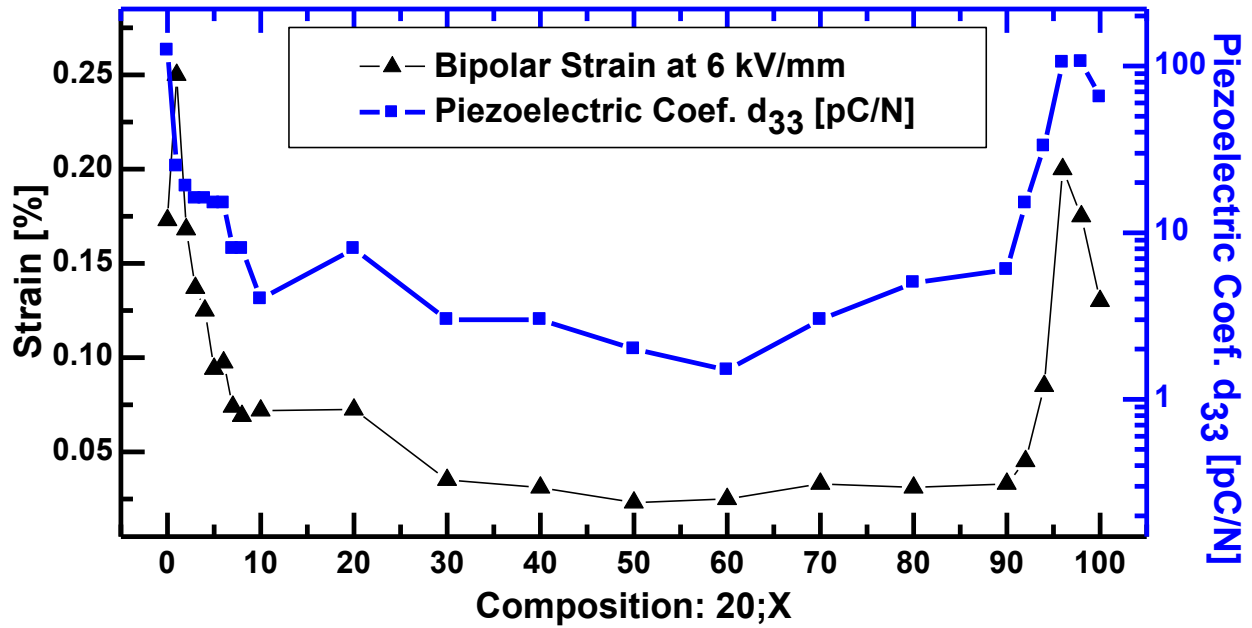


Fig 30: The results of the broad composition search. Bipolar strain at 6 kV/mm of compositions between 20;0 and 20;100 in 10 mol% KNN-BKT steps across the whole phase diagram (Fig 29a) were measured. The regions 20;0-20;10 and 20;90-20;100 were then refined in the second step with 1 mol% KNN-BKT and 2 mol% KNN-BKT steps, respectively.

Starting at 20;0, the bipolar and unipolar strain at 6 kV/mm are 0.172 % and 0.125 % with a corresponding small-signal  $d_{33}$  of 125 pC/N. At 20;1, the bipolar and unipolar large strain are nearly identical at 0.250 % and 0.248 % respectively with a small-signal  $d_{33}$  of 25 pC/N. Between 20;02 and 20;10, unipolar and bipolar large strain are identical and, together with small-signal  $d_{33}$  decrease continuously to 0.072 % and 4 pC/N at 20;10. Between 20;20 and 20;30 the large strain drops from 0.072 % to 0.035 % and remains there or below up to 20;90 with a minimum of 0.023 % at 20;50. The small-signal  $d_{33}$  between 20;10 and 20;90 fluctuates between 8 pC/N and the minimum of 1.5 pC/N at 20;60.

The region 20;90-20;100 has a peak bipolar and unipolar strain of 0.2 % and 0.1 % at 20;96 and a peak  $d_{33}$  at 20;98 of 106 pC/N. 20;100 (pure KNN-BKT) was found to have 0.13 % and 0.01 % bipolar and unipolar strain and a  $d_{33}$  of 65 pC/N.

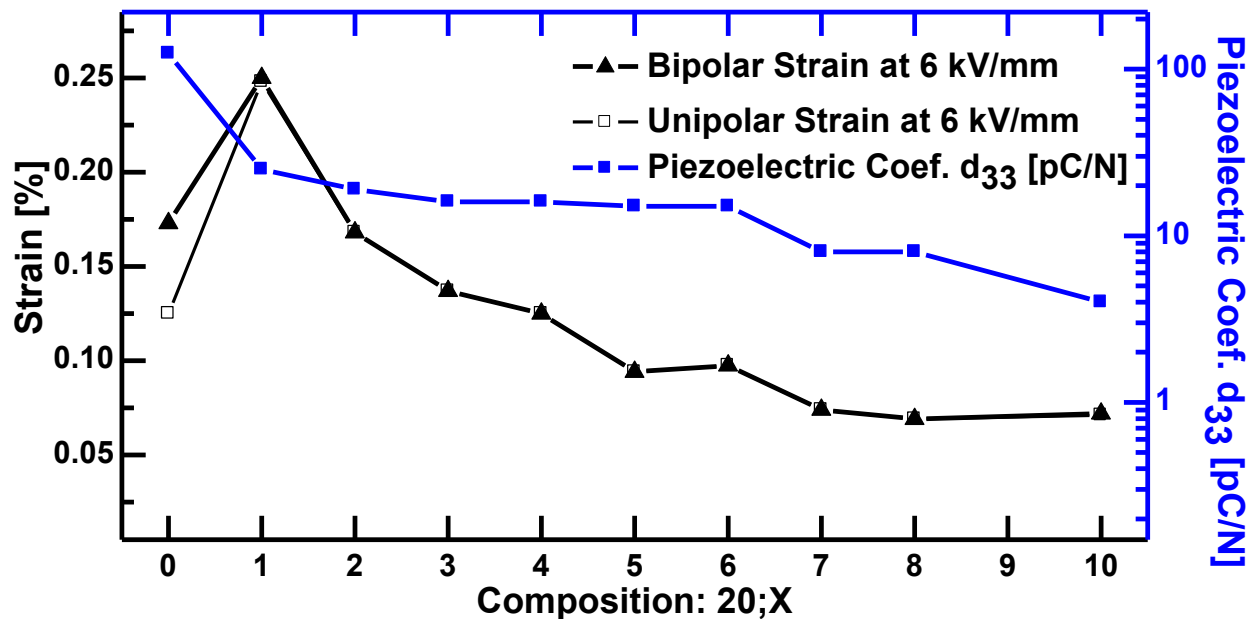


Fig 31: The refinement of the region 20;0 to 20;10. Bipolar and unipolar strain at 6 kV/mm of compositions between 20;1 and 20;8 in 1 % KNN-BKT and the previous data points at 20;0 and 20;10.

As a result of the refinement in the region 20;0 to 20;10, composition 20;1 was identified as having the highest unipolar and bipolar strain values overall. To investigate this behaviour further a 3x3 matrix of compositions X;Y centred on 20;01 (X: 19, 20, 21 and Y: 0, 1, 2) and also composition 20;0.5 were prepared as shown in Fig 29b.

## 5.3. Structure and Microstructure

### 5.3.1 Density

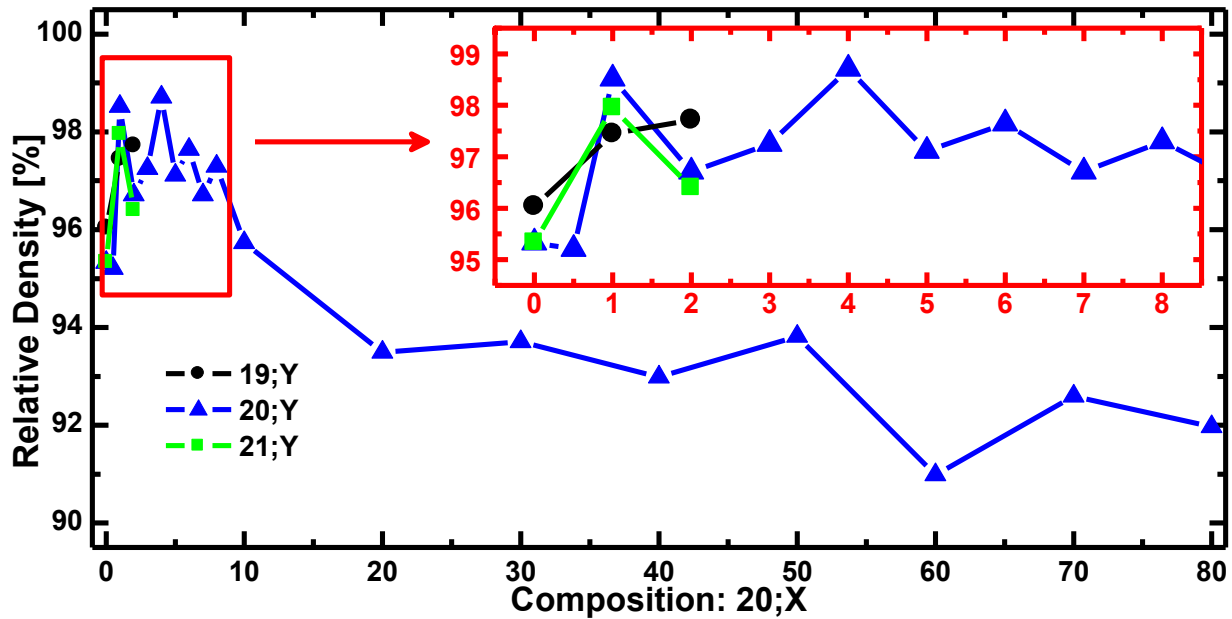


Fig 32: Relative density of the investigated compositions. The inlay (red) shows the marked area of the graph expanded. A general downwards trend in density to both sides of 20;4 can be seen.

The relative densities of all compositions up to 20;80 are shown in Fig 32. From the inset figure in Fig 32, 1 mol% KNN-BKT already increases the relative density by about 2.5 % on average. Further addition of KNN-BKT has no further improving effect. The relative density of compositions up to X;10 was always above 95 %, exact values of compositions up to composition X;2 are given in Tab 14 (page 138). The highest relative density was found at 20;4 with 98.7 % closely followed by 20;1 with 98.5 %. Between 20;20 and 20;80, the relative density fluctuates between 91 % and 94 % with a general downwards trend towards higher KNN-BKT content. Non-matrix compositions (i.e. above 2 mol% KNN-BKT) were not further investigated from this point onwards due to generally low strain and poor sinterability.

### 5.3.2 Powder Diffraction

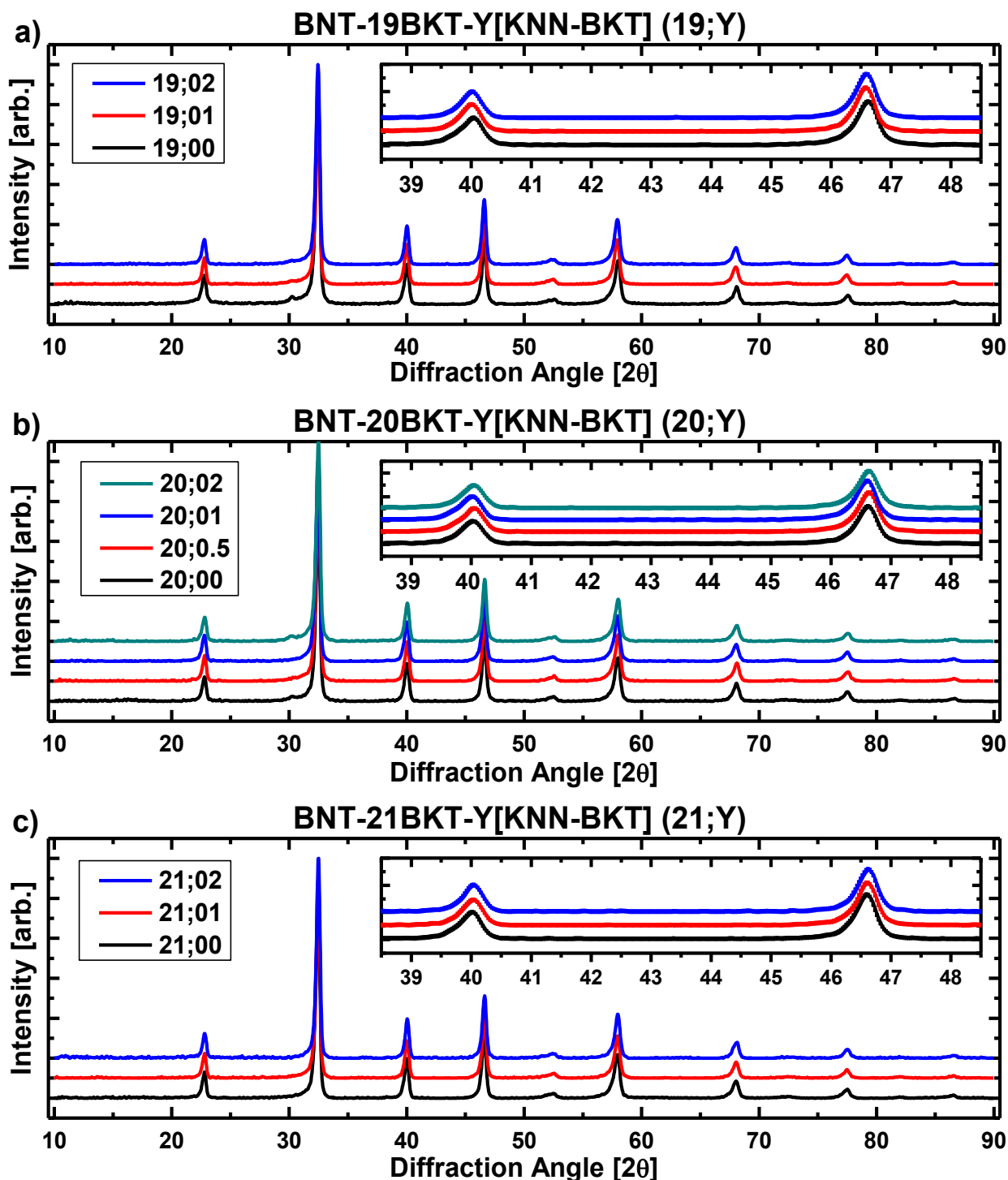


Fig 33: The diffraction patterns of all 10 matrix compositions after calcination and milling. All patterns show cubic perovskite structures. The 19;2, 20;0 and 20;2 show traces of a secondary phase at 30.3°, the others are single phase. The inlay shows the area between 39° and 48° where the first peak is the (111) reflex and the second (200) reflex.

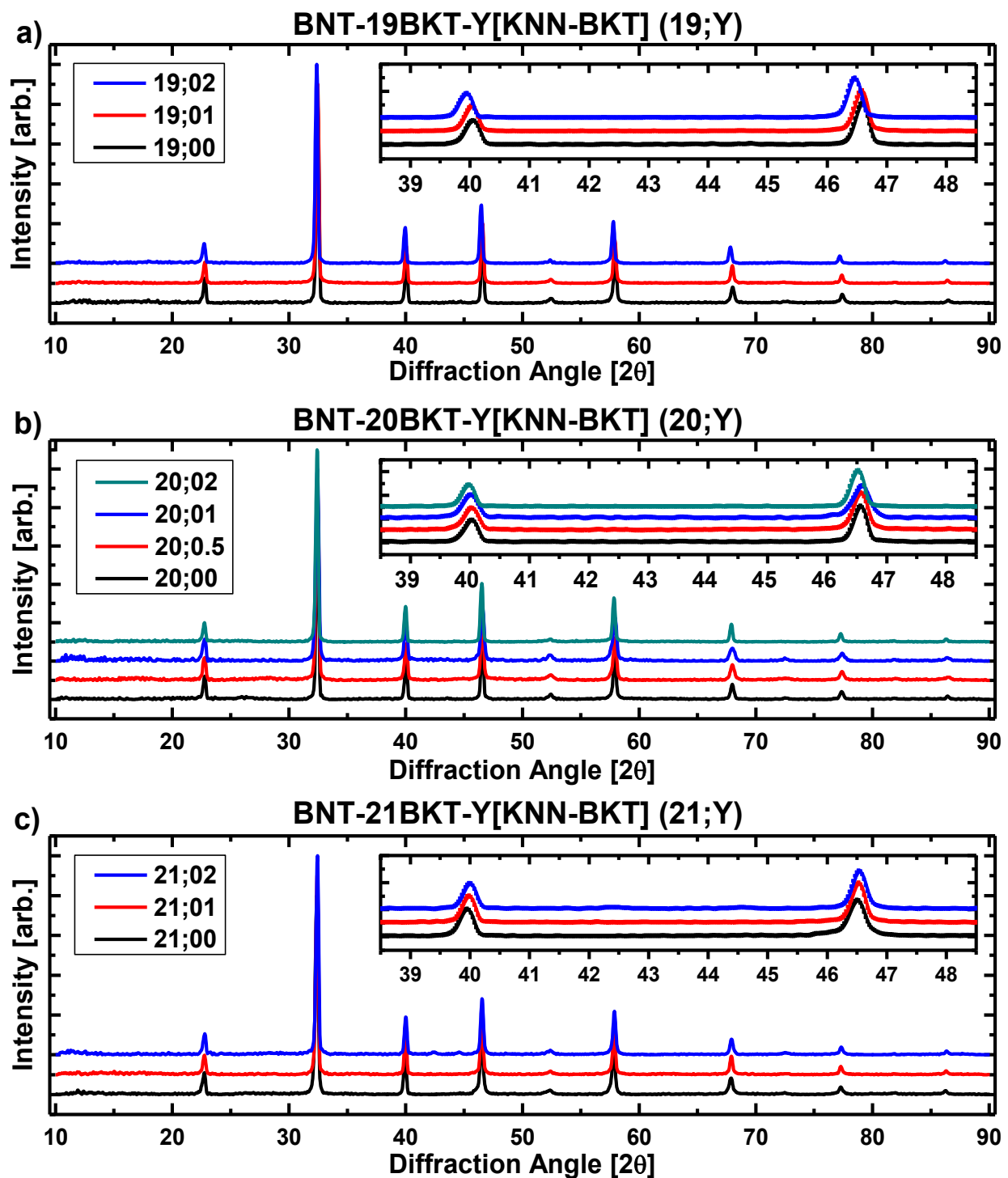


Fig 34: The diffraction patterns of all 10 matrix compositions crushed after sintering. All patterns show cubic perovskite structures. There are no more traces of secondary phases at 30.3°. The inlay shows the area between 39° and 48° where the first peak is the 111 reflex and the second 200 reflex.

The data plots in Fig 33 show all diffraction patterns and a magnification of the 111 and 200 reflex in the insets. The diffraction patterns of all 10 calcined powders were successfully fitted with space group  $Pm\bar{3}m$ , since none of the reflexes showed any distortions. Some compositions show a small secondary phase as a reflex at  $30.3^\circ$ . Except for the zero point offset and the unit cell length, all fitting parameters were equal within the limits of the equipment and Rietveld refinement method. Patterns of the sintered and crushed samples are shown in Fig 34. The slimmer peak width of the patterns is a result of the annealing process done to reduce the internal stresses. All 10 patterns show no evidence of a secondary phase anymore. The patterns were again Rietveld-fitted with space group  $Pm\bar{3}m$ .

The variations in unit cell lengths of all 10 compositions in their calcined and in their sintered state are graphically represented in Fig 35a) and b) respectively and can be compared to the variation in the Goldschmidt Tolerance Factor (Fig 35c). In the case of the calcined powder the composition 19;Y shows the lowest unit cell length at Y=0, which increases steadily with increasing KNN-BKT content. Composition 20;1 shows the lowest unit cell length of the 20;Y line and the unit cell length increases towards both higher and lower KNN-BKT content. The 21;Y line shows the present trend of the 19;Y line.

The unit cell lengths of the sintered materials 19;Y and 20;Y show the same trends as in the case of the calcined powders but less pronounced. The 21;Y line shows a constant unit cell length within the error margin of 0.002 Å. All unit cell lengths are shifted to higher values when moving from the calcined to the sintered material. The exact unit cell length values of both calcined and sintered materials and their corresponding tolerance factors are summarised in Tab 14 (page 138).

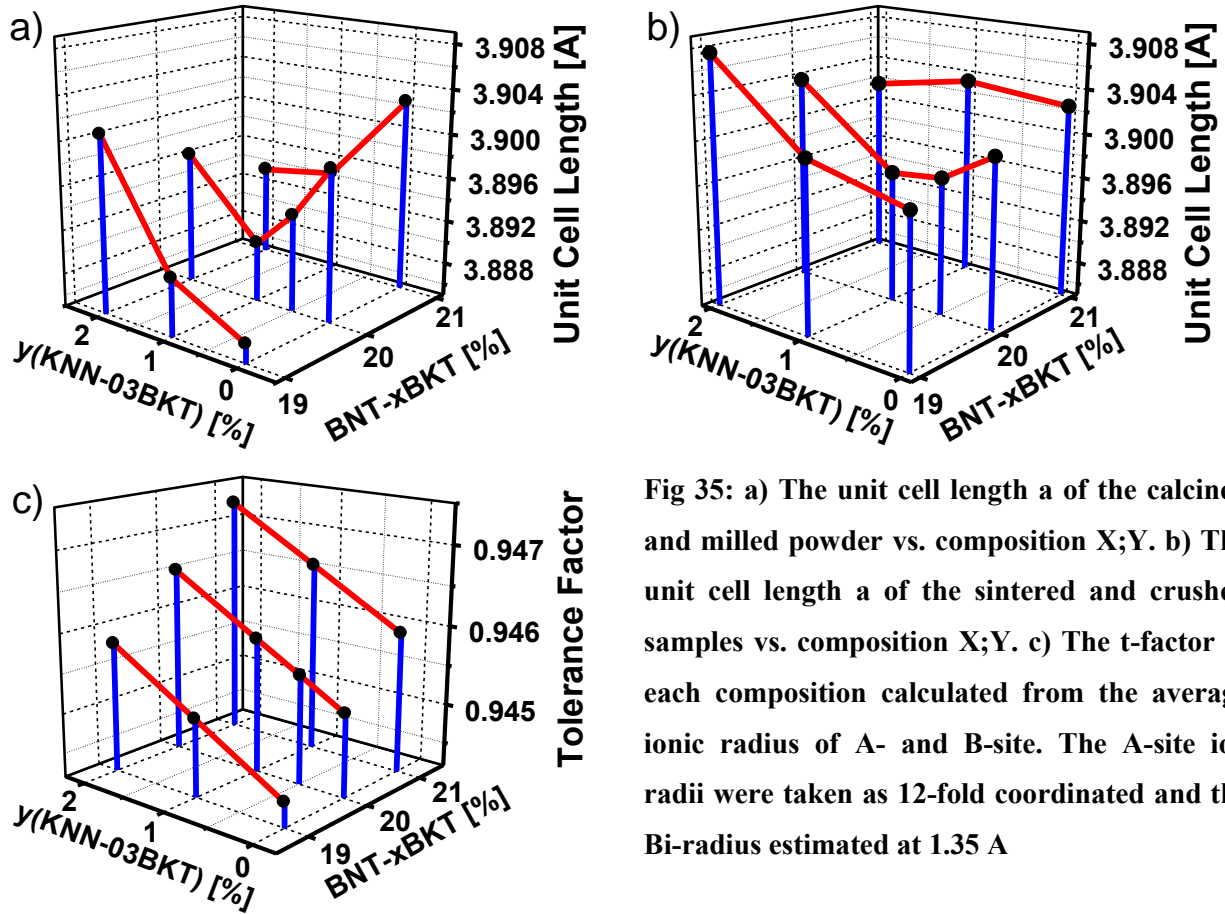


Fig 35: a) The unit cell length  $a$  of the calcined and milled powder vs. composition X;Y. b) The unit cell length  $a$  of the sintered and crushed samples vs. composition X;Y. c) The  $t$ -factor of each composition calculated from the average ionic radius of A- and B-site. The A-site ion radii were taken as 12-fold coordinated and the Bi-radius estimated at 1.35 Å

### 5.3.2.1 Patterns of Bulk Samples after unipolar electrical load

Unlike the powder diffraction patterns, which were recorded in transmission geometry, the diffraction patterns of the bulk samples were collected in reflective geometry. The collected patterns are shown in Fig 36. Splitting in both  $(111)_{pc}$  and  $(200)_{pc}$  indicates that the initially existing pseudocubic phase evolves into a mixed phase of rhombohedral and tetragonal on the application of an electric field. The reflexes at  $22.6^\circ$  and  $29.2^\circ$  arise from traces of silicon oil on the surface as well as the modelling clay used to hold the sample in position. The height ratio of the 200 and 002 reflexes is reversed when going from the 19;0 to 19;1 composition (Fig 36a). Similar behaviour is seen between 20;0 and 20;0.5 and back again between 20;0.5 and 20;2 with the reflex heights of 200 and 002 being exactly equal for 20;1 (Fig 36b). The 21;Y 200 reflex splitting increases with increasing KNN-BKT content (Y) (Fig 36c).

The 111 reflex remains unchanged in the case of the 21;Y with KNN-BKT content. The  $11\bar{1}$  reflex can be seen as a small broad shoulder to the left (towards lower angles). For the 20;Y line, all 111 reflexes are similar except the 20;1 reflex, which is lower and has a comparatively higher  $11\bar{1}$  reflex. For the 21;Y materials the ratio of the  $11\bar{1}$  reflex and the 111 reflex increases with increasing Y.



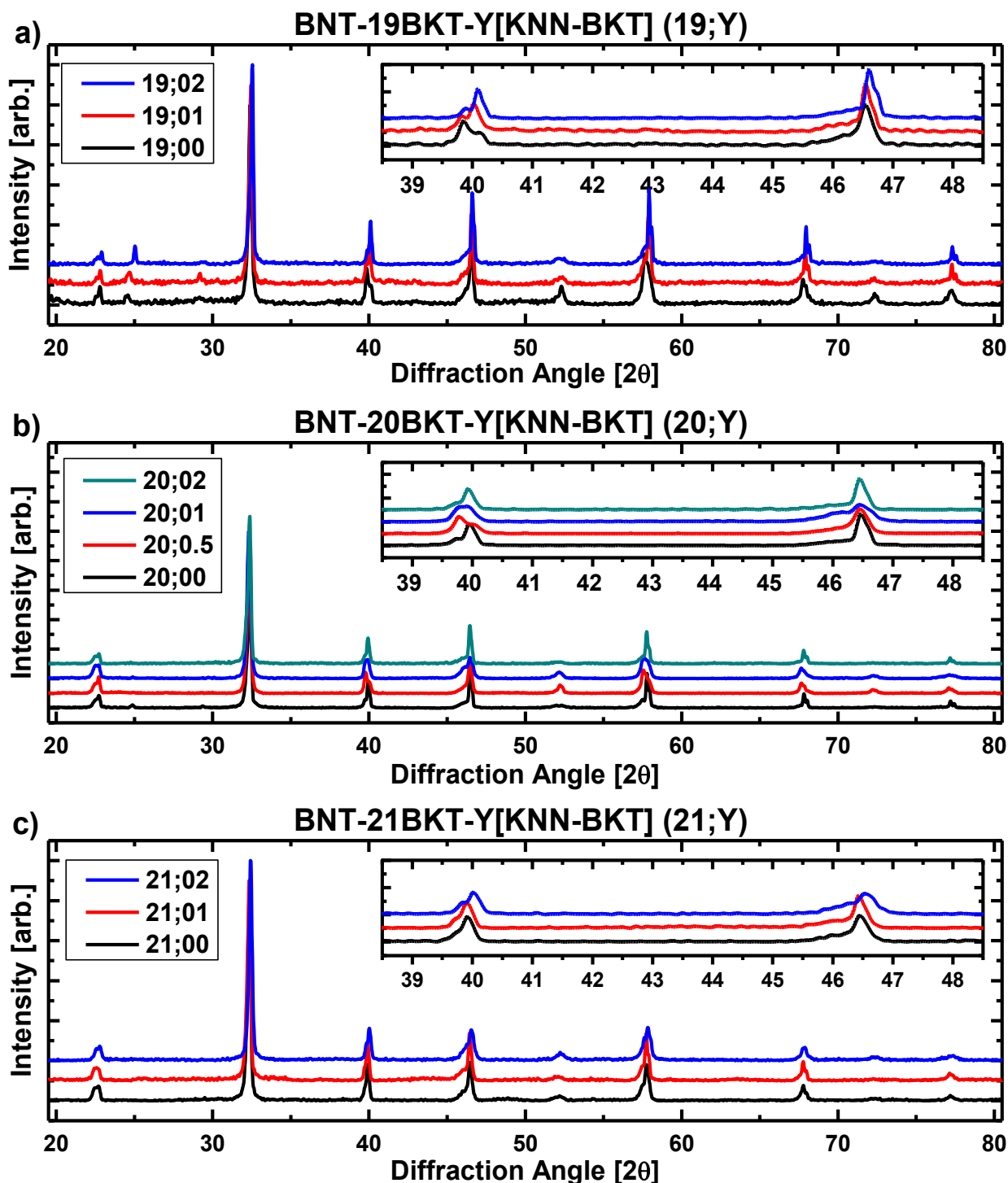
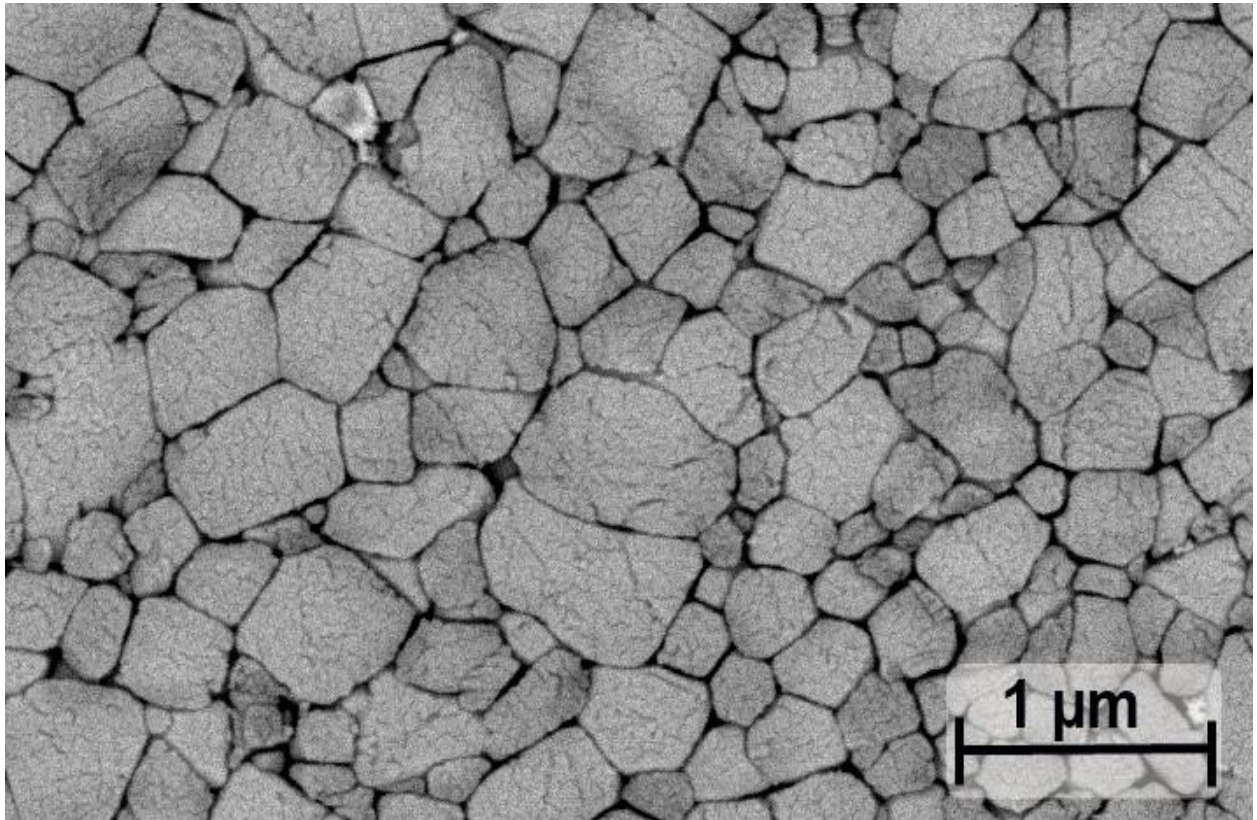


Fig 36: Diffraction patterns of a) 19;Y, b) 20;Y and c) 21;Y after unipolar load of 6 kV/mm for 15 seconds. The inlay shows the splitting of the 111 (pseudocubic) reflex at about 40°. The splitting of the 200 (pseudocubic) reflex at 45° is smaller and can only be seen as asymmetric broadening or a small shoulder at lower angles. The origin of the splitting is a mixed phase of rhombohedral and tetragonal perovskite structures. Phase ratios cannot be determined since the degree of orientation is unknown. Impurity peaks at 22.6° and 29.2° are silicon oil from the poling and modelling clay from the sample holder.

### 5.3.3 Scanning Electron Microscopy



**Fig 37: Typical microstructure of a polished and chemically etched BNT-BKT-KNN-BKT sample of composition 19;2 recorded in BSE mode with a voltage of 20.0 kV.**

SEM pictures were taken of all 10 compositions. In order to determine the grain size, the polished surface of the sample was chemically etched to expose the microstructure. Etching times fluctuated between five seconds and two minutes independent of composition. The etching was inhomogeneous for most compositions and topographic imaging using BSE mode was used to enhance the grain boundary contrast in those cases. Fig 37 shows a representative image of the microstructure of a KNN-BKT added BNT-BKT composition.

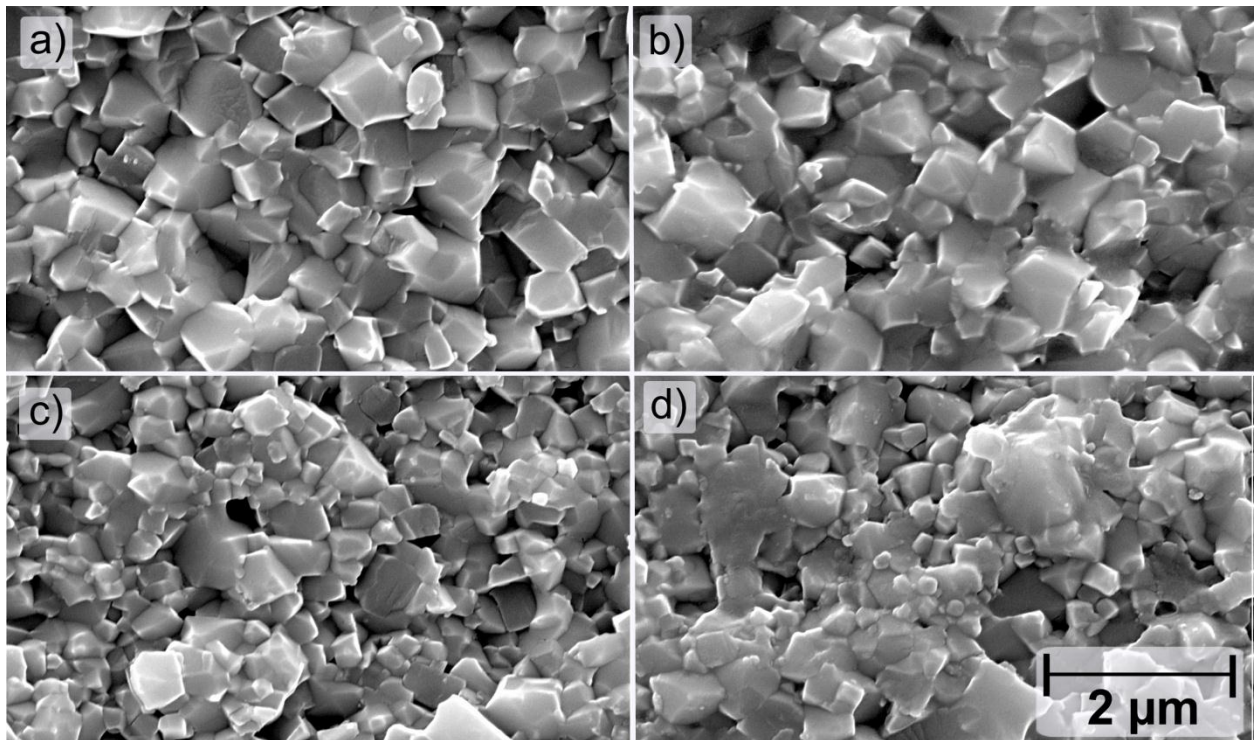


**Fig 38: Fracture surfaces of compositions a) 20;0, b) 20;0.5, c) 20;1, d) 20;2 recorded in SE mode at 20.0 kV.**

The grain sizes are tabled in Tab 14 (Page 138). Composition 21;2 disintegrated without a sufficient time window where the microstructure was exposed enough to have sufficient contrast of the microstructure. Composition 21;1 showed the same behaviour. However, a small number of etched grains (less than 100) were recorded and, therefore, not enough to accurately determine the average grain size. Thermal etching proved unsuitable since the volatile elements bismuth and potassium grow small needle like crystals on the surface during cooling, which cover the underlying microstructure fully. Generally, the grain sizes of compositions from pure BNT-BKT compositions 19;0 and then to 21;0 were between 0.6 and 0.7  $\mu\text{m}$ , while the grain sizes of the KNN-BKT added materials were around 0.5  $\mu\text{m}$ .

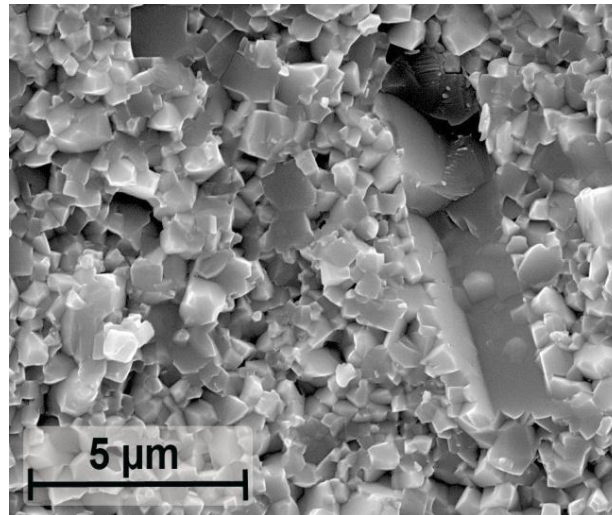


**Fig 39: The fracture surface of a sample of composition 20;0.5 showing the void left by an abnormal elongated grain of at least 6  $\mu\text{m}$  length.**

Visual inspection of the fracture surfaces (Fig 38) shows an increase in the bimodality of the grain size distribution with increasing KNN-BKT content. Irregular crystal shapes as well as a dense microstructure is found in all cases. The ratio of intragranular to intergranular fractures increases with increasing KNN-BKT content.

All compositions showed an even distribution of unusually elongated large grains throughout the bulk of the sample. An image of the space left by a grain that broke out of the fracture surface of a 20;0.5 composition sample is shown in Fig 39. These grains were approximately ten times larger than the average grain size. Energy dispersive x-ray analysis revealed no compositional deviation from the remaining bulk.

### 5.3.4 Transmission Electron Microscopy

TEM images of the compositions 20;0, 20;0.5, 20;1 and 20;2 were recorded to investigate the structure evolution between the ferroelectric 20;0 and non-ferroelectric 20;2. Fig 40 shows a microstructure overview of composition 20;1 which is representative of the other compositions as well. The microstructure is dense and consists of irregularly shaped grains of less than 1  $\mu\text{m}$ . The contrast of the grains increases with increasing KNN-BKT content. Long rectangular grains were also seen randomly distributed throughout all samples of all 4 compositions.

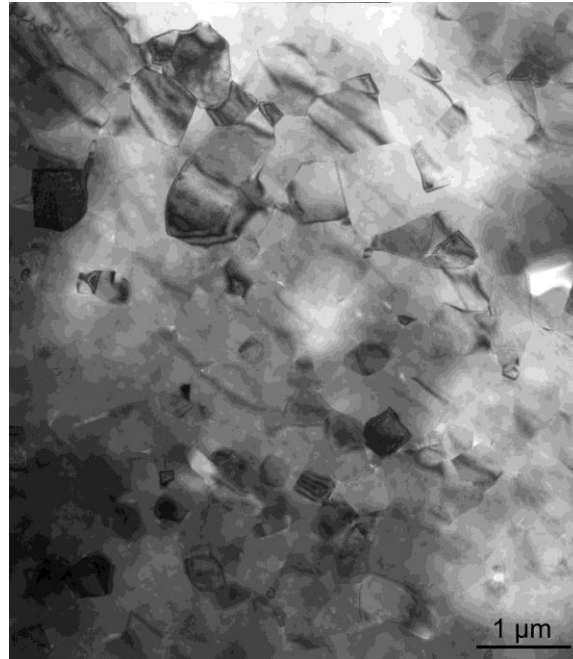


**Fig 40: TEM image of the microstructure of composition 20;1. The high contrast of some grains is a result of them being oriented to meet Bragg conditions.**

Fig 41 and Fig 42 show the bright-field (BF) micrographs of compositions 20;0 to 20;2. The inset depicts the selected area electron diffraction (SAED) pattern. The selected grain in each case is the one showing high contrast. For each composition, two orientations are shown. To expose tetragonal superstructure reflections the  $[001]_c$  or  $[111]_c$  orientation was selected and to expose the rhombohedral superstructure reflexes the  $[011]_c$  zone axis was selected. In all samples both  $\frac{1}{2}\{00e\}$  and  $\frac{1}{2}\{00o\}$  reflexes were found in their respective orientations. Selected area electron diffraction along the  $[111]_c$  zone axis shows streaking of  $\frac{1}{2}\{00e\}$  superstructure reflections, due to  $a^0a^0c^+$  octahedral tilting. This is visible in the inset of Fig 41 (composition 20;0.5). Streaking of  $\frac{1}{2}\{00e\}$  superstructure reflections along three different directions is visible, due to three tetragonal orientational variants<sup>[5]</sup>. Rhombohedral  $\frac{1}{2}\{00o\}$  superstructure reflections showed no such streaking.



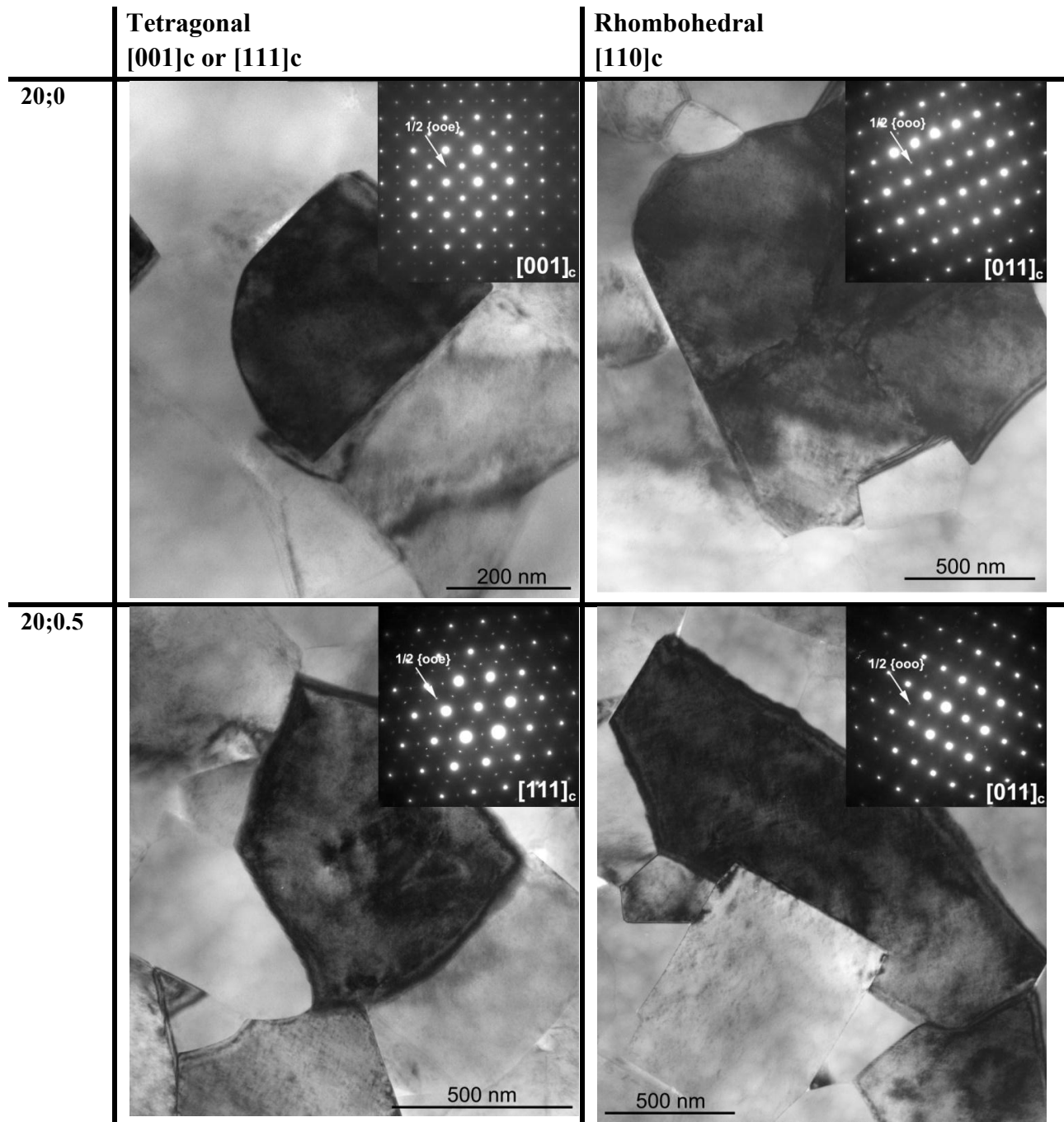


Fig 41: TEM images of single grains of 20;0 (top) and 20;0.5 (bottom). The high contrast grains are oriented as shown in the inlays. On the left, the orientation ( $[001]_c$  or  $[111]_c$ ) is such that it displays the  $\frac{1}{2}\{00c\}$  superstructure reflexes (marked in inlay). On the right, the  $[011]_c$  orientation is used to show the  $\frac{1}{2}\{000\}$  reflexes (marked in inlay).

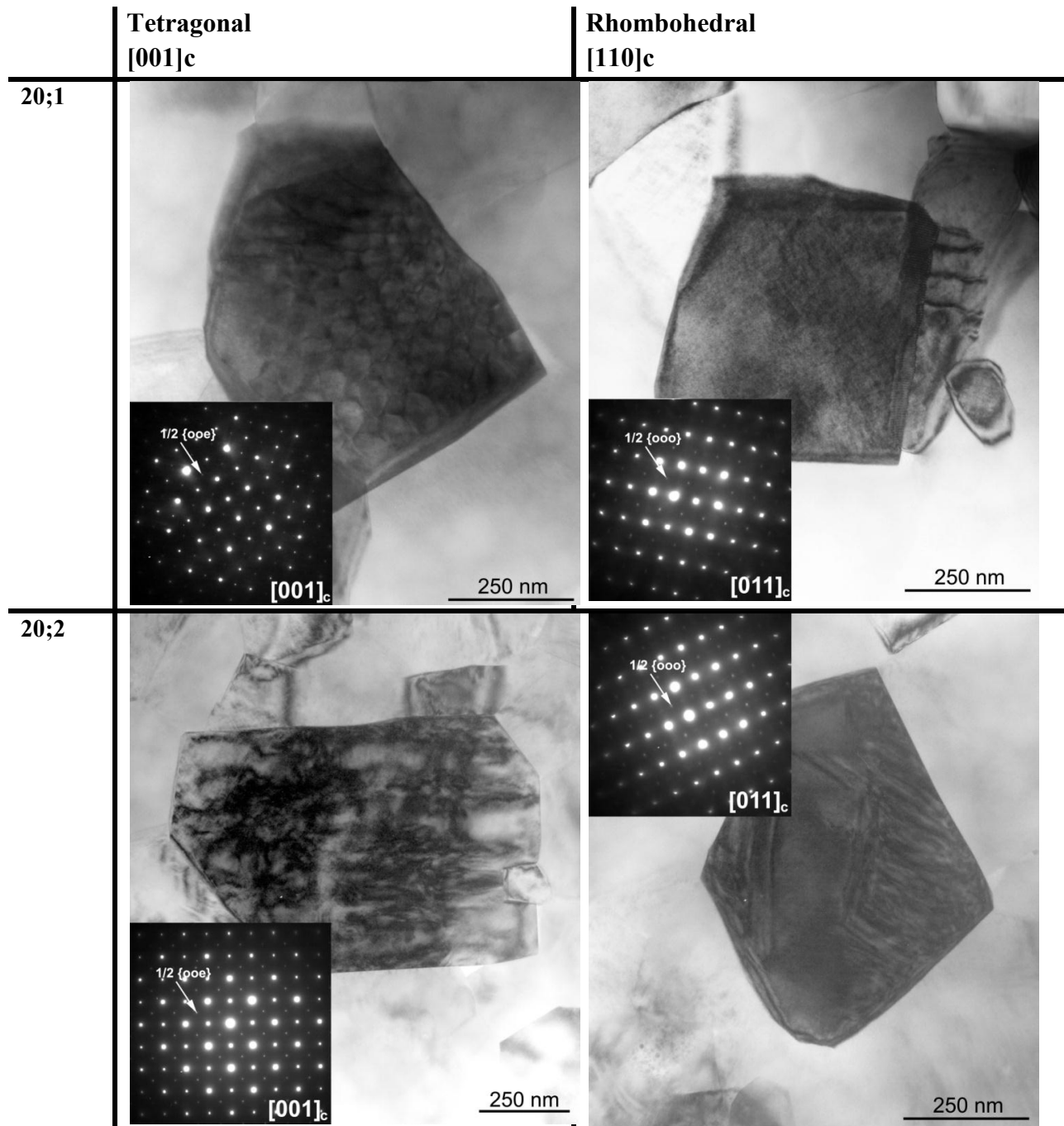
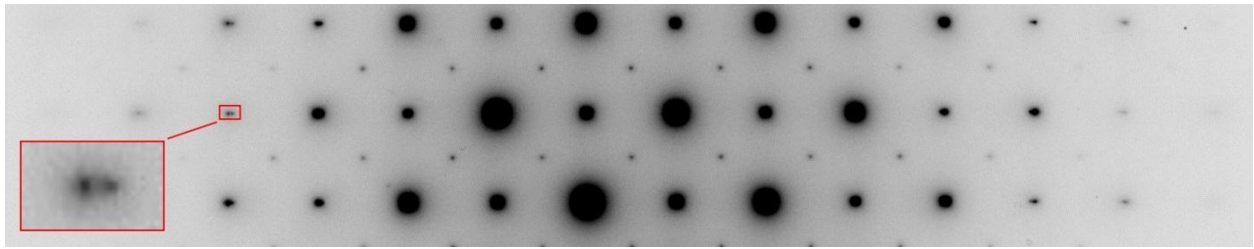


Fig 42: TEM images of single grains of 20;1 (top) and 20;2 (bottom). The high contrast grains are oriented as shown in the inlays. On the left, the [001]<sub>c</sub> orientation is such that it displays the  $\frac{1}{2}\{001\}$  superstructure reflexes (marked in inlay). On the right, the [011]<sub>c</sub> orientation is used to show the  $\frac{1}{2}\{000\}$  reflexes (marked in inlay).



**Fig 43: SAED pattern of sample 20;1 along [001]<sub>c</sub> zone. The splitting along [100] is marked with a red rectangle and zoomed in.**

The reflex splitting along the [001]<sub>c</sub> zone (Fig 43) showed reflex splitting due to the existence of a 90° a-c domain configuration, which was used to approximate the c/a ratio to  $1.01 \pm 0.003$  for composition 20;1. EDS of the long rectangular grains revealed no compositional difference within the measurement tolerances compared with the typical grains. To discount the effect of aging onto the crystal structure, a sample of 20;1 was deaged at 500 °C for 30 minutes with a 2 K/min heating and cooling ramp. Although the contrast increased, the superstructure reflections  $\frac{1}{2}\{00e\}$  and  $\frac{1}{2}\{00o\}$  remained present. A miniaturisation of the domain configuration was visible.

### 5.3.5 Summary of Structure and Microstructure Parameters

The structure and microstructure parameters, absolute density, relative density, unit cell length, tolerance factor and grain size are given in Tab 14 for reference and completeness.

**Tab 14: Summary of Structure and Microstructure Data**

Composition.	Density (abs.) [g/cm <sup>3</sup> ]	Density (rel.) [ %]	Unit cell Length [Å] (Calcined)	Unit cell Length [Å] (Sintered)	Tolerance Factor	Grain Size [μm]	Std. Dev. [+/-μm]
19;0	5.74	96.0	3.8866(8)	3.8983(1)	0.9445	0.7	0.1
19;1	5.83	97.4	3.8902(0)	3.9004(3)	0.9451	0.5	0.1
19;2	5.82	97.7	3.9010(7)	3.9076(0)	0.9458	0.5	0.1
20;0	5.70	95.3	3.8986(8)	3.9002(5)	0.9452	0.7	0.1
20;0.5	5.70	95.2	3.8937(6)	3.8973(8)	0.9456	0.5	0.1
20;1	5.90	98.5	3.8903(9)	3.8968(3)	0.9459	0.5	0.1
20;2	5.76	96.7	3.8971(1)	3.9036(5)	0.9465	0.5	0.1
21;0	5.70	95.3	3.9025(1)	3.9025(1)	0.9460	0.6	0.1
21;1	5.86	98.0	3.8944(6)	3.9033(1)	0.9466	0.8	0.5 <sup>1</sup>
21;2	5.74	96.4	3.8933(6)	3.9015(7)	0.9472	γ <sup>2</sup>	γ <sup>2</sup>

<sup>1</sup>too few intact grain

<sup>2</sup>etching failed



## 5.4. Room Temperature Electrical Results

### 5.4.1 Bipolar Strain

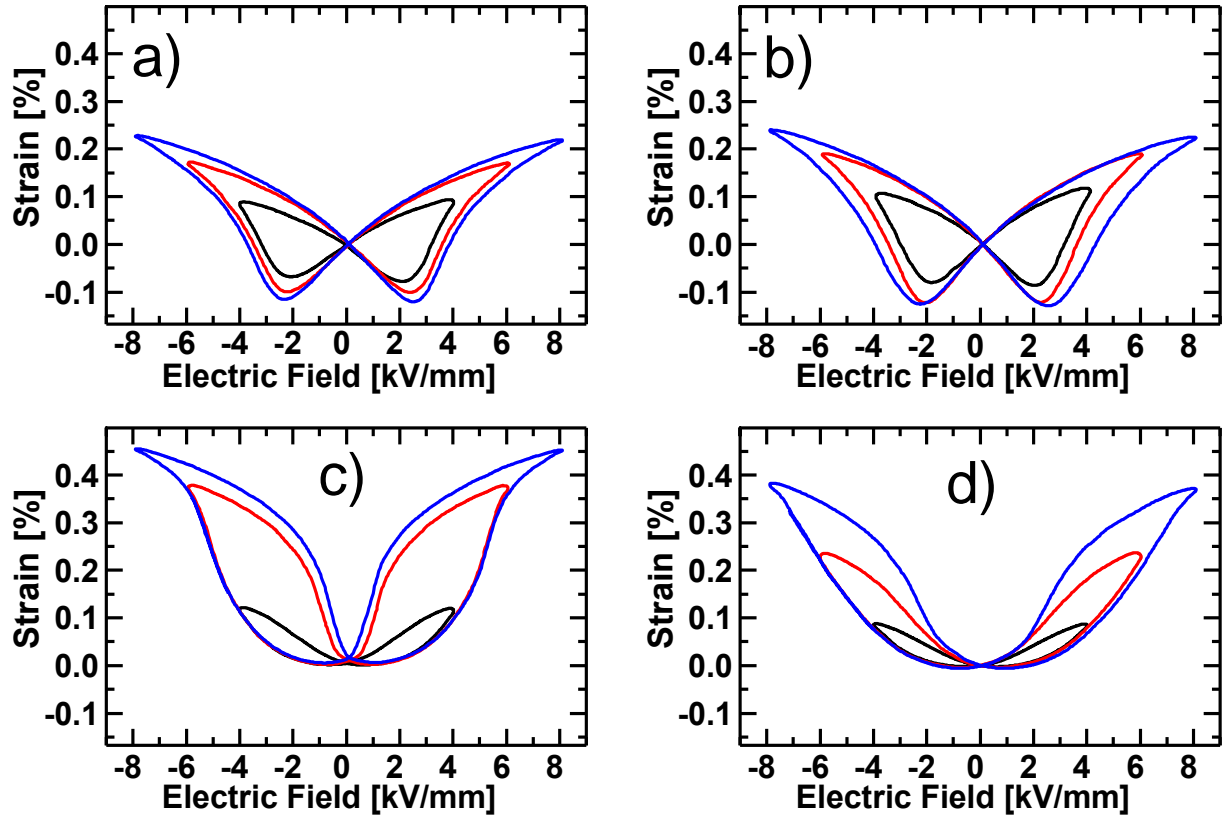


Fig 44: Bipolar Strain hystereses of a) 20;0, b) 20;0.5, c) 20;1 and d) 20;2 for fields of 4 kV/mm (black), 6 kV/mm (red) and 8 kV/mm (blue).

The bipolar strain at room temperature was recorded for all 10 compositions with maximum electric field of 4, 6 and 8 kV/mm. A typical strain evolution with increasing KNN-BKT content at the example of 20;0 to 20;2 is shown in Fig 44 with the corresponding polarisation hystereses in Fig 45. All Sawyer-Tower-type results were recorded at 55 mHz unless explicitly stated otherwise.

Fig 44a) shows a typical ferroelectric butterfly-shaped strain loop of pure BNT-BKT (20;0). The maximum bipolar strain is 0.16, 0.27 and 0.33 % at 4, 6 and 8 kV/mm. Fig 45a) shows typical ferroelectric polarisation hystereses of pure BNT-BKT (20;0). The polarisation loops tend to saturation at or above 6 kV/mm. Maximum and remanent polarisation are 32.9 and 25.7  $\mu\text{C}/\text{cm}^2$  at 4 kV/mm respectively, 40.7 and 30.7  $\mu\text{C}/\text{cm}^2$  at 6 kV/mm and 42.9 and 32.9  $\mu\text{C}/\text{cm}^2$  at 8 kV/mm. The coercive field is 2.4 kV/mm, recorded from the 8 kV/mm polarisation loop. Fig 44b) and Fig 45b) show the strain and polarisation hystereses of 20;0.5 at 4, 6 and 8 kV/mm. The shapes of the strain and polarisation loops are almost identical to the composition 20;0 loops. The

maximum bipolar strain values increase to 0.2, 0.31 and 0.35 % with the corresponding maximum and remanent polarisation value of 29.0 and 21.7  $\mu\text{C}/\text{cm}^2$  at 4 kV/mm, 40.2 and 29.3  $\mu\text{C}/\text{cm}^2$  at 6 kV/mm and 43.8 and 32.8  $\mu\text{C}/\text{cm}^2$  respectively. The coercive field of 20;0.5 is 2.77 kV/mm taken from the 8 kV/mm measurement cycle.

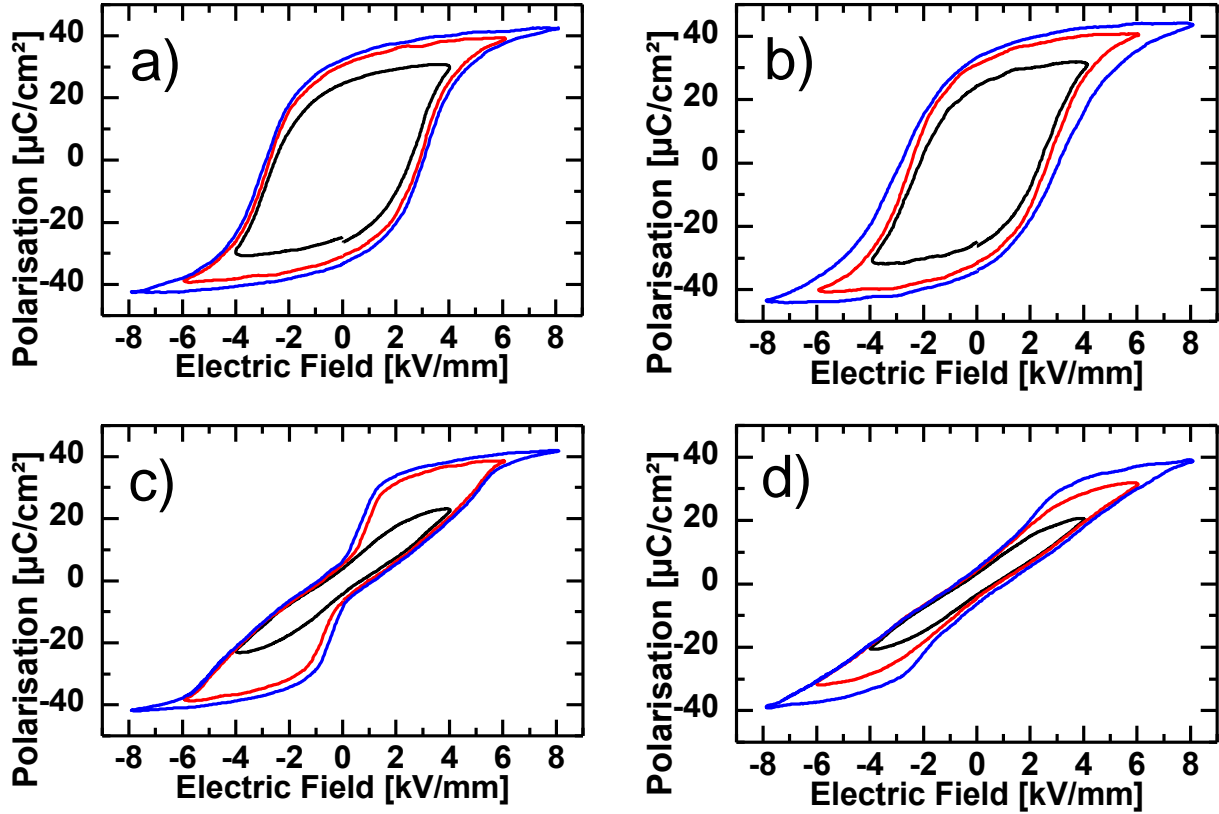


Fig 45: Bipolar polarisation hystereses of a) 20;0, b) 20;0.5, c) 20;1 and d) 20;2 for fields of 4 kV/mm (black), 6 kV/mm (red) and 8 kV/mm (blue).

Fig 44c) shows the strain hystereses of 20;1 at 4, 6 and 8 kV/mm. The strain during increasing field follows a nearly parabolic shape centred on the coercive field of +1.05 kV/mm up to about 5.5 kV/mm where the strain begins to level off. The 4 kV/mm cycle never reaches the levelling part of the curve. The maximum strain is 0.12, 0.38 and 0.45 % at 4, 6, and 8 kV/mm, respectively. When the field is reduced, the return path of the strain curve originally follows an approximate horizontal parabolic path down to about 1 kV/mm from which point onwards the strain almost linearly drops back to zero. The strain hysteresis is larger at 6 and 8 kV/mm and the linear segments of the strain path are shorter than in the ferroelectric case. The maximum negative strain at the coercive field is reduced from the 0.12 % of 20;0 and 20;0.5 to less than 0.02 % in composition 20;1 at 8 kV/mm. Values for lower fields are below the experimental error. The polarisation of 20;1 (Fig 45c) shows a nearly linear increase with increasing field before levelling off at 6 kV/mm. The return path shows a double-loop shape similar to an antiferroelectric hysteresis (pinching) but for fields below 0.3 kV/mm, the polarisation follows a

linear slope parallel to the rising slope but in opposite direction. The 4 kV/mm polarisation hysteresis shows no double-loop return path. The remanent polarisation is 4.2, 6.0 and 7.3  $\mu\text{C}/\text{cm}^2$  for 4, 6, and 8 kV/mm and the maximum polarisation 23.5, 39.6 and 42.6  $\mu\text{C}/\text{cm}^2$  with a coercive field of 1.2 kV/mm (8 kV/mm loop).

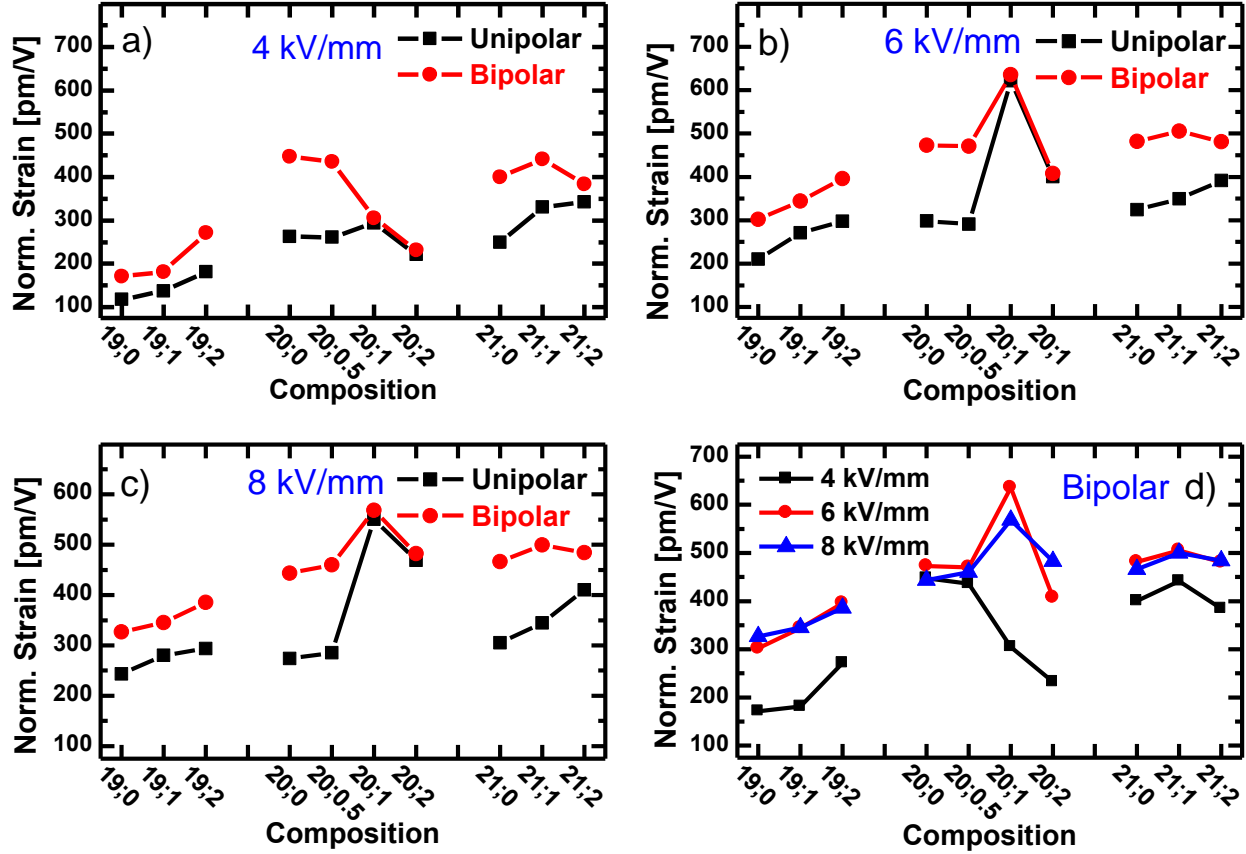


Fig 46: a), b) and c) show the maximum unipolar and bipolar normalised strain values of all 10 compositions at 4, 6 and 8 kV/mm, respectively. d) shows a comparison of the bipolar strain values of all compositions at these three field strengths. The values were normalised to their maximum electric field in each case for better comparison.

The strain (Fig 44d) and polarisation (Fig 45d) of 20;2 are systematically similar to 20;1 but the strain curves never level off at high fields and the return path is now only parabolic down to about 2.7 kV/mm. The linear section of the return path does not extend to zero field value but is followed by a vertical parabolic section below 2 kV/mm. The maximum strain is 0.09, 0.24 and 0.37 % at 4, 6, and 8 kV/mm. The negative strain is again 0.02 % for 8 kV/mm and below the experimental error for lower fields. The polarisation loops have much less pronounced double loop return paths at the equivalent maximum applied fields. The linear part of the polarisation return-path starts already at 2 kV/mm. The maximum and remanent polarisation values are 21.3 and 3.8  $\mu\text{C}/\text{cm}^2$  at 4 kV/mm, 32.6 and 4.3  $\mu\text{C}/\text{cm}^2$  at 6 kV/mm and finally 39.8 and 6.2  $\mu\text{C}/\text{cm}^2$  at 8 kV/mm with the coercive field of 1.1 kV/mm.

The shape of strain and polarisation loops of the remaining six compositions can be systematically related to the 20;Y series shown in Fig 44 and Fig 45. The 19;Y series and 21;0 and 21;1 compositions all show typical ferroelectric butterfly-shaped strain hystereses similar to 20;0 and 20;0.5. The bipolar strain values of all 10 compositions are summarised in Fig 46. They were normalised to the applied field for better comparison. The maximum and remanent polarisation and the coercive fields are summarised in Fig 47.

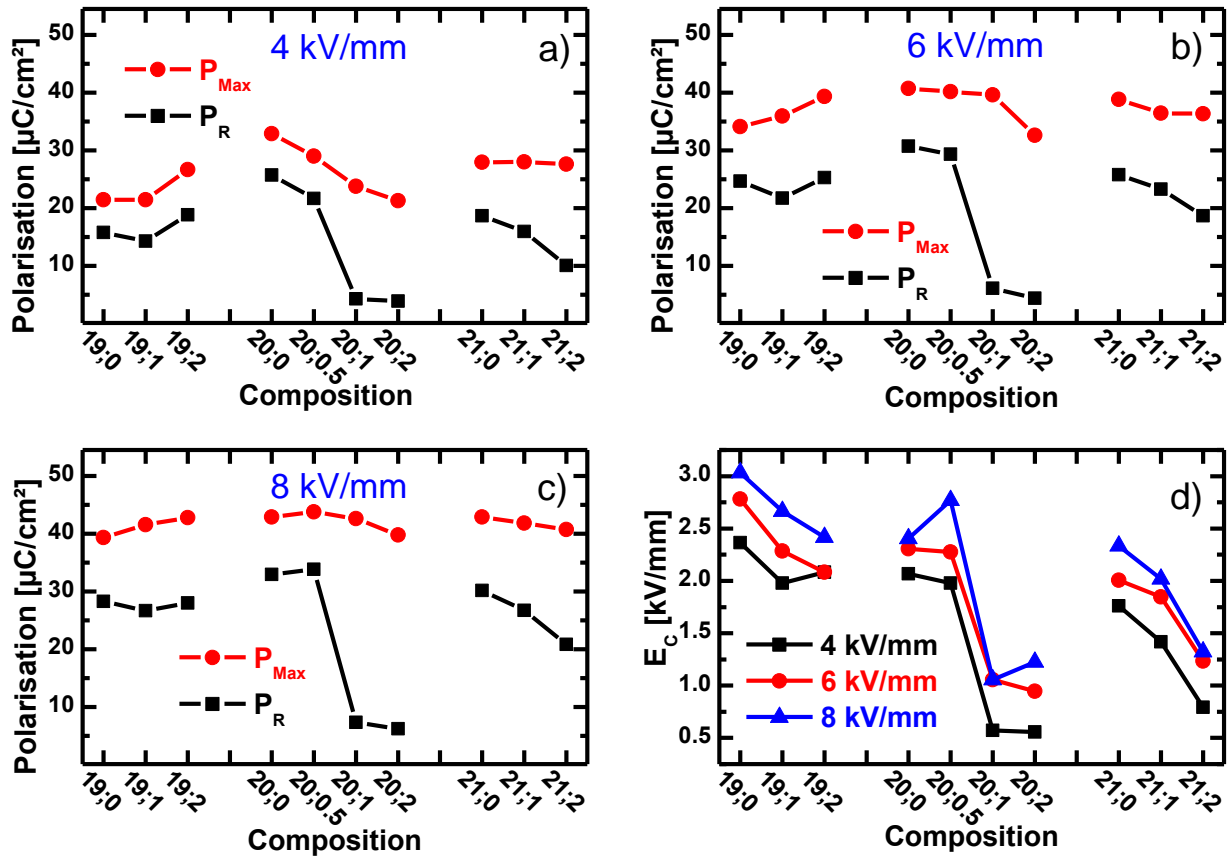
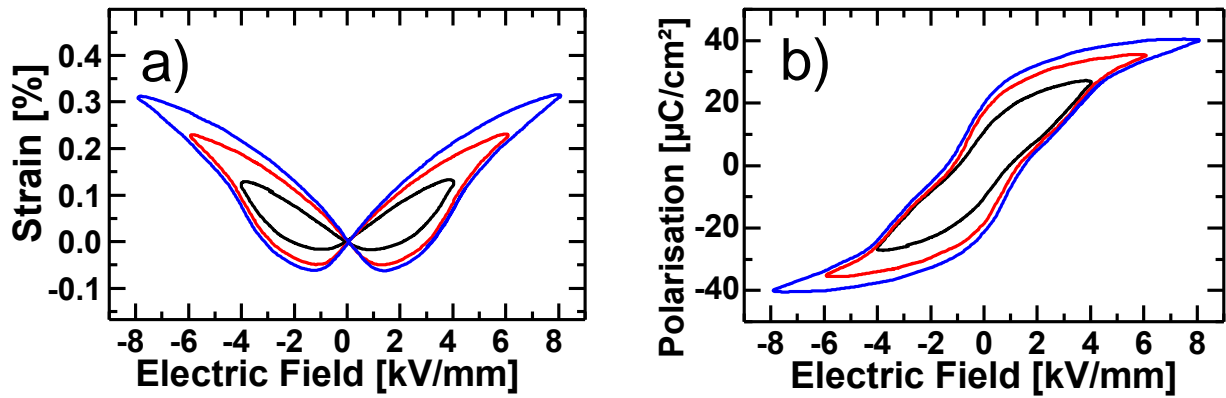


Fig 47: The maximum and remanent polarisation values at a) 4 kV/mm, b) 6 kV/mm and c) 8 kV/mm. The coercive field<sup>37</sup>, collected from the 4, 6 and 8 kV/mm polarisation hystereses is summarised in d). Since the coercive field is always at or below 3 kV/mm, the 6 and 8 kV/mm data gives true values, while the 4 kV/mm is only collected to aid later discussions.

The 19;Y series (Fig 46 and Fig 47 on the left) shows unsaturated strain and polarisation hystereses at 4 kV/mm saturated ones at 6 and 8 kV/mm. The negative strain remains nearly constant with increasing KNN-BKT content while the total bipolar strain increases. The remanent polarisation drops from 19;0 to 19;1 and increases again to 19;2 while the maximum polarisation increases continuously for field strengths of 6 and 8 kV/mm. 4 kV/mm values are unsaturated. The coercive field continuously decreases. 19;0 shows the highest coercive field of

<sup>37</sup> The measurement of the coercive field requires saturation of the polarisation hystereses. Conventionally a maximum electric field of twice the coercive field is assumed necessary.

all compositions at 3.03 kV/mm. From 19;0 to 19;2 the maximum polarisation remains nearly constant, while coercive field and remanent polarisation continuously decrease for all maximum field strengths.



**Fig 48: The strain and polarisation of composition 21;2 at fields of 4, 6 and 8 kV/mm.**

The 21;Y series (Fig 46 and Fig 47 on the right) shows a continuous reduction in negative strain with increasing KNN-BKT content. The maximum bipolar strain is highest at 21;1 for all fields. The composition 21;2 (Fig 48) shows characteristics lying exactly between the 20;0.5 and 20;1 type. The strain hysteresis still shows large negative strain but no linear regions. Its polarisation hysteresis already shows pinching but the pinching of the return path is less pronounced and is on the other side of the zero-field line compared with 20;1 and 20;2.

### 5.4.2 Unipolar Strain

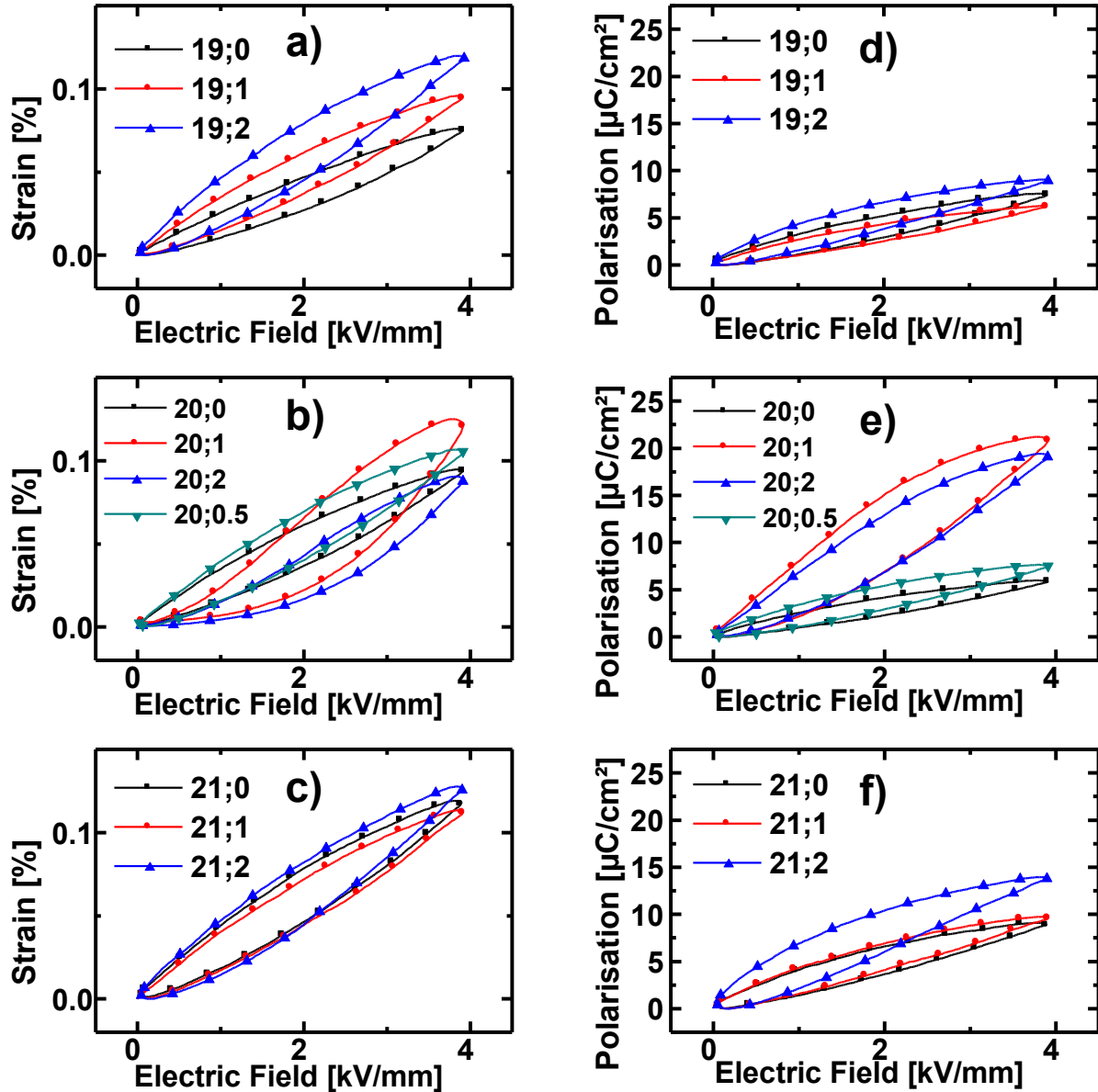


Fig 49: The unipolar strain of compositions a) 19;Y, b) 20;Y and c) 21;Y at 4 kV/mm is shown on the left. Their corresponding polarisation hystereses are shown in d), e) and f) on the right.

At room temperature the strain behaviour of all 10 compositions can be divided into two categories. All 19;Y as well as 20;0, 20;0.5, 21;0 and 21;1 shows strain behaviour characteristic of normal ferroelectric materials with rising and falling strain paths symmetric across the line connecting minimum and peak strains values. Their polarisation hystereses are of the same shape.

The unipolar maximum strain of 19;Y shows a continuous increase from 0.075 over 0.095 to 0.118 % at 4 kV/mm with increasing KNN-BKT content. The polarisation of  $7.5 \mu\text{C}/\text{cm}^2$  at 19;0 first decreases to  $6.3 \mu\text{C}/\text{cm}^2$  at 19;1 and increases again to  $8.8 \mu\text{C}/\text{cm}^2$ .

Between 20;0 and 20;0.5 the maximum strain increases from 0.094 to 0.106 % with the maximum polarisation going up from 5.9 to 7.6  $\mu\text{C}/\text{cm}^2$ . 19;0 and 19;1 show almost identical properties with 0.113 and 0.118 % maximum strain and 8.8 and 9.5  $\mu\text{C}/\text{cm}^2$  maximum polarisation.

20;1 and 20;2 belong to the second category, which shows a more non-linear strain behaviour and no symmetry. Their rising strain flank increases more slowly at low fields and more quickly at high fields compared with materials of the first category. Their maximum strain values are 0.123 and 0.090 %. The corresponding polarisation hystereses show much higher  $P_{\text{max}}$  values of 19.2  $\mu\text{C}/\text{cm}^2$  and 21.0  $\mu\text{C}/\text{cm}^2$  at 4 kV/mm compared with materials from the first category and they are non-symmetrical.

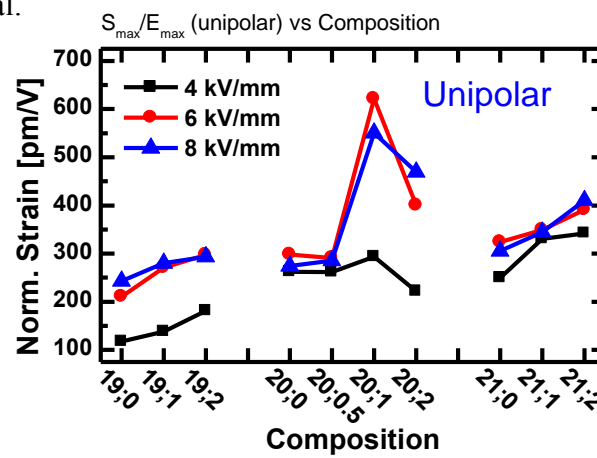


**Fig 50: Normalised unipolar strain values at 4, 6 and 8 kV/mm.**

Composition 21;2 shows intermediate behaviour in both strain and polarisation. The strain hysteresis is still nearly symmetric but already shows a slow rising flank at low fields and a fast driving flank at high fields peaking at 0.126 %. The polarisation, while still nearly symmetric, is already much higher with  $P_{\text{max}} = 13.9 \mu\text{C}/\text{cm}^2$ .

The normalised unipolar strain values at 4, 6 and 8 kV/mm are collected in Fig 50. The normalised strain at fields of 6 and 8 kV/mm shows identical trends within the 19;Y, 20;Y and 21;Y series. However, the absolute values of 19;Y as well as 20;1 and 20;2 approximately double when going from 4 to 6 kV/mm or 4 to 8 kV/mm. 21;Y the smallest variation in normalised strain with the maximum applied field. Unipolar polarisation values at 6 and 8 kV/mm were not collected due to conductivity from an equipment defect. Comparison of unipolar and bipolar normalised strain values in Fig 46 (Page 141) shows a constant ratio of approximately 1:1.4 between unipolar and bipolar strain at 4, 6 and 8 kV/mm for all compositions but 20;1 and 20;2, meaning that the bipolar strain is always 40 % larger at any given field than the unipolar value. The ratios in the case of 20;1 and 20;2 are  $\sim 1:1$ . 21;2 again shows intermediate behaviour with the ratio of 1:1.2.

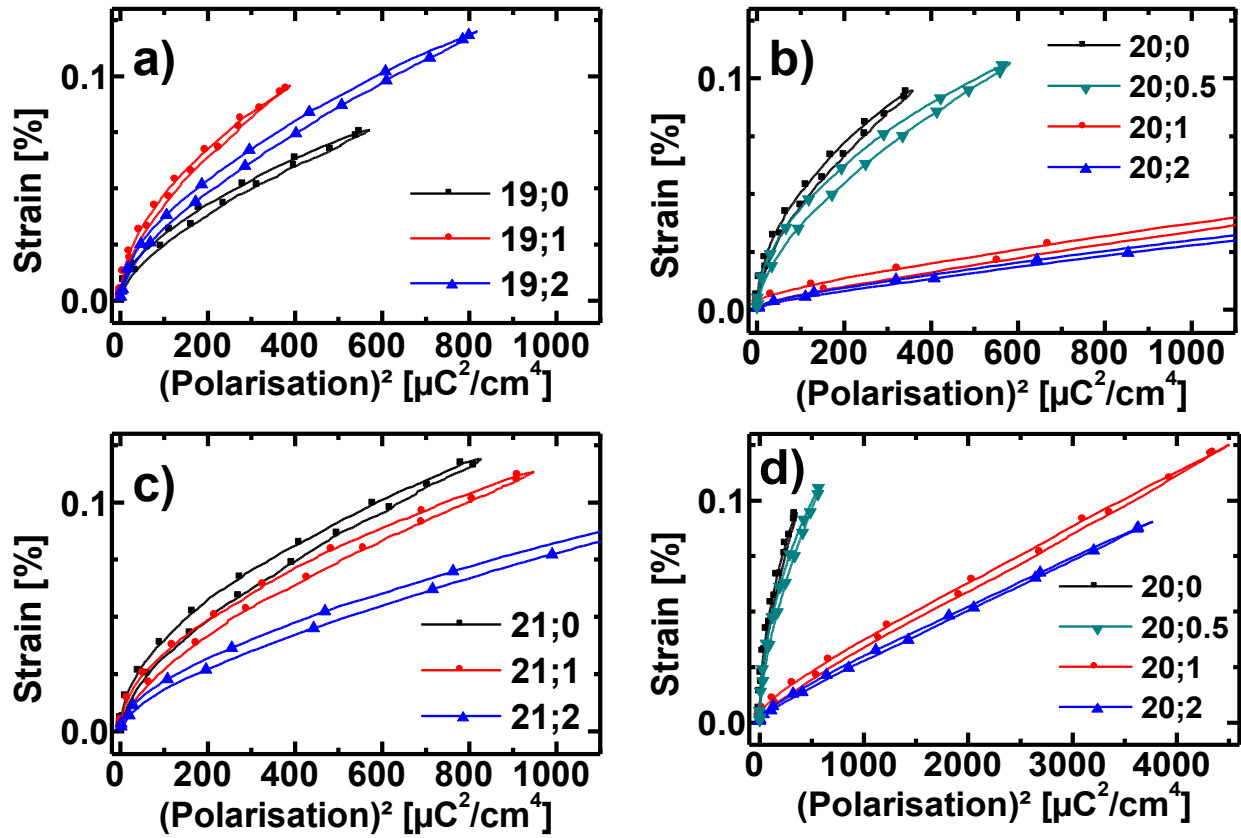


Fig 51: Strain versus the square of the polarisation for a) 19;Y, b) 20;Y and c) 21;Y. Since 20;1 and 20;2 show a higher polarisation, d) shows 20;Y with a larger scale.

The unipolar strain versus the square of the polarisation up to 4 kV/mm is shown in Fig 51. It shows non-linear behaviour for all compositions except 20;1 and 20;2. Compositions 20;1 and 20;2 show nearly linear behaviour with a slope (the electrostrictive coefficient  $Q_{33}$ ) of  $0.0266 \text{ m}^4\text{C}^{-2}$  and  $0.0234 \text{ m}^4\text{C}^{-2}$ . The degree of linearity was assessed by fitting each S vs.  $P^2$  curve with Eq 16:

$$S(P) = a * x^b$$

Eq 16

where „a“ is fitting parameter. „b“ varies between 0.5 for a purely quadratic and 1 for a purely linear relationship between strain and the square of the polarisation. The results are listed in Tab 15. The corresponding error is only the uncertainty in the fitting parameter „b“. Due to the hysteresis, the relative error increases continuously towards higher „b“ values to up to about 5 %. The 19;Y series has a minimum at 19;1 of 0.546. The 20;Y series shows a continuous increase towards higher Y. 20;0 and 20;0.5 as well as 20;1 and 20;2 are close to each other, respectively. 20;2 shows the highest values of all materials at 0.844, while 20;0 shows the lowest at 0.523. The



21;Y series also increases continuously with increasing Y. 21;1 is the only composition, whose „b“ value of 0.647 is not either below 0.6 or above 0.8 unlike all others.

**Tab 15: Results of Exponential Fit of the  $S(P^2)$  Graphs Shown in Fig 47.**

Composition	„b“ value of $S(P^2)=a*x^b$	Error (+/-) in „b“
19;0	0.57528	0.00367
19;1	0.54613	0.00245
19;2	0.58804	0.00287
20;0	0.52315	0.0032
20;0.5	0.54355	0.00365
20;1	0.82333	0.00054
20;2	0.84439	0.00298
21;0	0.5531	0.00356
21;1	0.57641	0.00355
21;2	0.64668	0.0031

The graphs in Fig 51 were fitted with the following function:  $S(P^2) = a * x^b$

where „a“ and „b“ are the constants to be determined. The constant „a“ is purely a fitting parameter of no intrinsic value. The „b“ constant is between 0.5 for purely quadratic and 1.0 for purely linear strain vs. polarisation behaviour.

The value of the „b“ parameter can only be used to estimate how ferroelectric or electrostrictive a certain material is. It should not be assumed that a value of 0.75 corresponds to a 50:50 ratio of electrostrictive and piezoelectric behaviour.

### 5.4.3 Energy Content

The energy content/loss of the polarisation hystereses of all 10 compositions was determined by integrating the area of the polarisation versus electric field curve. Unipolar values were recorded at 4 kV/mm, bipolar values at 4, 6 and 8 kV/mm. The results are visualised in Fig 52, exact numbers can be found in Tab 16. The 20;Y series shows a maximum loss of 214 kJ/m<sup>3</sup> for one unipolar cycle at 20;1 followed by 20;2 with 161 kJ/m<sup>3</sup>. All other compositions show unipolar loss values between about 50 to 85 kJ/m<sup>3</sup> with the exception of 21;2 with the value of 130 kJ/m<sup>3</sup>.

19;1 shows a minimum in the energy content for unipolar 4 kV/mm as well as 4 and 6 kV/mm bipolar cycles. The 8 kV/mm energy content decreases continuously with increasing Y.

The 21;Y series shows continuously decreasing bipolar energy loss at all field strengths with increasing Y. Continuously increasing unipolar energy loss with increasing KNN-BKT content is found at the same time.

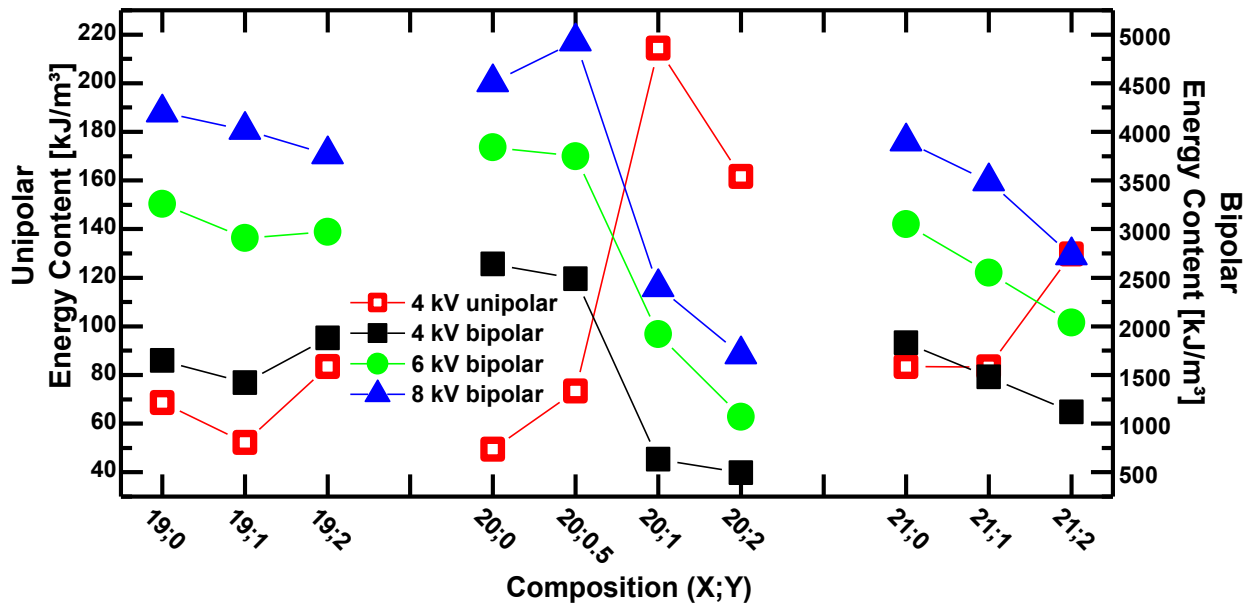
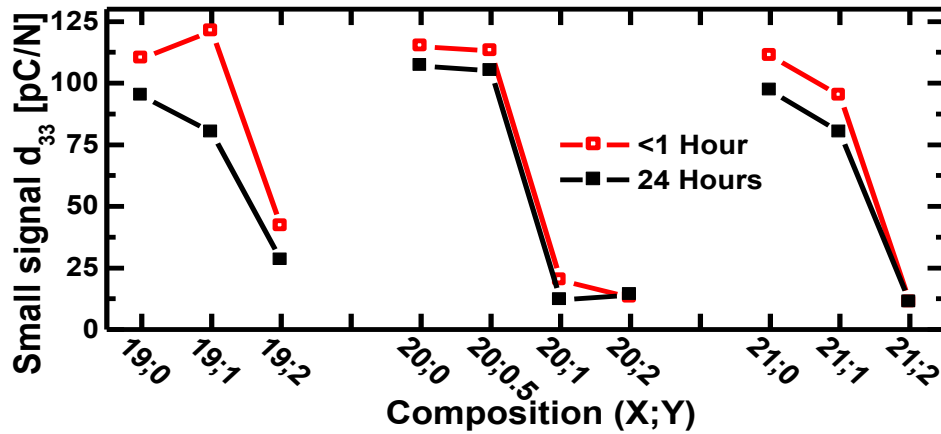


Fig 52: The energy content of the unipolar 4 kV/mm polarisation hysteresis are shown in red. The energy content of the bipolar 4, 6 and 8 kV/mm polarisation hysteresis are shown in black, green and blue, respectively. Please note the large difference of the unipolar scale between 40 and 220 kJ/m<sup>3</sup> and of the bipolar scale from 500 to 5000 kJ/m<sup>3</sup>.

Tab 16: Energy Content of Polarisation Hystereses

Composition	Bipolar [kJ/m <sup>3</sup> ]			
	4 kV/mm	6 kV/mm	8 kV/mm	
19;0	68.58	3260	4200	
19;1	52.25	2910	4020	
19;2	83.45	2970	3770	
20;0	49.38	3840	4510	
20;0.5	73.38	3750	4930	
20;1	214.34	1920	2404	
20;2	161.64	1070	1710	
21;0	83.42	3050	3900	
21;1	83.26	2550	3490	
21;2	129.68	2040	2730	
The energy content of one cycle of the unipolar and bipolar polarisation hystereses was measured by integration of the polarisation versus electric field cycle.				

#### 5.4.4 Small-Signal $d_{33}$



**Fig 53:** Small-signal  $d_{33}$  as a function of composition directly after poling and after 24 h.

The small-signal  $d_{33}$  values were recorded directly after poling at 8 kV/mm and again after the standardised 24-hour aging. All compositions show a continuous drop with increasing Y in their respective series after aging. Initially, the values of 19;1 is highest overall at 121 pC/N. However, it drops by 33 % to 80 pC/N within 24 h. 19;2 also drops 33 % within 24 h from 42 pC/N to a final value of 28 pC/N. All other compositions lost between 7 and 15 % of their  $d_{33}$  value within 24 h. After 24 h, only 20;0 and 20;0.5 show values above 100 pC/N with 107 pC/N and 105 pC/N, respectively; directly after poling 115 pC/N and 113 pC/N were measured. They are closely followed by 19;0 and 19;1 with 97 pC/N and 80 pC/N and 21;0 and 21;1 with 95 pC/N and 80 pC/N, respectively. The time-dependent variations seen for 20;1 and 20;2 as well as the minor increase from 20;1 to 20;2 are below the accuracy of the equipment and, therefore, within the experimental error. Their final values are 12 pC/N and 14 pC/N. 21;2 also shows a low value of 11 pC/N. Directly after poling, 19;0, 21;0 and 21;1 have  $d_{33}$  values around 100 also with 110, 111 and 95 pC/N each.

### 5.4.5 Radial Strain

Concurrently with the axial strain, the radial strain of the disk shaped samples of all 10 compositions was recorded under bipolar electrical load of 4, 6 and 8 kV/mm. The result of the 8 kV/mm run is shown in Fig 54 for the 19;Y series, in Fig 55 for the 20;Y series and in Fig 56 for the 21;Y series. The description of the axial strain curves was already done in section 5.4.1. The sum of the axial and twice the radial strain in per cent is the volume change also in per cent.

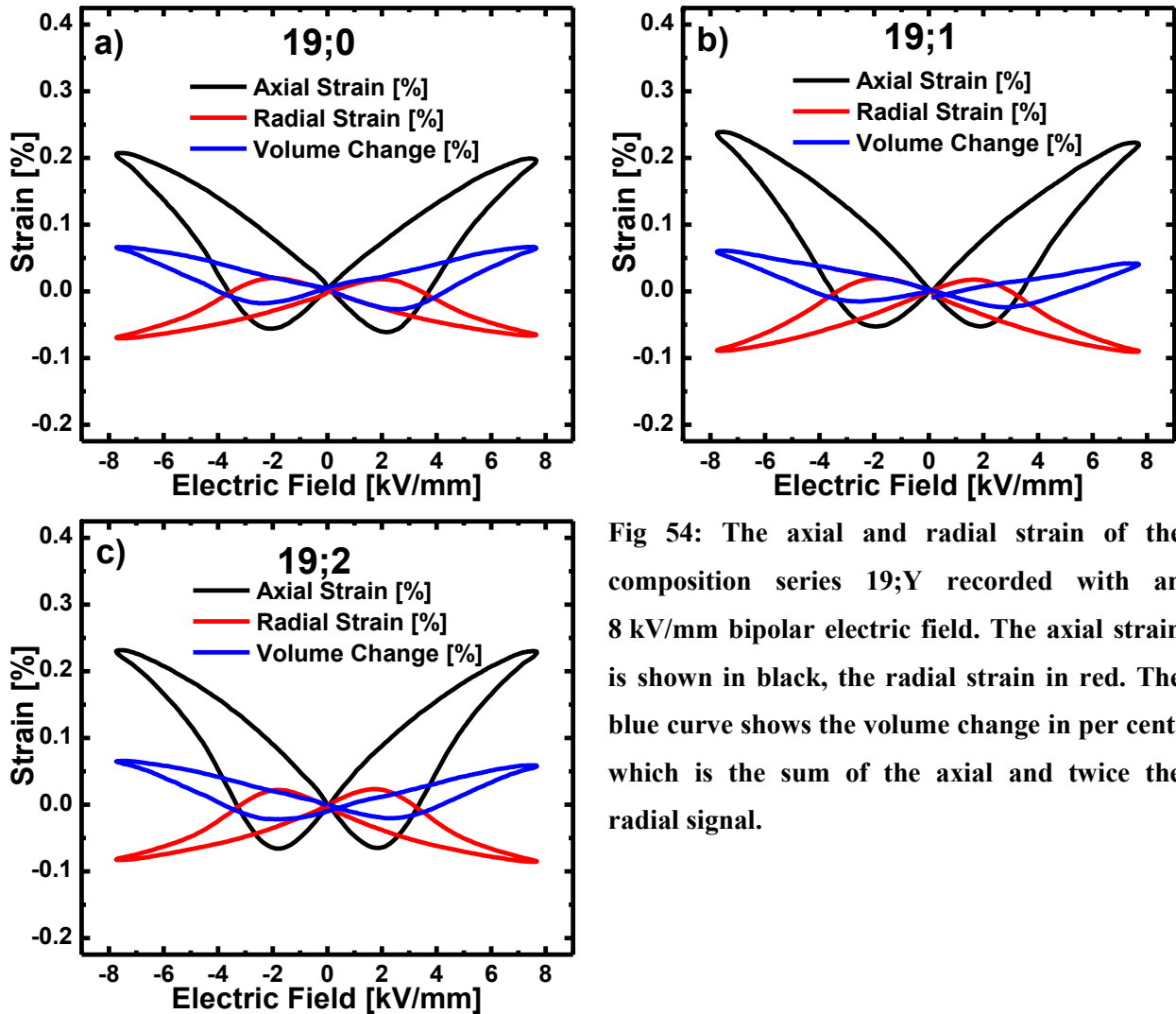


Fig 54: The axial and radial strain of the composition series 19;Y recorded with an 8 kV/mm bipolar electric field. The axial strain is shown in black, the radial strain in red. The blue curve shows the volume change in per cent, which is the sum of the axial and twice the radial signal.

The shape of the radial strain curve is identical for all compositions of the 19;Y series. The radial strain of each sample is as a first approximation the inverted and halved signal of the axial strain. However, the volume change shows a hysteretic path, which illustrates the deviation from this first approximation. The volume change (defined as zero with no applied field) is largest at the highest applied field with 0.064 %, 0.065 % and 0.065 % for 19;0, 19;1 and 19;2 respectively. The error, in this case due to drift of the sensor, is about 0.005 percentage points. This drift in the axial signal is a result of the continuous flow of silicon oil down the sample holder and, therefore, induced a small thermal drift in the axial signal only. The oil was at a different

temperature to the temperature of the room, since it was stored in a different part of the building. The relative volume change then decreases almost linearly when the field is reduced. If the field direction is reversed, the samples initially contract linearly and then approximately quadratically before expanding again first quadratically then linearly along most of the way towards the maximum at the maximum applied field.

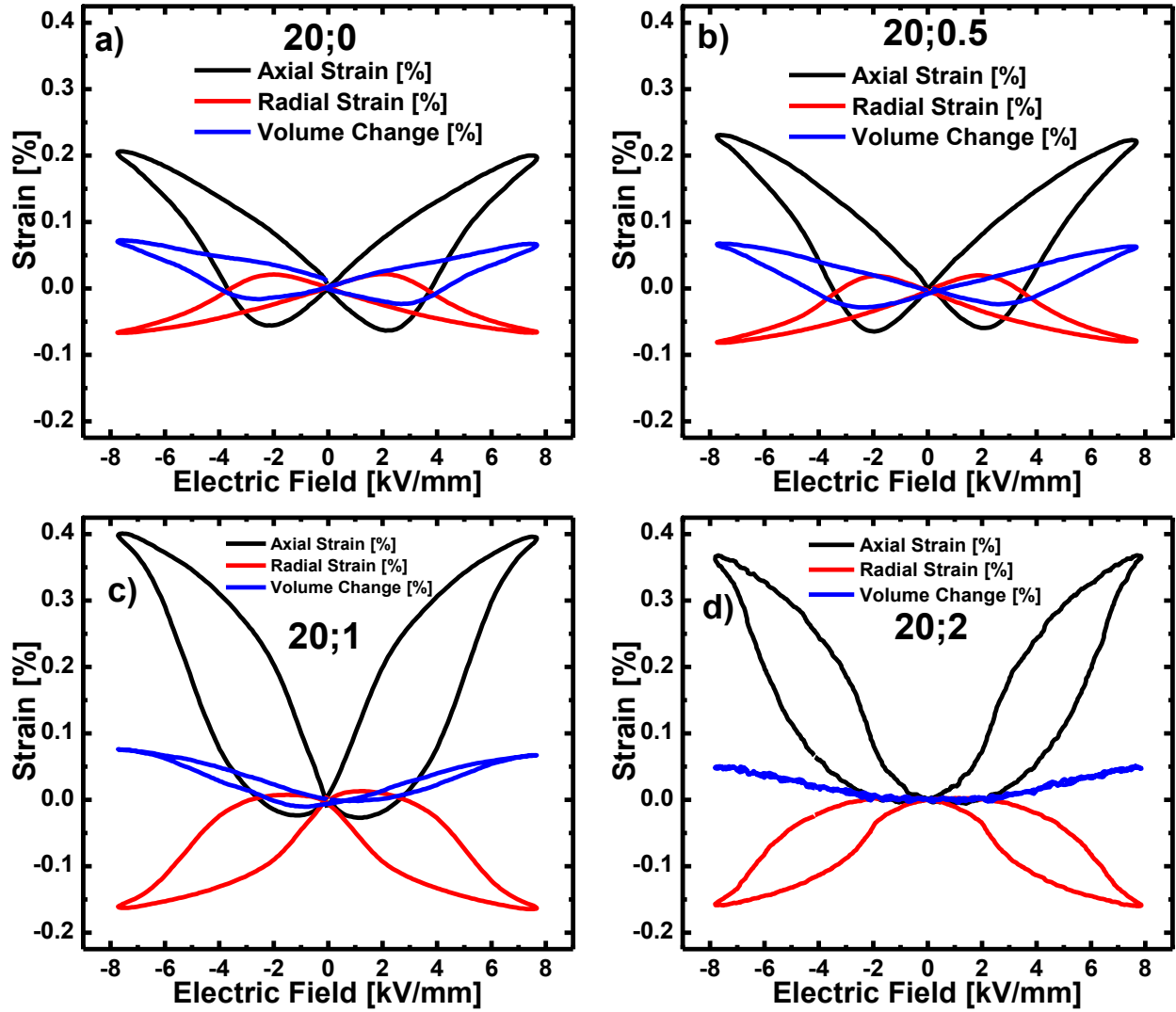


Fig 55: The axial and radial strain of the composition series 20;Y recorded with an 8 kV/mm bipolar electric field. The axial strain is shown in black, the radial strain in red. The blue curve shows the volume change in per cent, which is the sum of the axial and twice the radial signal.

The description of the radial strain and volume change hysteresis shapes of compositions 20;0 and 20;0.5 is identical to the 19;Y series description with the  $V_{\max}$  value of 0.066 % and 0.060 %. Composition 20;1 shows an even higher similarity between the axial strain and twice the inverse of the radial strain. This is expressed in the volume change with its much narrower hysteresis with much less volume contraction but about the same maximum volume expansion as the other two at 0.66 % at  $E_{\max}$ . Furthermore, the parts of the volume hysteresis that were described as

linear in the case of the 19;Y compositions are now also nonlinear. Composition 20;2 finally shows no volume hysteresis at all and neither any volume contraction. The volume change is quadratic at first and almost levels out at higher fields. Its maximum volume change of 0.03 % is half that of the previous composition even though the axial strain is comparable.

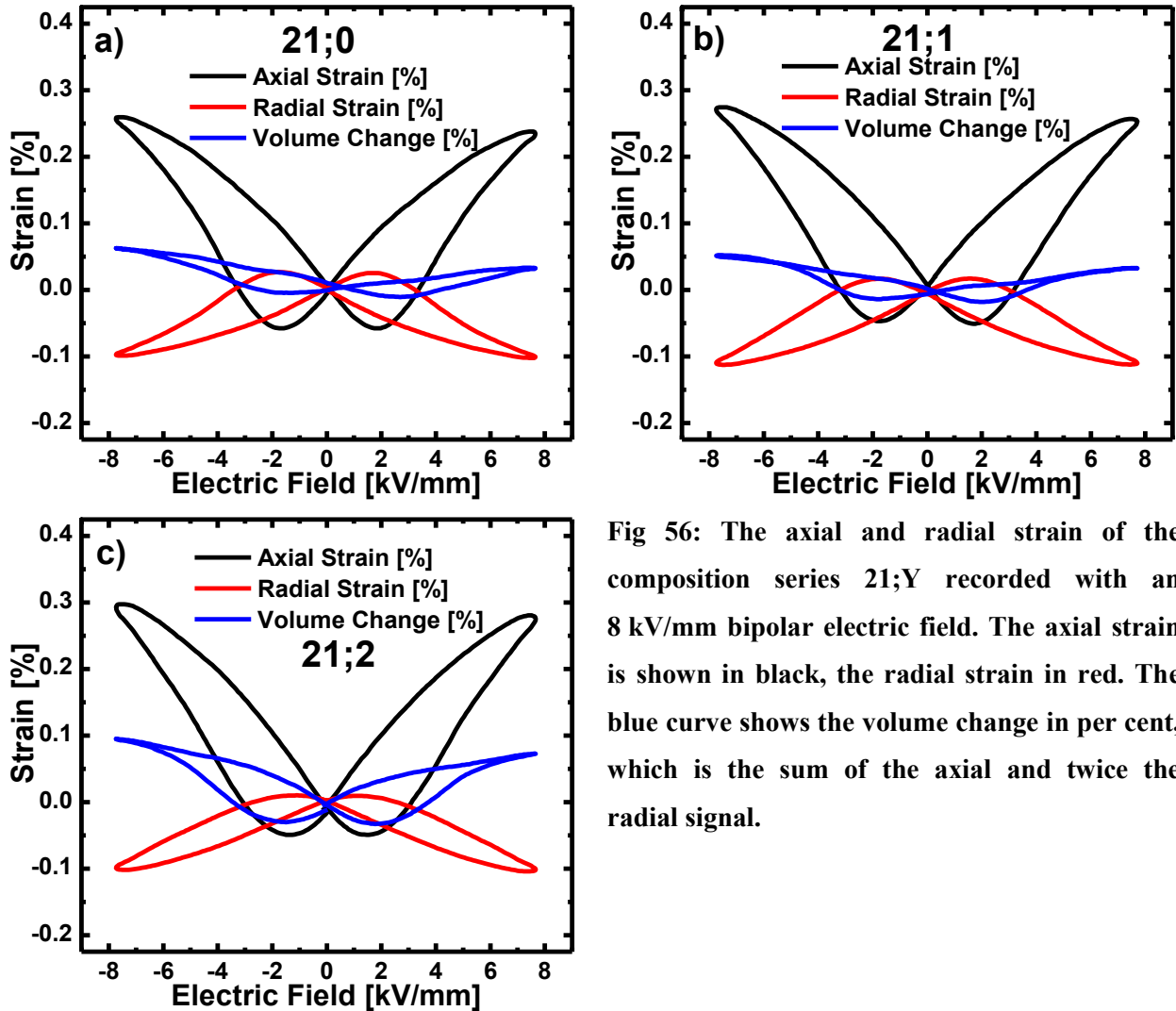
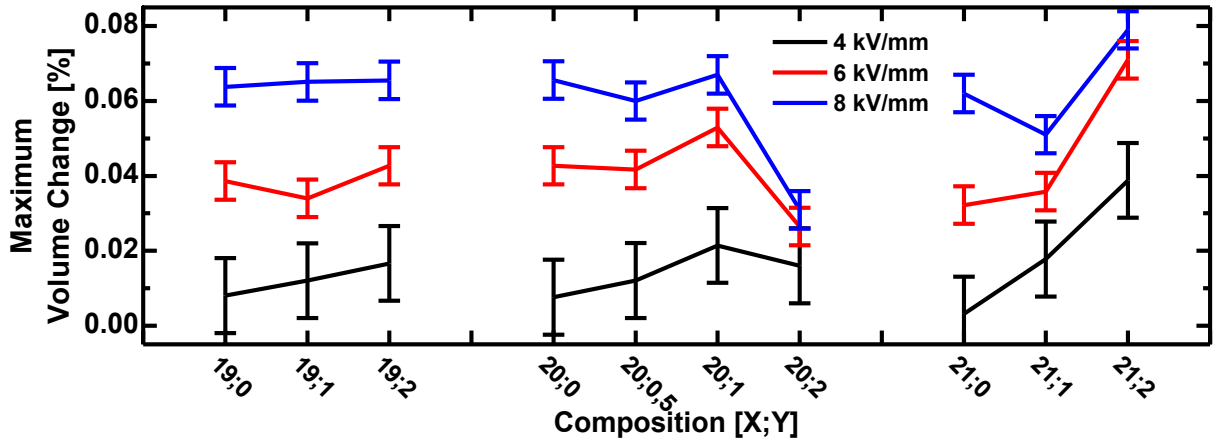


Fig 56: The axial and radial strain of the composition series 21;Y recorded with an 8 kV/mm bipolar electric field. The axial strain is shown in black, the radial strain in red. The blue curve shows the volume change in per cent, which is the sum of the axial and twice the radial signal.

The shape of the volume hysteresis of 21;0 is comparable to that of 19;0 as described above. Its maximum volume change at the maximum applied field is 0.062 %. The composition 21;1 shows a slightly broader hysteresis at low fields and almost no hysteresis at higher fields with a  $V_{\max}$  of 0.051 %. The composition 21;2 finally shows the largest volume hysteresis area of all 10 compositions. This is, however, not due to increased volume contraction or expansion but the expanded volume returns more slowly at high fields and faster at lower fields during reduction of the applied field than in the other compositions.



**Fig 57: The maximum volume expansion in per cent as a function of composition and electric field. The larger errors of the 4 kV/mm values are due to asymmetry of the axial strain curve.**

The maximum positive volume change (expansion) values ( $V_{\max}$ ) at  $E_{\max}$  values for all 10 compositions and  $E_{\max}$  of 4, 6 and 8 kV/mm are graphically summarised in Fig 57. The maximum volume contraction values were below the resolution of the equipment. The  $V_{\max}$  values at 4 kV/mm are so low that the absolute error is the same magnitude as the value of  $V_{\max}$  at 19;0. Furthermore, a small asymmetry of the axial strain (near the detection threshold of the equipment) adds another about 0.005 percentage points to the error of the 4 kV/mm values. The trends of the maximum volume changes described above for 8 kV/mm maximum field hold true for lower fields also in the case of the 19;Y and 20;Y series as well as 21;1 and 21;2. The 21;Y series shows a continuous almost linear increase of  $V_{\max}$  with increasing KNN-BKT content (Y) at 4 kV/mm maximum applied field. With increasing maximum applied field, the  $V_{\max}$  values of 21;0, however, increase faster than those of 21;1 and 21;2. At 6 kV/mm, the values of 21;0 and 21;1 are almost the same and at 8 kV/mm, the 21;0 value directly in between the values of 21;1 and 21;2. The value recorded for composition 19;1 is the average value of the positive and negative field value since there was a strong asymmetry.

## 5.5. Temperature-Dependent Properties

### 5.5.1 Strain and Polarisation at Elevated Temperatures.

#### 5.5.1.1 Strain and Polarisation Hystereses Shapes at Elevated Temperatures

The temperature-dependent strain and polarisation of all 10 compositions were recorded. A saw-tooth shaped signal with the maximum field strengths of 4 kV/mm was applied to frequency of 55 mHz. At each temperature step the sample and the sample holder, which was only partially submerged in temperature controlled silicon oil, was left to rest for around 5 to 15 minutes. During this time, the different materials, the sample holder with the strain sensor was made of, were allowed to reach thermal equilibrium to minimise thermal drift during the measurement.

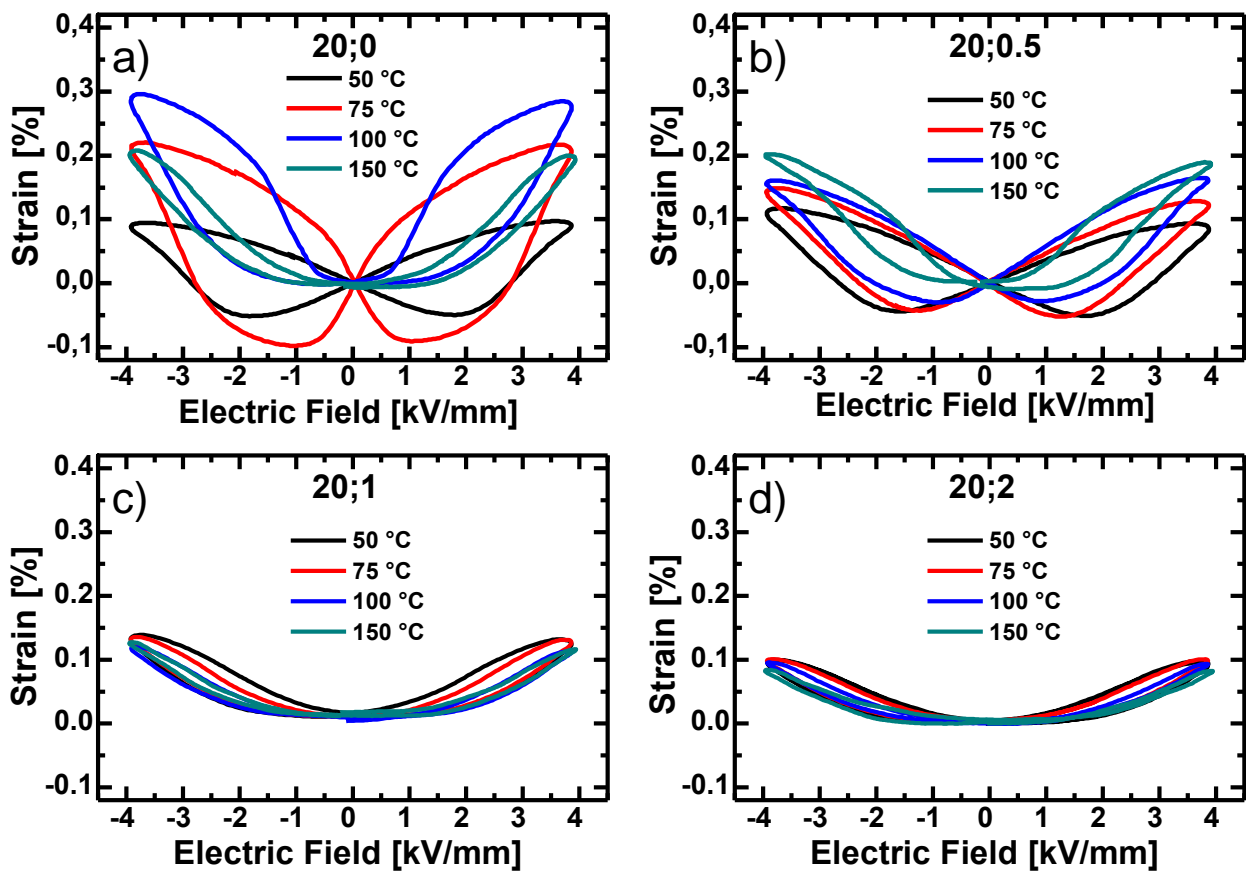


Fig 58: The bipolar strain evolution at 4 kV/mm recorded at 50, 75, 100 and 150 °C for compositions a) 20;0, b) 20;0.5, c) 20;1 and d) 20;2.

Measurements were repeated as needed until the thermal drift between the beginning and the end of the cycle was approximately less than 5 % of the maximum recorded strain in the mentioned cycle. During the measurement, the temperature of the convecting oil was within 1.5 K of the target temperature.

The strain and polarisation were recorded in 12.5 K steps between room temperature (25 °C) and 100 °C. Between 100 °C and 200 °C, the step size was 50 Kelvin. The resulting bipolar strain



curves of compositions 20;0, 20;0.5, 20;1 and 20;2 can be found in Fig 58; their corresponding polarisation hysteresis in Fig 59. The four temperatures and compositions shown were selected because they cover all possible shapes and types of the strain and polarisation hystereses, which can also be found in the other materials and at other temperatures as well.

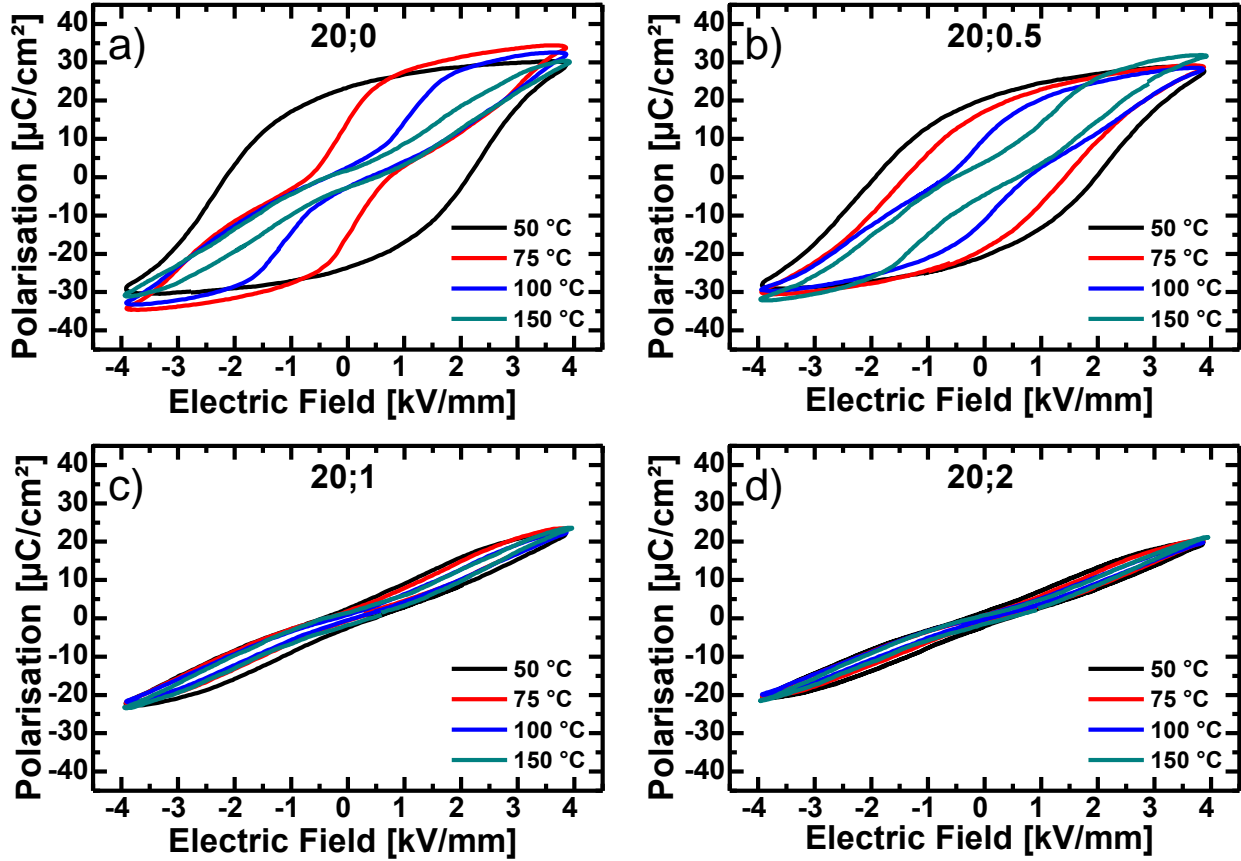


Fig 59: The bipolar polarisation evolution at 4 kV/mm recorded at 50, 75, 100 and 150 °C for compositions a) 20;0, b) 20;0.5, c) 20;1 and d) 20;2.

In this section, only the shape evolution is discussed. The bipolar strain hysteresis of 20;0 (Fig 58a) keeps its typical room temperature shape at 50 °C but with increased positive and negative strain. At 75 °C, positive and negative strain is again increased and the linear parts of the strain path become fewer and shorter. At 100 °C, the positive strain is highest while the negative strain has almost disappeared. The hysteresis shape is comparable to that of 20;2 at room temperature. The strain hysteresis at 150 °C shows reduced positive strain, no negative strain and less hysteretic behaviour. The evolution of the shape of the bipolar strain curve of 20;0.5 (Fig 58b) is identical to that of 20;0 but all changes happen more gradually over a wider range of temperatures, which is further described in section 5.5.1.2 through 5.5.1.4. However, unlike in the previous case, the positive strain continuously increases while the negative strain continuously decreases for all displayed the strain curves. The strain curves of 20;1 and 20;2 (Fig 58b and c) keep their room temperature strain hysteresis shapes at 50, 75, 100 and 150 °C. Their

maximum strain continuously decreases with temperature and so does their hysteretic behaviour, i.e. the width/area of the hystereses becomes smaller.

The shape of the polarisation hysteresis of 20;0 (Fig 59a) at 50 °C is identical to the room temperature hysteresis. At 75 °C, the polarisation hysteresis of 20;0 shows slight pinching but still remanent polarisation similar to composition 20;1 at room temperature. At 100 °C, the pinching becomes more pronounced and the remanent polarisation small like in the case described for 20;2 at room temperature. At 150 °C, the polarisation increases nearly linearly with the electric field. At 1 kV/mm field strength, the slope of the gradient between polarisation and electric field flattens out.

The polarisation of 20;0.5 (Fig 59b) shows a similar temperature-dependent evolution to 20;0 with all characteristic changes shifted upwards by about 25 K. In addition, all changes happen more gradually with temperature. At 75 °C, the room temperature shape is still maintained. The pinching at 100 °C has not yet crossed the zero field value. The hysteresis at 150 °C has about twice the width of composition 20;0 at the same temperature.

The polarisation hysteresis of 20;1 and 20;2 (Fig 59c and d) maintain their room temperature polarisation hysteresis shapes at 50 °C and 75 °C. The polarisation changes almost linearly with increasing electric field with a narrow hysteresis, which becomes narrower with increasing temperature. At 100 °C and 150 °C, the gradient of the slope of the polarisation is flatter for fields below 1 kV/mm.

All compositions show a small increase in maximum polarisation with temperature beginning at 75 °C. Compositions 19;Y and 21;Y all follow the strain and polarisation evolution described in the case of 20;0. However, the „transition“ temperatures between the different strain and polarisation curve types are different in each case as summarised below.

### 5.5.1.2 Temperature-Dependent Maximum Strain

A summary of the temperature-dependent maximum strain for all 10 compositions, including data from all temperature steps, can be found in Fig 60, Fig 61 and Fig 62 for composition series 19;Y, 20;Y and 21;Y, respectively. The corresponding remanent and maximum polarisation values are presented in Fig 63, Fig 64 and Fig 65 as well as the coercive field values in Fig 66.

The maximum unipolar and bipolar strain values of 19;0 (Fig 60a) to 19;2 (Fig 60a) have some basic characteristics in common. Unipolar and bipolar strain increases continuously from their respective room temperature values up to a certain temperature, whilst the difference between them continuously decreases. The maximum unipolar and bipolar strain is always reached just before they become identical. The apparent drop between 25 °C and 37.5 °C in 19;0 is a result of uncontrollable non-linear thermal drift due to fluctuating cooling water temperature. The change in slope at 50 °C in composition 19;1 occurs because the samples had to be replaced at 37.5 °C and new samples show a slightly higher strain for the first 5 to 10 bipolar cycles.

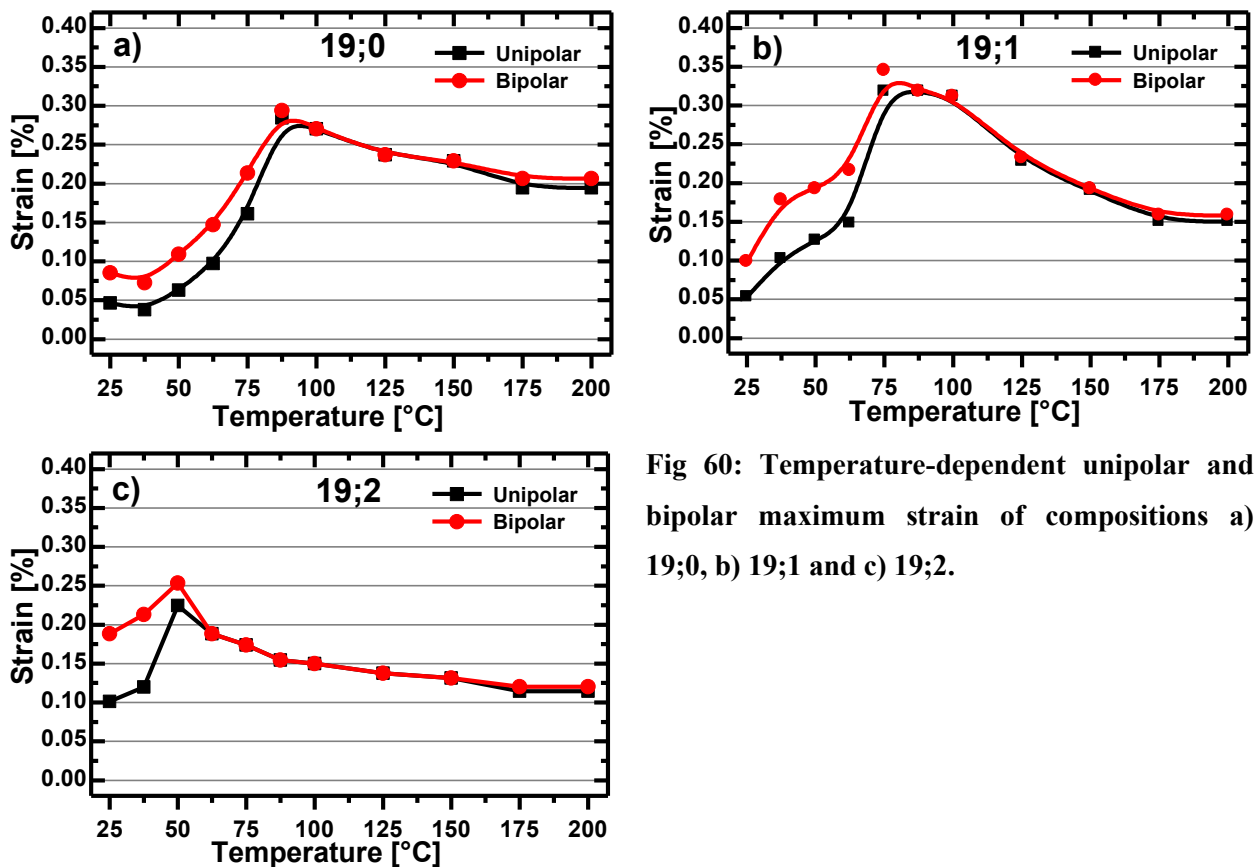


Fig 60: Temperature-dependent unipolar and bipolar maximum strain of compositions a) 19;0, b) 19;1 and c) 19;2.

The minor separation of unipolar and bipolar strain at above 150 °C is also a result of non-linear thermal drift. For unipolar measurements, the strain was always measured between the zero field value and the maximum. For the bipolar strain, always the highest and lowest values were taken from one side of the strain hysteresis. Even if there was no actual negative strain contribution, the

lowest value was sometimes lower than the value at zero field. This maximum deviation of 0.01 percentage points should be considered the maximum achievable accuracy of the experiment.

Composition 19;0 reaches its maximum strain of 0.29 % at 87.5 °C, composition 19;1 reaches 0.35 % at 75 °C and composition 19;2 reaches 0.26 % at 50 °C. After these respective maximum unipolar and bipolar strain remains equal and continuously decrease together until they reach 0.21 %, 0.16 % and 0.12 % at 200 °C, respectively.

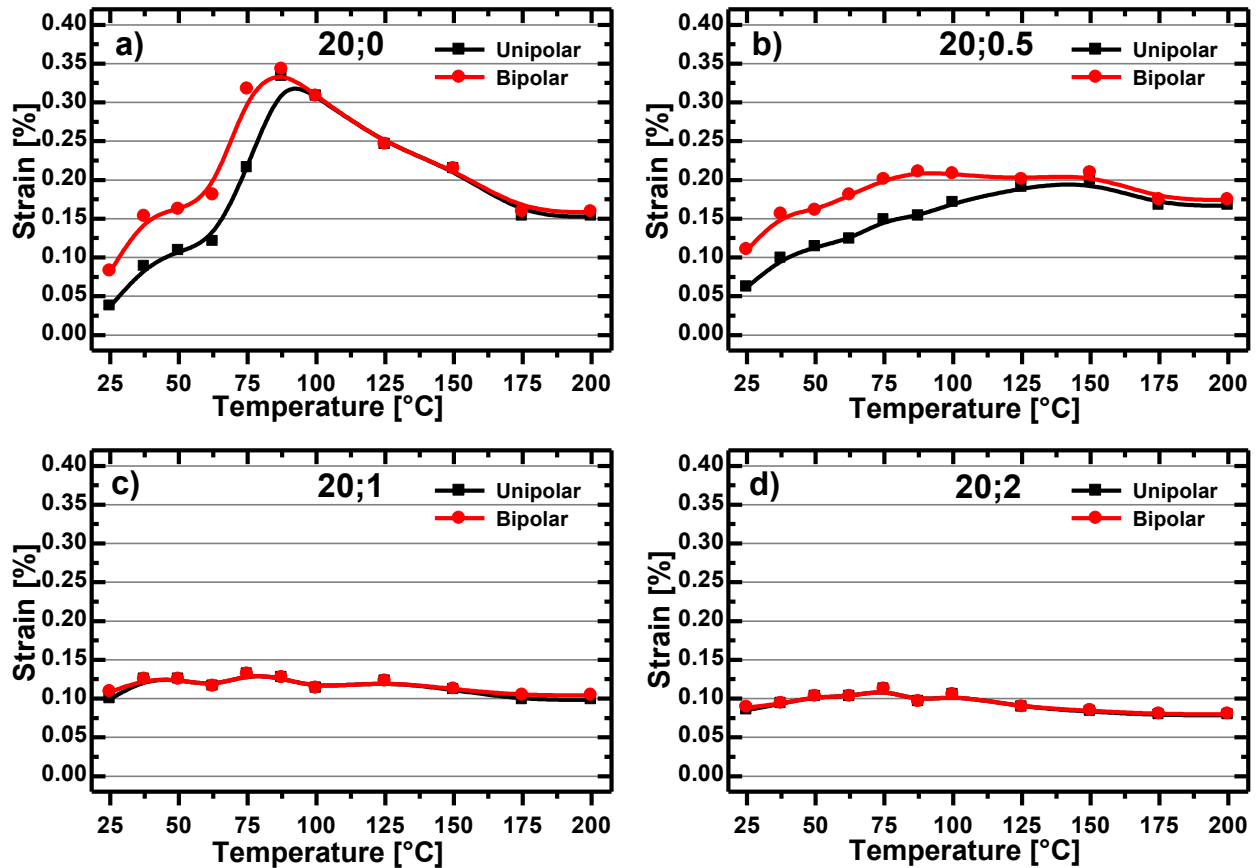


Fig 61: Temperature-dependent unipolar and bipolar maximum strain of compositions a) 20;0, b) 20;0.5, c) 20;1 and d) 20;2.

The bipolar and unipolar strain of compositions 20;0 (Fig 61a) shows the same type of behaviour as already discussed for compositions 19;Y. The highest strain is found at 87.5 °C at 0.34 %, which is reduced to 0.16 % at 200 °C.

The bipolar strain of composition 20;0.5 (Fig 61b) shows a much less defined broader maximum. The highest bipolar strain remains constant at 0.21 % between 87.5 °C and 150 °C. The unipolar strain peaks at 150 °C with 0.20 % and a strain of 0.17 % at 200 °C. Unipolar and bipolar strain of composition 20;1 are always identical at every temperature step and within the error margin of the experiment. The apparent increase from the room temperature value of 0.12 % to the maximum value of 0.13 % at 75 °C and its return to 0.11 % at 200 °C is only twice the assumed

maximum accuracy of the experimental setup. The corresponding values for composition 20;2 are 0.9 % , 0.11 % and 0.8 % at room temperature, 75 °C and 200 °C.

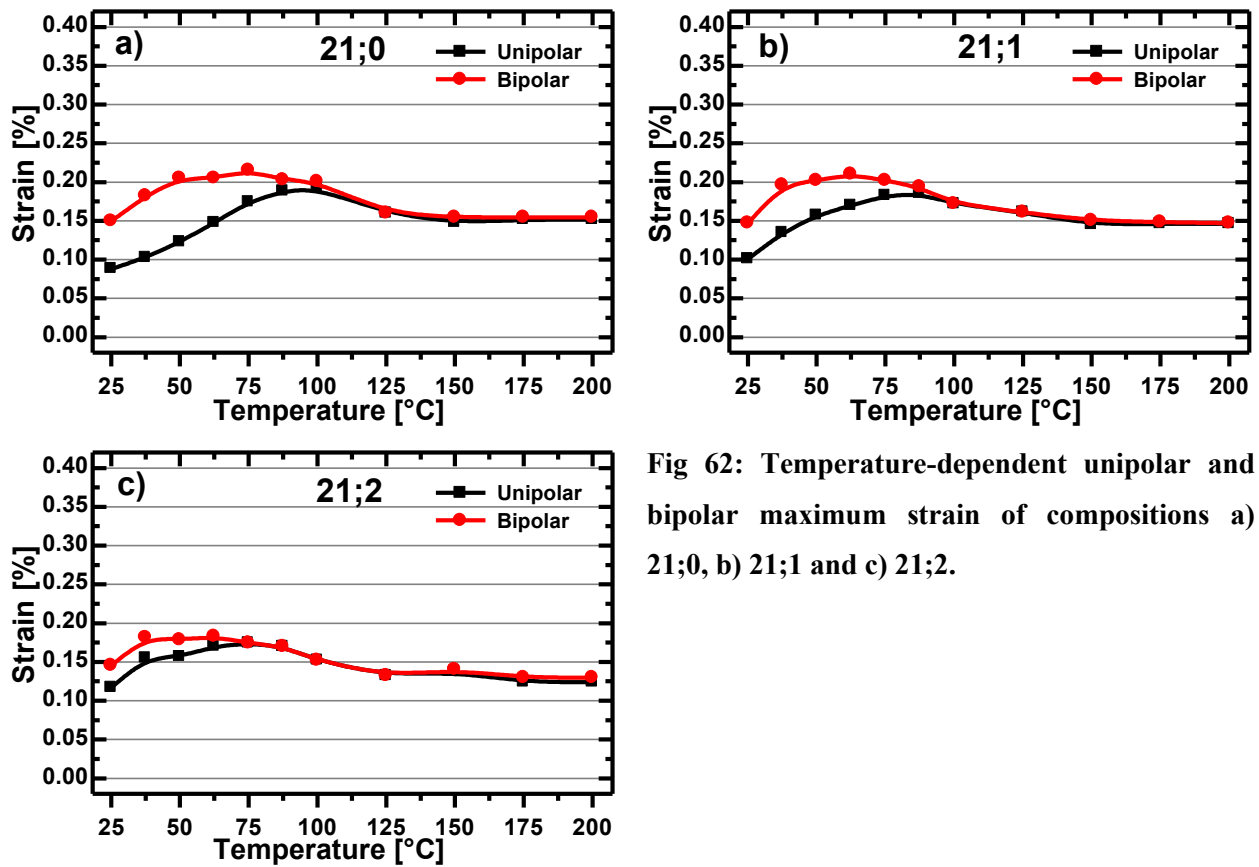


Fig 62: Temperature-dependent unipolar and bipolar maximum strain of compositions a) 21;0, b) 21;1 and c) 21;2.

The unipolar and bipolar strain of compositions 21;0 to 21;2 is shown in Fig 62a to c. Even though they are similar to composition 20;0 in the general strain shape evolution, the maximum of the bipolar strain is always at a 25 K lower temperature than the maximum of the unipolar strain. In all other materials, these maxima are at most 12.5 K apart. The maximum bipolar strain values of 21;0, 21;1 and 21;2 are 0.22 %, 0.21 % and 0.18 % at 75 °C, 62.5 °C and 50 °C, respectively, and the maximum unipolar strain is 0.19 %, 0.18 % and 0.17 %. At 200 °C, unipolar and bipolar strain values are equal and 0.15 %, 0.15 % and 0.13 % for compositions 21;0 to 21;2.

### 5.5.1.3 Temperature-Dependent Remanent and Maximum Polarisation

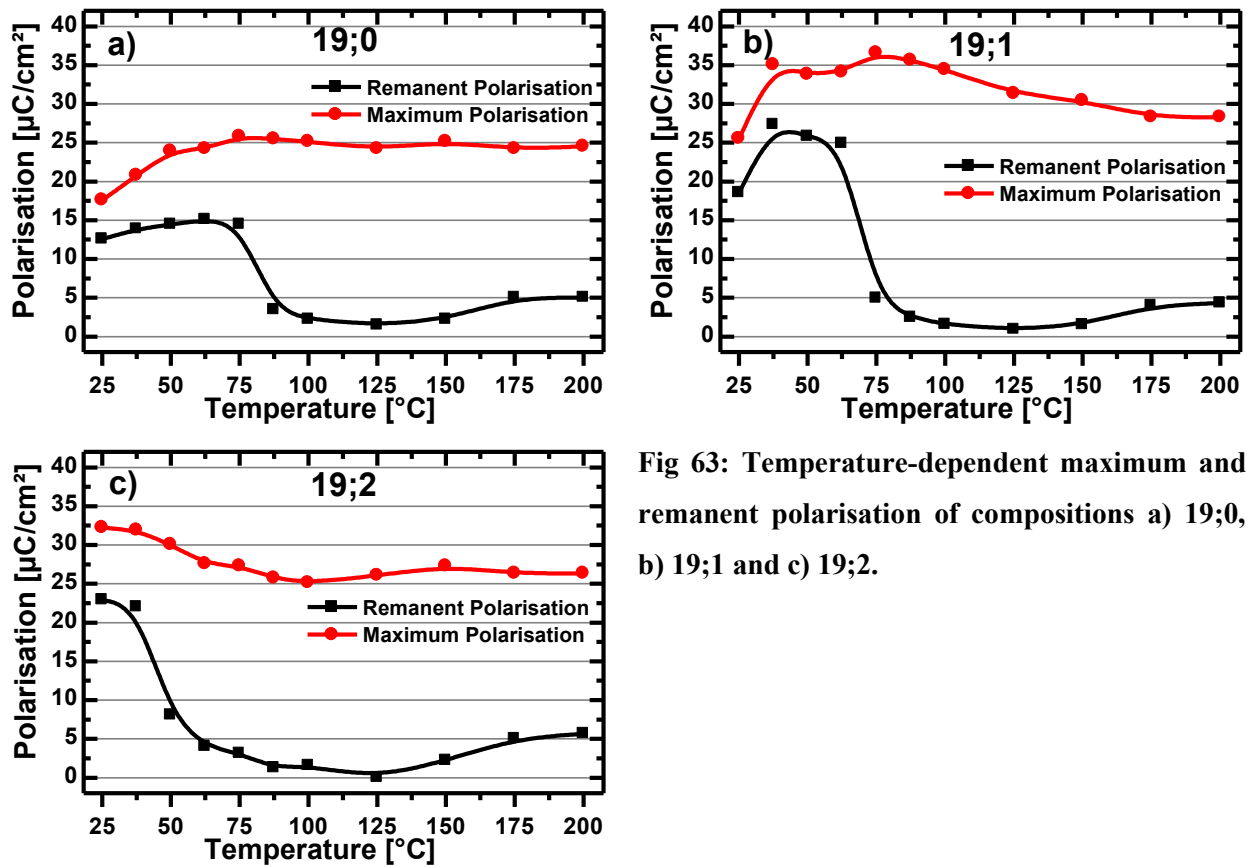


Fig 63: Temperature-dependent maximum and remanent polarisation of compositions a) 19;0, b) 19;1 and c) 19;2.

The temperature-dependent evolution of the remanent and maximum polarisation of compositions 19;0 to 19;2 can be found in Fig 63. The maximum polarisation of composition 19;0 increases continuously up to its maximum value of  $25.7 \mu\text{C}/\text{cm}^2$  at  $75^{\circ}\text{C}$ . It then decreases continuously to  $24.5 \mu\text{C}/\text{cm}^2$  at  $200^{\circ}\text{C}$ . The remanent polarisation increases continuously to its maximum value of  $15.1 \mu\text{C}/\text{cm}^2$  at  $62.5^{\circ}\text{C}$ . The lowest value of  $1.5 \mu\text{C}/\text{cm}^2$  is found at  $125^{\circ}\text{C}$ . At higher temperatures, an increased conductivity of the sample causes an apparent increase in the remanent polarisation. It can be assumed that the maximum polarisation actually decreases more quickly with temperature, but this cannot be seen due to the superimposed conductivity contribution. This conductivity contribution is found in all samples at  $125^{\circ}\text{C}$  and above. Therefore, for better comparability, the remanent polarisation value at  $125^{\circ}\text{C}$  will always be selected.

Composition 19;1 (Fig 63b) shows the same general behaviour as the previous composition. The highest maximum polarisation of  $36.5 \mu\text{C}/\text{cm}^2$  is found at  $75^{\circ}\text{C}$ . However, if the measurement artefact due to the sample replacement is ignored, the actual maximum is likely at  $62.5^{\circ}\text{C}$ . The corresponding remanent polarisation at  $62.5^{\circ}\text{C}$  is  $24.8 \mu\text{C}/\text{cm}^2$ . Again, lower temperature values are the result of the sample replacement. The minimum remanent polarisation of  $0.9 \mu\text{C}/\text{cm}^2$  is found at  $125^{\circ}\text{C}$ . The maximum polarisation at  $200^{\circ}\text{C}$  is  $28.3 \mu\text{C}/\text{cm}^2$ .

Composition 19;2 (Fig 63c) shows no initial increase of the maximum and remanent polarisation at low temperatures but the highest maximum and remanent polarisation values of  $32.2 \mu\text{C}/\text{cm}^2$  and  $22.9 \mu\text{C}/\text{cm}^2$  are found at  $25^\circ\text{C}$ . The lowest remanent polarisation at  $125^\circ\text{C}$  was below  $0.02 \mu\text{C}/\text{cm}^2$ , which is the signal-to-noise ratio limiting the experiment. It is therefore assumed to be zero. The maximum polarisation at  $200^\circ\text{C}$  is  $26.2 \mu\text{C}/\text{cm}^2$ .

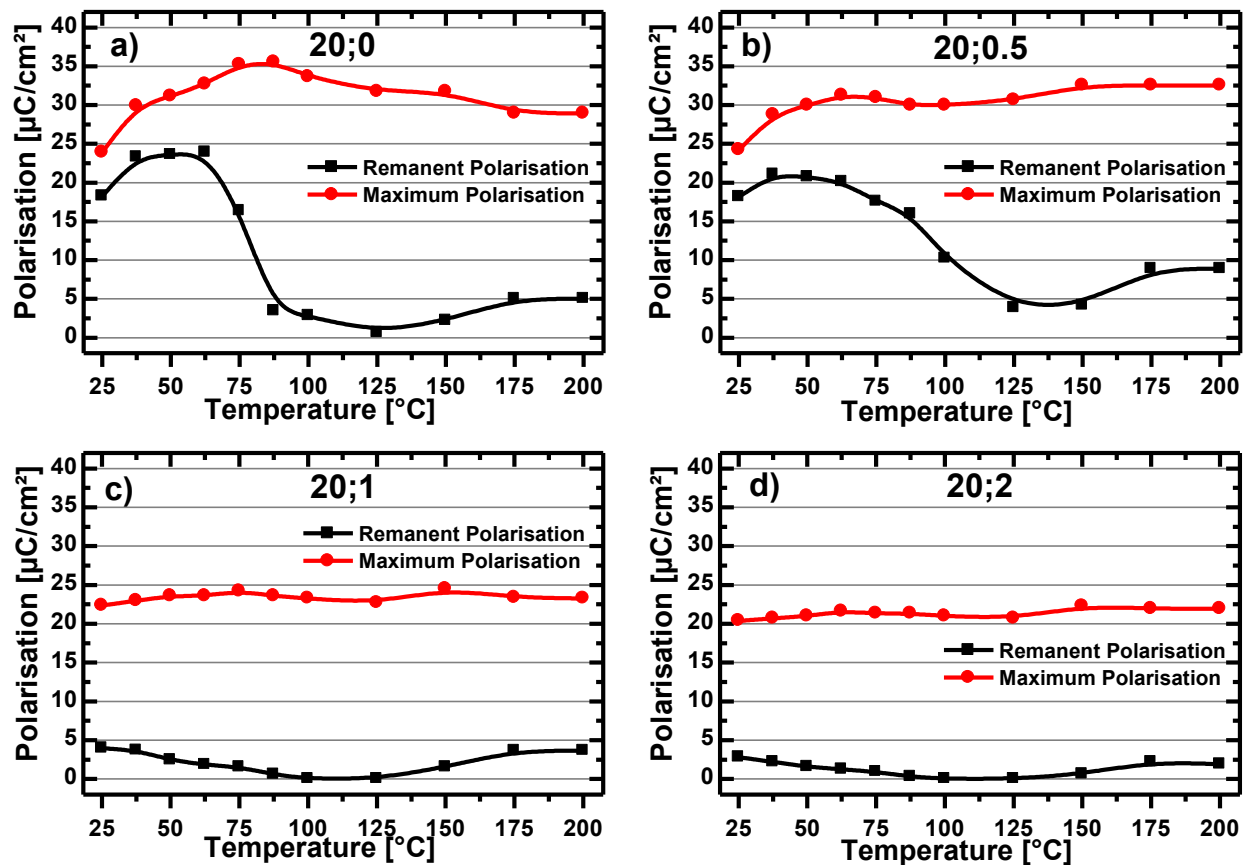


Fig 64: Temperature-dependent maximum and remanent polarisation of compositions a) 20;0, b) 20;0.5, c) 20;1 and d) 20;2.

Remanent and maximum polarisation of compositions 20;0 to 20;2 are found in Fig 64. Compositions 20;0 and 20;0.5 showed the same general behaviour as previously mentioned for compositions 19;Y. For composition 20;0 (Fig 64a) highest maximum polarisation of  $35.5 \mu\text{C}/\text{cm}^2$  is found at  $87.5^\circ\text{C}$ , its highest remanent polarisation of  $23.9 \mu\text{C}/\text{cm}^2$  at  $62.5^\circ\text{C}$ . The lowest remanent polarisation at  $125^\circ\text{C}$  is found to be  $0.65 \mu\text{C}/\text{cm}^2$  and the maximum polarisation at  $200^\circ\text{C}$  is  $28.9 \mu\text{C}/\text{cm}^2$ .

Composition 20;0.5 (Fig 64b) shows the steady almost linear decrease of the remanent polarisation from its highest value of  $21.0 \mu\text{C}/\text{cm}^2$  at  $32.5^\circ\text{C}$  to  $3.8 \mu\text{C}/\text{cm}^2$  at  $125^\circ\text{C}$ . The maximum polarisation peaks at  $62.5^\circ\text{C}$  with a value of  $31.2 \mu\text{C}/\text{cm}^2$ . Conductivity causes an apparent increase of the maximum polarisation above  $125^\circ\text{C}$  with a final value of  $32.5 \mu\text{C}/\text{cm}^2$ , which is likely at least 10 % lower if the conductivity contribution could be removed.

Composition 20;1 and 20;2 (Fig 64c and d) shows a nearly constant maximum polarisation of between  $22.4 \mu\text{C}/\text{cm}^2$  and  $24.5 \mu\text{C}/\text{cm}^2$  and between  $20.3 \mu\text{C}/\text{cm}^2$  and  $22.2 \mu\text{C}/\text{cm}^2$  respectively. Both show a continuous linear decrease of the remanent polarisation between room temperature and  $125^\circ\text{C}$ , after which there is again a conductivity contribution seemingly causing an increase. The minimum remanent polarisation of both composition 20;1 and 20;2 is zero within the signal-to-noise error margin.

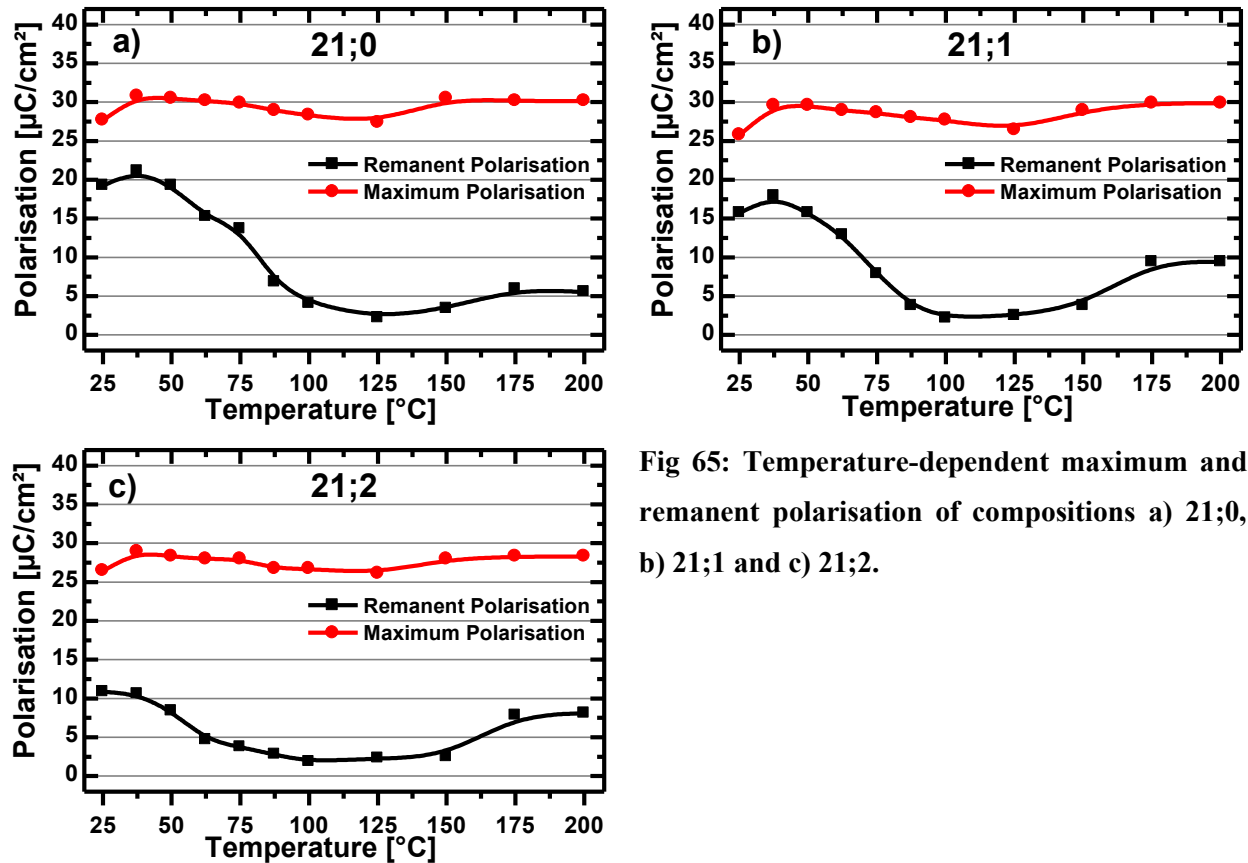


Fig 65: Temperature-dependent maximum and remanent polarisation of compositions a) 21;0, b) 21;1 and c) 21;2.

Compositions 21;0 to 21;2 have their remanent and maximum polarisation as a function of temperature presented in Fig 65. The highest maximum polarisation of all three is found at  $32.5^\circ\text{C}$  with  $30.7 \mu\text{C}/\text{cm}^2$ ,  $29.5 \mu\text{C}/\text{cm}^2$  and  $28.9 \mu\text{C}/\text{cm}^2$  in order of ascending KNN-BKT content. The highest remanent polarisation values of 21;0 and 21;1 are also found at  $32.5^\circ\text{C}$  with  $21.1 \mu\text{C}/\text{cm}^2$  and  $17.9 \mu\text{C}/\text{cm}^2$ , respectively. The highest value of 21;2 is found at room temperature. The lowest remanent polarisation values of 2.2, 2.1 and  $1.8 \mu\text{C}/\text{cm}^2$  are found at 125, 100 and  $100^\circ\text{C}$  for compositions 21;0, 21;1 and 21;2, respectively. The values of the latter two at  $125^\circ\text{C}$  already show some conductivity contribution. The maximum polarisation values of all three in order of ascending KNN-BKT content are 30.1, 29.9 and  $28.3 \mu\text{C}/\text{cm}^2$ .



#### 5.5.1.4 Temperature-dependent Coercive Field

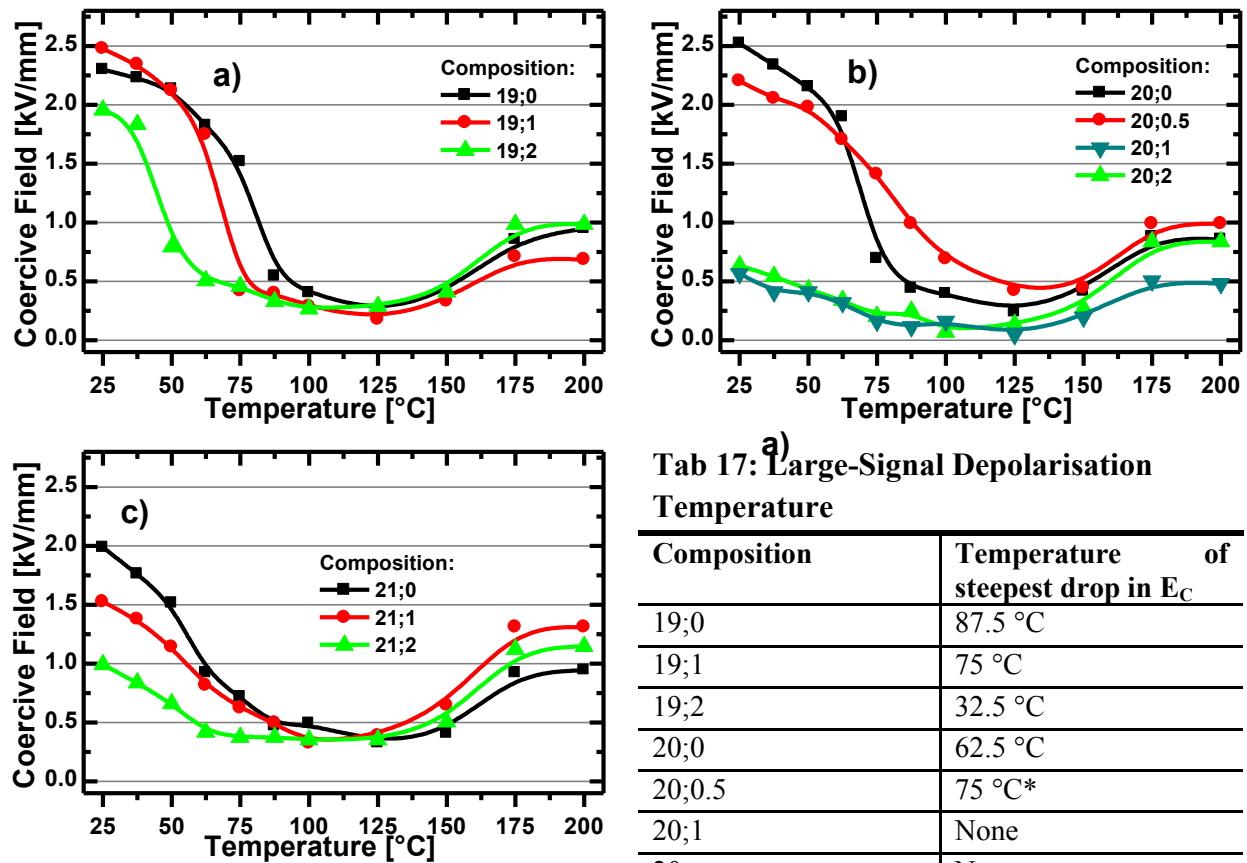


Fig 66: Temperature-dependent coercive field of a) 19;Y, b) 20;Y and c) 21;Y. The temperature, where the largest change in the coercive field occurs, is listed in Tab 17 on the right.

Tab 17: a) Large-Signal Depolarisation Temperature

Composition	Temperature of steepest drop in $E_C$
19;0	87.5 °C
19;1	75 °C
19;2	32.5 °C
20;0	62.5 °C
20;0.5	75 °C*
20;1	None
20;to	None
21;0	50 °C
21;1	50 °C
21;2	None

\* drop is almost steady

The temperature-dependent coercive field is shown in Fig 66 for all 10 compositions. All compositions except 20;1, 20;2 and 21;2 show an initial gradual decrease in the coercive field from their respective room temperature values followed by a steep drop after which the coercive field slowly approaches a minimum at 125 °C. The temperature where the deepest drop begins are listed in Tab 17. They correspond to the depolarisation temperature of the composition. Compositions with the coercive field of nearly 2 kV/mm or above all show this sudden drop in the coercive field value with the exception of 20;0.5 which shows a more gradual decrease comparable to the one found in 20;1 and 20;2 which is also seen in 21;1 and 21;2. Values above 2 kV/mm should not be considered actually a coercive field values since the maximum applied field was only 4 kV/mm. Similarly, values below 0.5 kV/mm should be viewed with caution since conductivity at higher temperatures broadened the polarisation hysteresis. The signal-to-noise ratio is highly dependent on the angle of intersection of the polarisation curve and zero field line, which makes values below 0.5 kV/mm unreliable.

### 5.5.2 Temperature-Dependent Remanent Strain

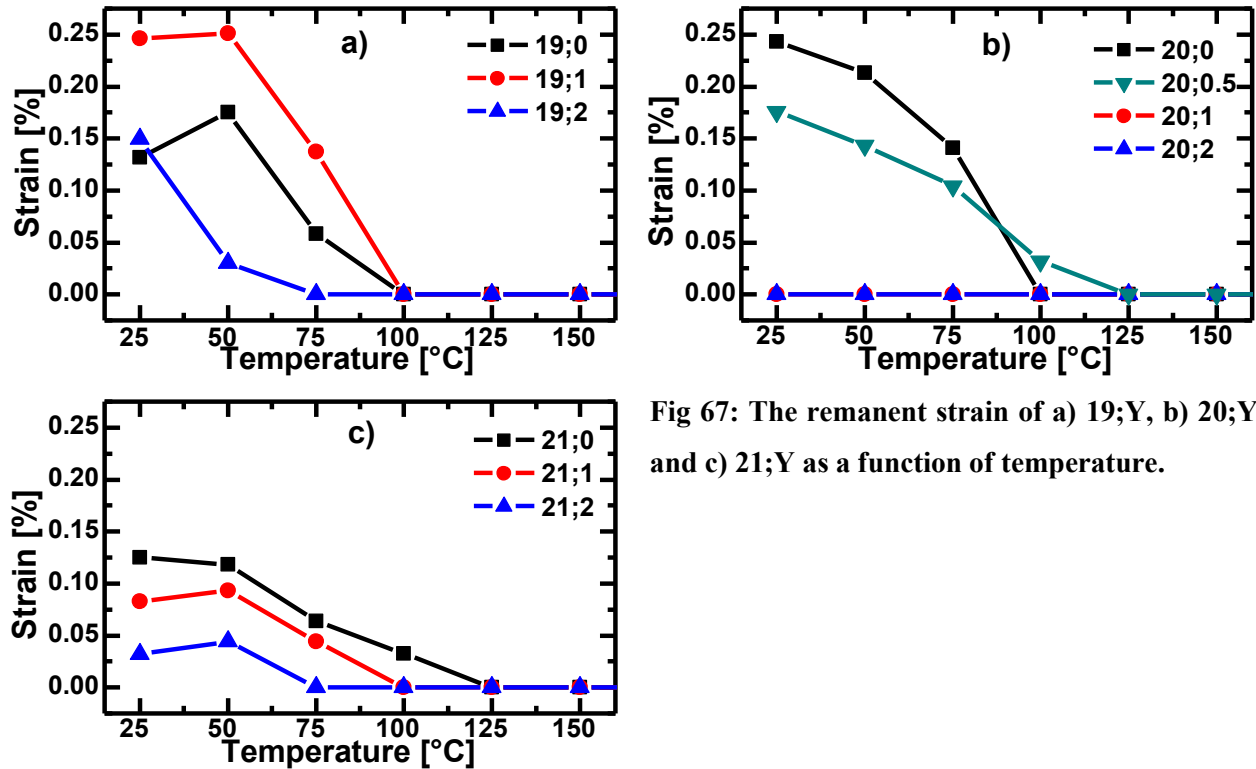


Fig 67: The remanent strain of a) 19;Y, b) 20;Y and c) 21;Y as a function of temperature.

The remanent strain for all 10 compositions was recorded as a function of temperature and is shown in Fig 67. Before each measurement, the sample was depoled at 450 °C for 15 minutes. The first two cycles were recorded at 4 kV/mm. The remanent strain, as reported, is the value when the electric field returns to zero for the first time after the first half of the cycle. Compositions 19;0 and 19;1 (Fig 67a) first show an increase in the remanent strain between 25 °C and 50 °C, after which the remanent strain continuously decreases reaching zero at 100 °C. Composition 19;2 shows no initial increase in the remanent strain but a continuous decrease to zero at 75 °C. Initially, the remanent strain values at room temperature are 0.13 %, 0.25 % and 0.15 % for compositions 19;0 to 19;2.

Compositions 20;0 and 20;0.5 (Fig 67b) start off at 0.24 % and 0.18 % at room temperature and continuously decrease to zero at 100 °C and 125 °C, respectively. Compositions 20;1 and 20;2 show no remanent strain at or above room temperature.

Compositions 21;0 to 21;2 (Fig 67c) initially show remanent strain of 0.12 %, 0.08 % and 0.03 % at room temperature. Compositions 21;1 and 21;2 show small increase in the remanent strain between room temperature and 50 °C. Afterwards, all 3 compositions show continuous decrease in remanent strain reaching zero at 125 °C, 100 °C, and 75 °C for compositions 21;0 to 21;2, respectively.

The graph of composition 21;0 at room temperature (Fig 68) shows the strain behaviour, which is typical for all compositions and temperatures where the remanent strain is non-zero. The first cycle (shown in black) is the one, from which the remanent strain value was taken (bottom blue dot).

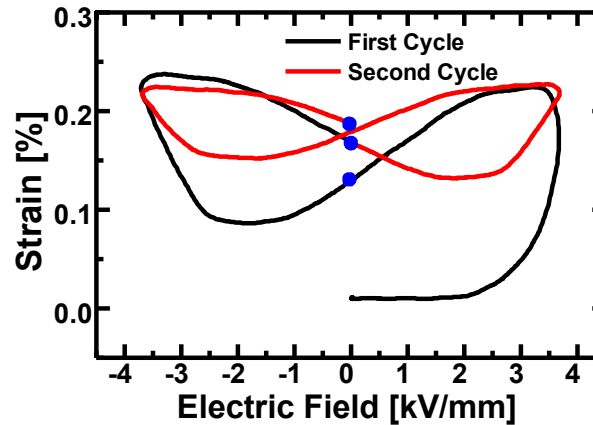


**Fig 68:** The first two strain versus electric field cycles recorded at room temperature for composition 21;0. The blue dots show the remanent strain values after 1/2 of a cycle (lowest), one full cycle (middle) and after two full cycles (top).

In all investigated compositions, which show a remanent strain, the remanent strain recorded after the first half cycle is lower than the value after a complete cycle or after two complete cycles. The example of 21;0 at room temperature shows 0.12 %, 0.17 % and 0.19 % at the mentioned cycle fractions. Furthermore, all these compositions show a much larger strain hysteresis during the second half of the first cycle in particular with a bipolar strain usually 50 % larger than found during the 2nd cycle. The remanent strain value after 2 cycles could not be evaluated reliably in most compositions, since the strongly asymmetric strain curves do not allow the detection of thermal drift and other measurement artefacts.

### 5.5.3 Temperature-Dependent Ferroelastic Properties

The ferroelastic properties of compositions 20;0 to 20;2 were investigated as a function of temperature between room temperature and 150 °C with the step size of 25 K. Before each measurement, the samples were annealed at 450 °C for 15 minutes. After the 200 °C step, each sample was measured again at room temperature to ensure, that no sample degradation had occurred. The results are shown in Fig 69 to Fig 72 for compositions 20;0 to 20;2 with the exception of the 200 °C step. A graphical summary of the maximum and remanent strain as well as the energy dissipated during one cycle can be found in Fig 73.

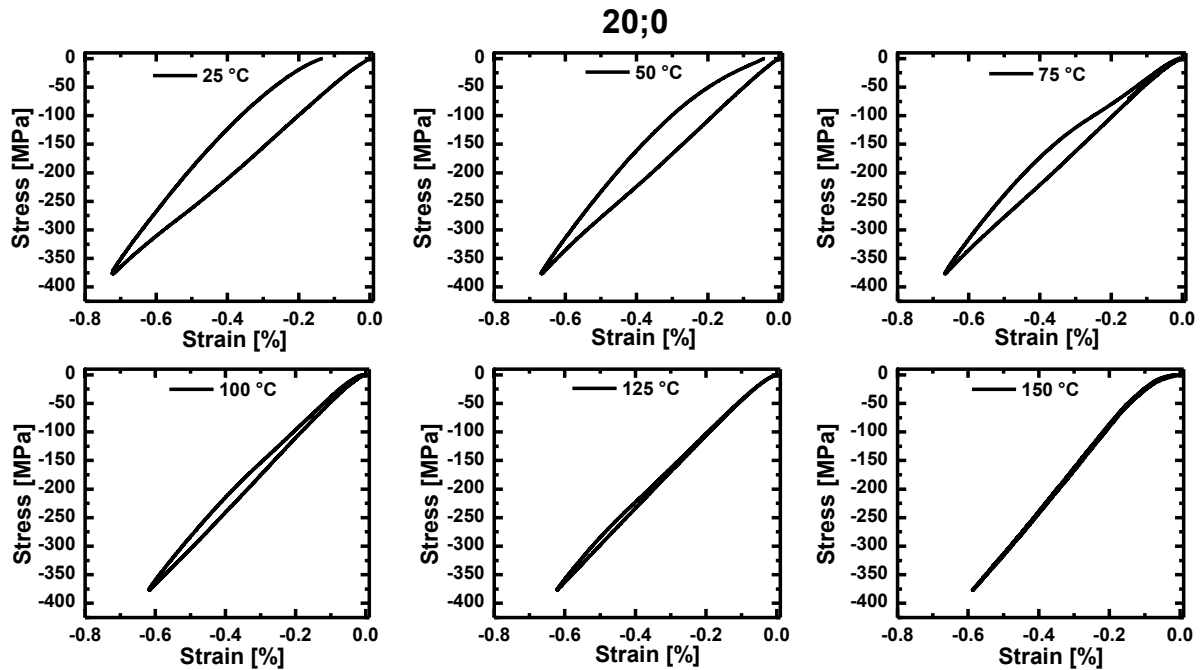


**Fig 69: Compressive strain versus applied stress at temperatures of 25 °C to 150 °C in steps of 25 K for composition 20;0.**

Composition 20;0 (Fig 69) shows a typical ferroelastic stress versus strain curve at room temperature. However, the onset stress<sup>38</sup>, where ferroelastic switching begins, as well as the coercive stress, cannot be reported, since the changes in the gradient are too small to reliably determine the inflection point<sup>38</sup>, which defines the coercive stress. It is likely that the onset stress<sup>38</sup> is too close to the maximum applicable stress and, therefore, the inflection point cannot be seen. At 50 °C, the return path of the strain curves for stresses above -50 MPa and the remanent strain is reduced. At 75 °C, the strain versus stress hysteresis is fully closed for stresses above -50 MPa but hysteresis is still visible between -375 MPa and -50 MPa. Between 100 °C and 150 °C the return path of the stress strain hysteresis becomes more and more linear and the area of the hysteresis smaller. At 150 and 200 °C, there is no more hysteresis and only purely

<sup>38</sup> A description, how the onset stress and coercive stress are determined can be found in Webber et al.<sup>[6]</sup>.

linear strain behaviour. The curvature of the strain path for stresses above -25 MPa is a result of sample misalignment, since the equipment was in an early stage of development, and/or dust was present on the sample surfaces.

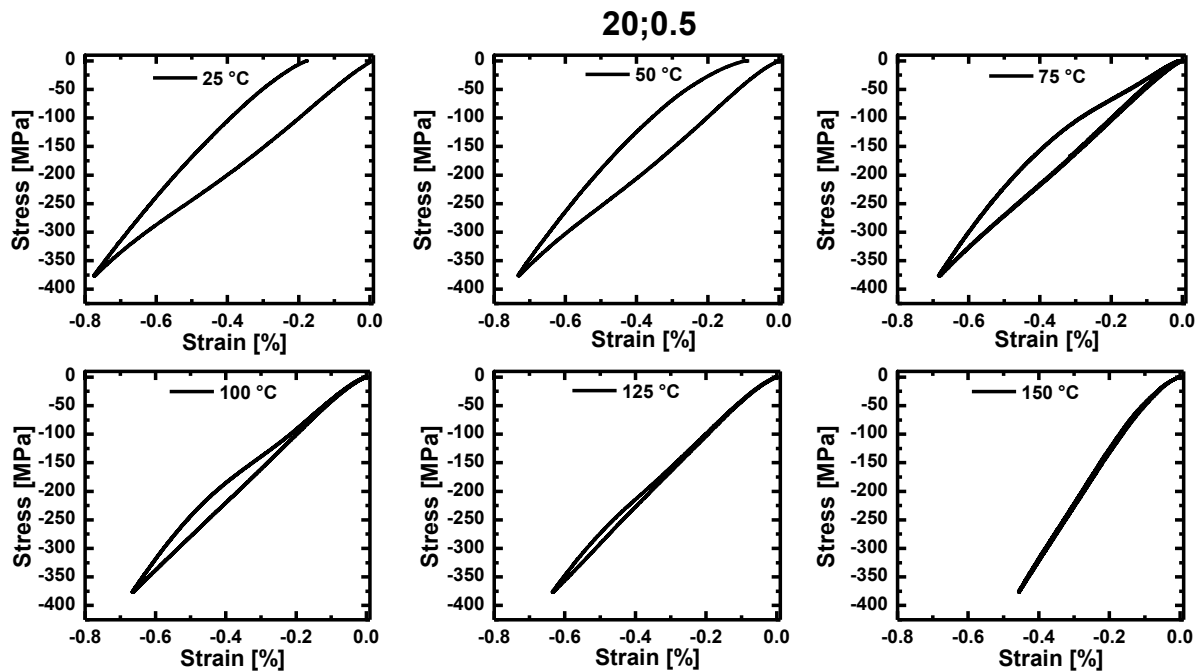


**Fig 70: Compressive strain versus applied stress at temperatures of 25 °C to 150 °C in steps of 25 K for composition 20;0.5.**

Composition 20;0.5 (Fig 70) shows a wider stress-strain hysteresis at room temperature with a larger remanent strain. The inflection point corresponding to the coercive stress can be seen between approximately -200 MPa and -300 MPa. Otherwise, the evolution of the shape with temperature is identical to composition 20;0 except that the area of the loop is larger in each case.

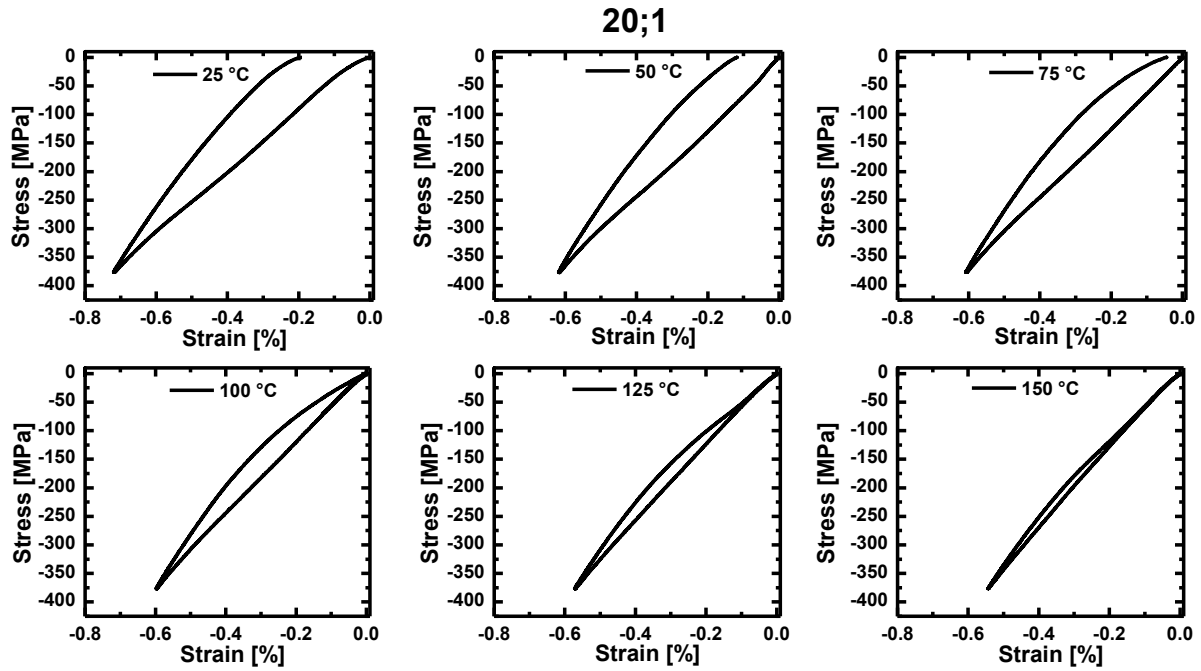


**Fig 71: Compressive strain versus applied stress at temperatures of 25 °C to 150 °C in steps of 25 K for composition 20;1.**

Composition 20;1 (Fig 71) shows all significant changes in the shape at higher temperatures compared to 20;0.5. The loop is still not fully closed at 75 °C; there is remanent strain. Also, there is still a small hysteresis at 150 °C. The behaviour at 200 °C is, however, purely linear.

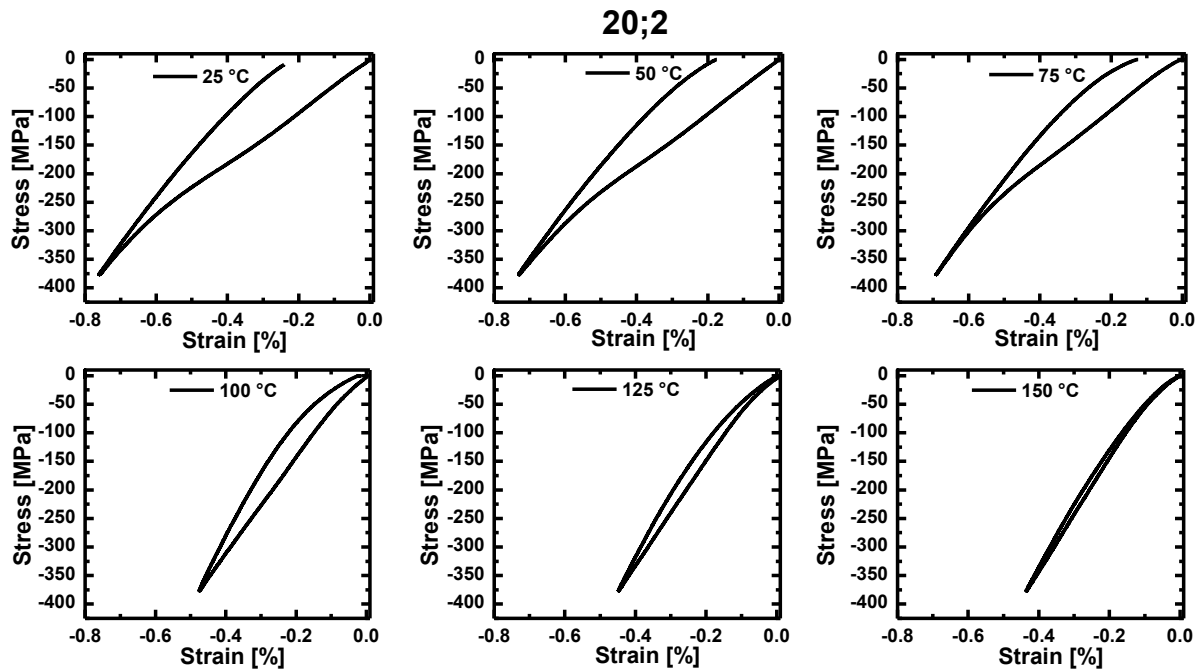


**Fig 72: Compressive strain versus applied stress at temperatures of 25 °C to 150 °C in steps of 25 K for composition 20;2.**

Composition 20;2 (Fig 72) still shows remanent strain at 100 °C and hysteretic behaviour at 150 °C. The stress strain curves at 200 °C is again completely linear.

A graphical summary (Fig 73) of the actual values of the previously described stress strain hystereses shows that the maximum strain at room temperature decreases continuously from -0.72 %, -0.77 %, -0.72 % and -0.75 % for compositions 20;0 to 20;2, respectively reaching -0.57 %, -0.42 %, -0.50 % and -0.40 % at 200 °C. The remanent strain values at room temperature are -0.14 %, -0.18 %, -0.19 % and -0.24 % in order of ascending KNN-BKT content and linearly reaches zero at 75 °C, 75 °C, 100 °C and 125 °C.

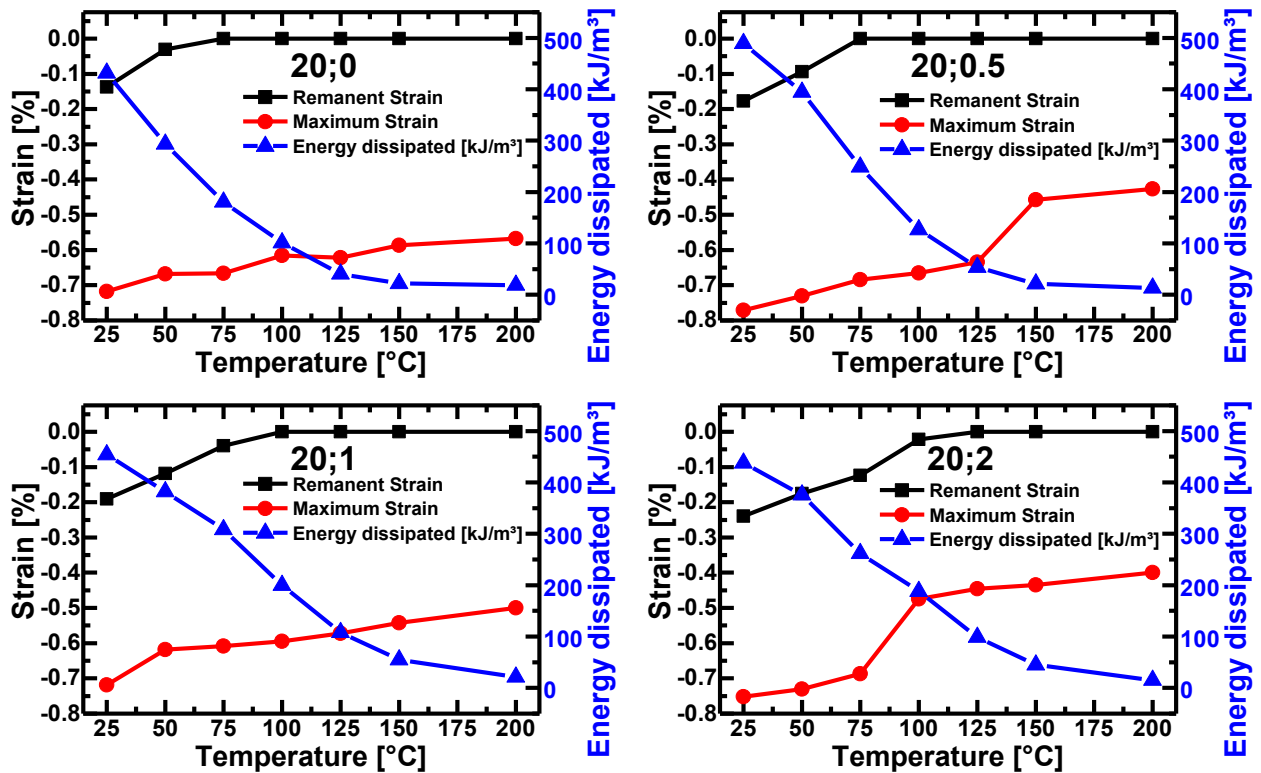


Fig 73: Summary of the maximum and remanent strain and the energy dissipated during the cycle for compositions 20;0 to 20;2.

The energy dissipated during one stress strain cycle between 25 MPa and 385 MPa is highest at room temperature with 430 kJ/m<sup>3</sup>, 490 kJ/m<sup>3</sup>, 450 kJ/m<sup>3</sup> and 440 kJ/m<sup>3</sup> for compositions 20;0 to 20;2 in ascending order. The energy dissipation per cycle of compositions 20;0 and 20;0.5 reduces to 22 kJ/m<sup>3</sup> and 21 kJ/m<sup>3</sup> at 150 °C then remains almost constant with 19 kJ/m<sup>3</sup> and 13 kJ/m<sup>3</sup> at 200 °C. In compositions 20;1 and 20;2, however, the energy dissipation is still twice as high at 150 °C with 55 kJ/m<sup>3</sup> and 45 kJ/m<sup>3</sup> compared to the 200 °C value of 21 and 15 kJ/m<sup>3</sup>.

### 5.5.4 Temperature-Dependent Permittivity and Loss

The loss and capacitance for all 10 compositions were recorded as a function of temperature and frequency. From the capacitance, the material parameter „relative permittivity“ was then calculated. The programmed temperature range was originally between room temperature and 500 °C. However, subsequent investigation with a thermocouple revealed that the actual temperature at that position of the sample was accurate at room temperature but was in fact 0.20 K lower per 1 K increase recorded. Since the deviation was linear, the actual temperature range was up to approximately 400 °C only. The results are shown in Fig 74, Fig 75 and Fig 76 for compositions 19;0 to 19;2, 20;0 to 20;2 and 21;0 to 21;2.

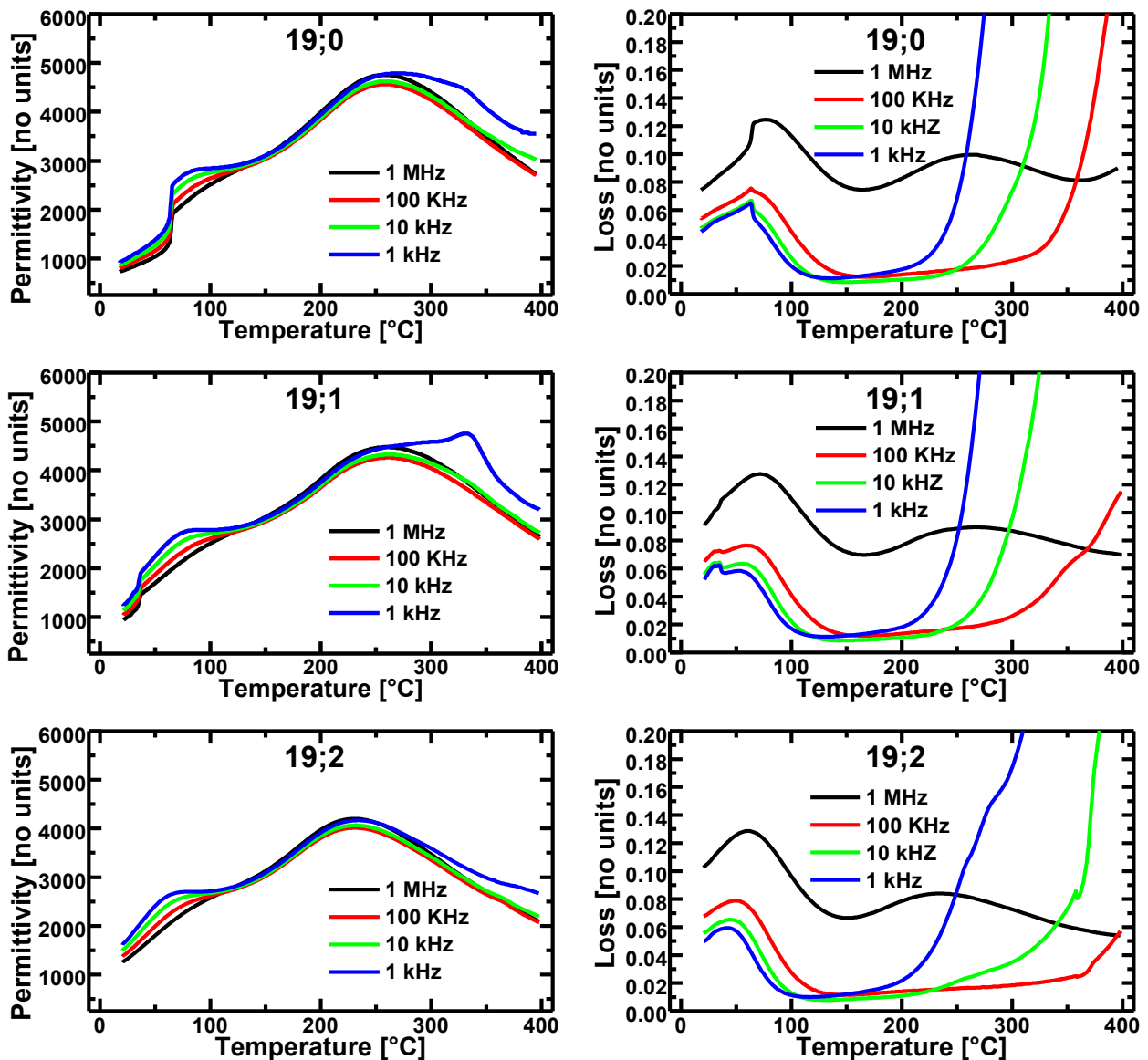


Fig 74: The dielectric permittivity and loss for compositions 19;0 to 19;2 from room temperature to 400 °C recorded every order of magnitude between 1 kHz and 1 MHz.



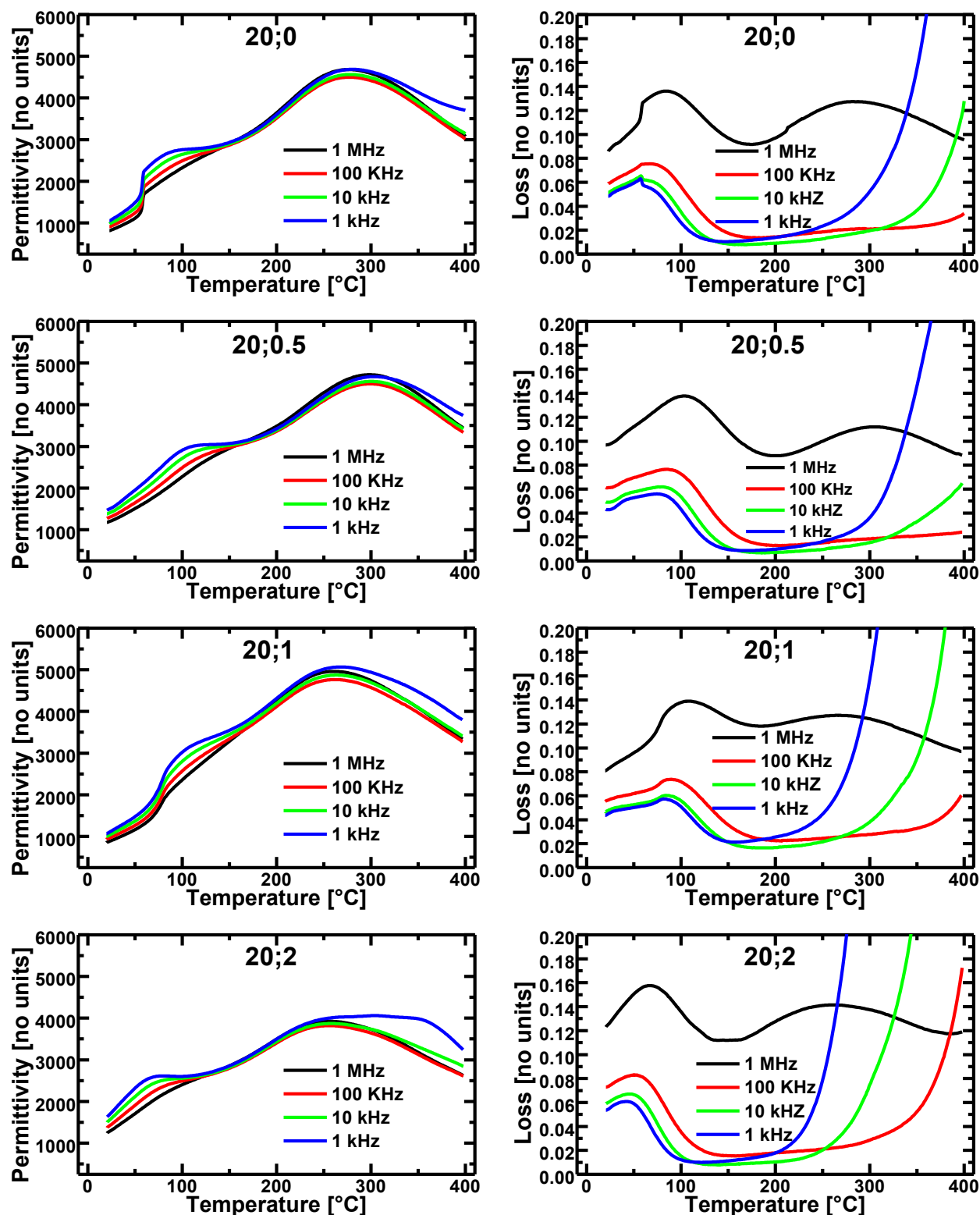


Fig 75: The dielectric permittivity and loss for compositions 20;0 to 20;2 from room temperature to 400 °C recorded every order of magnitude between 1 kHz and 1 MHz.

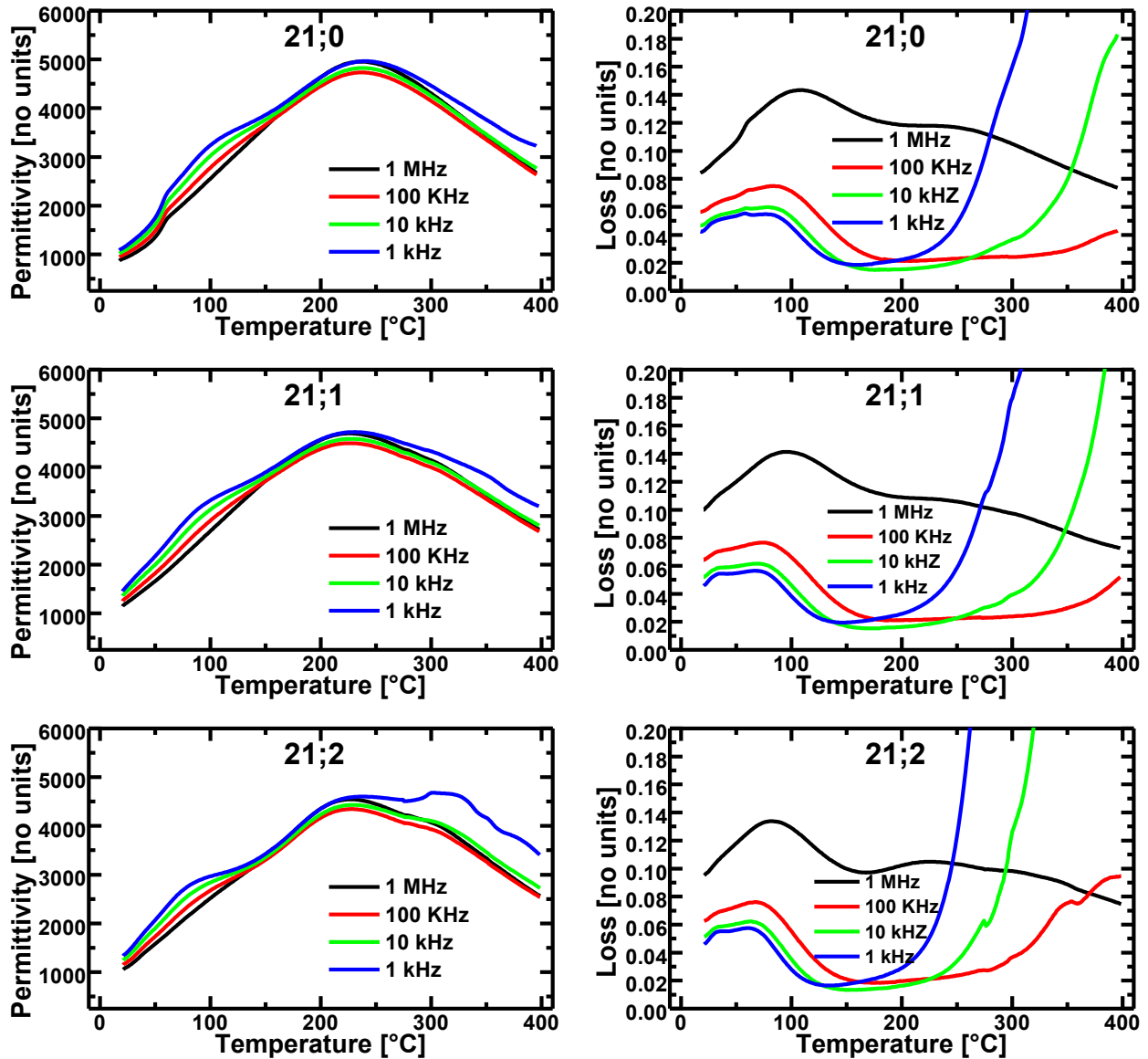


Fig 76: The dielectric permittivity and loss for compositions 21;0 to 21;2 from room temperature to 400 °C recorded every order of magnitude between 1 kHz and 1 MHz.

Since there are a lot of similarities, compositions 19;0 to 19;2 (Fig 74) will be used to describe all the relevant features common to all compositions of the permittivity versus temperature and the loss versus temperature graphs. Looking at the permittivity graphs of composition 19;0, a gradual increase in the permittivity with temperature can be seen at first. At 65 °C, there is a sudden jump in the permittivity with the corresponding jump in the dielectric loss, which corresponds to the depolarisation temperature ( $T_d$ ). In composition 19;2, no such jump is visible. However, independent of whether a depolarisation temperature can be identified, all 10 compositions show a local maximum/peak between about 70 °C and 110 °C labelled  $T_2$ . This local maximum shows a frequency dispersion and is also accompanied by a frequency dispersive maximum in the dielectric loss. This local maximum is followed by the absolute maximum

permittivity ( $\epsilon_M$ ) at the temperature ( $T_M$ ) between about 220 and 300 °C. This temperature as well as the absolute value of the permittivity is almost completely independent of frequency. The loss values decrease and remain low above  $T_2$  and to just above 200 °C first the 1 kHz dielectric loss rises sharply, followed by the 10 kHz and 100 kHz loss at higher temperatures owing to increasing conductivity. Similarly, the deviation of the 1 kHz dielectric permittivity at temperatures above 300 °C, which even shows as a local maximum in compositions 19;1 (Fig 74), 20;2 (Fig 75) and 21;2 (Fig 76), is just an artefact due to equipment limitations. The actually temperatures of  $T_d$ ,  $T_2$ ,  $T_M$  as well as the room temperature loss, room temperature dielectric permittivity and the maximum permittivity, all collected from the 1 kHz measurement, can be found in Tab 18 below.

**Tab 18: Summary of Temperature-Dependent Permittivity and Loss Data**

Composition	$T_d$ [°C]	$T_2$ [°C]	Loss [%]	$T_M$ [°C]	$\epsilon(RT)$ [rel.]	$\epsilon_M$ [rel.]
19;0	64.9	78.8	4.5	259	960	4769
19;1	35.2	74.8	5.2	260	1219	4476
19;2	--	68.9	5.0	230	1607	4210
20;0	57.6	84.9	4.8	277	1051	4698
20;0.5	27.2	109.9	4.3	303	1470	4721
20;1	--	101.0	4.4	266	1063	5066
20;2	--	72.0	5.4	252	1627	3999
21;0	--	108.8	4.2	237	1082	4977
21;1	--	93.9	4.6	227	1453	4716
21;2	--	84.9	4.6	224	1329	4586

**-If  $T_d$  is not reported, it was below the minimum temperature of the setup (room temperature).**  
**-All values were collected from the 1 Hz measurement cycle.**

The depolarisation temperature is reduced with the introduction of KNN-BKT, similarly the temperature  $T_2$  with the exception of 20;0, which is lower than the others of its series. The loss varies randomly between 4.2 and 5.2 %.  $T_M$  decreases with KNN-BKT content again with the exception of composition 20;0. For pure BNT-xBKT the room temperature dielectric permittivity increases with increasing BKT content.  $T_M$  is highest at BNT-20BKT content independent of KNN-BKT content and drops off towards either higher or lower xBKT content (Fig 77).

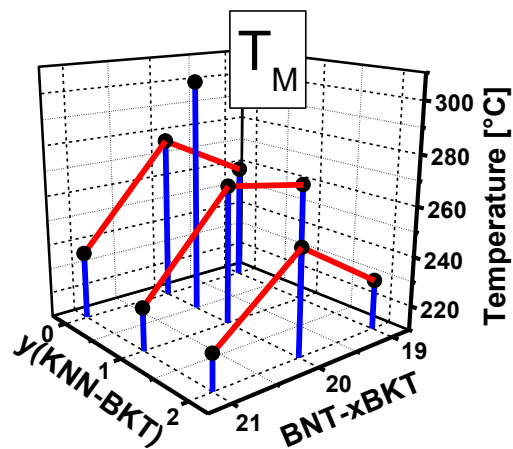


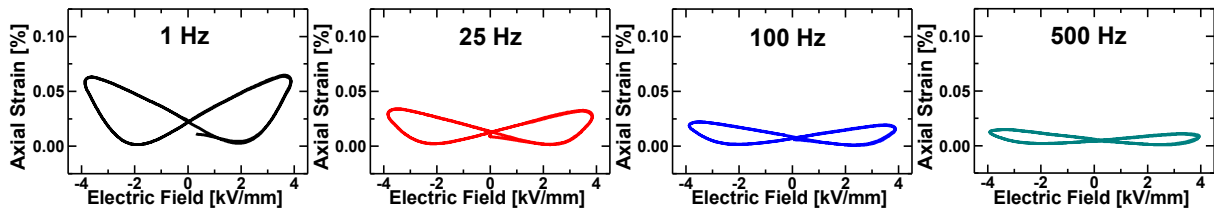
**Fig 77: Variation of  $T_M$  with composition**

## 5.6. Frequency-Dependent Large-Signal Behaviour

The frequency dependence of the bipolar large-signal strain and polarisation for frequencies up to 500 Hz was investigated. Since it had previously been determined that the natural frequency of the optical strain sensor was approximately 3000 Hz, it can be assumed that the setup will provide accurate measurements in the selected frequency range. Depending on the maximum polarisation of the samples investigated, the setup was also limited to between 250 Hz and 500 Hz by the current limit of the power supply. Whether such a limit is reached, can be identified by comparing the input and control signal of the power supply. If a deviation was found, the sample surface area was reduced to about one quarter of the original size by drilling out disk-shaped samples of 3.8 mm diameter. Since that reduces the diameter to thickness ratio to below 10:1, the absolute polarisation values given should not be considered, but rather the change with frequency. All measurements were done with a maximum field of 4 kV/mm. The dielectric permittivity of each sample was recorded at the same frequencies except 50 mHz. Again, for the reasons given above, only relative values should be considered.

### 5.6.1 Bipolar Strain

20;0



20;2

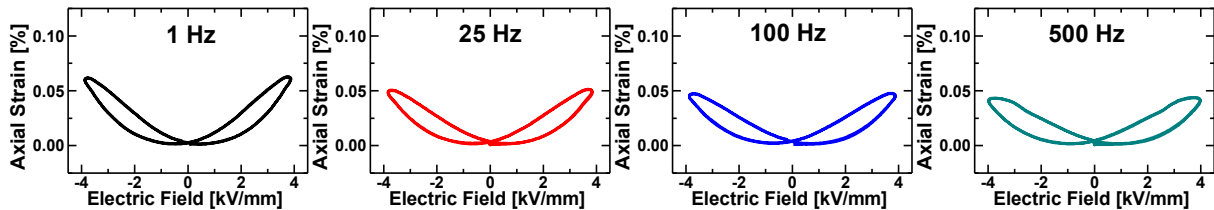


**Fig 78: Bipolar large-signal strain evolution with frequency at 4 kV/mm for compositions 20;0 and 20;2 between 1 Hz and 500 Hz.**

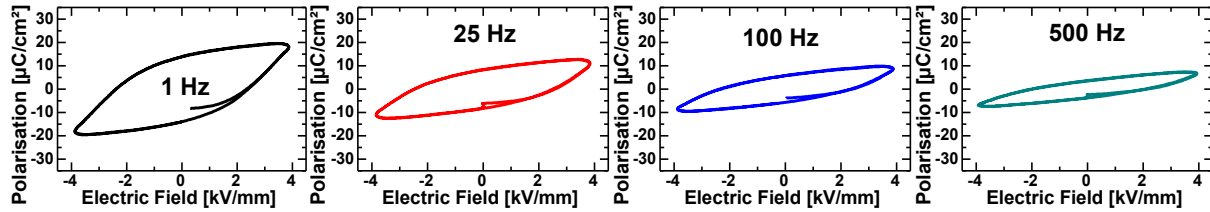
The strain evolution with frequency for the ferroelectric and non-ferroelectric materials is shown at the example of composition 20;0 and 20;2 in Fig 78. In the case of composition 20;0 the total strain decreases by 600 % between 1 Hz cycle and the 500 Hz cycle. The ratio of positive to negative strain remains constant with frequency. The general shape is maintained with the exception of the increasing electric field value of the minimum strain (maximum negative strain).

The turning points at the maximum and minimum strain values become more rounded with increasing frequency.

Composition 20;2 represents the typical strain behaviour of the non-ferroelectric compositions. Its maximum total strain decreases by only 50 % between 1 Hz and 500 Hz. The strain path on the rising flank of the electric field remains flatter at low fields strengths when the frequency increases. The shape of the return strain path from the maximum field value to zero is independent of frequency. Both effects in combination lead to a larger area of the strain hysteresis at higher frequencies.

## 5.6.2 Polarisation

20;0



20;2

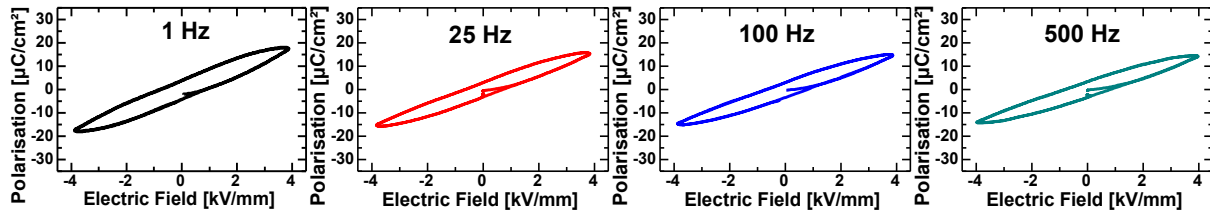


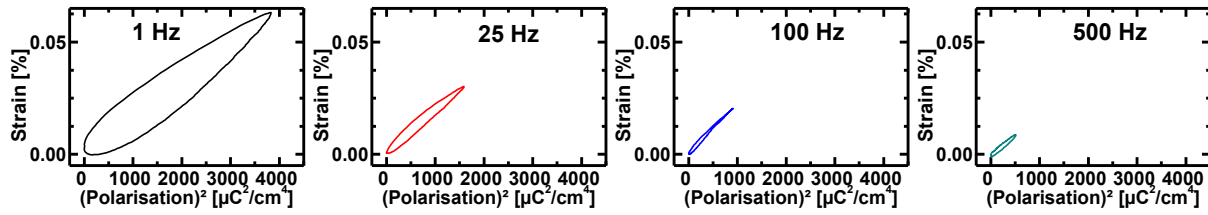
**Fig 79: Bipolar large-signal polarisation evolution with frequency at 4 kV/mm for compositions 20;0 and 20;2 between 1 Hz and 500 Hz.**

The frequency evolution of the polarisation of composition 20;0 and 20;2 between 1 Hz and 500 Hz is shown in Fig 79. With increasing frequency the polarisation loop of composition 20;0 flattens. Maximum and remanent polarisation decreased by 350 and 500 %, respectively, between 1 Hz and 500 Hz. The coercive field also visibly increases with frequency but since the maximum electric field is less than twice the coercive field no absolute values can be cited.

The shape of the polarisation hysteresis of composition 20;2 remains unchanged with increasing frequency. Maximum and remanent polarisation decreased proportionately by 25 % between 1 Hz and 500 Hz.

### 5.6.3 Bipolar Strain Versus Square of Polarisation

20;0



20;2

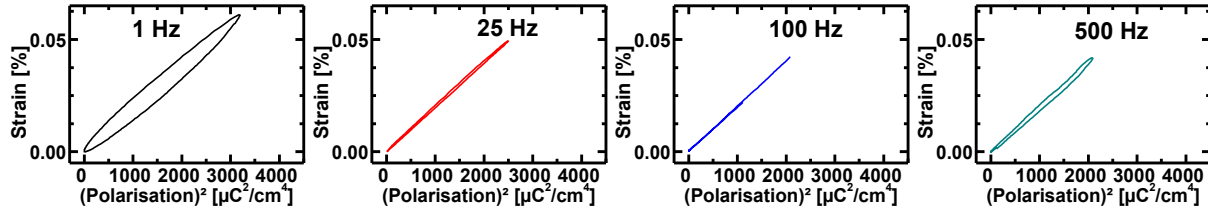


**Fig 80: Strain vs. square of polarisation evolution with frequency at 4 kV/mm for compositions 20;0 and 20;2 between 1 Hz and 500 Hz.**

The strain versus the square of the polarisation was plotted as a function of frequency to investigate differences in the strain evolution compared to the polarisation evolution. The graphs in Fig 80 shows the behaviour of compositions 20;0 and 20;2, which is exemplary for the ferroelectric and non-ferroelectric materials investigated. Composition 20;0 shows a hysteresis, which is symmetric along the line connecting the lowest and highest square of polarisation value. This symmetry is broken at 25 Hz. While the shape of the return path is maintained, the rising path (lower path) becomes more linear. This behaviour is maintained at higher frequencies. Composition 20;2 shows that the hysteresis is reduced between 1 Hz and 25 Hz. There is no measurable hysteresis at 100 Hz. The slight hysteresis at 500 Hz may be an equipment limitation. The slope of the line fitted through all graphs, which corresponds to the electrostrictive coefficient, is constant with frequency for compositions.

#### 5.6.4 Summaries of Frequency-Dependent Strain and Polarisation

The frequency-dependent large-signal strain behaviour of all 10 compositions is summarised for frequencies between 50 mHz and 500 Hz on the left of Fig 81 to Fig 83 combined with the low frequency permittivity. The right side of Fig 81 to Fig 83 show the corresponding maximum and remanent polarisation and the coercive field. The data for composition 19;1 was replaced with an earlier dataset, since the original sample was later found to be defective.

All compositions show a different degree of frequency dependence of the measured quantities. Since the behaviour of most compositions is qualitatively similar, not all compositions will be described in detail but only their deviations from the behaviour of composition 19;0 will be pointed out. A quantitative description of the results is given later.

Composition 19;0 (Fig 81) shows a proportional decrease of the total and the positive strain with frequency relative to one another. The positive and the total strain show a logarithmic decrease with frequency, i.e. linear with the logarithm of the frequency. Maximum and remanent polarisation also decrease in the same fashion. The low frequency permittivity also shows a logarithmic decrease for frequencies above 5 Hz. Below 5 Hz, the measurement was influenced by conductivity. The coercive field initially increases with frequency and then drops off again at higher frequencies.

Compositions 19;1 and 19;2 show equivalent behaviour. The non-linear increase in the maximum and remanent polarisation as well as the coercive field and permittivity in composition 19;2 are again conductivity artefacts.

Compositions 20;0, 20;0.5 (Fig 82) and 21;0 (Fig 83) also show the same general behaviour in all measured quantities. Composition 21;1 (Fig 83) shows a purely logarithmic increase of the coercive field with frequency across the measurement range. All other quantities vary as described above for the other compositions.

Compositions 20;1 and 20;2 (Fig 82) as well as 21;2 (Fig 83) show a nearly frequency independent (very small) remanent polarisation above 25 Hz. The higher remanent and maximum polarisation values of the latter two compositions and composition 19;2 are conductivity artefacts due to an electric breakdown in the strain sensor, which caused the leakage current and which could not be repaired in time.

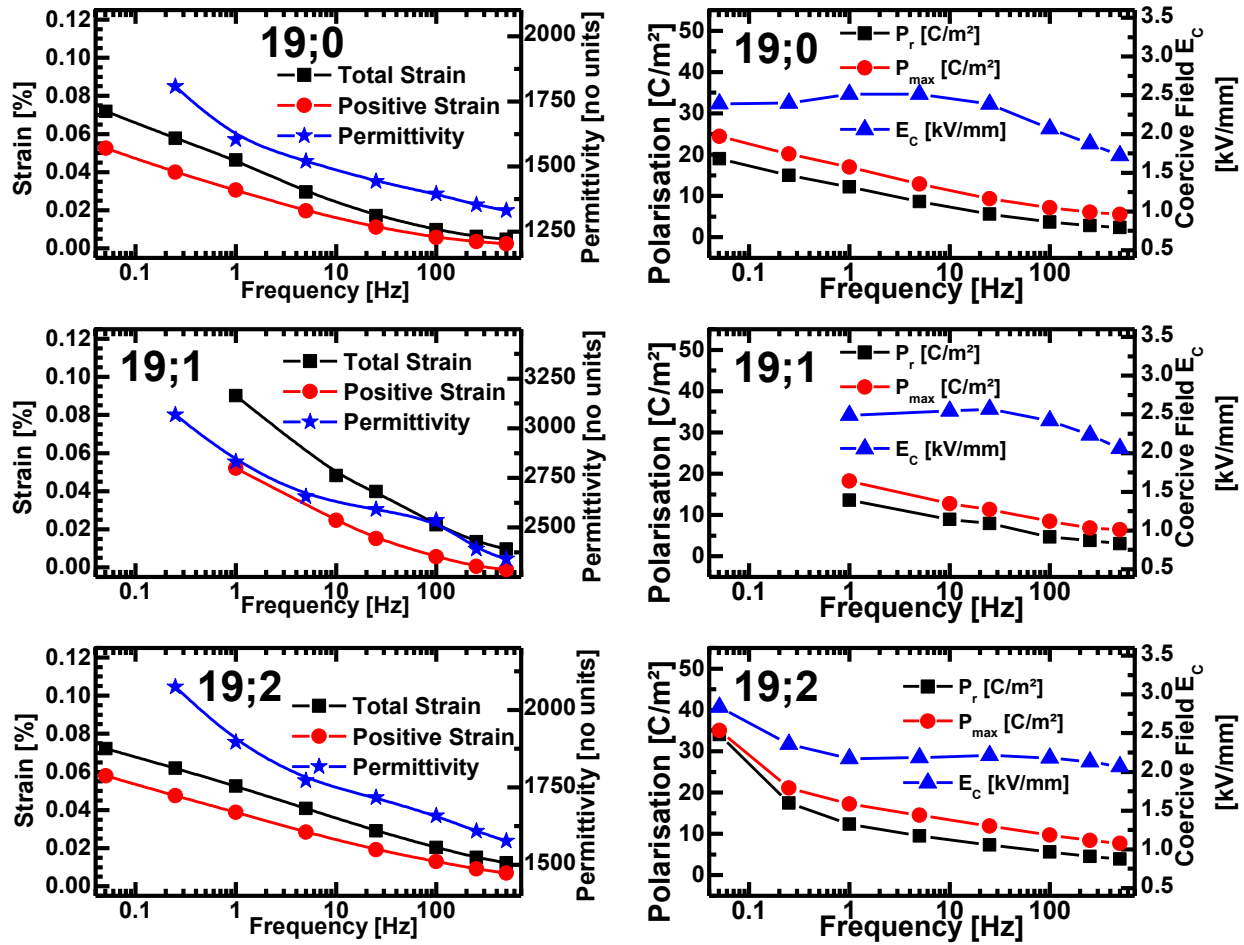


Fig 81: The frequency dependence of permittivity, positive and total bipolar strain of compositions 19;0, 19;1 and 19;2 are shown on the left. On the right, the frequency dependence of the maximum polarisation, remanent polarisation and the coercive field is shown.

The quantitative analysis of the strain and polarisation revealed purely logarithmic behaviour with frequency if conductivity artefacts are excluded. The coercive field also linearly increases with the logarithm of the frequency, for as long as the coercive field is less than half the maximum applied field. In order to quantify the changes with frequency, the percentage of the total strain, maximum polarisation and remanent polarisation remaining at 100 Hz was calculated with respect to be 1 Hz values. This quantity is summarised in Tab 19.

Composition 19;0 shows 21 % of the strain measured at 1 Hz is still remaining at 100 Hz. At the same time 35 % of the maximum polarisation and 24 % of the remanent polarisation remain. Composition 19;1 and 19;2 show 25 % and 39 % of the strain remaining combined with a remaining maximum polarisation of 46 % and 56 % and the remanent polarisation of 35 % and 45 % each.



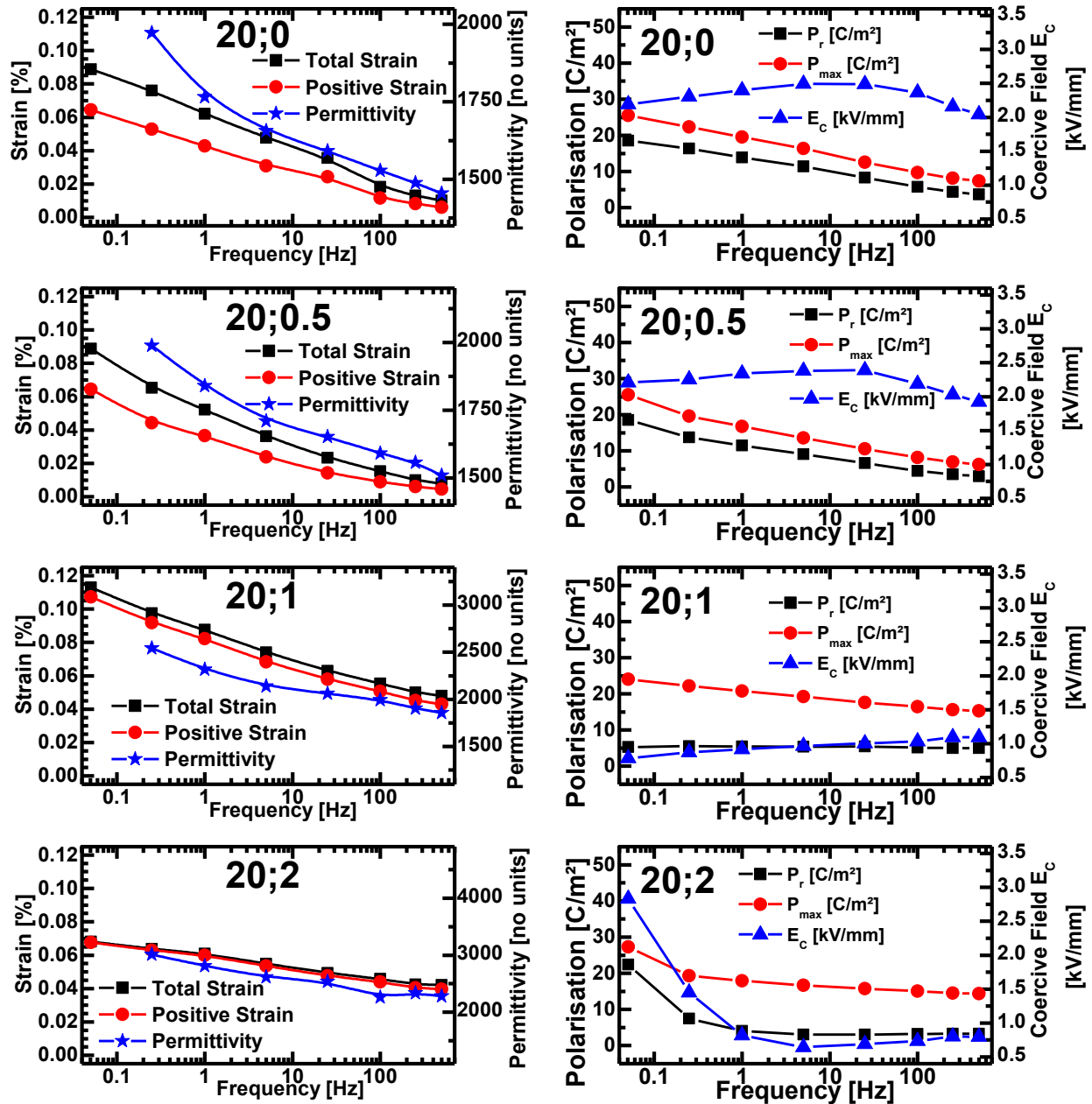


Fig 82: The frequency dependence of permittivity, positive and total bipolar strain of compositions 20;0, to 20;2 are shown on the left. On the right, the frequency dependence of the maximum polarisation, remanent polarisation and the coercive field is shown.

Between composition 20;0 and 20;0.5 there is a drop in total strain, maximum polarisation and remanent polarisation from 29 %, 50 % and 41 % to 21 %, 48 % and 31 % remaining at 100 Hz, respectively. Between composition 20;1 and 20;2, the total strain increases from 29 % to 63 % with the corresponding increase in maximum polarisation from 79 % to 87 % remaining at 100 Hz compared to the respective 1 Hz values. Composition 20;1 shows that the remanent polarisation at 100 Hz is 94 % of the value measured at 1 Hz. The remanent polarisation of composition 20;2 is too low to make an accurate assessment of a frequency stability.

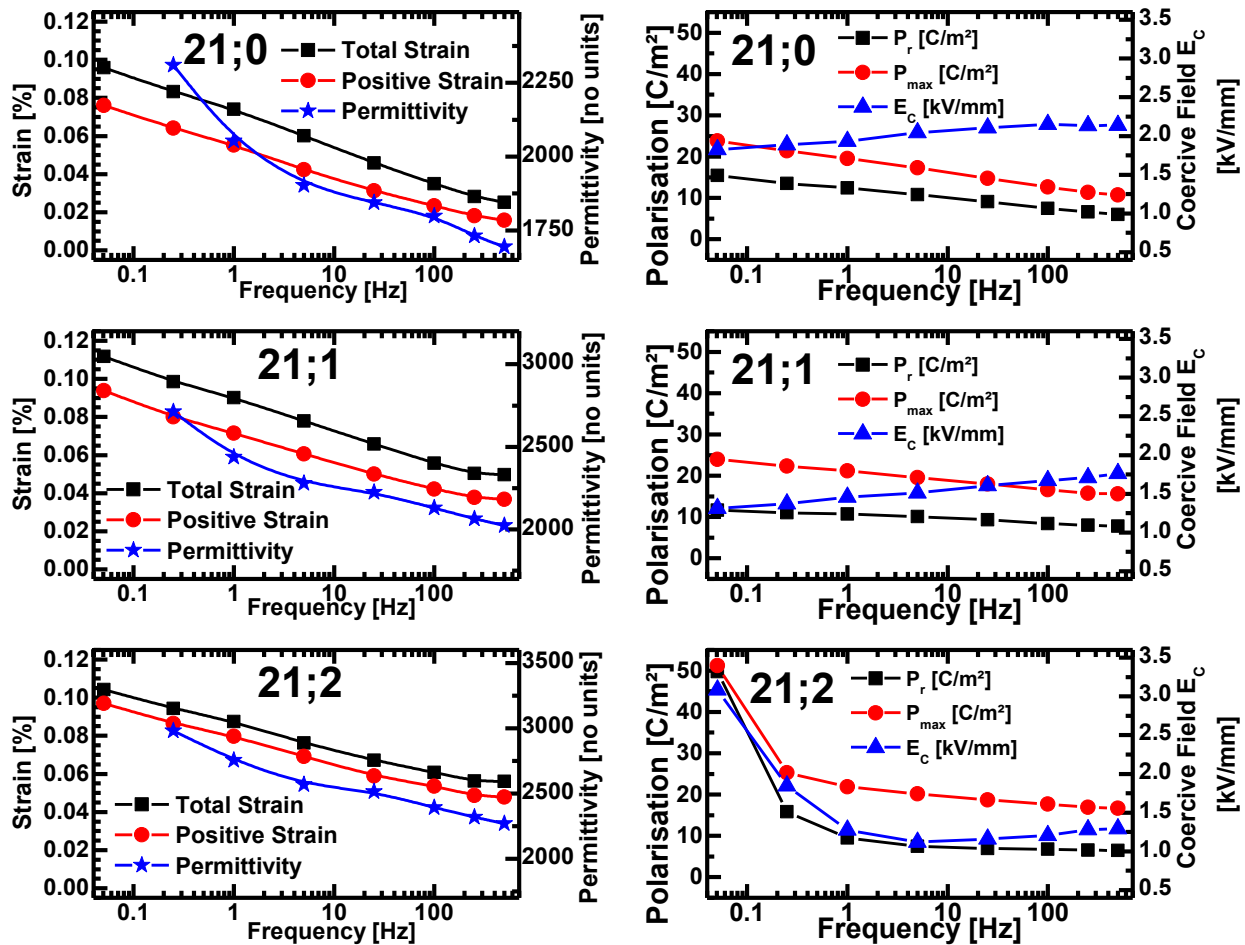


Fig 83: The frequency dependence of permittivity, positive and total bipolar strain of compositions 21;0, 21;1 and 21;2 are shown on the left. On the right, the frequency dependence of the maximum polarisation, remanent polarisation and the coercive field are shown.

Composition 21;0 shows the highest remaining total strain, maximum polarisation and remanent polarisation of all pure BNT-xBKT materials. The maximum and remanent polarisation again increased with increasing KNN-BKT content. The values of composition 21;2 were still influenced by conductivity at 1 Hz. Therefore, the interval between 5 Hz and 500 Hz was taken instead. Composition 21;1 shows the highest frequency stability, i.e. the largest remaining strain after a two order of magnitude frequency increase of all ferroelectric compositions. When the conductivity artefacts are removed composition 21;2 shows the highest remaining strain out of all ferroelectric and non-ferroelectric compositions at 69 % accompanied by at least 87 % and 82 % remaining maximum and remanent polarisation.

**Tab 19: Change in Strain and Polarisation with Frequency**

<b>Composition</b>	<b>Total strain at 100 Hz [% of 1 Hz value]</b>	<b>Maximum polarisation at 100 Hz [% of 1 Hz value]</b>	<b>Remanent polarisation at 100 Hz [% of 1 Hz value]</b>
19;0	21	35	24
19;1	25	46	35
19;2	39	56	45
20;0	29	50	41
20;0.5	21	48	31
20;1	29	79	94
20;2	63	87	78*
21;0	55**	64	53
21;1	62	78	78
21;2	69	87***	82***

\* The absolute values are so close to zero that the error is +/- 25 percentage points. The actual value is likely between 90 and 100 %.

\*\* 250 mHz to 25 Hz range selected due to measurement artefact at 1 Hz.

\*\*\* The low frequency conductivity causes the 1 Hz  $P_{\max}$  and  $P_r$  to be artificially increased, which in turn makes the ratio with the respective 100 Hz values to be lower than they otherwise should be. Therefore, the interval between 5 Hz and 500 Hz was taken instead.

The summary of the results in Tab 19 shows that the pure BNT-xBKT materials are most strongly frequency-dependent. The remaining strain and polarisation is lowest in composition 19;0 and increases as a function of increasing xBKT content and increasing KNN-BKT content for all ferroelectric compositions. In the ferroelectric compositions, the remanent polarisation always decreases faster with frequency than the maximum polarisation. The remanent polarisation of the non-ferroelectric compositions 20;1, 20;2 and 21;2 appears almost independent of frequency. However, since the remanent polarisation of the three materials is only 3 to 5 times higher than the signal-to-noise ratio of the equipment, this cannot be said with certainty.

## 5.7. References

- [1] R. Zuo, X. Fang, and C. Ye, "Phase structures and electrical properties of new lead-free  $(\text{Na}_{0.5}\text{K}_{0.5})\text{NbO}_3$ - $(\text{Bi}_{0.5}\text{Na}_{0.5})\text{TiO}_3$  ceramics," *Applied Physics Letters*, **90**[9] 092904-3 (2007).
- [2] A. Sasaki, T. Chiba, Y. Mamiya, and E. Otsuki, "Dielectric and piezoelectric properties of  $(\text{Bi}_{1/2}\text{Na}_{1/2})\text{TiO}_3$ - $(\text{Bi}_{0.5}\text{K}_{0.5})\text{TiO}_3$  systems," *Japanese Journal of Applied Physics Part 1-Regular Papers Short Notes & Review Papers*, **38**[9B] 5564-7 (1999).
- [3] A. B. Kouna, S.-T. Zhang, W. Jo, T. Granzow, and J. Rödel, "Morphotropic phase boundary in  $(1-x)\text{Bi}_{0.5}\text{Na}_{0.5}\text{TiO}_3$ - $x\text{K}_{0.5}\text{Na}_{0.5}\text{NbO}_3$  lead-free piezoceramics," *Applied Physics Letters*, **92**[22] 222902-3 (2008).
- [4] R. Zuo, X. Fang, C. Ye, and L. Li, "Phase Transitional Behavior and Piezoelectric Properties of Lead-Free  $(\text{Na}_{0.5}\text{K}_{0.5})\text{NbO}_3$ - $(\text{Bi}_{0.5}\text{K}_{0.5})\text{TiO}_3$  Ceramics," *Journal of the American Ceramic Society*, **90**[8] 2424-8 (2007).
- [5] V. Dorcet and G. Trolliard, "A transmission electron microscopy study of the A-site disordered perovskite  $\text{Na}_{0.5}\text{Bi}_{0.5}\text{TiO}_3$ ," *Acta Materialia*, **56**[8] 1753-61 (2008).
- [6] K. G. Webber, Y. Zhang, W. Jo, J. E. Daniels, and J. Rödel, "High temperature stress-induced "double looplike" phase transitions in Bi-based perovskites," *Journal of Applied Physics*, **108**[1] 014101 (2010).

## 6. Discussion

### 6.1. Concepts for the Development of New Lead-Free Ferroelectrics

In chapter 3.2, a number of considerations and concepts were introduced, which can form the basis of a search for new lead-free ferroelectrics. Some general considerations, such as toxicity, material availability and price provide a convenient start towards limiting the element choices before more complex investigations are required.

The choice of starting materials according to the above-mentioned criteria should be regularly subjected to re-evaluation. Misconceptions, such as the previously perceived toxicity of bismuth, are likely not unique. Already much more difficult is the decision whether a material should be considered hazardous or not. Silver and copper as well as their respective oxides are, for example, considered non-toxic but almost all other silver salts are toxic and the usage of copper in cookware is hazardous to children.

Based on this choice of elements, a number of search concepts were introduced. High temperature  $\text{BiMeO}_3\text{-PbTiO}_3$  materials have shown the potential of bismuth and Jahn-Teller active ions in improving phase transition temperatures. While it was found that simply replacing lead with barium is not a viable solution, restricting oneself to either two barium or two bismuth-based end members may yet prove successful.

The potential of barium copper tungstenate and barium copper niobate has not yet been fully investigated. The conductivity of copper and similarly its poor sinterability is often mentioned as the limiting factor. This conductivity is the result of some  $\text{Cu}^{1+}$  found in the material, which  $\text{Cu}^{2+}$  that was reduced during sintering. Similar issues are also found in  $\text{BiFeO}_3\text{-PbTiO}_3$  ( $\text{Fe}^{3+}$  with some  $\text{Fe}^{2+}$ )<sup>[1]</sup>, where they are frequently the focus of research purely because its relation with  $\text{PbTiO}_3$  makes it appear more appealing. There is only been one serious attempt to address these issues in barium copper niobate so far<sup>[2]</sup>, which already proved the existence of ferroelectricity in barium copper niobate.

A number of unexplored avenues have been presented to create further lead-free perovskite structures by replacing single ions in a non-lead-free material such as BNT with a combination of other ferroelectrically active or Jahn-Teller active ions.

Doping to increase the phase transition temperatures of existing materials is a futile exercise in most instances, since the materials with the highest purity will also usually have the highest

phase transition temperatures. To overcome this issue, doping materials have to be selected, which form or would form compositions with similar structures with higher phase transition temperatures, if they existed.

Identifying morphotropic phase boundaries between newly developed materials and already known similar systems is the logical next step in enhancing ferroelectric properties. Preliminary investigations into combining  $\text{Bi}(\text{X},\text{Y})\text{O}_3$  with  $\text{BaTiO}_3$ ,  $\text{Ba}(\text{Cu}_{1/2}\text{W}_{1/2})\text{O}_3$ ,  $\text{Ba}(\text{Cu}_{1/3}\text{Nb}_{2/3})\text{O}_3$  have revealed a number of conditions, which would increase the success rate of such an endeavour. The number of different ions should be as few as possible to reduce likelihood of secondary phases and to minimise relaxor-type behaviour. Choosing new end members, which are stable on their own account increases the likelihood that a large percentage of the newly developed MPB composition can consist of the new end members, when mixed with known ferroelectric end members. The tolerance factor of the new end members should be chosen to be as close to 1 as possible since end members with particularly low or particularly high tolerance factors will form MPBs with only a small percentage of the new end member in the MPB composition.

## 6.2. The MPB-to-MPB Search

One aim of this work was to find out, whether the concept of the triple MPB introduced in section 3.2.7, could be verified. To approach this triple MPB between rhombohedral BNT, tetragonal BT and orthorhombic KNN, the line in the pseudo-ternary phase diagram (Fig 29, p. 123) connecting the already known morphotropic phase boundary compositions BNT-BKT (20;0) and KNN-BKT (20;100) was investigated.

The broad composition search revealed the central region of this line between 20;20 and 20;90 shows no large field strain or small-signal  $d_{33}$  to speak of. X-ray powder diffraction showed no deviation from pseudocubic in any composition between 20;0 and 20;90. Between composition 20;91 and 20;100 only a tetragonal and orthorhombic mixed phase was found. It was therefore concluded that this triple MPB would not be found along this line in the phase diagram.

However, since composition 20;1 showed the largest bipolar strain known for BNT-BKT-based materials, it was further investigated as a candidate for replacing PZT in certain applications. Moreover, it shows a transitional behaviour between ferroelectric composition 20;0 and non-ferroelectric composition 20;2, which also merited further investigation.

Therefore, a matrix of 10 compositions surrounding 20;1 was created and produced to give a clearer picture of the behaviour of composition 20;1 with respect to its surrounding.

### 6.2.1 Processing and Storage

The processing route was continuously modified and improved throughout the course of the experiments. Initially milling was done at 180 rpm with the powder to milling ball ratio of 1:5. This ratio was later decreased to 1:10 and 10 mm milling balls were added to the 3 and 5 mm milling balls to break up large lumps of carbonate and oxides, which were previously found in milled powder. This improved reproducibility within a single sample batch and reduced the amounts of secondary phases previously found. This was attributed to a higher compositional homogeneity due to improved mixing.

An increase in milling speed to 250 rpm increased the dielectric breakdown strength of the ceramic from between 4 and 6 kV/mm to between 6 and 8 kV/mm, which could be attributed to better sintering due to the smaller grain size.

The cylindrical pressing die was replaced with a custom made model with a very slightly larger diameter on one end of the die than the other, which allows removal of the green body without damaging the edges via the larger diameter opening. This greatly reduced the sample edge quality and consequently the reliability during high field measurements.

Potassium carbonate was eventually stored at a temperature of 90 °C to minimise the absorption of moisture, which improved the reproducibility between different powder batches. Batches produced from newly acquired potassium carbonate and older remaining potassium carbonate were also more comparable once this change had been introduced. These results suggest that the potassium carbonate contained a significant and constantly changing amount of moisture, before this change was introduced.

Long-term storage of the sintered and electroded samples in air proved unsuitable. After 4 to 8 weeks the initial dielectric breakdown strength dropped from around 8 kV/mm to around 4 kV/mm. Storage of the samples submerged in silicon oil proved more successful. However, it did not completely prevent sample degradation. The heating step at above 200 °C for 3 to 5 minutes proved successful in restoring the original dielectric breakdown strength. It is assumed that this is the result of moisture absorption possibly due to small amounts of unreacted potassium within the sample. 10-15 samples of different BNT-BKT-KNN-BKT compositions were submerged in water to test this assumption. After a few months, several had decomposed into powders and after one year only one sample remained visually intact but disintegrated when touched firmly. Since the BNT-BKT-KNN-BKT powder itself appears non-soluble in water, the cause of the reduced dielectric breakdown strength and the sample disintegration is likely a soluble secondary phase at the grain boundaries.

## 6.2.2 Structure and Microstructure

The structure and microstructure of the 10 compositions 19;0 to 21;2 was investigated using powder x-ray diffraction in transmission geometry, x-ray diffraction of the bulk sample in reflective geometry, as well as transmission electron microscopy and scanning electron microscopy.

### 6.2.2.1 X-ray Diffraction

The hard sphere model, which is the basis of the calculation of the Goldschmidt tolerance factor, suggests a linear increase in the unit cell length with increasing xBKT and y(KNN-BKT) proportional to the calculated tolerance factor. Therefore, composition 19;0 would have to have the smallest and composition 21;2 the largest unit cell length, like shown in Fig 35 (p. 130).

The actual trends in the unit cell lengths with composition deviate strongly from this suggested hard sphere model. The exception are compositions 19;0 to 19;2, which show the expected increase in unit cell length with KNN-BKT content. Between the calcined powder and the bulk sample there is a large increase in unit cell length visible for all compositions. This increase in unit cell length can be explained by unreacted potassium still present in the calcined powder, which gives rise to the impurity reflex at  $30.3^\circ$ . This impurity reflex consequently disappears during sintering, which means that the unreacted potassium with the large ionic radius is now incorporated into the perovskite phase.

Regarding line 20;0 to 20;2, there is also a minimum in the unit cell length at composition 20;1. A similar minimum can be found on line 21;0 to 21;2 at composition 21;2.

Normally, the unit cell length of a material changes monotonously with changing composition. At a phase transition, this may change<sup>[3]</sup>. It is, therefore, an indication that a change in structure exists at compositions 20;1 in the 20;Y series and at or beyond composition 21;2 in the 21;Y series. However, since this is only a weak indication of a phase transition and there were no other detectable differences in the diffraction patterns, this conclusion should be viewed with caution. Also, this conclusion only applies to the sintered material, since the amount of secondary phase in the calcined powder is clearly not constant across the 10 compositions, since not all show an impurity reflex of equal magnitude.

The x-ray diffraction patterns collected from the surfaces of poled samples in reflective geometry show the existence of a mixed phase of tetragonal and rhombohedral perovskite type structures. The changes in relative reflex intensity as a function of KNN-BKT content are just the result of different degrees of orientation achieved by the poling process. This mixed phase of tetragonal and rhombohedral perovskite type structures is found in all 10 investigated compositions, which



suggests that the mixed phase region of pure BNT-BKT extends at least between 19 mol% and 21 mol% BKT.

### 6.2.2.2 Microstructure and TEM

The average grain sizes for pure BNT-BKT compositions (19;0 to 21;0) and composition 20;0.5 show an average grain size of 0.7  $\mu\text{m}$ . All other compositions, which contain at least 1 mol% KNN-BKT, show an average grain size of 0.5  $\mu\text{m}$ . The fracture surfaces of compositions 20;0 to 20;2 show highly faceted grains with polyhedral shapes. This suggests that the microstructure is mainly a consequence of solid-state sintering with a high density<sup>[4]</sup>.

Compositions with 1 mol% or more KNN-BKT also show a bimodal grain size distribution, which implies that KNN-BKT acts as a grain growth inhibitor in BNT-BKT. This theory is further supported by the increase in relative density between the KNN-BKT free compositions and the ones containing at least 1 mol% KNN-BKT, since grain growth suppression frequently leads to better densification<sup>[4,5]</sup>.

Large rectangular grains are distributed evenly throughout the bulk of the sample. Initially it was thought that these might be grains with a higher KNN content, since a similar effect is reported in KNN<sup>[6]</sup>. However, TEM and SEM both show the existence of these grains also in the compositions not containing any KNN-BKT. EDS also showed no compositional abnormalities of these grains. The origin of these large rectangular grains can therefore not be conclusively explained.

TEM investigations were done on compositions 20;0 to 20;2. Visual inspection of the microstructure overview shows that the grain size determined by SEM is accurate. The bimodality of the grain size distribution is also confirmed by the TEM overview image.

The increase in contrast to the bright-field micrographs with increasing KNN-BKT content suggests an increase in the number of domains present within the material. At the same time, the streaking of the  $\frac{1}{2}\{00e\}$  tetragonal superstructure reflections shows the existence of the lamellar domain structure with a domain size of only 1 to 2 nm.

Superstructure reflexes prove the existence of a rhombohedral and tetragonal mixed phase. The intensity of the reflexes is sample thickness dependent and cannot be seen as a possible increase or decrease in phase ratios with composition. With the exception of the larger c/a ratio of the tetragonal phase, there are no notable differences seen in the TEM investigation compared with the similar BNT-BT-KNN system<sup>[7-10]</sup>. The two space groups to be assigned to the rhombohedral and tetragonal phases are, therefore, most likely also R3c and P4bm due to the same octahedral tilting a-a-a- and a<sup>0</sup>a<sup>0</sup>c+ respectively, which was reported for the BNT-BT-KNN system<sup>[11]</sup>. The

fact that the mixed phase cannot be seen in the original, not yet electrically cycled, materials, may be attributed to the complex internal stress state of the un-cycled sample. However, TEM investigation clearly proved that the mixed phase seen in the electrically cycled samples is already present in the original un-cycled state. This is also supported by similar results in the BNT-BT-KNN system<sup>[12]</sup>.

### 6.2.2.3 Density

The calculation of the relative density from x-ray powder diffraction results and the Archimedes method showed that the introduction of 1 mol% KNN-BKT into BNT-BKT visibly improves the relative density by approximately 2.5 percentage points. A one percentage point error is assumed due to the necessary deviation from ASTM C20-00 (section 4.2.1). The solubility of potassium and sodium during submersion in water will also affect the values of the absolute density since small amounts of potassium and sodium may still exist in the form of secondary phases beyond the detection limit of X-ray powder diffraction. Interpolation of the data suggests that between 1 mol% and 4 mol% KNN-BKT provides optimum density.

1 mol% KNN-BKT has only negligible effect on the relative ratios of sodium, potassium, bismuth and titanium in pure BNT-BKT compared to the step size between BNT-20BKT and BNT-21BKT. Since there is almost no change in relative density with BKT content in BNT-BKT, it is, therefore, an indication that the densification effect arises from the addition of KNN. Further experiments using only KNN or even  $\text{K}_{0.2}\text{Na}_{0.8}\text{NbO}_3$  to keep the ratio of  $\text{Na}^+$  to  $\text{K}^+$  constant would be necessary to fully verify this.

## 6.3. Room Temperature Electrical Properties

The introduction of KNN-BKT into BNT-BKT leads to significant changes in the room temperature properties, as well as the temperature and frequency dependence of the investigated compositions. The introduction of KNN-BKT causes the high-temperature non-ferroelectric phase to move towards room temperature. The evolution of the composition series 20;0 to 20;2 shows both extremes. Composition 20;0 behaves as the normal relaxor-ferroelectric at room temperature. Composition 20;0.5 shows unexpected results in many measurements and will be excluded from the general discussion. The possible origin of this unexpected behaviour will be discussed separately later.

### 6.3.1 Large Field Strain and Polarisation Behaviour

At 1 mol% KNN-BKT (20;1), a giant strain response can be induced in the material by an electric field. Unlike in the case of the normal ferroelectric 20;0, the strain response shows non-linear behaviour throughout the strain cycle at any given field strength. The largest strain contribution is induced between 4 kV/mm and 6 kV/mm. This phenomenon is already well-documented in BNT-BT-KNN<sup>[11]</sup> and other BNT-based systems<sup>[13]</sup>. In the case of the presented BNT-BKT-KNN-BKT system, composition 20;1 shows a large strain at 6 kV/mm already, while the equivalent BNT-BT-KNN system requires 8 kV/mm for a similarly large strain.

Composition 20;2 still shows a large strain response at 8 kV/mm. The maximum strain at 6 kV/mm is, however, already reduced, which suggests that the onset field for inducing the giant strain response has moved to above 6 kV/mm.

This can be easily verified when comparing the polarisation hysteresis of compositions 20;1 and 20;2 at 6 kV/mm (Fig 44, p. 139 and Fig 45, p. 140). Composition 20;1 shows the antiferroelectric-like double loop behaviour at 6 kV/mm. This double loop behaviour is the result of a field-induced non-ferroelectric-to-ferroelectric phase transition<sup>[14]</sup>. Due to the fact that this type of double loop behaviour is commonly seen in antiferroelectric-to-ferroelectric transition in lead containing antiferroelectrics<sup>[15]</sup> and due to the initial literature report on BNT-BT<sup>[16]</sup>, the non-ferroelectric phases in BNT-BKT derived systems sometimes are considered antiferroelectric. Recent Raman investigations, however, show no antiferroelectric properties in the case of BNT-BT<sup>[17]</sup> and the non-ferroelectric phase is currently just considered nonpolar. Composition 20;2 shows almost no double loop behaviour at 6 kV/mm but some at 8 kV/mm. Unlike in an antiferroelectric material, the polarisation loops of composition 20;1 and 20;2 show no sudden increase in polarisation at a certain onset field. The double loop is only a result of the

way the material depolarises, when the electric field strength is reduced continuously. Most of the polarisation is maintained down to a certain electric field strength, which is 1 kV/mm in the case of composition 20;1 and 3 kV/mm in the case of composition 20;2. This is similar to what is reported for antiferroelectric materials, but no decisive evidence for antiferroelectricity has been reported yet.

The large-signal unipolar strain at 4 kV/mm was recorded for all 10 compositions. The graphs in Fig 49 (p. 144) show that the ferroelectric and non-ferroelectric compositions are easily distinguished by the shape of the polarisation and strain hystereses. The strain and polarisation of the ferroelectric materials are relatively linear with small symmetric hystereses. Composition 20;1 shows the highest unipolar strain and polarisation, which is closely followed by composition 19;2. However, the strain and polarisation of composition 20;1 and 20;2, and to some degree 21;2, are not linear, which would make them unsuitable for applications, which require a linear strain response. The plot of the strain versus polarisation squared (Fig 51, p. 146) can be used to assess the dependence of polarisation and strain with respect to one another. The function  $S(P^2)=a \cdot x^b$  can be used to assess whether the composition is ferroelectric or electrostrictive. A „b“ value of 0.5 and 1 defines perfectly piezoelectric and perfectly electrostrictive behaviour, respectively. Composition 20;0 shows the highest degree of linearity between polarisation and strain and composition 20;2 the highest degree of quadratic behaviour. The intermediate behaviour of composition 21;2 is also best seen in the parameter since it is the only composition whose „b“ parameter is neither below 0.6 (piezoelectric) nor above 0.8 (almost fully electrostrictive). The presented „b“ parameter values between 0.5 and 1 can be used to categorise the developed compositions. However, they should not be used to determine a ratio between ferroelectric and electrostrictive contributions to the strain. As mentioned in the chapter “Basics of Ferroelectrics”, all dielectric materials are inherently electrostrictive. This electrostrictive effect cannot be eliminated but can only be dominated by a large piezoelectric effect. Even accepted purely piezoelectric materials will therefore never show a „b“ parameter of exactly 0.5.

The summaries of the normalised strain, polarisation and coercive field (Fig 46, p. 141 and Fig 47, p. 142) show that the unipolar and bipolar strain always increases and the coercive field<sup>39</sup>

<sup>39</sup> The coercive field value of composition 19;2 at 4 kV/mm poling field does not follow this trend. It is an expected measurement artefact since the true coercive field is too close to the poling field and the materials are therefore not fully poled.

always decreases with increasing KNN-BKT content, as long as the material remains a pure ferroelectric.

The highest normalised strain is found in composition 20;1 at 6 kV/mm. The unipolar value of 620 pm/V is 11 % higher than the 560 pm/V<sup>[11]</sup>, which were reported for the giant strain response in BNT-BT-KNN at 8 kV/mm. The bipolar value of 635 pm/V is only surpassed by textured doped KNN in the field of lead-free piezoceramics<sup>[18]</sup>. For comparison the unipolar and bipolar value of pure BNT-BKT were measured at 300 and 475 pm/V. Pure BNT-BT shows the unipolar value of 240 pm/V<sup>[11]</sup>.

Composition 21;2 (Fig 48, p. 143) is the only material out of the 6 „off-MPB“ compositions (19;Y and 21;Y), whose bipolar strain and polarisation hysteresis suggest that the material is approaching the ferroelectric to non-ferroelectric phase boundary. However, it does not show a giant strain response at room temperature. It then shows more ferroelectric characteristic than composition 20;1. For example its remanent polarisation is still about 50 % of the maximum polarisation while composition 20;1 only shows about 12 %.

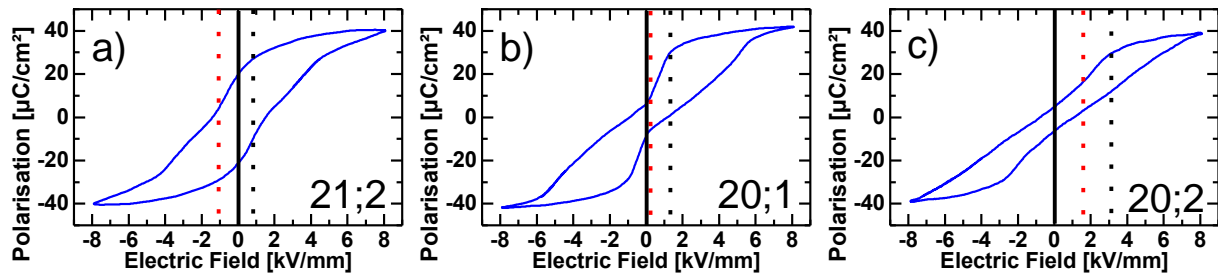


**Fig 84:** The polarisation hystereses of compositions 21;2, 20;1 and 20;2 were used to identify the exact polarisation hysteresis shape required for the induction of a giant strain response. The black dotted line marked the beginning of the field region where the most amount of depolarisation occurs. The red dotted line marked the end of the region where the most amount of depolarisation occurs.

The polarisation hystereses in Fig 45 are of the three compositions, which show pinching in their polarisation hystereses. This pinching is the result of rapid depolarisation within a certain field region. Since composition 20;1 shows the highest strain response of the three compositions, which show a pinched polarisation hysteresis, the conditions for the giant strain response can be identified as follows. The material needs to depolarise as much as possible before the field returns to zero. This allows the material to begin its new strain cycle as if it were a virgin (poling) cycle<sup>[19]</sup>. The second condition is that this region of depolarisation needs to be at the lowest possible electric field strength. Since the region of depolarisation marks the field range, in which this field-induced ferroelectric phase returns to the zero field non-ferroelectric phase. It is reasonable to assume that the field of equal or higher strength is required to induce the mentioned

ferroelectric phase in the first place, even though this onset field cannot be seen on rising flank of the polarisation curve as it would be in an antiferroelectric material. Therefore, if the field region of depolarisation moves to higher field strengths, eventually the ferroelectric phase cannot be fully induced anymore at fields below 8 kV/mm. Composition 20;2 shows this phenomenon. Its polarisation does not reach saturation levels at 8 kV/mm unlike composition 20;1.

Composition 21;2 does not satisfy the first criterion. It only partially depolarises when the field is removed. It can therefore not begin from its unpoled „virgin“ state when the field is reapplied and the recoverable strain is reduced. The issue of recoverable strain will later be further discussed using temperature-dependent results.

### 6.3.1.1 Energy Content/Loss

The energy content/loss of all 10 compositions was calculated from their polarisation hystereses at 4, 6 and 8 kV/mm for bipolar load and at 4 kV/mm unipolar electric load. The energy lost during a single bipolar field cycle generally decreases as the composition series moves through the ferroelectric to non-ferroelectric phase boundary. This behaviour is most clearly shown in composition series 20;Y. The energy content of the ferroelectric materials is reduced with increasing KNN-BKT content as long as the material is fully poled. The deviation seen in composition 20;0.5 will be discussed later.

The energy lost during a unipolar large field cycle shows a maximum at composition 20;1, which is a composition that shows the field-induced phase transition at very low fields. This maximum can be explained by the cycling through the field-induced phase transition, which appears to have significant energy loss associated with it. This maximum in the unipolar energy content is, therefore, one of the most precise ways to identify the compositions showing a field-induced phase transition during a compositional search process.

The unipolar energy loss of composition 20;1 is nearly three times higher than the average energy loss of their purely ferroelectric compositions during the same cycle. This will require the applications for this material to be well-cooled or non-continuous usage scenarios. The decrease in unipolar energy loss seen between composition 20;1 and 20;2 suggests that compositions with higher KNN-BKT content may be more suitable for continuously operating systems. Alternatively, composition 19;2 shows nearly one third of the energy loss but almost the same unipolar strain as composition 20;1 at 4 kV/mm. Furthermore, its strain behaviour is also linear, as expected for a ferroelectric. The energy lost during one unipolar cycle of the ferroelectric compositions is between 60 % and 180 % higher than that of a soft commercial PZT sample<sup>40</sup>

---

<sup>40</sup> Data courtesy of Julia Glaum

(PIC151, PI Ceramics, Lederhose, Germany), which shows a value of 30 kJ/m<sup>3</sup> under the same conditions. This means that BNT-BKT-based lead-free piezoceramics will likely always require an improved thermal design compared to current component designs.

### 6.3.2 Small-Signal $d_{33}$

The small-signal  $d_{33}$  versus composition is an ideal way of identifying the materials, which are capable of showing a field-induced giant strain response. During the initial search process, a step size of 1 mol% KNN-BKT is necessary to identify the compositions with a potential for the field-induced giant strain response. Since the small-signal  $d_{33}$  does not require the sample to survive large field strain and polarisation measurements but only a poling process, it can be used to search a larger number of compositions without having to optimise sintering conditions as much. The necessary poling process is less demanding of sample quality. Starting from purely ferroelectric BNT-xBKT, the composition showing the giant strain response will be the one within 0 to 1 % KNN-BKT of the lowest KNN-BKT content that reduces the small-signal  $d_{33}$  to below approximately 20 % of the value found in the pure BNT-xBKT.

### 6.3.3 Radial Strain

Axial and radial strain were collected simultaneously for all 10 compositions at room temperature applying a maximum electric field strength of 4, 6 and 8 kV/mm. The purpose of this was to determine, whether the field-induced phase transition responsible for the giant strain response in composition 20;1 is the result of a volume change associated with the mentioned phase transition.

The 8 kV/mm bipolar strain cycle of composition 20;1 (Fig 55, p. 151) reveals that there is no significant difference in the volume at any field strength when compared with the ferroelectric compositions. Composition 20;2 also shows no such feature.

The data for composition 20;1 and 21;2 (summarised in Fig 57, p. 153) suggests that a material, which is closest to the field-induced phase transition, also shows the highest increase in volume at 8 kV/mm. However, if these values are set in relation to the corresponding axial strain at 8 kV/mm (Fig 85), it can be deduced that for the ferroelectric compositions the ratio of maximum volume change to maximum axial strain is constant at approximately 30 %. The relative volume contribution decreases in fact as the ferroelectric nature of the material is lost in composition 20;1 and 20;2. It can therefore be concluded that the opposite of the proposed hypothesis is true. Not only is there no increase in volume responsible for the giant strain

response of composition 20;1 but the volume contribution is actually lower in the non-ferroelectric materials than the ferroelectric ones.

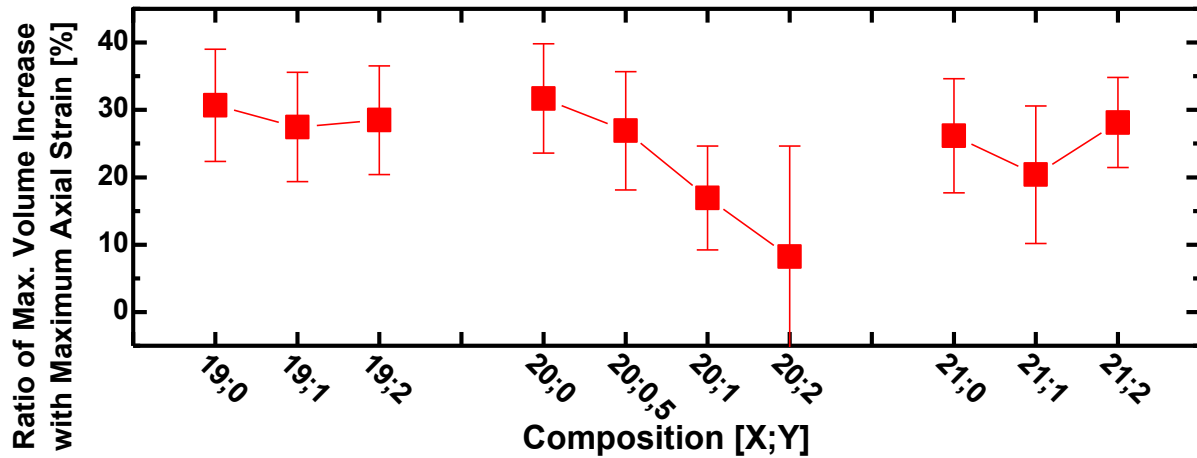


Fig 85: The ratio of the maximum volume increase relative to the maximum strain plotted as a function of composition at 8 kV/mm with the combined error of both values.

Composition 20;2 shows no field-dependent volume hysteresis and composition 20;1 only shows a very small volume hysteresis compared to the purely ferroelectric materials. This suggests that the volume hysteresis is the result of the ferroelectric domain switching process, which causes a small volume contraction during back switching at the coercive field.

### 6.3.4 Composition 20;0.5

Composition 20;0.5 shows the behaviour expected for undoped BNT-BKT. Similar behaviour can be found in PZT, where a small amount of doping is occasionally required to achieve, what is commonly considered the standard behaviour of undoped PZT. In the case of PZT, this is usually explained predominantly as acceptor or donor behaviour of the impurities of the starting materials<sup>[20]</sup>. BiFeO<sub>3</sub>-PT can also show this effect<sup>[21]</sup>. In BF-PT, small amounts of La-doping can reduce the maximum and remanent polarisation although it is generally accepted that the pure BF-PT always shows lower values than the doped material<sup>[22]</sup>. The increase in depolarisation temperature between composition 20; and 20;0.5 may also simply be the result of a systematic deviation during processing. Since the same calcination and sintering containers were used every time to reproduce the same composition it may simply be that the container of composition 20;0.5 sealed more tightly or less tightly and, therefore, prevented or supported bismuth and potassium evaporation more readily than the other containers. Such potential non-stoichiometry has been shown to improve ferroelectric properties<sup>[23,24]</sup>.



## 6.4. Temperature-Dependent Properties

### 6.4.1 Large Field Strain and Polarisation

The large field strain and polarisation was recorded for all 10 compositions between room temperature and 200 °C with the maximum field of 4 kV/mm. It was shown that all compositions, which are ferroelectric at room temperature, show a giant strain response even at 4 kV/mm at their respective depolarisation temperatures. The depolarisation temperature in this case is considered the temperature, where the remanent polarisation shows its steepest drop during the 50 mHz measurement cycle. Equivalently, this is the temperature, where the coercive field decreases the most.

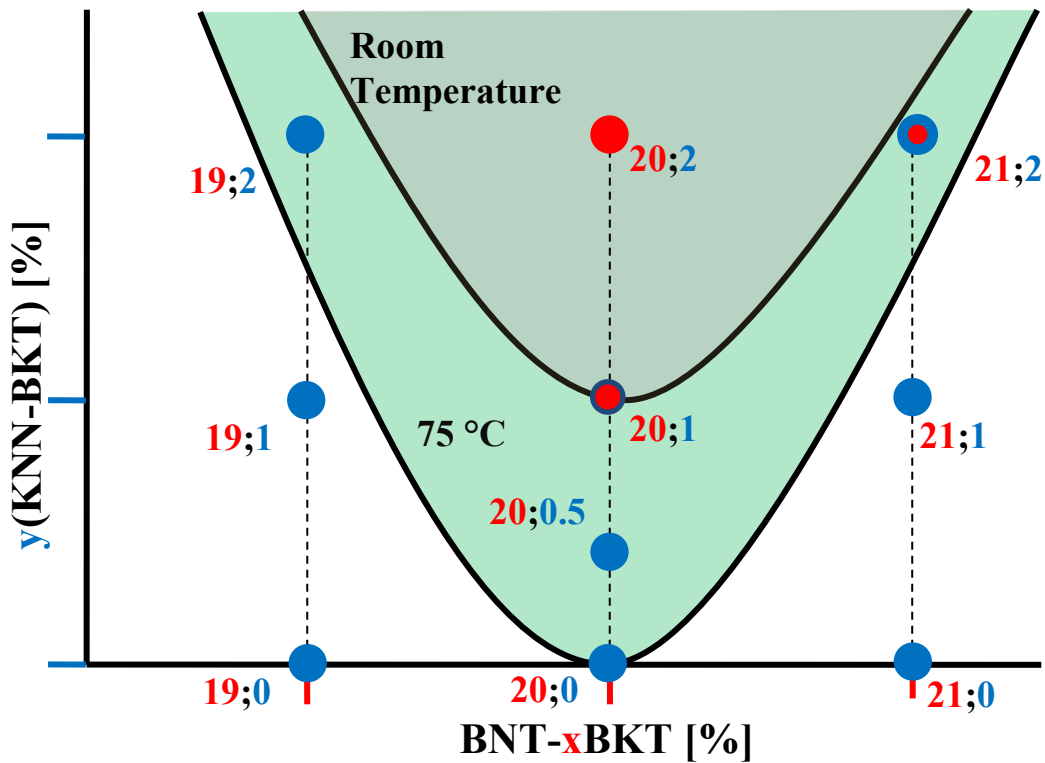


Fig 86: Phase diagram deduced from the matrix of the 10 investigated compositions. The polar phase (white) and the non-polar phase region (green) are shown at room temperature. The room temperature ferroelectric and non-ferroelectric nature of the compositions is denoted by the blue and red colour respectively. The transitional materials 20;1 and 21;2 are coloured according to which type of behaviour dominates at room temperature. At 75 °C, this region encompasses more compositions as shown in light green.

The temperature-dependent giant strain response of composition 19;0, 19;1 and 20;0 is approximately 50 % higher than the one found in compositions 21;0 to 21;2. It was previously determined that the same phenomenon is seen in pure BNT-BT<sup>[25]</sup>, where the material on the tetragonal side of the MPB shows less pronounced giant strain. Even though the tetragonal phase

in composition 21;0 is not seen in the powder x-ray measurements, the behaviour is similar to the one found in tetragonal BNT-9BT.

Compositions 20;1 and 20;2 show almost no temperature dependence of the unipolar and bipolar strain between room temperature and 200 °C, which makes them candidates for actuator applications in this temperature range. However, since they are not piezoelectric, the relationship between the electric field and their resulting strain is not linear but quadratic at all temperatures.

Compared to BNT-BT<sup>[25]</sup> and KNN doped BNT-BT<sup>[26]</sup>, the investigated BNT-BKT-KNN-BKT compositions all show lower conductivity onset temperature of between 100 °C and 125 °C, at which the conductivity of the sample becomes significant enough to affect the polarisation measurements at 50 mHz. Pure BNT-BT shows this issue first at 150 °C and for KNN doped BNT-BT this is reported only at 200 °C.

The remanent strain of all 10 compositions was investigated as a function of temperature. The remanent strain disappears at the temperature, where the giant strain response is found. This is also the temperature, where the unipolar and bipolar strain curves fully overlap.

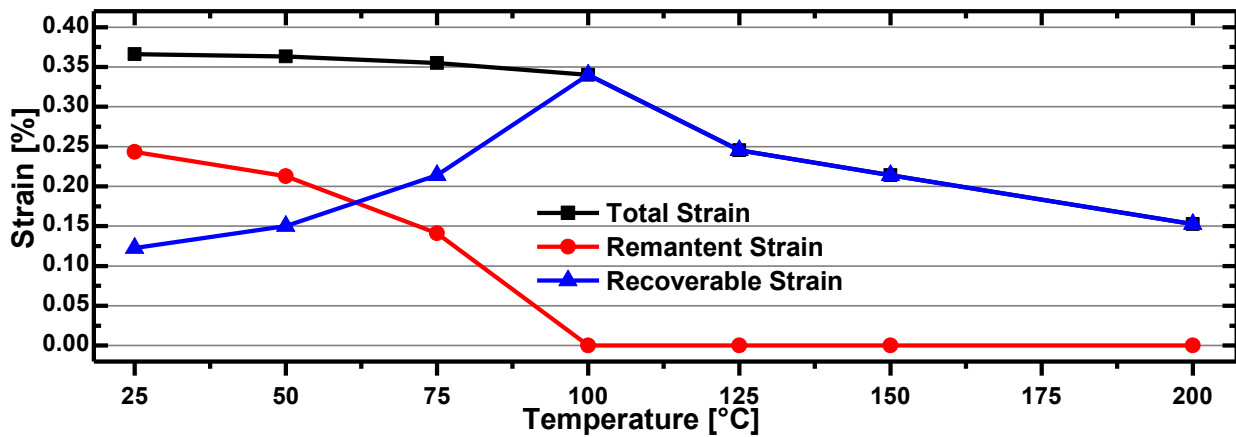


**Fig 87: Remanent and total strain vs. temperature (4 kV/mm) for composition 20;0**

This further supports the assumption that the giant strain response is the result of a depolarisation process within the sample, which allows the sample to return to almost its initial state. Ferroelectrics at room temperature exhibit a remanent strain once poled. If the total strain (i.e. the strain shown by a virgin ferroelectric sample when the field is first applied) is plotted against temperature (Fig 87, black squares), it is found to be nearly identical for all ferroelectric BNT-BKT compositions. It continuously decreases with increasing temperature. The remanent strain (Fig 87, red circles) also continuously decreases with increasing temperature but more quickly. The giant strain response is found at the temperature, where the remanent strain completely disappears, which in turn provides a maximum recoverable strain at this temperature.

During the investigation of the remanent strain with temperature, it was also discovered that the strain response during approximately the first three bipolar field cycles is much larger than the

one seen after three more cycles. This phenomenon is seen in all investigated ferroelectric compositions and at all temperatures where the remanent strain is present. This may be an extreme form of fatigue but its origin was not further investigated. This effect can be restored in the same sample if the sample is unfatigued at 400 °C for only a few minutes. The phase diagram constructed from the temperature-dependent and room temperature large and small-signal behaviour is shown in Fig 86. It was also shown in Fig 68 (p. 165) that the remanent strain increases in composition 19;0 amongst others between room temperature and 37.5 °C. This unusual effect can be explained by the fact that the remanent strain would still increase significantly after one or more cycles (Fig 69, p. 166), which is not the case at higher temperatures. Therefore, the values at higher temperatures are almost the total achievable remanent strain whereas the room temperature values are not.

### 6.4.2 Temperature-Dependent Ferroelastic Properties

An investigation of the temperature-dependent ferroelastic properties of compositions 20;0 to 20;2 revealed unusual effects. It was found that the ferroelastic properties at room temperature are almost independent of KNN-BKT content. Even composition 20;2, which shows no remanent strain in large field strain measurements, shows strong ferroelastic behaviour at room temperature. At elevated temperatures, all materials eventually show no remanent strain anymore. However, before the ferroelastic behaviour disappears completely at around 200 °C, there is a temperature range, where a closed stress-strain loop is seen. This behaviour is the result of a stress-induced ferroelastic phase. The same behaviour is also found in pure BNT-BT where it is attributed to a stress-induced phase transition between nonpolar non-ferroelastic tetragonal space group  $P4/mmm$  and the polar ferroelastic tetragonal space group  $P4mm$ <sup>[27]</sup>. It is proposed, that the same holds true for the BNT-BKT-KNN-BKT system.

### 6.4.3 Temperature-Dependent Permittivity

The temperature-dependent permittivity and loss at frequencies between 1 kHz and 1 MHz was used to identify phase transitions and the depolarisation temperature. It was found that there are two phase transitions, one at  $T_2$  and one at  $T_M$ , which are nearly independent of KNN-BKT content. The depolarisation temperature  $T_d$  is also fully independent of  $T_2$ . The measured depolarisation temperatures are lower than the temperatures reported, where the remanent polarisation almost disappears during the large field electrical measurements. This is expected, since during the large field electrical measurement cycle, the material only has a short time to

depolarise and will therefore show remanent polarisation up to higher temperatures during cycling.

Since the depolarisation process is time-dependent and this time-dependence is a function of temperature, a sample at elevated temperatures may still show remanent polarisation during the 50 mHz large field polarisation cycle since it does not have enough time to fully depolarise at that measurement frequency. The temperature ramp of the temperature-dependent dielectric measurement on the other hand was approximately 2 K per minute, which allows more time for the sample to depolarise at any given temperature.

The time-dependent small-signal  $d_{33}$  measurement also showed that this slow depolarisation is even significant at room temperatures.

The independence of  $T_2$  and  $T_M$  from composition can also be directly correlated with the composition-independent but temperature-dependent ferroelastic behaviour. The phase at temperatures below  $T_2$  shows normal ferroelastic behaviour. The phase between  $T_2$  and  $T_M$  is nonpolar and non-ferroelastic that can be converted into a ferroelastic phase through stress or into a ferroelectric phase through the application of an electric field. The stress-induced ferroelastic phase and the field-induced ferroelectric phase are most likely identical<sup>[27]</sup>.

## 6.5. Frequency-Dependent Properties

The frequency-dependent large-signal bipolar strain and polarisation behaviour was recorded for all 10 compositions. The results show that the frequency dependence of the materials is much higher in the ferroelectric compositions than in the non-ferroelectric compositions. The ferroelectric compositions show that at most 50 % of the strain and polarisation found at 1 Hz is still remaining at 100 Hz. The non-ferroelectric compositions and even the intermediate composition 21;2 maintain around 80 % of their 1 Hz strain and polarisation at 100 Hz. This frequency dependence can be directly correlated with the measured energy dissipation per bipolar cycle. Materials with a large energy loss also show a significantly higher frequency dependence. This suggests that the frequency dependence is mainly due to the slow domain switching process in BNT-BKT-based materials. This conclusion also means that the frequency dependence of the ferroelectric and non-ferroelectric materials would be reversed under unipolar large field conditions. As is the case in PZT-based materials and in BNT-BT<sup>[25]</sup>, the coercive field increases with frequency. The results suggest that BNT-BKT-based ferroelectric materials are unsuitable for any frequency-dependent bipolar applications.

The frequency-dependent strain versus the square of polarisation evolution also supports the theory of the slow domain switching process. It can be seen that as the frequency increases that electrostrictive behaviour of the ferroelectric and non-ferroelectric materials becomes more and more dominant. Composition 20;2 was shown to be almost but not fully electrostrictive at room temperature with a „b“ parameter of 0,84<sup>41</sup>. At 25 Hz and above, composition 20;2 becomes perfectly electrostrictive with a „b“ parameter of 0.98.

---

<sup>41</sup> The function  $S(P^2)=a \cdot x^b$  can be used to assess the degree to which the material is ferroelectric or electrostrictive. A „b“ value of 0.5 and 1 defines perfectly piezoelectric and perfectly electrostrictive behaviour respectively

## 6.6. References

- [1] J.-R. Cheng, N. Li, and L. E. Cross, "Structural and dielectric properties of Ga-modified BiFeO<sub>3</sub>-PbTiO<sub>3</sub> crystalline solutions," *Journal of Applied Physics*, **94**[8] 5153-7 (2003).
- [2] S. Priya, C. W. Ahn, and S. Nahm, "Dielectric Properties of (Ba<sub>0.6</sub>Sr<sub>0.4</sub>)(Cu<sub>1/3</sub>Nb<sub>2/3</sub>)O<sub>3</sub> system," *Ferroelectrics*, **322** 75-82 (2005).
- [3] Y. Hiruma, H. Nagata, and T. Takenaka, "Phase-transition temperatures and piezoelectric properties of (Bi<sub>1/2</sub>Na<sub>1/2</sub>)TiO<sub>3</sub>-(Bi<sub>1/2</sub>Li<sub>1/2</sub>)TiO<sub>3</sub>-(Bi<sub>1/2</sub>K<sub>1/2</sub>)TiO<sub>3</sub> lead-free ferroelectric ceramics," *IEEE Transactions on Ultrasonics Ferroelectrics and Frequency Control*, **54**[12] 2493-9 (2007).
- [4] W. Jo, D.-Y. Kim, and H. Y. Hwang, "Effect of interface structure on the microstructural evolution of ceramics," *Journal of the American Ceramic Society*, **89**[8] 2369-80 (2006).
- [5] C. H. Hsueh, A. G. Evans, and R. L. Coble, "Microstructure development during final/intermediate stage sintering--I. Pore/grain boundary separation," *Acta Metallurgica*, **30**[7] 1269-79 (1982).
- [6] H. Y. Park, C. W. Ahn, H. C. Song, J. H. Lee, S. Nahm, K. Uchino, H. G. Lee, and H. J. Lee, "Microstructure and piezoelectric properties of 0.95(Na<sub>0.5</sub>K<sub>0.5</sub>)NbO<sub>3</sub>-0.05BaTiO<sub>3</sub> ceramics," *Applied Physics Letters*, **89**[6] - (2006).
- [7] L. A. Schmitt and H. J. Kleebe, "Single Grains Hosting two Space Groups - A Transmission Electron Microscopy Study of a Lead-Free Ferroelectric," *Functional Materials Letters*, **3**[1] 55-8 (2010).
- [8] L. A. Schmitt, M. Hinterstein, H. J. Kleebe, and H. Fuess, "Comparative study of two lead-free piezoceramics using diffraction techniques," *Journal of Applied Crystallography*, **43** 805-10 (2010).
- [9] J. Kling, X. Tan, W. Jo, H. J. Kleebe, H. Fuess, and J. Rödel, "In Situ Transmission Electron Microscopy of Electric Field-Triggered Reversible Domain Formation in Bi-Based Lead-Free Piezoceramics," *Journal of the American Ceramic Society*, **In Press** DOI: 10.1111/j.551-2916.010.03778.x (2010).
- [10] L. A. Schmitt, R. Theissmann, J. Kling, M. J. Hoffmann, and H. Fuess, "In situ hot-stage transmission electron microscopy of Pb(Zr<sub>0.52</sub>Ti<sub>0.48</sub>)O<sub>3</sub>," *Phase Transitions*, **81**[4] 323-9 (2008).
- [11] S.-T. Zhang, A. B. Kouna, E. Aulbach, H. Ehrenberg, and J. Rödel, "Giant strain in lead-free piezoceramics Bi<sub>0.5</sub>Na<sub>0.5</sub>TiO<sub>3</sub>-BaTiO<sub>3</sub>-K<sub>0.5</sub>Na<sub>0.5</sub>NbO<sub>3</sub> system," *Applied Physics Letters*, **91**[11] 112906-3 (2007).
- [12] M. Hinterstein, M. Knapp, M. Hölzel, W. Jo, A. Cervellino, H. Ehrenberg, and H. Fuess, "Field induced phase transition in lead-free 0.92BNT-0.06BT-0.02KNN," *Journal of Applied Crystallography*[in press] (2010).
- [13] Y. Hiruma, H. Nagata, and T. Takenaka, "Phase diagrams and electrical properties of (Bi<sub>1/2</sub>Na<sub>1/2</sub>)TiO<sub>3</sub>-based solid solutions," *Journal of Applied Physics*, **104**[12] 124106 (2008).
- [14] B. Jaffe, W. R. Cook, and H. Jaffe. In *Piezoelectric Ceramics*. Academic Press, London, 1971.
- [15] S.-E. Park, M.-J. Pan, K. Markowski, S. Yoshikawa, and L. E. Cross, "Electric field induced phase transition of antiferroelectric lead lanthanum zirconate titanate stannate ceramics," *Journal of Applied Physics*, **82**[4] 1798-803 (1997).
- [16] T. Takenaka, K. Maruyama, and K. Sakata, "(Bi<sub>1/2</sub>Na<sub>1/2</sub>)TiO<sub>3</sub>-BaTiO<sub>3</sub> system for lead-free piezoelectric ceramics," *Japanese Journal of Applied Physics Part 1-Regular Papers Short Notes & Review Papers*, **30**[9B] 2236-9 (1991).
- [17] S.-T. Zhang, A. B. Kouna, W. Jo, C. Jamin, K. Seifert, T. Granzow, J. Rödel, and D. Damjanovic, "High-strain lead-free antiferroelectric electrostrictors," *Advanced Materials*, **21**[46] 4716 - 20 (2009).
- [18] Y. Saito, H. Takao, T. Tani, T. Nonoyama, K. Takatori, T. Homma, T. Nagaya, and M. Nakamura, "Lead-free piezoceramics," *Nature*, **432**[7013] 84-7 (2004).
- [19] W. Jo, T. Granzow, E. Aulbach, J. Rödel, and D. Damjanovic, "Origin of the large strain response in (K<sub>0.5</sub>Na<sub>0.5</sub>)NbO<sub>3</sub> - modified (Bi<sub>0.5</sub>Na<sub>0.5</sub>)TiO<sub>3</sub> - BaTiO<sub>3</sub> - lead-free piezoceramics," *Journal of Applied Physics*, **105** 094102 (2009).
- [20] H. Kungl, "Private Communication," (2007).
- [21] T. Leist, "Private Communication," (2010).
- [22] T. Leist, T. Granzow, W. Jo, and J. Rödel, "Effect of tetragonal distortion on ferroelectric domain switching: A case study on La-doped BiFeO<sub>3</sub>-PbTiO<sub>3</sub> ceramics," *Journal of Applied Physics*, **108**[1] 014103 (2010).
- [23] M. Spreitzer, M. Valant, and D. Suvorov, "Sodium deficiency in Na<sub>0.5</sub>Bi<sub>0.5</sub>TiO<sub>3</sub>," *Journal of Materials Chemistry*, **17**[2] 185-92 (2007).
- [24] Y. R. Zhang, J. F. Li, B. P. Zhang, and C. E. Peng, "Piezoelectric and ferroelectric properties of Bi-compensated (Bi<sub>1/2</sub>Na<sub>1/2</sub>)TiO<sub>3</sub>-(Bi<sub>1/2</sub>K<sub>1/2</sub>)TiO<sub>3</sub> lead-free piezoelectric ceramics," *Journal of Applied Physics*, **103**[7] 074109 (2008).
- [25] C. Jamin, "Influence of the Antiferroelectric Phase on the Strain Level in Bismuth Sodium Titanate - Barium Titanate Lead-Free Piezoelectric Ceramics," *Diploma Thesis, Materials Science, TU Darmstadt* (2008).

- 
- [26] S. T. Zhang, A. B. Kouna, E. Aulbach, and Y. Deng, "Temperature-Dependent Electrical Properties of  $0.94\text{Bi}_{(0.5)}\text{Na}_{(0.5)}\text{TiO}_{(3)}\text{-}0.06\text{BaTiO}_{(3)}$  Ceramics," *Journal of the American Ceramic Society*, **91**[12] 3950-4 (2008).
- [27] K. G. Webber, Y. Zhang, W. Jo, J. E. Daniels, and J. Rödel, "High temperature stress-induced "double looplike" phase transitions in Bi-based perovskites," *Journal of Applied Physics*, **108**[1] 014101 (2010).

## 7. Conclusion

The purpose of this work was to develop new lead-free ferroelectrics, which may eventually replace PZT, the predominantly used ferroelectric material today. A number of concepts were developed with the purpose of broadening the selection of currently known lead-free ferroelectrics. Some initial concepts were later disproven by experiment. The results of these experiments were used to refine the initial concepts into the concepts presented and present number of new potential candidates for investigation.

The concept of combining two ferroelectric materials, which are both already morphotropic phase boundary compositions, in order to further increase the ferroelectric properties was studied in detail. The two base compositions chosen were BNT-BKT<sup>[1]</sup> ( $80\text{Bi}_{0.5}\text{Na}_{0.5}\text{TiO}_3$ - $20\text{Bi}_{0.5}\text{K}_{0.5}\text{TiO}_3$ ) and KNN-BKT<sup>[2]</sup> ( $\text{K}_{0.5}\text{Na}_{0.5}\text{NbO}_3$ - $\text{Bi}_{0.5}\text{K}_{0.5}\text{TiO}_3$ ). Both are morphotropic phase boundary compositions in the pseudo-ternary phase diagram of orthorhombic KNN, rhombohedral BNT and tetragonal BKT.

The study of BNT-BKT-KNN-BKT revealed the presence of a giant strain response owing to a non-polar-to-ferroelectric field-induced phase transition. The magnitude of this giant strain response translates to a unipolar normalised strain of 620 pm/V, which is 11 % higher than previously reported values<sup>[3]</sup> of BNT-BT-based materials using the same general concept of combining MPB compositions. This is mainly due to the lower onset field of the nonpolar-to-ferroelectric phase transition of the BNT-BKT-based systems compared with the BNT-BT-based material, which allows for a 6 kV/mm driving field compared to 8 kV/mm in previous reports. The lower maximum electric field requirement is also important for the development of multilayer actuators since the size of inactive regions inherent in the multilayer design is proportional to the maximum applied field.

The compositional matrix centred on the giant strain composition was used to find a convenient and precise way of searching for further materials of this type using easily obtained small-signal  $d_{33}$  values. This search can then be improved by evaluating the large-signal polarisation behaviour with composition. The condition for a maximal strain response is a high depolarisation at the lowest possible non-negative field strength during the large field polarisation cycle. This allows the material to utilise the total strain, some of which is normally tied up in the form of



remanent strain in normal ferroelectrics. In agreement with results of an investigation into BNT-BT based materials, the highest strain response is found using the MPB composition of the base composition BNT-20BKT or BNT-6BT. The predominantly tetragonal „off-MPB“ compositions based on BNT-21BKT show a less pronounced giant strain.

The temperature-dependent ferroelastic and ferroelectric properties were successfully associated with the temperature-dependent dielectric properties. The phase regions for ferroelectric and non-polar as well as ferroelastic and non-ferroelastic could be correlated with the  $T_d$ ,  $T_2$  and  $T_M$  phase transition temperatures, which separate the ferroelectric and ferroelastic phase regions from the non-polar and non-ferroelastic phase regions.

The developed materials show a range of useful features, which make them interesting for various applications. The highest overall unipolar and bipolar strain provided by composition 20;1 makes it a potential candidate for room temperature actuating applications. Since the material is non-polar at room temperature, depolarisation at higher temperatures is not an issue. It is therefore ideally suited for medical applications where high temperature sterilisation procedures prevent the use of other lead-free materials such as Li-modified KNN<sup>[4]</sup>.

The highest strain at 4 kV/mm with linear behaviour is provided by composition 19;2. Its temperature dependence limits its usability to room temperature, however.

Almost temperature and frequency independent behaviour at 4 kV/mm is provided by compositions 20;1 and 20;2 between room temperature and 200 °C and 50 mHz to 500 Hz. Out of the two materials, 20;1 shows a generally slightly higher strain and composition 20;2 the better frequency and temperature stability.

The actual nature of the non-polar-to-ferroelectric phase transition and the mechanism behind it are still not yet fully understood. Field-dependent TEM investigations are a promising approach in shedding more light on this subject<sup>[5]</sup>. The unipolar frequency dependence of the compositions cannot be correlated to the measured bipolar frequency dependence. Unipolar frequency dependence of materials around the non-polar-to-ferroelectric phase transition has not yet been reported for any material but merit further attention.

## 7.1. References

- [1] A. Sasaki, T. Chiba, Y. Mamiya, and E. Otsuki, "Dielectric and piezoelectric properties of  $(\text{Bi}_{1/2}\text{Na}_{1/2})\text{TiO}_3$ - $(\text{Bi}_{0.5}\text{K}_{0.5})\text{TiO}_3$  systems," *Japanese Journal of Applied Physics Part 1-Regular Papers Short Notes & Review Papers*, **38**[9B] 5564-7 (1999).
- [2] R. Zuo, X. Fang, C. Ye, and L. Li, "Phase Transitional Behavior and Piezoelectric Properties of Lead-Free  $(\text{Na}_{0.5}\text{K}_{0.5})\text{NbO}_3$ - $(\text{Bi}_{0.5}\text{K}_{0.5})\text{TiO}_3$  Ceramics," *Journal of the American Ceramic Society*, **90**[8] 2424-8 (2007).
- [3] S.-T. Zhang, A. B. Kouna, E. Aulbach, H. Ehrenberg, and J. Rödel, "Giant strain in lead-free piezoceramics  $\text{Bi}_{0.5}\text{Na}_{0.5}\text{TiO}_3$ - $\text{BaTiO}_3$ - $\text{K}_{0.5}\text{Na}_{0.5}\text{NbO}_3$  system," *Applied Physics Letters*, **91**[11] 112906-3 (2007).
- [4] E. Hollenstein, D. Damjanovic, and N. Setter, "Temperature stability of the piezoelectric properties of Li-modified KNN ceramics," *Journal of the European Ceramic Society*, **27**[13-15] 4093-7 (2007).
- [5] J. Kling, X. Tan, W. Jo, H. J. Kleebe, H. Fuess, and J. Rödel, "In Situ Transmission Electron Microscopy of Electric Field-Triggered Reversible Domain Formation in Bi-Based Lead-Free Piezoceramics," *Journal of the American Ceramic Society*, **93**[9] 2452-5 (2010).

## **8. Curriculum vitae**

### **8.1. Education:**

Lancing College, Worthing, UK

09/1998 - 07/2000

Oxford University, Oxford, UK: MPhys

10/2001 - 07/2005

Technische Universität Darmstadt: Dr.-Ing

10/2005 – 10/2010

### **8.2. Work history:**

Technische Universität Darmstadt, Reseacher

10/2005 - 9/2009

## 9. Publications

S.-T. Zhang, A. B. Kouna, W. Jo, C. Jamin, K. Seifert, T. Granzow, J. Rödel, and D. Damjanovic, "High-strain lead-free antiferroelectric electrostrictors," *Advanced Materials*, **21**[46] 4716 - 20 (2009).

J. Rödel, W. Jo, K. Seifert, E.-M. Anton, T. Granzow, and D. Damjanovic, "Perspective on the Development of Lead-free Piezoceramics," *Journal of the American Ceramic Society*, **92**[6] 1153-77 (2009).

K. Seifert, W. Jo, and J. Rödel, "Temperature-Insensitive Large Strain of  $(\text{Bi}_{1/2}\text{Na}_{1/2})\text{TiO}_3$ - $(\text{Bi}_{1/2}\text{K}_{1/2})\text{TiO}_3$ - $(\text{K}_{0.5}\text{Na}_{0.5})\text{NbO}_3$  Lead-Free Piezoceramics," *Journal of the American Ceramic Society*, **93**[5] 1392-6 (2010).

## 10. Erklärung

Hiermit versichere ich an Eides Statt, dass ich die vorliegende Dissertation selbständig und nur unter Verwendung der angegebenen Hilfsmittel angefertigt habe. Von mir wurde weder an der Technischen Universität Darmstadt noch an einer anderen Hochschule ein Promotionsversuch unternommen.

Darmstadt, den 14. December 2010,

Klaus Seifert